UNIVERSITÉ DE SHERBROOKE
and
UNIVERSITÉ CATHOLIQUE DE LOUVAIN

Simulations Numériques Avancées d'Éjecteurs Diphasiques au CO_2

Advanced Numerical Simulations of Two-phase CO_2 Ejectors

Thèse de doctorat
Spécialité : génie mécanique

Yu FANG

Jury : Prof. Yann Bartosiewicz (Université catholique de Louvain), co-supervisor
Dr. Matthieu Duponcheel (Université catholique de Louvain), examiner
Dr. Hakim Nesreddine (Hydro-Québec), examiner
Dr. Michal Palacz (Silesian University of Technology), examiner
Prof. Sébastien Poncet (Université de Sherbrooke), supervisor
Prof. Pierre Proulx (Université de Sherbrooke), rapporteur

Sherbrooke (Québec) Canada November 2019

"When nothing seems to help, I go and look at a stonecutter hammering away at his rock perhaps a hundred times without as much as a crack showing in it. Yet at the hundred and first blow it will split and I know it was not that blow that did it — but all that had gone before." —Jacob Riis

Résumé

L'objectif principal de ce travail de thèse est de développer une approche numérique complète capable de simuler de manière précise et rapide l'écoulement et les transferts exergétiques au sein d'éjecteurs transcritiques au CO_2.
Tout d'abord, une méthode tabulée basée sur l'équation d'état de Span-Wagner (SW) est développée pour calculer les propriétés du CO_2 [59] à l'état de vapeur, liquide, supercritique et diphasique. Cette approche est précise et efficace. Les écarts relatifs maximaux par rapport à l'équation d'état de SW sont de 0.23% et 1.2% pour la pression et la vitesse du son, respectivement et l'écart absolu maximal pour la température est de 0.06 K. Dans le cas d'un tube à choc 1D, cette approche s'avère de 66.6 à 90 fois plus rapide que si on utilise l'équation d'état de SW.
Deuxièmement, cette méthode tabulée est couplée à trois solveurs basés sur la densité : CLAWPACK pour les simulations d'écoulements inviscides, *rhoCentralFoam* pour des modélisations RANS (Reynolds-Average Navier-Stokes) essentiellement et AVBP pour des simulations des grandes échelles. Différents cas tests en 1D et 2D sont effectués pour valider l'implémentation de la méthode dans ces trois solveurs. Ces cas incluent les problèmes du tube à choc, de la dépressurisation et de la cavitation.
Troisièmement, afin de se rapprocher des éjecteurs, les tuyères convergentes-divergentes de Nakagawa *et al.* [126] dans des conditions supercritiques et sous-critiques sont simulées à l'aide des solveurs CLAWPACK et *rhoCentralFoam*. On constate que le modèle de turbulence a une influence significative sur les résultats numériques, en particulier pour les tuyères ayant un petit angle divergent. La tuyère de Berana *et al.* [20] est étudiée également. Un choc épais est prédit, ce qui correspond bien aux mesures expérimentales.
Quatrièmement, l'éjecteur de Li *et al.* [110] est examiné via le solveur *rhoCentralFoam* pour une condition on-design. L'analyse des tubes d'exergie proposée par Lamberts *et al.* [100] pour un éjecteur à air est appliquée. La sensibilité de la méthode est discutée. La résolution des gradients a une influence significative sur les termes de destruction. Par conséquent, le maillage et les schémas numériques peuvent affecter fortement l'analyse des tubes d'exergie. Enfin, la théorie de "compound-choking" est étendue à l'écoulement diphasique au CO_2. Elle prédit que l'écoulement est choqué au début de la section de mélange, tandis que selon la ligne sonique, l'écoulement est choqué à la fin de cette section. Finalement, des calculs RANS d'un éjecteur complet sont comparées à de nouvelles mesures faites sur le banc expérimental développé au Laboratoire des Technologies de l'Énergie (LTE, Shawinigan). Un bon accord est obtenu pour le profil de pression pariétale. Les tubes de transport de quantité de mouvement et d'énergie cinétique [124] sont analysés et révèlent une zone de recirculation à l'entrée du flux secondaire. Cependant, la condition de fonctionnement n'est pas appropriée pour les cycles d'éjecteur à expansion (régime off-design).

Mots-clés : CO_2, tuyère, éjecteur, CFD, solveur basé sur la densité, écoulement diphasique, onde de choc, analyse exergétique

ABSTRACT

The main objective of this PhD work is to develop a complete and advanced numerical approach which can achieve a reliable numerical investigation of two-phase CO_2 transcritical flows within supersonic ejectors.
First, a look-up table approach based on the Span-Wagner (SW) EoS is developed to compute the properties of CO_2. It covers the vapor state, liquid state, supercritical state and two-phase state. This look-up table approach is accurate and efficient. The maximum relative discrepancies are 0.23%, 1.2% for the pressure and the speed of sound, respectively and the maximum absolute discrepancy for the temperature is 0.06 K. Moreover, for a 1D shock tube, the speed-up factor ranges from 66.6 to 90 compared to the original SW EoS.
Secondly, this look-up table approach is coupled to three density-based solvers: CLAWPACK for inviscid flow simulations, *rhoCentralFoam* mainly for Reynolds-Average Navier-stokes (RANS) simulations, and AVBP for Large-Eddy simulations (LES). Various test cases in 1D and 2D are performed to validate and verify these three solvers, which include the shock tube problem, the depressurization problem, the cavitation problem, converging-diverging nozzles, and the critical mass flow rate.
Thirdly, in order to investigate more complex phenomena in realistic configurations, the converging-diverging nozzles considered by Nakagawa *et al.* [126] under supercritical and subcritical conditions are investigated through CLAWPACK and *rhoCentralFoam*. The turbulence model is found to have a significant influence on the numerical results, especially for nozzles having a small diverging angle. The converging-diverging nozzle of Berana *et al.* [20] is investigated subsequently. A thick shock is predicted, which agrees well with experimental measurements.
Fourthly, the ejector of Li *et al.* [110] is investigated through the *rhoCentralFoam* solver for one on-design condition. The exergy tube analysis developed by Lamberts *et al.* [100] for a single-phase air ejector is applied, and the sensibility of the method is discussed. The resolution of gradients has a significant influence on the destruction terms. Hence, the mesh and the numerical scheme can strongly affect the exergy tube analysis. Finally, the compound-choking theory is extended for two-phase CO_2 flows to predict the choking condition. The compound-choking theory predicts that the flow chokes at the beginning of the mixing duct while according to the local sonic line the choking location is at the end of the mixing duct. Additionally, the simulations of the CO_2 ejector available at Laboratoire des Techonologies de l'Énergie (LTE, Shawinigan) are performed and compared to new experiments. The wall pressure profile agrees particularly well with the experiments. The transport tubes of momentum and kinetic energy [124] are analysed and a recirculation zone appears at the secondary inlet. However, the operating condition is not appropriate for ejector-expansion cycles (off-design regime).

Keywords: CO_2, converging-diverging nozzle, ejector, CFD, density-based solver, two-phase flow, shock wave, exergy analysis

ACKNOWLEDGEMENTS

This thesis would not have been possible without the kind help, understanding and dedication of many people who, through their presence and advice, have provided me with valuable support. I would like to acknowledge in particular :

My supervisors, Prof. Yann Bartosiewicz and Prof. Sébastien Poncet, for their patience, the wise advice they gave me, and their guidance not only for scientific research but also for personal life. May they find here the expression of all my gratitude.

I would like also to thank the examiners : Prof. Pierre Proulx, Dr. Michal Palacz, Dr. Hakim Nesreddine and Dr. Matthieu Duponcheel for accepting to examine this thesis and giving their important comments.

This project is part of the NSERC chair on industrial energy efficiency established in 2014 at Université de Sherbrooke with the financial support of Hydro-Québec (Laboratoire des Technologies de l'Énergie in Shawinigan), Natural Resources Canada (CanmetEnergy in Varennes) and Rio Tinto Alcan. All calculations have been done using the facilities provided by the Compute Canada (Calcul Québec) network and the Consortium des Équipements de Calcul Intensif (CÉCI), funded by the Fonds de la Recherche Scientifique de Belgique (F.R.S.-FNRS) under Grant No. 2.5020.11. The AVBP solver is provided by Centre Europeéen de Recherche et de Formation Avancée en Calcul Scientifique (CERFACS). The look-up table approach for CO_2 has been developed with the help of the IMSIA Lab of EDF in France. They are all also gratefully acknowledged.

I am also grateful to my friends and colleagues, especially to : Denis-Gabriel, William, Gauthier, Oliver, Philippe, and the rest of the TFL team, my compatriots Yan, Yazhou, Zimin, Ranyan at Université catholique de Louvain ; Marco, Michele in the research group of EDF in France ; Sergio, Srijit, Ibai, Alla-Eddine, my compatriots Hao, Chaofan, Manqi at Université de Sherbrooke. It has been a pleasure to work with you and share laughs, doubts, kicks and goals together.

Last but not the least, I would like to thank my wife and my parents for supporting me throughout this thesis and my life in general.

TABLE OF CONTENTS

LIST OF FIGURES

LIST OF TABLES

LIST OF SYMBOLS

Alphabetic Letters	Units	Definition
a	-	Coefficient for Van der Waals EoS and Peng-Robinson EoS
A	m^2	Cross-section
A	-	Coefficient of interpolation
$\mathcal{A}^-\Delta\mathbf{Q}$	-	Fluctuation propagating to the left along x
$\mathcal{A}^+\Delta\mathbf{Q}$	-	Fluctuation propagating to the right along x
b	-	Coefficient for Van der Waals EoS and Peng-Robinson EoS
b	-	Coefficient for Span-Wagner EoS
B	-	Coefficient for Span-Wagner EoS
B	-	Coefficient of interpolation
$\mathcal{B}^-\Delta\mathbf{Q}$	-	Fluctuation propagating to the left along y
$\mathcal{B}^+\Delta\mathbf{Q}$	-	Fluctuation propagating to the right along y
c	-	Coefficient for Peng-Robinson EoS
c	$m.s^{-1}$	Speed of sound
C	-	Coefficient of interpolation
C_l	-	Coefficient for Span-Wagner EoS
C_p	$J.(kg.K)^{-1}$	Isobaric specific heat
C_S	-	Coefficient in the Smagorinsky model
C_v	$J.(kg.K)^{-1}$	Isochoric specific heat
C_ω	-	Coefficient in the WALE model
d	-	Coefficient for Span-Wagner EoS
d	-	Number of molecular degrees of freedom
d	m	Nozzle's diameter
D	m	Ejector's diameter
D	-	Coefficient of interpolation
D_m	-	Coefficient for Span-Wagner EoS
e	$J.kg^{-1}$	Specific internal energy
e_s	$J.kg^{-1}$	Specific sensible energy
E	$J.kg^{-1}$	Specific total energy
F	-	Flux vector
$\mathbf{F}^h$	-	Correction flux vector along x
F_m	$kg.m^{-1}.s^{-2}$	Momentum flux
F_K	$kg.s^{-3}$	Kinetic energy flux
F_q	$kg.s^{-3}$	Heat transfer flux
F_ξ	$kg.s^{-3}$	Total exergy flux
g	$J.kg^{-1}$	Gibbs energy
g_{ij}	s^{-1}	Velocity gradient
$\mathbf{G}^h$	-	Correction flux vector along y
h	$J.kg^{-1}$	Specific enthalpy
i	-	Numbering of the cell along Y in the $X-Y$ space
I	-	Dimensionless cumulative transfer quantities along the dividing streamline
$\mathbf{I}$	-	Identity matrix
j	-	Numbering of the cell along X in the $X-Y$ space
j	$J.m^{-2}.s^{-1}$	Heat diffusion term
J		Dimensionless cross-sectional total exergy flux
k	$J.kg^{-1}$	Turbulence kinetic energy
K	-	Relaxation coefficient of NSCBC
K	$J.kg^{-1}$	Mean-flow kinetic energy
l	m	Nozzle's length
L	m	Ejector's length
L	-	Vector of characteristic waves

Ma	-	Mach number
$\dot{m}$	$kg.s^{-1}$	Mass flow rate
n	-	Coefficient for Span-Wagner EoS
n	-	Normal vector
p	Pa	Static pressure
P_c	Pa	Critical pressure
p_∞	Pa	Pressure correction for stiffened gas EoS
Pr_t	-	Turbulent Prandtl number
$\mathbf{Q}$	-	Vector of variable in the Godunov-type method
q	$J.m^{-2}.s^{-1}$	Heat diffusion term
Q_r	$J.m^{-3}.s^{-1}$	Chemical source term for reacting flow
r	$J.(kg.K)^{-1}$	Specific gas constant, R/W
r	m	Radius
R	$J.(mol.K)^{-1}$	Perfect-gas constant
Re	-	Reynolds number
s	$J.kg^{-1}$	Specific entropy
S	$m.s^{-1}$	Wave propagating speed
S	-	Speed-up factor
Sc_t	-	Turbulent Schmidt number
S_{ij}	s^{-1}	Stain rate tensor
t	-	Coefficient for Span-Wagner EoS
t	-	Tangential vector
t	s	Time
T	K	Temperature
$\mathbf{T}$	$N.m^2$	Stress tensor
T_c	K	Critical temperature
Tr	-	Trace of a matrix
$\mathbf{u}$	$m.s^{-1}$	Velocity vector
u, v, w	$m.s^{-1}$	Velocity components in the x, y, z directions
U	-	Vector of conservative variables
v	$m^3.kg^{-1}$	Specific volume
V	m^3	Molar volume of the gas
$\mathcal{W}$	-	Vector of wave strength in the HLLC solver
W	$kg.mol^{-1}$	Molar mass
x	-	Thermodynamic quality or vapor quality
X	-	Coordinate in transformed space
$\overline{x}$	-	Equilibrium quality
y^+	-	Dimensionless wall coordinate
Y	-	Coordinate in transformed space
Y	-	Fraction of species
Δs	$J.(kg.K)^{-1}$	Entropy change across a shock
Δt	s	Time step
Δx	m	Space step in the x-direction
Δy	m	Space step in the y-direction
∂U	-	Vector of conservative variables
∂V	-	Vector of primitive variables
∂V_n	-	Vector of primitive variables normal to boundary
∂W	-	Vector of characteristic variables

Greek Letters	Units	Definition
α_k	-	Void fraction, phase density function, space fraction
α	-	Coefficient for Span-Wagner EoS
α	-	Weight factor
β	-	Coefficient for Span-Wagner EoS
β	-	Total pressure loss across a shock
β_a	$Pa.m^3.kg^{-1}$	Formulation of derivatives in AVBP
δ	-	Reduced density
δ	m	Shock location
Δ	-	Coefficient for Span-Wagner EoS
Δ	-	Dimensionless balance of the total exergy
ϵ	$J.(kg.s)^{-1}$	Dissipation rate of the turbulence kinetic energy
ϵ	-	Coefficient for Span-Wagner EoS
γ	-	Heat capacity ratio
γ	-	Coefficient for Span-Wagner EoS
γ	-	Coefficient of interpolation
γ	-	Pressure ratio across a shock
Γ	-	Dimensionless cumulative destruction of the total exergy in an exergy tube
κ	$Pa.s$	Bulk viscosity
λ	-	Eigenvalues of Jacobian matrix
μ_t	$Pa.s$	Turbulent viscosity
μ	$Pa.s$	Dynamic viscosity
ν_{sgs}	$m^2.s^{-1}$	Eddy-viscosity in SGS model
ω	-	Entrainment ratio
ω	T^{-1}	Rate of turbulent dissipation
ω	-	Acentric factor
ω_f	$m^3.s^{-1}$	Volumetric flux based on speed of sound
ω_T	$J.m^{-3}.s^{-1}$	Chemical source term for reacting flow
Ω	-	Integration domain
ϕ	-	Friction coefficient
ϕ_f	$m^3.s^{-1}$	Volumetric flux at the interface
ψ	-	Dimensionless Helmholtz free energy
Ψ	-	Converted variables
Φ	$J.K^2.m^{-3}.s^{-1}$	Destruction terms of the total exergy
Π	-	Dimensionless cumulative destruction of the total exergy in a secondary stream
ρ	$kg.m^{-3}$	Density
θ	^{o}	Diverging angle
θ	-	Asymptotic function
τ	-	Reduced temperature
τ	s^{-1}	Relaxation time
τ	$N.m^2$	Stress tensor
ξ	$J.kg^{-1}$	Total exergy

superscript	Definition
2nd	2^{th} order
0	Ideal part of dimensionless Helmholtz free energy
-1	Inverse of a matrix
adv	Advective part
h	High-order correction term
m	Numbering of the wave
r	Residual part of dimensionless Helmholtz free energy
T	Transpose of a matrix
WALE	Quantities for WALE model
t	Sub-grid term
n	Numbering of the time step
subscript	
01	Stagnation pressure at primary inlet
1	Primary inlet
02	Stagnation pressure at secondary inlet
2	Secondary inlet
b	Back pressure at the ejector's outlet
c	Converging part
cro	Croquer et al.
d	Diverging part
diff	Diffuser
e	Derivative at constant internal energy
exp	Experiment
h	Hydraulic diameter
in	Inlet
K	Quantities related to the kinetic energy
L,l	Left state
l	Liquid state
m	Mixture
m	Quantities related to the momentum
max	Maximum value
min	Minimum value
mix	End of the diffuser
n	Normal vector
out	Outlet
p	Derivative at constant pressure
pm	Primary nozzle exit
prim, primary	Primary nozzle
q	Quantities related to the heat transfer
R,r	Right state
ref	Reference value
NXP	Primary nozzle exit position
s	Derivative at constant entropy
sec, secondary	Secondary inlet
sa	State before a normal shock
sat	Saturation state
sgs	Sub-grid quantities
sb	State after a normal shock
sm	Suction nozzle
smo	Smolka et al.

t	Time derivative
t	Turbulent quantities
ta	Taslimi Taleghani et al.
tar	Target pressure at outlet boundary
tot	Total quantities
th, t	Primary nozzle throat
U	Conservative variables
v	Vapor state
V	Primitive variables
v	Derivative at constant specific volume
w	Width
x	Derivative at constant quality
y	Inlet of the mixing duct
δ	Derivative of reduced density
ρ	Derivative at constant density
τ	Derivative of the reduced temperature
Θ	Exergy destruction term through heat transfer
ξ	Quantities related to the total exergy
*	Middle state

LIST OF ACRONYMS

Abbreviations	Definition
ARK	Equation of State of Aungier
AUSM	Advection Upstream Splitting
BWR	Benedict-Webb-Rubin
CDPC	Compressor Discharge Pressure Cycle
CERFACS	Centre Européen de Recherche et de Formation Avancée en Calcul Scientifique
CFD	Computational Fluid Dynamics
CFL	Courant–Friedrich–Levy
COP	Coefficient Of Performance
CR	Compression Ratio
DNS	Direct Numerical Simulation
DEM	Delayed Equilibrium Model
EAbRS	Ejector-absorption Refrigeration System
EAdRS	Ejector-adsorption Refrigeration System
EERC	Ejector Expansion Refrigeration Cycle
EERS	Ejector Expansion Refrigeration System
EoS	Equation of State
ERS	Ejector Refrigeration System
FORCE	First Order Centered scheme
GWP	Global Warming Potential
HEM	Homogeneous Equilibrium Model
HLLC	Harten-Lax-van Leer-Contact
HRM	Homogeneous Relaxation Model
HT	High Temperature
LES	Large-Eddy Simulation
IAPWS	International Association for the Properties of Water and Steam
IFP	Institut Français du Pétrole
LH	Left High subdomain
IHE	Isentropic Homogeneous Equilibrium
IHEC	Internal Heat Exchanger Cycle
LKP	Plöcker and Knap and Prausnitz EoS
LL	Left Low subdomain
LRC	Liquid Recirculation Cycle
LTE	Laboratoire des Technologies de l'Énergie
LW	Lax-Wandroff scheme
MERS	Multi-components Ejector Refrigeration
MUSCL	Monotone Upstream-Centered scheme for Conservation Law
MUSTA	MUlti-STAge predictor-corrector approach
NSCBC	Navier-Stokes Characteristic Boundary Condition
NXP	Nozzle Exit Position
ODP	Ozone Depletion Potential
OP	Operation Point
OUCL	Oxford University Computing Laboratory
PR	Peng-Robinson
PRBM	Boston and Mathias
RANS	Reynolds-Averaged Navier-Stokes
RGP	Real Gas Properties
RHS	Right Hand Side
RK	Runge-Kutta
RNG	Renormalisation group model
RSM	Reynolds Stress equation model
R744	Carbon Dioxide

SERS	Single Ejector Refrigeration System
SG-EoS	Stiffened Gas Equation of State
SGS	Sub-Grid Scale
SIMPLEC	Semi-Implicit Method for Pressure-Linked Equations Consistent
SoERS	Solar-driven Ejector Refrigeration System
SRK	Soave-Redlich-Kwong
SST	Shear-Stress Transport
SW	Span-Wagner Eos
TERS	Transcritical Ejector Refrigeration System
TPH	Two-Phase High subdomain
TPL	Two-Phase Low subdomain
TPM	Two-Phase Middle subdomain
TTGC/TTGC4A	Two-step Taylor-Galerin schemes
UCL	Université catholique de Louvain
VCRC	Vapor Compression Refrigeration Cycle
VJRC	Vapor Jet Refrigeration Cycle
WALE	Wall Adapting Linear Eddy model

CHAPTER 1

Introduction

Ejectors have been widely used in various fields, such as in refrigeration, desalination, petroleum refining and chemical systems. Depending on the application, the length of the ejector varies from several meters for the desalination of sea water [152] to several centimeters for the air-conditioning in a vehicle [180]. Regarding refrigeration applications, the use of ejectors has various advantages. Firstly, it can reduce the throttling losses caused by the expansion valve in a conventional cycle. Secondly, in Ejector Refrigeration Systems (ERS), compression can be achieved by using low-grade thermal energy, such as solar energy or industrial waste heat, which can reduce the combustion of fossil fuels and limit the emission of greenhouse gases. Moreover, no moving part is involved in the device, thus the construction, the installation and the maintenance are very simple with low cost.

In this chapter, the main features of supersonic ejectors are presented, including the principle and their characteristic parameters. The second part is dedicated to the main applications of ejectors in the refrigeration industry including different refrigeration cycles published so far. Finally, one will consider the particular case of a CO_2 two-phase ejector used in a transcritical cycle, which represents the main objective of this thesis.

1.1 Main features of supersonic ejectors

An ejector is composed of two converging-diverging nozzles, named the primary and the secondary nozzles as shown in Figure 1.1(a). These two nozzles are coaxial and the primary nozzle is located inside the secondary one. The principle of a supersonic ejector can be summarized as follows : the primary high pressure flow (p_{01}, T_{01}) expands through the primary (motive) nozzle and becomes supersonic at the outlet of the motive nozzle. The supersonic flow entrains the secondary flow at lower stagnation pressure (p_{02}). Then, the two flows with different velocities and temperatures mix in the mixing duct by exchanging momentum and energy. Finally, the mixture flow is compressed in the diffuser. Two aims can be achieved : one is the entrainment of the secondary flow, the other being its compression. Hence, the performance of an ejector is generally assessed by two characteristic parameters :

- The compression ratio, $CR = \frac{p_b}{p_{02}}$, which is the ratio of the total pressure between the ejector outlet (p_b) and the secondary inlet (p_{02}) ;
- The entrainment ratio, $\omega = \frac{\dot{m}_2}{\dot{m}_1}$, which is the ratio between the secondary ($\dot{m}_2$) and primary ($\dot{m}_1$) mass flow rates.

Figure 1.1(b) illustrates the characteristic curve of an ejector, which is presented by the entrainment ratio versus the back pressure. In this curve, by keeping the inlet pressures (primary and secondary) constant and increasing the back pressure gradually, three distinct regimes are obtained. In the on-design regime, the primary flow and the secondary flow are both choked, which means that the variation of the back pressure cannot affect the entrainment ratio. The outlet information cannot propagate upstream the chocked section. Beyond the critical point, as the back pressure increases, the entrainment ratio decreases, because the secondary flow is no longer choked. The ejector works in the off-design regime and the efficiency of the ejector decreases. Increasing further the back pressure beyond a breakdown pressure, a reverse flow occurs at the secondary inlet and the ejector does not work properly. Usually the choking condition of the secondary stream can be defined when the sonic line reaches the ejector wall. The secondary stream becomes then totally supersonic. Recently, Lamberts *et al.* [101] proposed a novel criterion for the choking condition by using the compound choking theory.

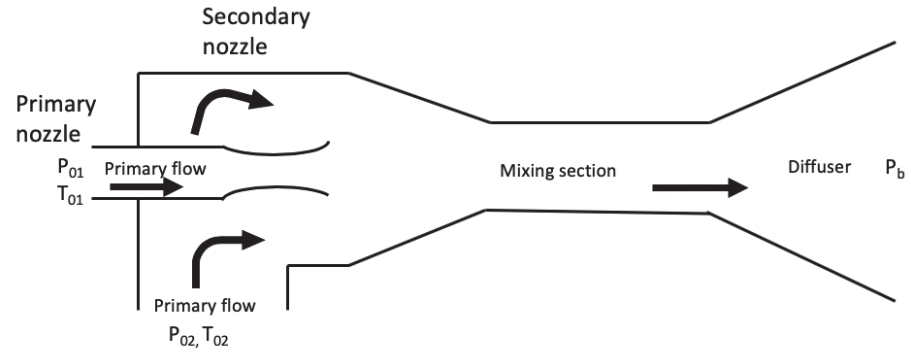

(a)

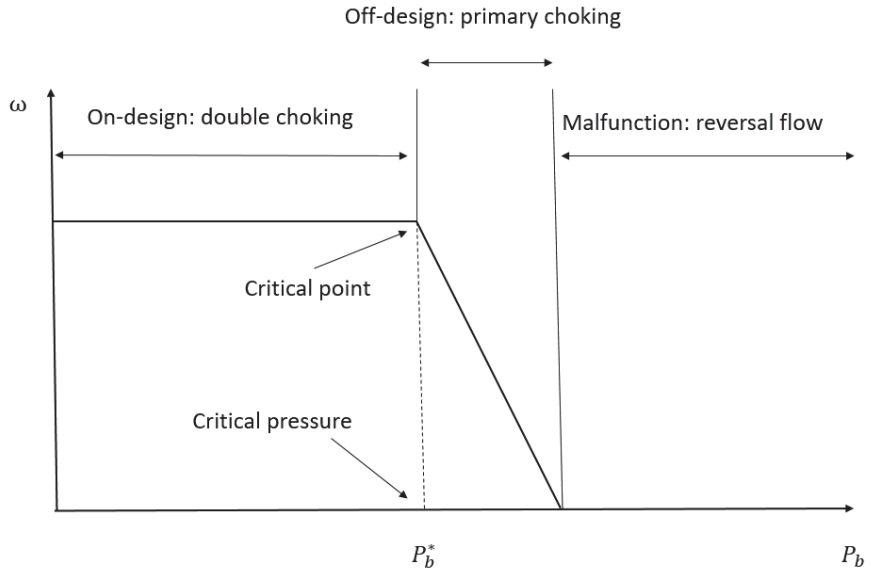

(b)

Figure 1.1 (a) Schematic view of a typical ejector. (b) Ejector characteristic curve.

1.2 Ejector refrigeration systems

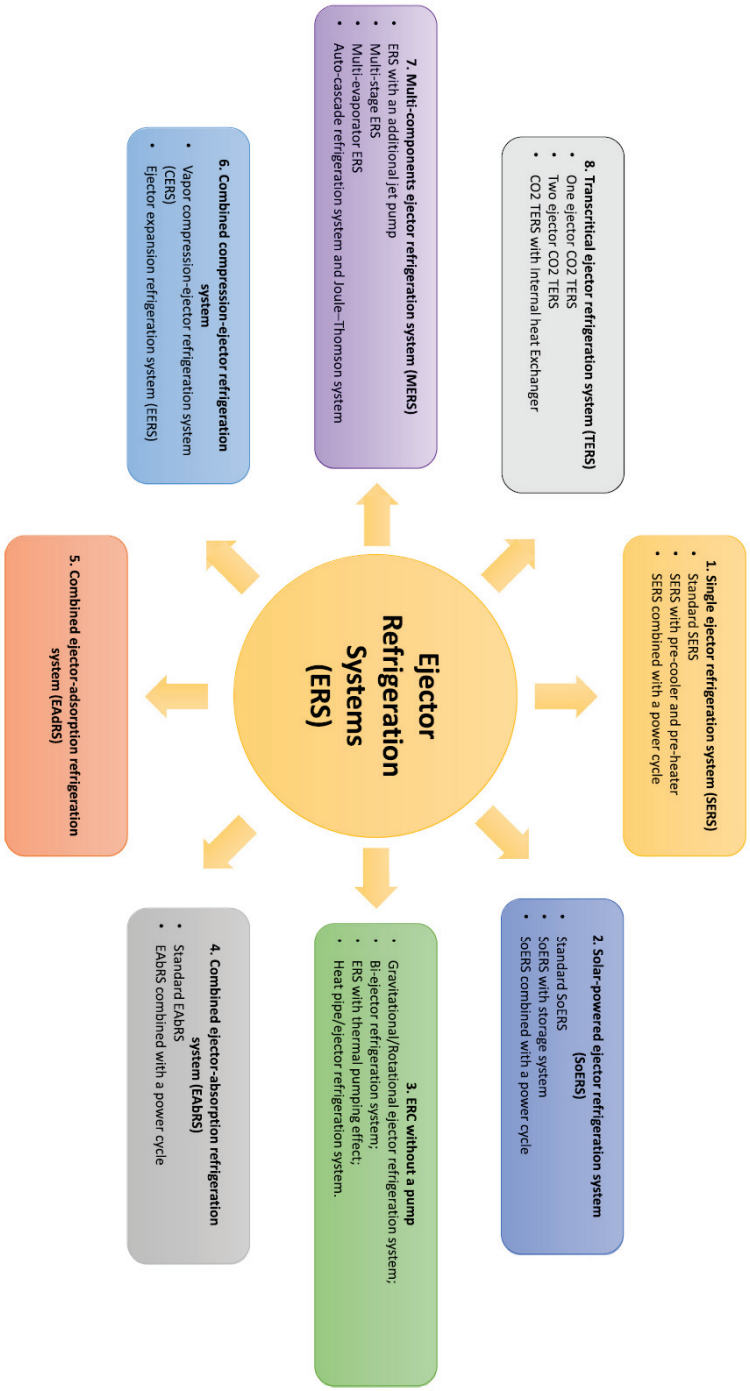

Figure 1.2 Overview of ejector-based refrigeration systems, after Besagni *et al.* [22].

In the literature, ejector technologies have been reviewed by Aidoun *et al.* [2, 3], Chen *et al.* [35], Chunnanond and Aphornratana [37], Elbel and Lawrence [55], Grazzini *et al.* [75], Riffat *et al.* [145], Sarkar [154], Sumeru *et al.* [168]. Besagni *et al.* [22] proposed recently eight ERS covering the main refrigeration technologies as shown in Figure 1.2.

The **first** category shown in Figure 1.2 is the Single Ejector Refrigeration System (SERS) which is divided into three sub-categories : (i) standard SERS, (ii) SERS with a pre-cooler and a pre-heater and (iii) SERS combined with a power cycle. The SERS is depicted in Figure 1.3(a). The generator supplies the high pressure saturated vapor to entrain the low pressure vapor from the evaporator into the ejector. The mixed flow leaves the ejector into the condenser, where the condensation releases the heat to the environment. Then, one part of the liquid expands through the throttling valve and is supplied to the evaporator. The other part of the liquid is pumped back to the generator. For the second SERS presented (not shown here), a pre-cooler and pre-heater are added in SERS to reduce the heat in the generator and cooling load in the evaporator and to improve the efficiency of the system [37]. The third SERS is combined with the Organic Ranking or Gas Turbine in order to absorb and reuse the rejected heat energy [202] (not shown here).

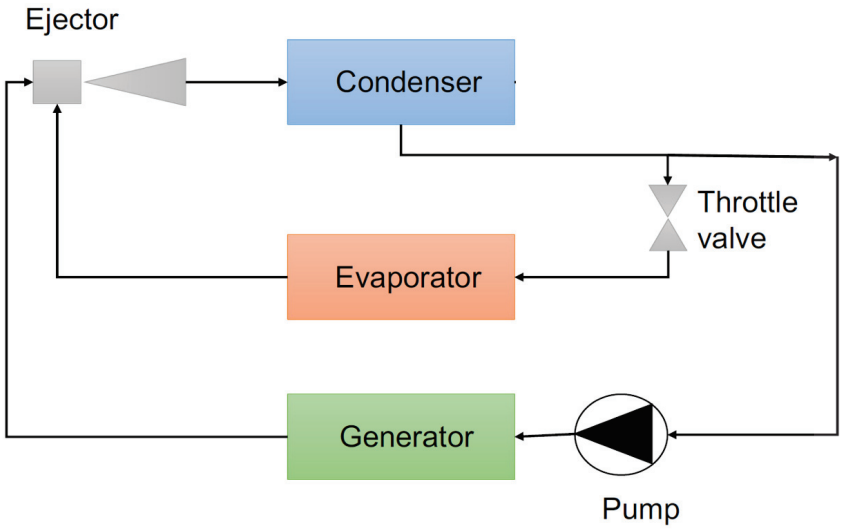

Figure 1.3 Standard ejector refrigeration system, after Besagni *et al.* [22].

The **second** category is the Solar-driven Ejector Refrigeration System (SoERS), in which two types of system are presented, Standard SoERS and SoERS with storage as shown in Figure 1.4. The SoERS is the combination of the SERS with a solar system (Figure 1.4) which offers an amount of energy to the generator. In the SoERS with storage, the storage tank makes sure the continuous energy supply to overcome changes in the ambiant conditions [35].

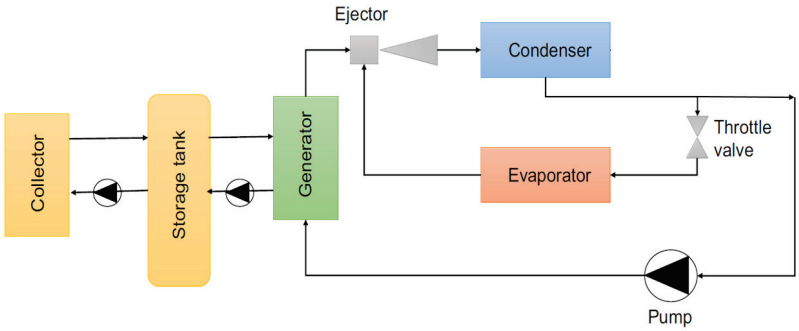

Figure 1.4 Solar-driven ejector refrigeration system, after Besagni *et al.* [22].

The **third** category is the Ejector Refrigeration System without pump. In this category, there are gravitational/rotational ejector refrigeration system, bi-ejector refrigeration system, ERS with thermal pumping effect, and heat pipe/ejector refrigeration system. The main idea is that in these systems, the pump work is provided by other methods without the use of electricity in order to save energy and to extend the lifetime of the system.

The Combined Ejector-Absorption Refrigeration Systems (EAbRS) [35] is the **fourth** category. The advantage of adding the ejector in the absorption cycle is to improve the system performance. The Coefficient of Performance (COP) can reach up to 2.4 and the mass flux of refrigerant from the evaporator can increase [35]. The Combined Ejector-Adsorption (EAdRS) (**fifth**), Combined compression-ejector refrigeration system (**sixth**), and Multi-components Ejector Refrigeration System (MERS) (**seventh**) are not detailed here.

The last one is the Transcritical Ejector Refrigeration System (TERS) which is considered in this thesis. In this system, two-phase CO_2 ejectors are used to replace the expansion valve. As a result, the compression work and the throttling losses are reduced, to lead efficiency improvement. In Figure 1.5, an ejector-expansion refrigeration cycle proposed by Li and Groll [109] is shown. This is somehow different to a standard ejector-expansion cycle. One more throttle valve is used to feed back a part of the vapor to the evaporator, in order to maintain the steady-state operating condition.

Different to the subcritical ejector refrigeration system, the TERS operates with refrigerants over the critical conditions. The ejector could be a two-phase ejector due to the flashing phenomenon in the primary nozzle. The COP of TERS is typically around 0.75, which is 67% higher than that of the subcritical cycle [199]. Two possible TERS are presented in Figure 1.5, one with an ejector, the other with two ejectors. It has been proven

that the performance of the TERS depends significantly on the ejector itself [30], thus more attention should be paid to ejectors both from experimental and numerical aspects.

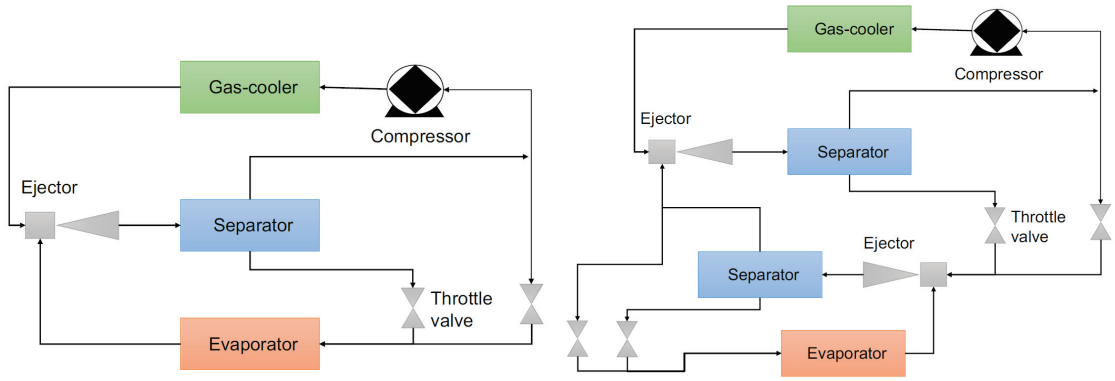

Figure 1.5 (a) Transcritical ejector expansion refrigeration system and (b) Two-stage transcritical ejector expansion refrigeration system proposed by Li and Groll [109].

1.3 CO_2 two-phase ejector in transcritical cycles

Over the last decades, the refrigeration, air conditioning and heat pump industries have been forced through major changes caused by restrictions on refrigerants. According to the present European legislation (Regulations EC No 2037/2000 and No 842/2006) [57, 129], there are some restrictions for the use of refrigerants having a Global Warning Potential, $GWP > 150$ and high Ozone Depletion Potential (ODP). Most of currently used synthetic refrigerants do not meet such requirement, as shown in Table 1.1.

Table 1.1 GWP and ODP of working fluids used in refrigeration systems.

Working fluids	GWP	ODP
R11	4750	1
R12	10,900	1
R22	1790	0.05
R134a	1370	0
R410a	2100	0
R245fa	1050	0
R290 (Propane)	20	0
R744 (CO_2)	1	0
R717 (Ammoniac)	0	0

Carbon dioxide (R744) as one of the natural fluids can be treated as a potential substitute for most of synthetic refrigerants commonly used in refrigeration, air-conditioning and heat

pump systems. CO_2 is a natural substance non-toxic, non-flammable, and easily obtained. It has a low GWP and zero ODP [1, 13, 30, 48, 109, 127, 194, 201]. CO_2 properties are summarized in Table 1.2.

Table 1.2 CO_2 (R744) Properties.

Property	Value
molar mass $[kg.mol^{-1}]$	0.0440098
ASHRAE class	A1
Triple point temperature $[K]$	216.59
Triple point Pressure $[Pa]$	517964.34
Critical point temperature $[K]$	304.12
Critical point pressure $[MPa]$	7.3773
Critical point density $[kg.m^{-3}]$	467.6

Due to its thermodynamic properties under nominal operating conditions (the critical temperature of CO_2 is about $31°C$), the CO_2 cycle needs to operate under transcritical conditions. However, important losses occur during the expansion of CO_2 through the throttling valve [94]. Those throttling losses are large because of the large pressure ratio through the valve. As shown in Figure 1.6, the throttling losses through an isenthalpic process are higher for CO_2 than other synthetic refrigerants (R134a, R140a) in a conventional refrigeration system (using expansion valve). However, it also means that CO_2 has higher potential of efficiency improvement.

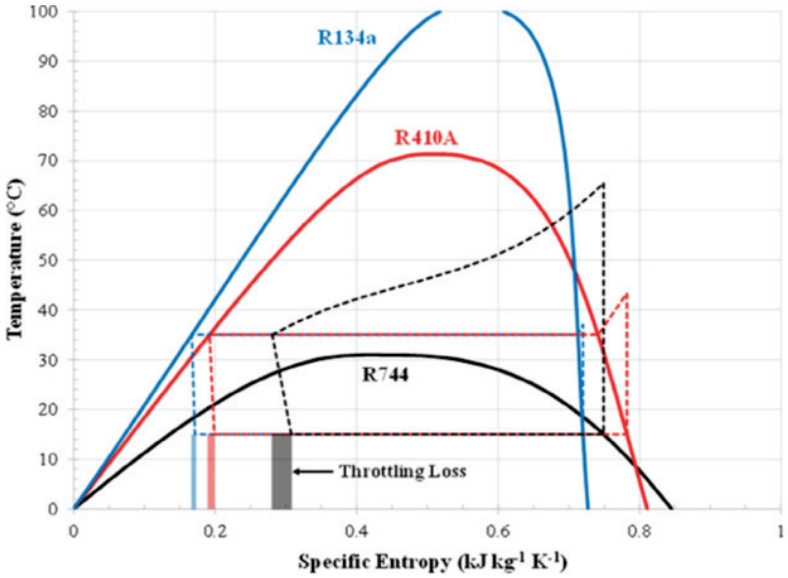

Figure 1.6 Vapor-compression cycle with isenthalpic expansion shown on a temperature-specific entropy diagram for R744 (CO_2), R410A, and R134a, after Elbel and Lawrence [55].

In fact, there are several ways to improve the performance of vapor-compression refrigeration cycles. The use of an internal heat exchanger is a classical and widely used method [128]. A promising technology to recover a significant part of these losses is to replace the classical throttling valve by a two-phase ejector (see Figure 1.7). It can also get a compression work on the refrigerant stream coming from the evaporator. The idea of using a two-phase ejector in a vapor-compression refrigeration cycle has been first proposed by Lorentzen [115] and further developed during the last decades [96, 121, 153, 169, 203]. The first ejector expansion transcritical CO_2 refrigeration cycle was proposed by Liu *et al.* [114]. By integrating a CO_2 two-phase ejector in TERS, one can obtained the same performance compared to standard systems using standard synthetic refrigerants. The experimental investigations on the CO_2 transcritical cycle by Elbel and Hrnjak [54] reported an improvement in terms of COP and cooling capacity by 7% and 8%, respectively compared to the conventional refrigeration cycle using CO_2. Moreover, in Canada, one estimates that 10% of the total energy consumption comes from cooling and 1% of improvement could save about 270 MWh per year equivalent to 1.3 millions of oil barrels [141].

A typical schematic sketch of CO_2 TERS is shown in Figure 1.7(a) and pressure-specific enthalpy diagram is depicted on Figure 1.7(b). The motive flow coming from the gas cooler is in the supercritical state (point 3). It is expanded through the primary converging-diverging nozzle (from point 3 to point 4). As a result, its high stagnation pressure is converted into kinetic energy. In the $p-h$ diagram, the flow state penetrates the saturation curve on the liquid side (blue curve) and finally becomes two-phase (point 4). This rapid phase transition is usually named 'flashing' and it occurs usually near the throat of the converging-diverging nozzle. Due to flashing, the speed of sound decreases rapidly, thus the flow could become supersonic immediately. Hence, at the exit of the motive nozzle, a low-pressure supersonic two-phase jet can be obtained. It can entrain the secondary vapor flow from the evaporator (from point 9 to point 5). The entrained secondary vapor flow mixes with the two-phase supersonic flow in the mixing duct at point 6. The turbulent mixing occurs and this mixing process is often accompanied with condensation and evaporation. Shock waves are usually observed and they interact with the thin boundary layers. Therefore, complex boundary/shock flow structures can be encountered in the mixing duct and diffuser (from point 6 to point 7). Moreover, these flow features are extremely complex and they depend on the geometry of ejectors and operating conditions [119].

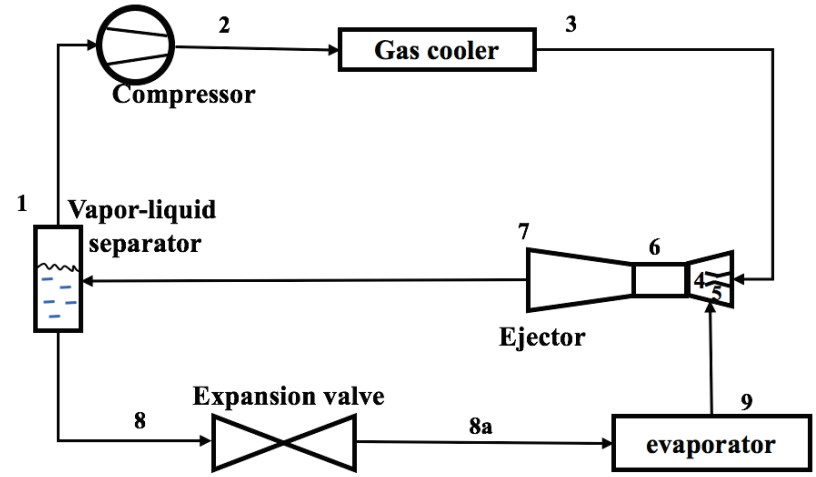

(a)

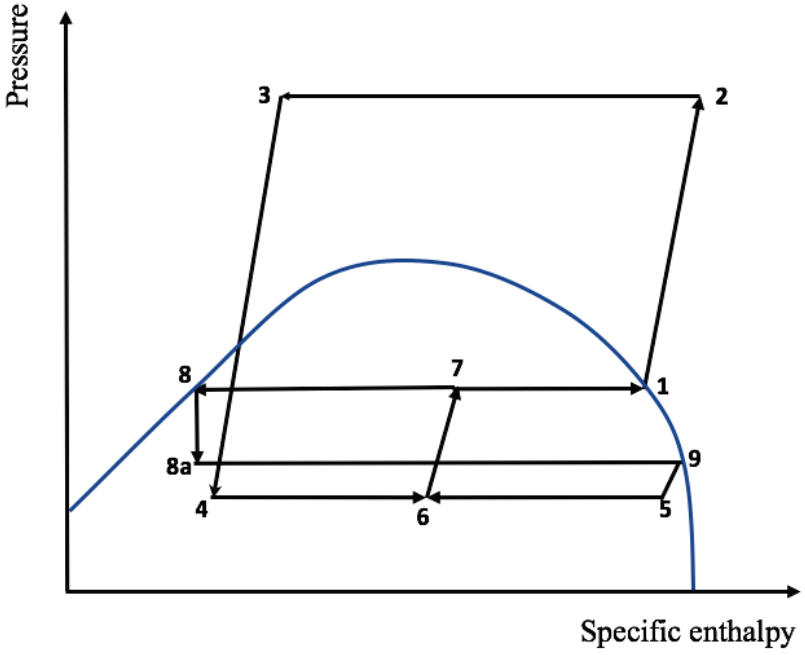

(b)

Figure 1.7 Schematic of (a) the transcritical CO_2 refrigeration cycle using a two-phase ejector for expansion work recovery and (b) the corresponding $p-h$ diagram.

In order to have a deep understanding of the complex local flow features occurring in such ejector, including flashing, choking, turbulence, and shock-boundary layer interactions, Computational Fluid Dynamics (CFD) simulations show some advantages compared to experimental investigations. CFD simulations provide a direct access to the local flow fields such as velocity, temperature, density which are not always easily measured by

experiments. Furthermore, CFD simulations can assist to determine efficiency coefficients such as polytropic efficiencies to optimize thermodynamic models still widely used in the industry. Moreover, regarding the small scale of CO_2 ejectors, experimental measurements are challenging. Although numerous CFD investigations have been done for two-phase CO_2 ejectors [39, 81, 117, 131, 162, 195], the numerical approaches need to be assessed more deeply in terms of two-phase modelling, flow solver and CO_2 properties. Most of the open literature on two-phase CO_2 ejector simulations have been published based on pressure-based solvers, whereas it is now well known in the fluid mechanics community that density-based flow solvers are more natural for computing compressible flows (AVBP [31], CLAWPACK [107], NEPTUNE CFD [77]). The density-based solver is originally designed to capture flow features such as shock waves, expansion waves in a compressible flow. It has been already extensively used for water transient simulations, combustion applications, and single-phase ejectors. However, no CFD simulation has been done based on the density-based solver for two-phase CO_2 ejectors, which is mainly due to numerical stability issues of commercial solvers when it is coupled with an external real gas properties database such as the Refprop database [104] or any other external subroutines. As a results, in this PhD thesis, a novel numerical approach is proposed based on a density-based solver to correctly predict compressible flow features (i.e. acoustic waves).

CHAPTER 2

State-of-the-Art

In this chapter, the numerical investigations about two-phase CO_2 ejectors, including the thermodynamic cycles and models and 1D and CFD models are presented. Then, the experimental works involving two-phase CO_2 ejectors are reviewed.

2.1 Analytical cycle models for refrigeration applications

The overall performance of refrigeration systems is closely related to the ejector which is considered as a critical component. At first, in order to perform the thermodynamic analysis of the expansion transcritical CO_2 cycle, a constant pressure-mixing model was used to model the ejector by Li and Groll [109]. The effect of the entrainment ratio and pressure drop was investigated for air conditioning operating conditions. The COP of the cycle combined with a CO_2 ejector was found 16% higher than a conventional cycle [109]. A theoretical analysis of the CO_2 transcritical EERC was performed by Deng *et al.* [48]. They found that the COP was up to 18.6% higher than internal heat exchanger cycle (IHEC) and 22% higher than the conventional vapor compression refrigeration cycle (VCRC). Bai *et al.* [13] combined the energetic and exergetic analyses to predict the cycle performance. Their simulations showed that the ejector enhanced cycle exhibited better performance than the conventional vapor injection cycle under specified operating conditions, such that the COP was 7.7% higher, and the volumetric heating capacity was 9.5% higher. Yari and Sirousazar [194] performed a theoretical analysis for the ejector-expansion transcritical CO_2 refrigeration cycle with a two-stage cycle and proposed to add an internal heat exchanger and an intercooler to improve the performance. Recently, CO_2 multi-ejector systems have also been considered both numerically by Hafner *et al.* [78] and experimentally by Haida *et al.* [79] confirming a COP improvement over conventional valve expansion refrigeration cycles for supermarket applications.

In conclusion, the cycle models for ejector refrigeration cycles (ERS) have demonstrated that the ejector is able to improve the performance of the refrigeration system. However, only global parameters like the COP, entrainment ratio and compression ratio can be pre-

dicted but complex flow phenomena cannot be considered, such as flashing, condensation, evaporation, and shock waves. Hence, a more complete model is still needed.

2.2 Thermodynamic models for two-phase CO_2 ejectors

Thermodynamic models for the two-phase CO_2 ejector are based on the conservation equations, equation of state, and isentropic relations associated for each part of the ejector. For example, the different parts of the ejector are illustrated in Figure 2.1.

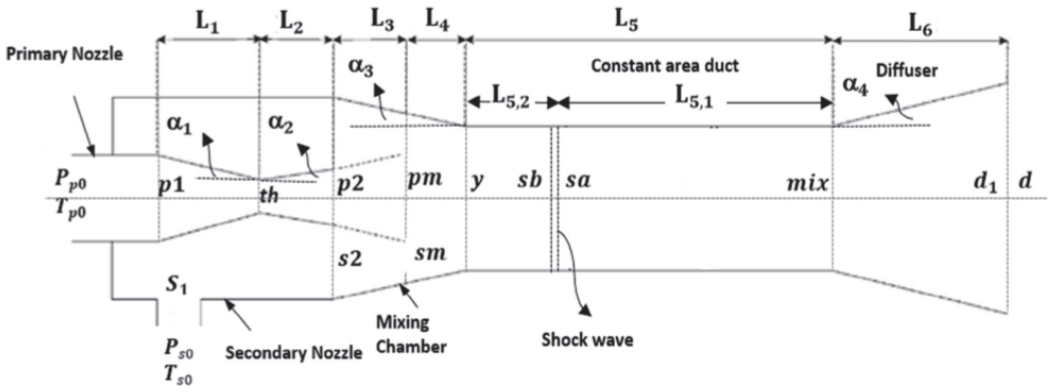

Figure 2.1 Geometry of the ejector considered by Taslimi Taleghani *et al.* [172].

Taslimi Taleghani *et al.* [171] proposed a thermodynamic model through Engineering Equaion solver (EES) to compare four configurations of the ejector-based CO_2 refrigeration system. Through energy and exergy analyses, they found that the EERC exhibited the highest performance in terms of COP and exergy efficiency. The COP was 5.6 times higher and the exergy efficiency was increased by 56.2% compared to those in a liquid recirculation cycle (LRC), an increasing compressor discharge pressure cycle (CDPC) and a vapor jet refrigeration cycle (VJRC). Then, the irreversibilities due to the friction in the primary nozzle and in the diffuser as well as crossing a normal shock wave were considered by the thermodynamic model under on-design and off-design operating conditions [172]. Some assumptions have been made for this model :

- The homogeneous equilibrium model (HEM) is considered for one dimensional steady state flow.
- No heat transfer at the ejector wall.

- The inlet velocities of the primary and secondary flows are negligible (stagnation condition).

- Constant polytropic efficiency coefficients are used to consider the friction losses for the primary nozzle and the diffuser. A friction factor is used for the mixing duct.

- For on-design conditions, the primary and secondary flows are both choked.

- If any, a normal shock is assumed at the inlet of the mixing duct.

- The flow at the diffuser inlet is subsonic.

It should be noted that all the thermodynamic properties of CO_2 are computed through the Refprop database [104]. Figure 2.2 shows the flowchart of this thermodynamic model.

- First of all, the critical state at the nozzle throat is found through the isentropic expansion by finding the maximum mass flow rate ($\dot{m}_{th}$, p_{the}, T_{th}, h_{th} can be determined). The polytropic efficiency coefficient can be applied to consider enthalpy losses during the expansion.

- The same procedure is used for the secondary flow to reach the hypothetical throat (cross section 'm') (p_{sm}, T_{sm} and h_{sm} are determined).

- Then, the primary flow is assumed to reach the same pressure as the secondary flow at the cross section 'm' (p_{pm}, T_{pm}, h_{pm}, and A_{pm} are determined).

- By estimating the entrainment ratio, the secondary mass flow rate can be determined as well as the secondary hypothetical cross section A_{sm}. Then, the total hypothetical throat is compared to the diameter of the mixing duct. One of the subloops can be chosen, as shown in Figure 2.2.

- If $A_m > A_y$, the choking of the secondary flow occurs before the mixing duct. The pressure is computed through mass and momentum conservation equations. Then, a normal shock wave is assumed to occur just at the inlet of the mixing duct. So the flow state before the shock wave is assumed to be the same as that at the section 'y'. By using the conservation of mass, total enthalpy and momentum, the state 'a' after the shock can be determined. The friction losses are considered for the mixing duct from the state 'sa' to 'mix'. Finally, in the diffuser, a subsonic flow is assumed and by increasing the pressure, the velocity may converge to the same value for mass and energy conservation equations.

- If $A_m < A_y$, the secondary flow does not chock before the mixing duct. The ejector works in the single chocking condition. As a result, A_m is assumed to be equal to A_y. p_m is estimated through an iterative calculation based on $p_m = p_{pm} = p_{sm}$. Then, the properties of the primary and secondary flows at 'm' can be determined. Simultaneous mixing is assumed from 'm' to 'y'. Then, there is no shock wave in the mixing duct. The state 'mix' is the same as 'y'. The same computation is performed in the diffuser.

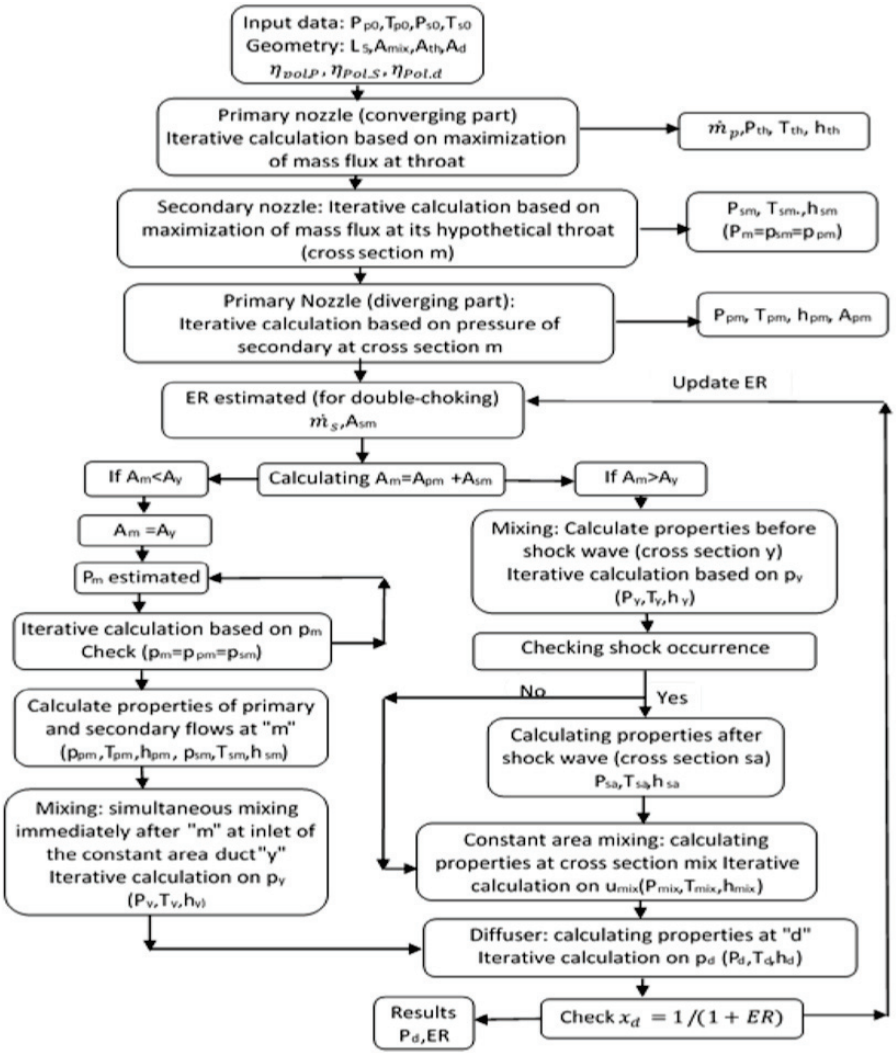

Figure 2.2 Procedure of the thermodynamic model proposed by Taslimi Taleghani *et al.* [172] and used to predict the performances of two-phase CO_2 ejectors for a given geometry.

Taslimi Taleghani *et al.* [172]'s model was validated though the experimental data of Banasiak and Hafner [14], Smolka *et al.* [162], Zhu *et al.* [206] in terms of primary mass flow rate and pressure ratio [162]. The maximum difference in terms of primary mass flow rate

was 15.7% between the thermodynamic model and the former works of [14, 162, 206]. The maximum error for the pressure ratio was 4.06% between the thermodynamic model and the work of Smolka *et al.* [162]. However, it can be noted that many hypotheses are considered and component efficiency coefficients are used. Hence, more verifications are needed. For example, the stagnation condition is assumed at the primary and secondary inlets, but during calculation depending on the mass flow rate, these velocities may be not negligible. So it should be verified at each iteration that they can be neglected compared to the total pressure. Moreover, the thermodynamic model strongly depends on the equation of state, because all the properties used in the isentropic expansion and the enthalpy conservation are computed by the EoS. As a result, the accuracy of the equation of state should be also verified before, especially for the properties in the neighbourhood of the saturation line and the critical point. One should be sure that at each step all the variables have a physical meaning. Furthermore, the shock wave prediction depends on the upstream and downstream conditions. In reality, there are complex interactions between the shock wave and the boundary layer. However, if the shock is imposed at a fixed position, all flow features could be changed. For efficiency coefficients, they are case-dependent and mostly used to optimize the model. Moreover, the geometry of the ejector is not sufficiently considered in the thermodynamic model, such as the length of the primary nozzle, and the dividing angle.

Liu *et al.* [111] developed an empirical correlation for the ejector components instead of using fixed values. The diameter of the motive nozzle throat and the diameter of the mixing section were evaluated to optimize COP and cooling capacity. Improvements of COP and cooling capacity were 30.7% and 32.1% compared to a conventional transcritical system. Correlations for the ejector efficiency and the primary mass flow rate were developed by Lucas and Koehler [116]. Errors of 10% on the ejector efficiency and errors of 5% on the mass flow rate were obtained compared to the experimental data.

In conclusion, good agreements in terms of mass flow rate and pressure ratio can be obtained by using thermodynamic models. However, many assumptions are imposed and the efficiency coefficients are always used. Hence, CFD simulations could be useful to determine these efficiency coefficients by considering complex flow phenomena within ejectors and then optimize thermodynamic models.

2.3 One-dimensional models for ejectors

Due to limitations of thermodynamic models, 1D models are developed using the concept of continuum mechanics. The local flow characteristics such as the speed of sound and the thermodynamic non-equilibrium could be considered. Less constraints are imposed to the flow. 1D models have been extensively considered for water [17], but for CO_2 they are still limited in the literature.

Banasiak and Hafner [14, 15] developed a 1D model for a transcritical CO_2 ejector in which the flow path was discretized along the axial direction of the ejector. A mixture model is used in the mixing duct and diffuser to consider the mixing of the two streams. This model takes into account the ejector geometry, the metastability effect, the mixing, and shock waves. Angielczyk *et al.* [7] proposed a 1D Homogeneous Relaxation Model (HRM) for CO_2 nozzle simulations. The numerical results are compared to Nakagawa *et al.* [126] measurements (black dots in Figure 2.3(a) and 2.3(b)).

Better agreements are obtained for the nozzle having a large diverging angle (Figure 2.3(b)) than that having a small diverging angle (Figure 2.3(a)). Berana *et al.* [20], Raman and Kim [140] also used a 1D gas dynamic model to simulate shock waves within the nozzle. A normal shock wave much thinner and stronger than that measured in the experiments [20] was obtained.

Due to the simplicity of 1D models, complex multi-dimensional effects can not be considered, for example the vorticity, the interaction of shock waves with the boundary layers, and the turbulent mixing.

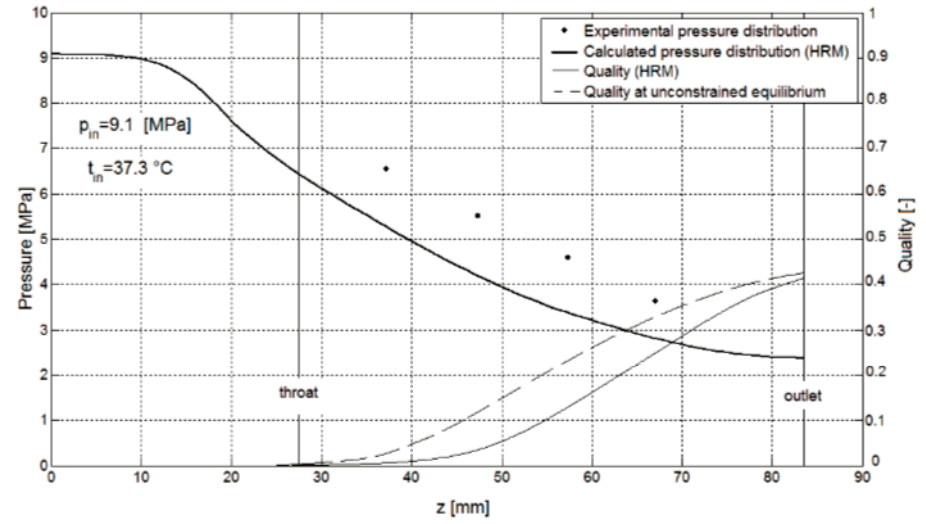

(a)

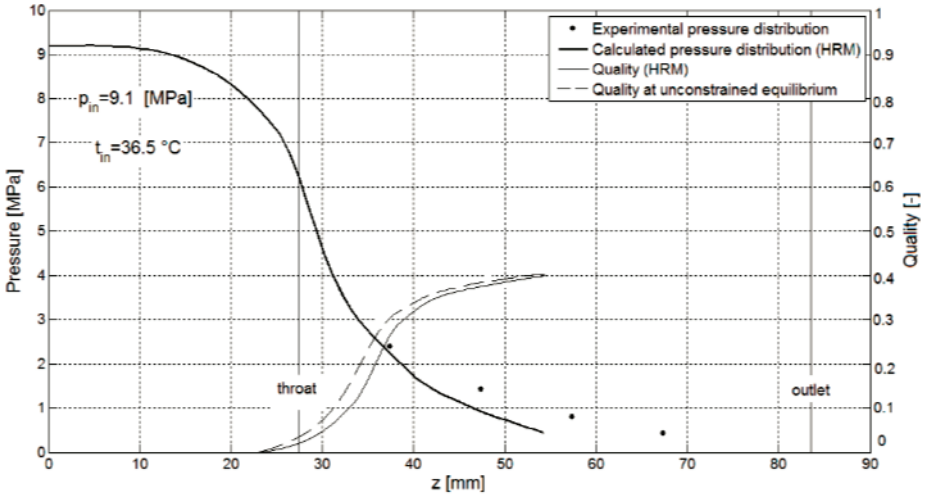

(b)

Figure 2.3 Pressure distributions along two-phase CO_2 converging-diverging nozzles with different diverging angles : (a) 0.153^o and (b) 0.612^o. After Angielczyk *et al.* [7].

2.4 CFD modelling

CFD approach is considered as a promising tool to provide more reliable and accurate results with an access to 3D fields of velocity, pressure and temperature. At the early stage of CFD simulations for ejectors, imcompressible flow simulations were considered [22, 144] and the turbulence effects [34, 190] were not taken into account. Moreover, coarse meshes were also used, which were too dissipative to capture shock waves properly [146].

With the increased capacity of supercomputers, a large number of numerical investigations have been done recently. ANSYS Fluent [8] as a popular commercial CFD software is mostly used to simulate the flows within ejectors. ANSYS Fluent exhibits the stable convergence of its solver and an easy control interface, which make the users more comfortable to perform a simulation and to get acceptable results. However, it is still difficult to modify the code and adapt it to specific cases. For this reason, open-source codes were developed and also demonstrated their capacity to provide comparable results [39, 117, 158].

In the literature, two types of ejectors are investigated : single-phase ejectors and two-phase ejectors. The first ones have been widely investigated since 2003. Gas-gas ejector was studied by Sobieski [163] who carried out CFD simulations with ANSYS Fluent. But due to the uncertainties of the key geometrical parameters and the uncertainties on the operating conditions between the experiments and the numerical simulations, the results showed significant discrepancies. Recently other refrigerants were also investigated for single-phase ejectors, working with R141b, R142b, R245fa, R152a, R600a, or R134a [4, 43, 44, 68, 83]. Hemidi *et al.* [88, 89] have shown that they obtained the same entrainment ratio with different turbulence models, but the Mach number and pressure profiles were significantly different along the ejector. As a matter of fact, more attentions need to be paid to the local flow features which cannot be easily obtained by experiments due to mechanical and security constraints when using synthetic refrigerants.

Regarding two-phase ejectors, the physical phenomena are more complex than for single-phase ejectors due to the mechanical and thermodynamic transfers between the two phases. Although many CFD studies of two-phase ejectors have been done since the last ten years, various aspects are still not clearly understood and elucidated.

In the context of this thesis, one mainly focuses on the CO_2 two-phase flows within ejectors under transcritical/supercritical operating conditions. The state-of-art on CO_2 two-phase flows within converging-diverging then ejectors are presented in the following subsections.

2.4.1 Converging-diverging two-phase CO_2 nozzles

Before focusing on two-phase CO_2 ejectors, the converging-diverging Laval nozzle is considered first. It is indeed a major part of the ejector, which has a significant influence on CO_2 ejector performances. It transforms the pressure energy of the primary flow into kinetic energy. As a result, the flow becomes supersonic. Meanwhile, due to the pressure drop, the flashing occurs near the throat where the pressure gradient is the highest. Eventually, a (low-pressure) supersonic two-phase jet at the outlet of the primary nozzle is obtained which entrains the secondary flow. The flow condition at the outlet of the primary nozzle affects considerably the entrainment of the secondary flow and the mixing phenomenon in the mixing duct and diffuser.

Nakagawa *et al.* [126] provided a very useful experimental database in terms of pressure and temperature measurements for validation purpose. According to their measurements, the flow in the diverging part was nearly in thermodynamic equilibrium for supercritical (p = 9.1 MPa), transcritical (p = 7.1 MPa) and subcritical (p = 6.1 MPa) conditions. Nozzles with diverging angles ranging from 0.076^o to 0.612^o were investigated. Berana *et al.* [20] also measured the temperature along the nozzle with and without the appearance of shock waves. The pseudo-shock and dispersed shock waves were obtained, which were much thicker and weaker than normal shock waves [20]. A two-phase CO_2 nozzle was investigated through flow visualizations by Li *et al.* [110]. They revealed that the phase-change position can be after or before the nozzle throat depending on the operating conditions.

Raman and Kim [140] used 1D gas dynamic equations to simulate the occurence of a shock wave within the nozzle of Berana *et al.* [20]. Aungier (ARK) [11], Peng and Robinson (PR) [134], Boston and Mathias (PRBM) [27], Plöcker (LKP) [136], Benedict-Webb-Rubin (BWR) [167] and, Span-Wagner (SW) [164] EoS were assessed. It should be noted that the Refprop database [104] which is based on SW EoS is actually considered in this work instead of the original SW EoS. Moreover, solutions for supercritical CO_2 were compared to the gaseous CO_2 results (denoted by G-CO_2 in Figure 2.4) with the same pressure ratio. Figure 2.4 showed a significant influence on the prediction of the shock wave position and intensity. It is also noted that the operating conditions are based on the pressure ratio rather than the pressure in Berana *et al.* [20]. In fact, in order to avoid the phase change in the nozzle, the pressure range was changed, but the pressure ratio kept constant.

Yazdani *et al.* [196] considered the cavitation and boiling phase change theory in their simulations. The pressure-based solver of ANSYS Fluent was employed to simulate one small and one large diverging angle nozzle (θ = 0.306 and 0.612) of Nakagawa *et al.* [126].

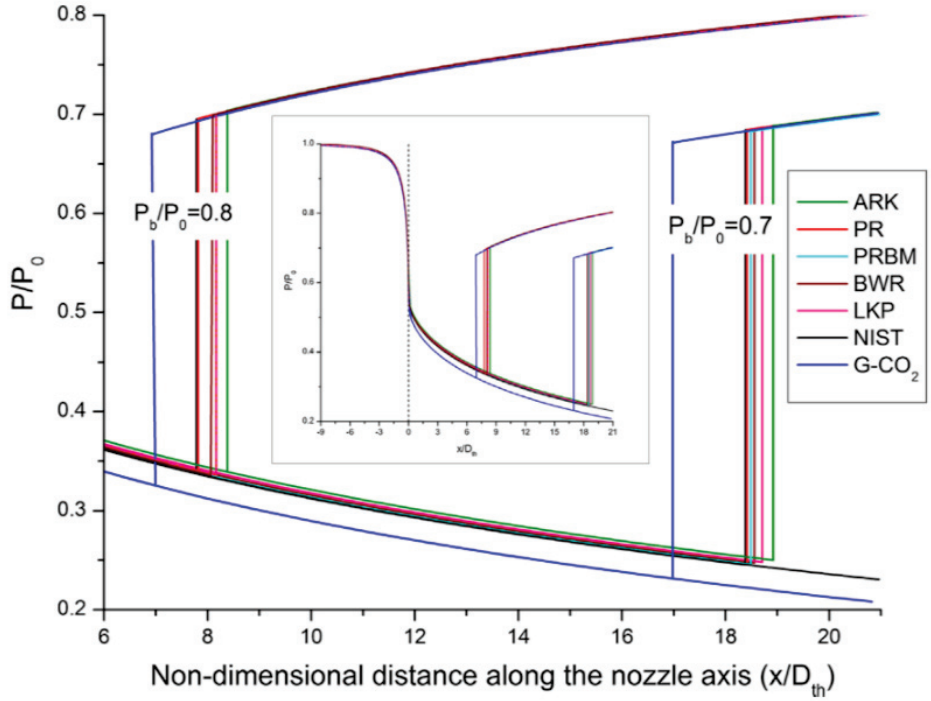

Figure 2.4 Pressure profiles along the nozzle for different EoS, after Raman and Kim [140].

The $k-\omega$ SST model was used to predict the turbulence effect together with the Refprop database [104] and Peng-Robinson [134] EoS for the CO_2 thermodynamic properties. Figure 2.5 shows a good agreement in terms of pressure compared to the experimental measurements of Nakagawa *et al.* [126]. However, some oscillations were observed at the outlet, which could be related to both the numerical solver and inappropriate boundary conditions.

Ameli *et al.* [5] simulated the nozzle of Berana *et al.* [20] using ANSYS CFX [9]. A non-homogeneous phase change model was used based on the nucleation and droplet growth theories associated with an Euler-Euler model to describe the continuous and dispersed phases and a Real Gas Properties (RGP) table built from the Refprop database [104] to compute CO_2 properties. The turbulent effect was predicted by the $k-\omega$ SST model. A 3D mesh with 300000 elements was used leading to a wall coordinate y^+ close to 1. It can be observed in Figure 2.6(a), that the pressure is well predicted. However, an abnormal shock wave is observed near the outlet, shown in Figure 2.6(b). In fact, the geometry in their simulation has a longer diverging part than that in Berana *et al.* [20]'s experiments. As the shock appears at the end of the nozzle, it does not appear in Figure 2.6(a).

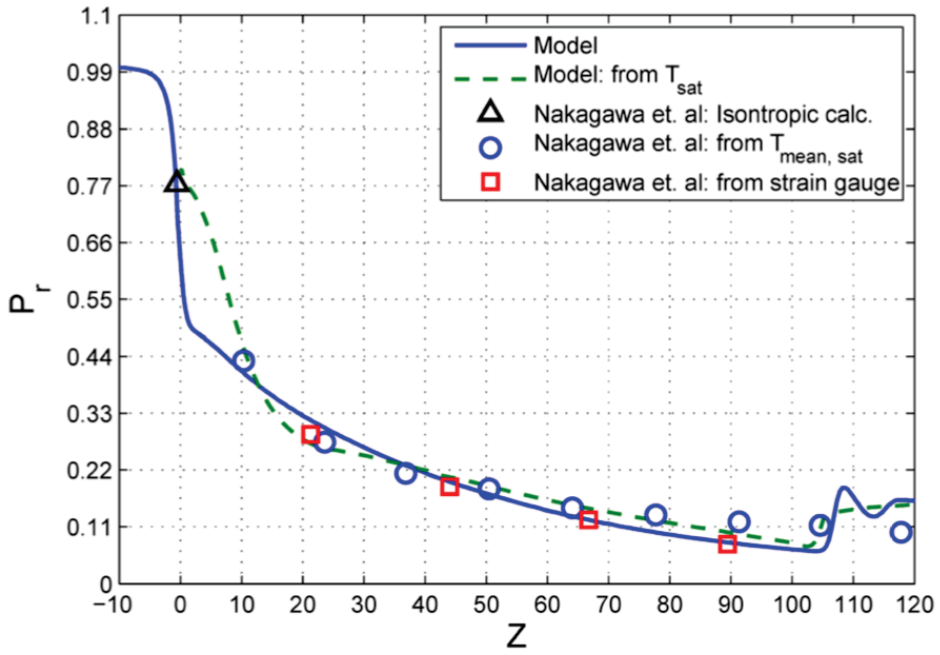

Figure 2.5 Pressure distribution along the diverging part of the converging-diverging nozzle with supercritical inlet conditions, after Yazdani *et al.* [196].

The nozzles having a diverging angle equal to $\theta = 0.076^o$ and $\theta = 0.153^o$ in Nakagawa *et al.* [126] were investigated by Giacomelli *et al.* [71]. A tabulated property calculation approach based on the Refprop database was coupled with the pressure-based solver of ANSYS Fluent. The sensitivity to different types of boundary condition was analyzed without exhibiting significant difference. However, an unphysical pressure drop was predicted at the outlet in all cases. Moreover, accommodation coefficients for the evaporation model were calibrated based on subcritical conditions [71]. Good results were obtained for the largest diverging angle ($\theta = 0.153^o$) as shown in Figure 2.7(a).

Figure 2.7(b) shows the Mach number map in the diverging part. It can be seen that significant differences are observed depending on the formulation of the sound speed. The Wallis formulation predicts a subsonic flow in the diverging part and the flow becomes supersonic at the outlet, while the Brennen formulation [196] predicts the supersonic flow after the throat, and a shock wave is observed at the outlet. It should be noted that the Wallis formulation is the default formulation of the sound speed in ANSYS Fluent [8]. It is not still clear how this term is accounted for in the pressure-based solver. However, in general, the speed of sound is intrinsic to the system of equations and it should not affect the final solution. As the information is not currently available within ANSYS Fluent, it is hard to evaluate the influence of the sound speed on the final solution.

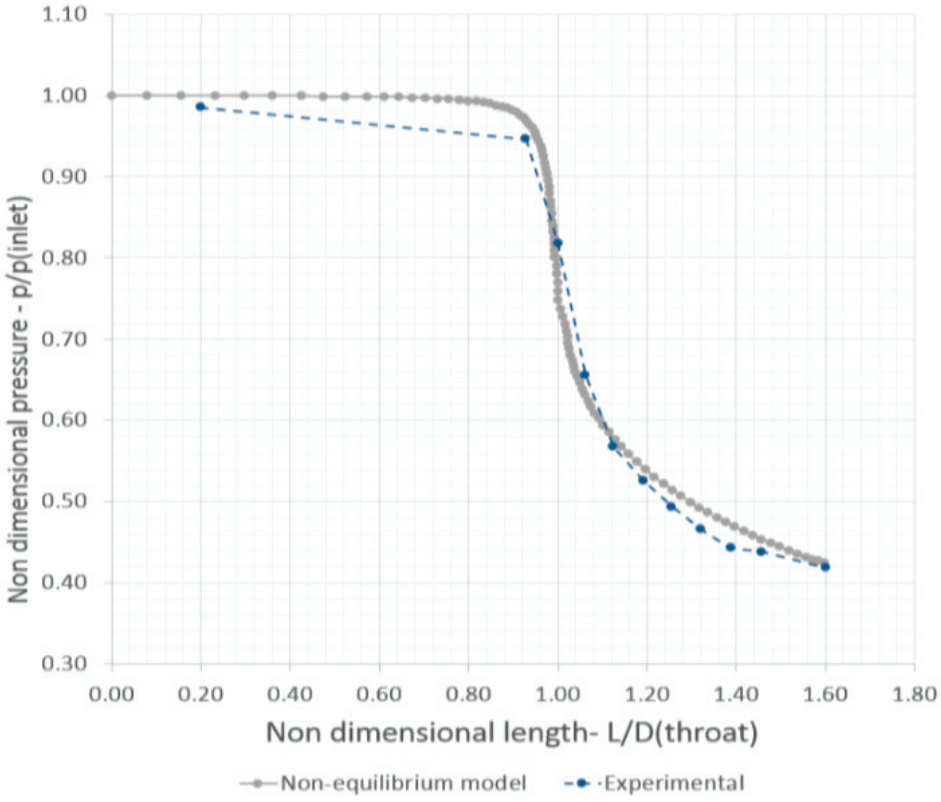

(a)

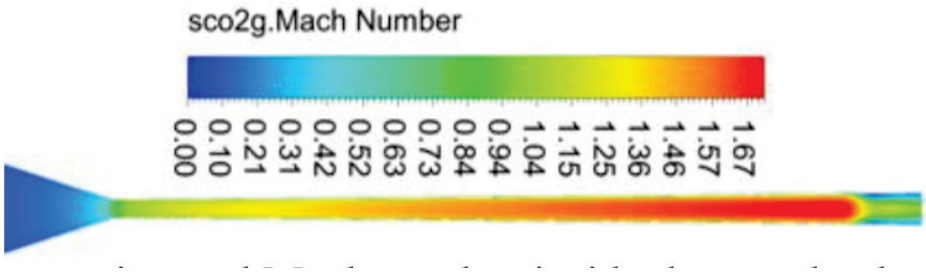

(b)

Figure 2.6 (a) Streamwise distribution of the normalized pressure and (b) Mach number map for the nozzle of Berana *et al.* [20], after Ameli *et al.* [5].

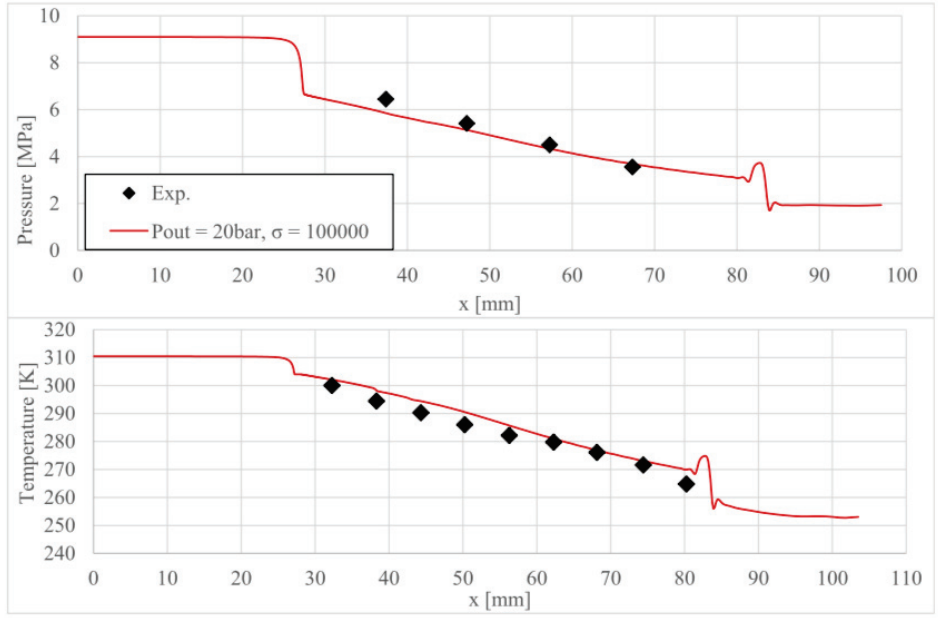

(a)

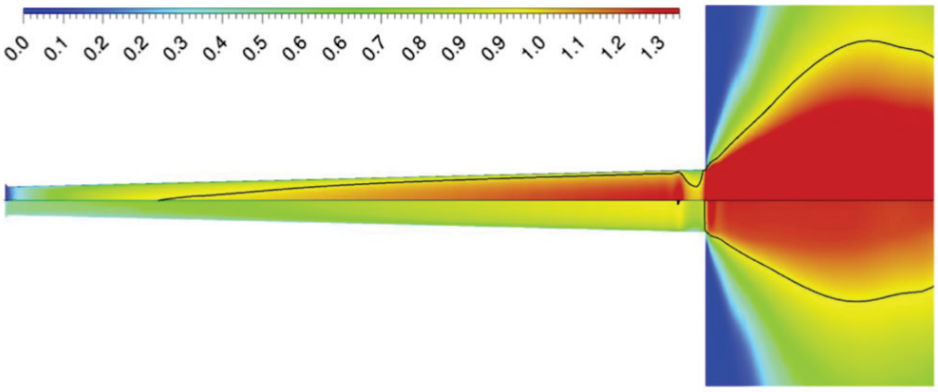

(b)

Figure 2.7 (a) Pressure and temperature profiles for the nozzle with $\theta = 0.153^o$ and supercritical conditions ; (b) Mach Number computed by the Brennen Equation (top) vs Mach Number computed by the Wallis Equation (bottom), after Giacomelli *et al.* [71].

2.4.2 Two-phase CO_2 ejectors

A two-phase CO_2 ejector was simulated by Smolka *et al.* [162] through the mixture model in ANSYS Fluent [8]. The homogeneous equilibrium model (HEM) was coupled with the Refprop database [104] for the property calculation and a pressure-based solver. The pressure is then coupled with the velocity field, whereas density is computed by the EoS. The temperature-based energy equation is replaced by an enthalpy-based equation. The $k-\epsilon$ Re-Normalisation Group (RNG) model was considered to predict turbulent effects. The mass flow rate agreed well with the experimental results, whereas relatively large discrepancies were obtained for the pressure distribution within the mixing duct. Furthermore, the vapor quality is computed based on pressure and enthalpy through the Refprop database. There is no shock found in this simulation. The same method was used by Banasiak and Hafner [15] to conduct an irreversibility analysis on the cross-sectional and overall entropy generation. Palacz *et al.* [131] also applied the same approach to assess the accuracy of the HEM. A vast range of operating conditions was tested. It can be seen in Figure 2.8 that accurate results were obtained near or above the CO_2 critical point. However deviations were observed for subcritical conditions near the saturation line.

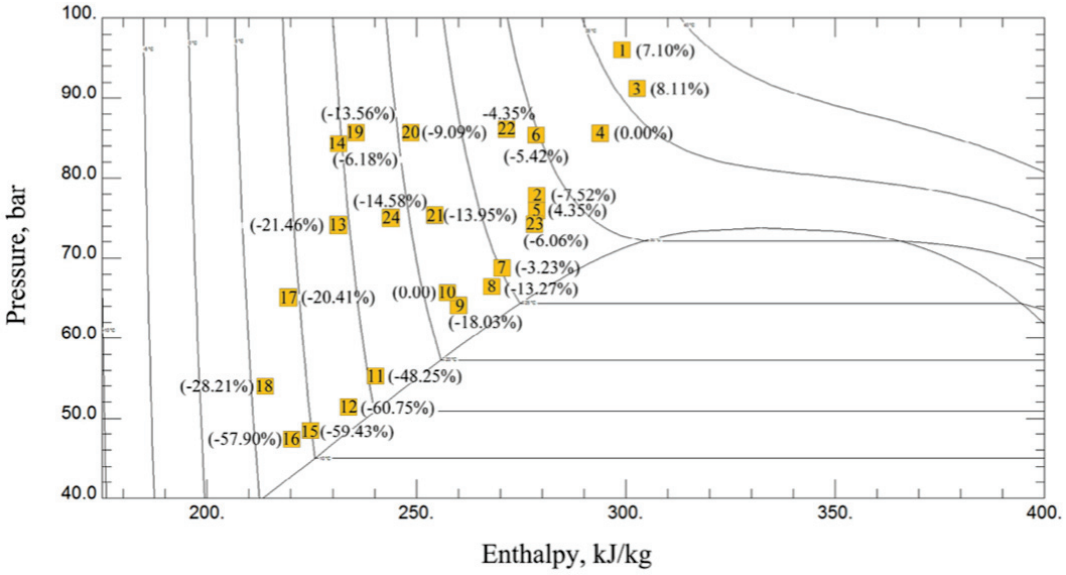

Figure 2.8 Motive nozzle mass flow rate discrepancies in the $p-h$ diagram, after Palacz *et al.* [131].

Palacz *et al.* [130] further implemented the HRM and compared the results to the HEM for two-phase CO_2 ejectors in supermarket refrigeration conditions. Their numerical results were compared to experimental ones in terms of entrainment ratio and primary mass flow rate. For operating conditions above the critical point, the HEM was found to be more

accurate than the HRM, while for operating conditions far below the critical point, the HRM performed around 5% better than the HEM in terms of primary mass flow rate. Based on that, Haida *et al.* [80, 81] proposed a modified HRM in which the relaxation time was optimized through a genetic algorithm. A short relaxation time was obtained for the supercritical and transcritical regimes, such that the modified HRM tends to the HEM. A higher relaxation time was obtained for pressures lower than 5.9 MPa leading to relative errors in terms of primary mass flow rate below 15%. Beside, this approach has also been used to investigate the swirl flow influence at the inlet [25] and the multi-ejector module for the CO_2 supermarket refrigeration system [24].

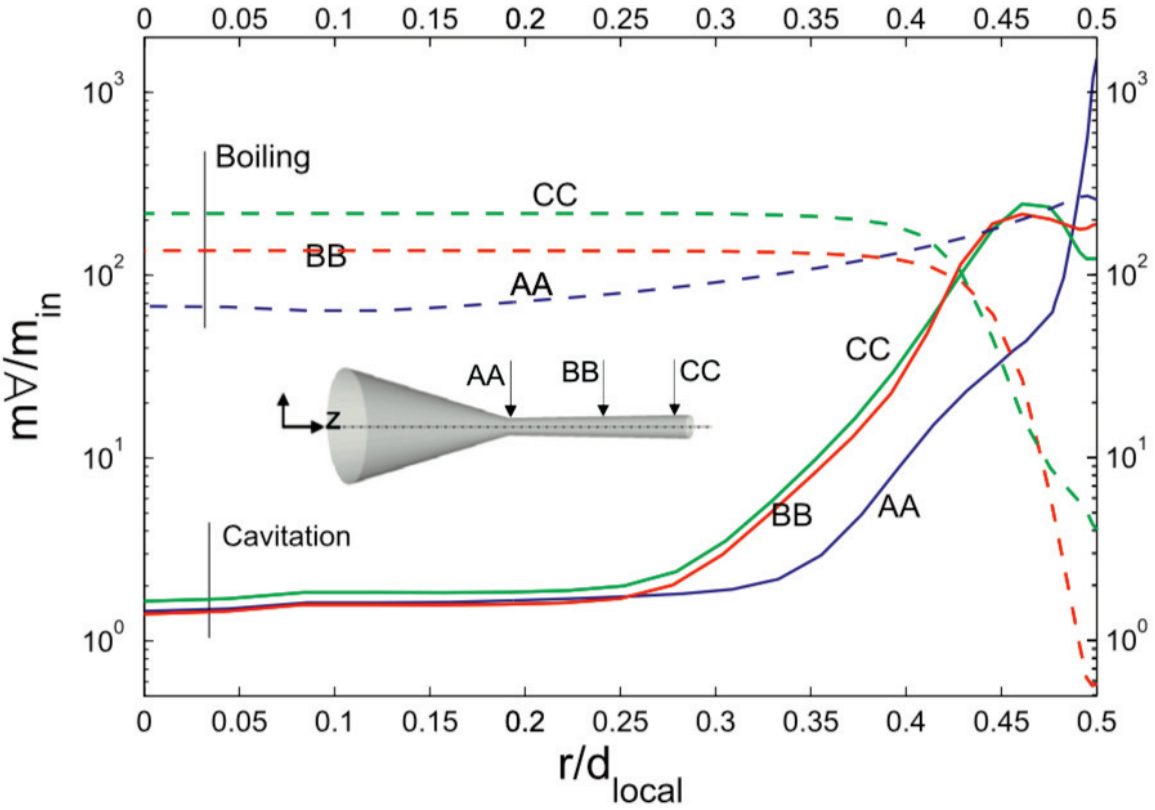

Figure 2.9 Contribution of cavitation and boiling phase change mechanisms across different cross sections of the motive nozzle, after Yazdani *et al.* [195].

Yazdani *et al.* [195] proposed a non-homogeneous model and the phase change is considered by a cavitation model and a boiling model. The phase change is not assumed to follow an instantaneous process to reach the thermodynamic equilibrium, but a finite-rate phase change model is adopted to account for non-equilibrium transition. The vaporisation and condensation rates are inherited from the dynamics of bubble growth and the kinetic theory of phase change. The segregated pressure-based solver of ANSYS Fluent was used to perform the simulations together with a $k-\omega$ SST closure. Figure 2.9 shows that the

cavitation portion of phase change dominates in the near-wall region but it is generally small in the bulk of the flow.

Lucas *et al.* [117] carried out a two-phase ejector simulation with a pressure-based solver of the OpenFOAM library [191]. The HEM was considered for the flashing mechanism and was associated with a $k-\omega$ SST model. Through comparisons with experimental data, the authors obtained a 10% (resp. 20%) relative errors in terms of primary mass flow rate without (resp. with) the secondary suction flow.

Colarossi *et al.* [39] coupled the HRM with the pressure-based solver of the OpenFoam library [191]. They reported an average error of 18.6% in terms of pressure differences between the inlets and outlet (the mass flow rate is fixed at the inlet and outlet). They attributed these discrepancies to first the choice of the $k-\epsilon$ turbulence model and second to the imposed boundary conditions. The iso-contours of the instantaneous quality x and equilibrium quality $\overline{x}$ are shown in Figure 2.10. According to the authors, the flow was near thermodynamic equilibrium in the diffuser and they suggested that the choice of the apppropriate turbulence model remains one of the greatest challenge in the modelling of two-phase ejectors and that the HEM could be suitable for this kind of flows.

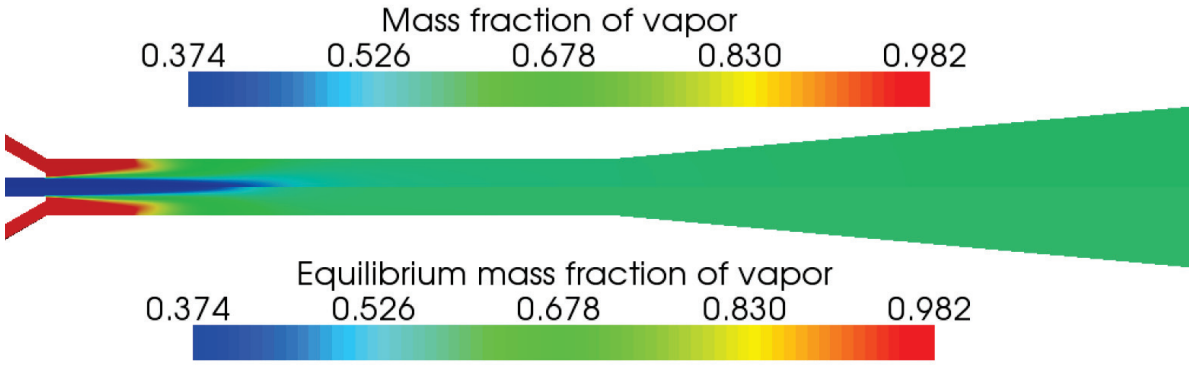

Figure 2.10 Instantaneous quality x shown on the top half of ejector and equilibrium quality $\overline{x}$ shown on the bottom half, after Colarossi *et al.* [39]. The operating conditions are based on the experimental data of Nakagawa *et al.* [128].

2.4.3 Conclusion

The CFD approaches used to model two-phase CO_2 flows inside ejectors and converging-diverging nozzles are summarized in Table 2.1.

Table 2.1 Summary of the CFD approaches used for two-phase CO_2 supersonic flows inside ejectors and nozzles.

Ref	Two-phase model	Solver	EoS	Turbulence model
[15, 130, 131, 162]	HEM	pressure-based (Fluent)	Refprop	$k-\epsilon$
[80, 81]	HRM	pressure-based (Fluent)	Refprop	$k-\epsilon$
[117]	HEM	pressure-based (OpenFoam)	TEMO-Media library	$k-\omega$ SST
[195, 196]	mixture model with cavitation/boiling	pressure-based (Fluent)	Refprop	$k-\omega$ SST
[39]	HRM	pressure-based (OpenFoam)	Refprop	$k-\epsilon$
[71]	HEM	pressure-based (Fluent)	lookup table	$k-\omega$ SST
[5]	mixture model with nucleation/droplet growth	pressure-based (CFX)	lookup table	$k-\omega$ SST

In Table 2.1, different numerical aspects are listed such as the two-phase model, the numerical solver, the EoS and the turbulence model. These are the main aspects which should be considered when performing CFD simulations of two-phase CO_2 flows. It can be seen that HEM is the most considered in the literature. Compared to the HRM, similar results are obtained [39, 81, 130] for supercritical and transcritical operating conditions. Hence, the HEM is considered in this thesis. In Chapter 4, the model has been compared to experimental data, other HEM-based models, and isentropic expansion theory in terms of nozzle critical mass flow rate.

Table 2.1 shows that there is no density-based solver used for simulations of CO_2 ejectors. However, density-based solvers are naturally used to solve high-Mach number compressible flows, while pressure-based solvers are more suitable to solve low-Mach number incompressible flows. In fact, the sets of equations for compressible and incompressible flows are characterised by different physical assumptions. For compressible flows, the conservation equations (mass, momentum, energy) are coupled and the resulting system is closed by an EoS which relates pressure, density, and internal energy. As a result, all variables are interdependent in thermodynamic and hydrodynamic ways. The pressure in compressible flows has both hydrodynamic and thermodynamic meaning. For incompressible flows, the energy equation is decoupled from the mass and momentum equations. It separates the internal energy from the kinetic one. Moreover, the density is not a variable in the conservation equations. The pressure is not a function of density and temperature, whereas it is indeed related to the whole velocity field. Therefore, the pressure loses its thermodynamic character but has only a hydrodynamic nature [26].

Considering pressure-based solvers, usually by manipulating the continuity and momentum equations, a Poisson's equation for pressure can be obtained [138]. Actually, two equations are segregately solved in pressure-based solvers : one pressure equation and one energy equation. Moreover, whether using a segregated or coupled method [8], the energy equation is always decoupled. Conversely, for density-based solvers, the mass, momentum,

and energy equations are solved and the density is a variable in all equations. The pressure is determined by the density and internal energy through an EoS. Hence, the density-based solver is more appropriate for compressible flows in order to respect the flow physics.

Asproulias *et al.* [10] have compared density-based solvers and pressure-based solvers for an inviscid shock tube case and a compression ramp case. They found that the density-based solver was less dissipative in steep-gradient regions than the pressure-based solver and the density-based solver gave more accurate prediction of the shock location, wall pressure, and the size and shape of the separation bubble. Park and Rhee [132] also evaluated a density-based solver and a pressure-based solver for cavitating flows. They found that the density-based solver had more accurate resolution on flow details and cavity dynamics. Moreover, in this thesis, a vapor shock tube case was performed by using density-based solvers and pressure-based solvers of Ansys Fluent [8]. One found some oscillations at the contact surface and the shock location when the pressure-based solver with PRESTO! scheme was used. Hence, in this thesis, density-based solvers are considered in order to accurately capture compressible flow features.

Most of works used the Refprop database instead of the original Span-Wagner (SW) EoS. However, no assessment of the accuracy between the Refprop database and the original SW EoS has been performed. Moreover, the outlet boundary condition could be important for compressible flow simulations. Hence, the HEM, the EoS, and the outlet boundary condition are addressed as well.

2.5 Experimental works

Although many experimental investigations have been carried out for single-phase ejectors, experiments of two-phase CO_2 ejectors are still limited. Elbel and Hrnjak [54] compared a transcritical R744 ejector system to a conventional expansion valve system. They found an improvement of cooling capacity and COP up to 7% and 8%, respectively. They also installed a needle in the primary nozzle to control the high-side pressure. The highest ejector efficiency was achieved when the primary pressure was lowest.

Chaiwongsa and Wongwises [32] found that the maximum COP and cooling capacity were obtained for a primary throat diameter equal to 0.8 mm. Liu *et al.* [113] obtained the maximum COP when the primary throat is equal to 2 mm. They also found that when the distance between the motive nozzle exit and the mixing duct is 3 times the diameter of the mixing duct, the cooling capacity and COP reach their maxima.

Lee and Kim [103] carried out an experimental investigation of a CO_2 air-conditioning system using an ejector. The effects of the ejector geometry are addressed, including the motive nozzle throat diameter, the distance between the motive nozzle exit and the diffuser, the mixing duct diameter. They also found that the COP is about 15% higher than that of the conventional system under the same operating condition. It was confirmed later by Liu *et al.* [112]. They showed also that the COP was affected by the outdoor air temperature and the compressor frequency.

Xu *et al.* [193] used an adjustable ejector to optimize the high-side pressure for a transcritical CO_2 heat pump system. They found that the increased high-side pressure has a positive effect on the system performance and the highest efficiency was achieved at the maximum throat of the motive nozzle.

Through the experiments of Nakagawa *et al.* [128], the entrainment ratio and the pressure recovery were found to be significantly related to the mixing duct length, and a 10% decrease of the COP was reported. Nakagawa *et al.* [126] carried out the investigations of three converging-diverging nozzles. The pressure and the temperature were measured along the nozzle wall. They demonstrated that the thermodynamic equilibrium was a good assumption for this kind of flow. Due to the limited amount of reliable experimental data, their measurements will be considered for validation purpose.

Berana *et al.* [20] also investigated a converging-diverging nozzle operating in supercritical and subcritical conditions. A thick and weak shock wave was found through temperature measurements. Their experimental measurements will be compared to the present numerical results.

Haida *et al.* [79] carried out an experimental investigation of the R744 vapour compression rack equipped with a multi-ejector expansion work recovery module. The COP and exergy efficiency can be improved by up to 7% and 13.7%, respectively. The maximum COP and exergy efficiency were obtained when the tank lift pressure was maximum for the multi-ejector refrigeration system.

Zhu *et al.* [206] carried out an experimental study on a transcritical CO_2 ejector-expansion system. A coefficient of mass balance was introduced based on the liquid mass balance in and out the vapor-liquid separator. The COP decreases from 18.9% to 11% when increasing the mass balance from -0.1 to 0.1. Zhu *et al.* [207] also performed a visualisation of the supersonic CO_2 flow in an ejector embedded in a refrigeration system. They found that the expansion angle of the primary flow at the nozzle exit decreases by increasing

the secondary pressure and the large expansion angle could lead to a decrease of the entrainment performance.

Li *et al.* [110] performed experiments for two-phase CO_2 ejector flows. Their flow visualisation focused on the primary nozzle. Depending on the operation condition, the flashing could occur before or after the throat.

It can be seen that most of the experimental results are reported by using global parameters (cooling capacity and COP). However, the mass flow rate at the inlets and outlet, and the pressure/temperature measurements along the ejector wall are needed to validate more deeply the numerical model. Among the experiments mentioned above, only the works of Berana *et al.* [20], Liu *et al.* [112, 113], Nakagawa *et al.* [126, 128] provided local parameters within the ejector. However, the measurement accuracy is not always reported, as in the work of Nakagawa *et al.* [126].

Moreover, in some numerical investigations, authors used in-house experimental measurements of mass flow rate to validate their numerical model [130, 131, 162]. Hence, these mass flow rate measurements can also be used for our validations.

2.6 Objectives and routing of the thesis

The main objective of this thesis is to develop a reliable numerical tool to carry out a complete and advanced investigation of the two-phase CO_2 supersonic flow in an ejector. As mentioned above, most of the numerical investigations have been done so far using commercial software such as ANSYS Fluent or by more simple 1D or purely thermodynamic models. In 1D and thermodynamic models, many assumptions are used. As a result, the local flow features can not be captured and well understood. The commercial softwares are limited for users. Hence, in this thesis, an in-house numerical approach is developed step by step and validated considering various benchmark cases.

Firstly, a tabulated Equation of State (EoS) approach based on Span-Wagner (SW) EoS is developed to compute the properties of CO_2 accurately and efficiently [59]. As the EoS is independent of the numerical solver, it can be validated separately. Then, it could be coupled to the numerical solver. SW EoS is known as an international reference EoS for CO_2 covering a wide range of temperature and pressure, from the triple-point temperature to 1100 K and the pressure up to 800 MPa [164]. It has been already implemented in the Refprop database [104] and Coolprop [19] to produce CO_2 properties. Hence, SW EoS is chosen as the basis of the tabulated approach. Moreover the tabulated method is designed

for the conservative formulation, which provides flexibility to any compressible solver. This method is based on the former works of De Lorenzo *et al.* [47], Kunick *et al.* [97], which concern water-steam fast transient simulations.

Secondly, in order to evaluate the speed and accuracy of this tabulated EoS for the CO_2 compressible flow simulation, it was coupled with the CLAWPACK solver [106, 107]. This is a compressible solver used to perform 1D and 2D inviscid simulations. CLAWPACK solves hyperbolic equation systems in the conservative form with Riemann solvers (e.g. the Harten-Lax-van Leer-Contact (HLLC) [106, 107, 178]). The accuracy and efficiency of the simulation using the tabulated EoS have been evaluated against the available results in the literature.

Thirdly, in order to predict more complex phenomena for real applications, a density-based solver was developed based on *rhoCentralFoam* proposed in the OpenFOAM library. It uses the conservative formulation, which guarantees to correctly capture the acoustic waves within the computational domain. The thermodynamic properties of CO_2 are computed by the tabulated EoS covering the supercritical, vapor, liquid and vapor-liquid states. Moreover, the Navier-Stokes characteristic boundary condition (NSCBC) is implemented for the outlet boundary, which ensures the correct ingoing and outgoing of acoustic waves at the boundary and so enhances the stability of the simulation. It should be noted that the NSCBC is also coupled with EoS in order to compute the ingoing and outgoing waves. The present solver is then used to perform Reynold-Average-Navier-Stokes (RANS) simulations to investigate CO_2 flashing converging-diverging nozzles as well as two-phase CO_2 ejectors.

All the works done during this thesis have been published through three journal papers and five conference papers as follows :

- [1] Y. Fang, S. Croquer, S. Poncet, Z. Aidoun, and Y. Bartosiewicz, Drop-in replacement in a R134 ejector refrigeration cycle by HFO refrigerants, *International Journal of Refrigeration*, **77** : 87-98,2017

- Y. Fang, M. De Lorenzo, P. Lafon, S. Poncet, and Y. Bartosiewicz, An Accurate and Efficient Look-up Table Equation of State for Two-phase Compressible Flow Simulations of Carbon Dioxide, *Industrial & Engineering Chemistry Research*, **57** : 7676-7691, 2018.

[1] this article is presented in Appendix A.

- Y. Fang, S. Poncet, H. Nesreddine, and Y. Bartosiewicz, An open-source density-based solver for two-phase CO_2 compressible flows : verification and validation, *International Journal of Refrigeration*, **106** : 526-538, 2019.

- S. Croquer, Y. Fang, S. Poncet, Z. Aidoun, and Y. Bartosiewicz, *26th Canadian Congress of Applied Mechanics (CANCAM2017)*, Victoria, 2017.

- Y. Fang, M. De Lorenzo, P. Lafon, S. Poncet, Y. Bartosiewicz, and H. Nesreddine, Fast And Accurate CO_2 Properties Calculation Algorithm For Massive Numerical Simulations Of Supersonic Two-phase Ejectors, *17th International Refrigeration and Air Conditioning Conference*, Purdue, 2018.

- Y. Fang, S. Poncet, Y. Bartosiewicz, and H. Nesreddine, Shock analysis for two-phase CO_2 flows in a converging-diverging nozzle, *10th International Conference on Multiphase Flow*, Rio de Janeiro, 2019.

- Y. Fang, S. Poncet, and Y. Bartosiewicz, Analysis of transport phenomena in a two-phase CO_2 supersonics ejector, *27th Canadian Congress of Applied Mechanics (CANCAM2019)*, Sherbrooke, 2019.

- Y. Fang, S. Poncet, Y. Bartosiewicz, and H. Nesreddine, A density-based solver using real gas properties for R744 supersonic flashing simulations, *25e Congrès International du Froid (ICR2019)*, Montréal, 2019.

In this thesis, the results and developments which have been published are reproduced and completed. They are organized as follows : In Chapter 3, the numerical methods are described with a particular emphasis on the two-phase model, the density-based solver, the tabulated approach, the Navier-Stokes Characteristic Boundary Condition (NSCBC), and the transport tube method. Then, in Chapter 4, validation and verification cases are presented for the tabulated approach, the CLAWPACK solver, and the density-based solver. In Chapter 5, different converging-diverging Laval nozzles are simulated under supercritical and subcritical operating conditions. The pressure profiles are compared against the numerical and experimental results of Nakagawa *et al.* [126]. Then, the bulk viscosity and turbulence effects are analyzed. In Chapter 6, the ejector of Li *et al.* [110] is investigated. The exergy tube approach is used and the sensibility of the method is discussed. Finally, the conclusion is presented in Chapter 7.

CHAPTER 3

Methodology

In this chapter, the physical model and numerical techniques are successively presented, starting from the Homogeneous Equilibrium Model (HEM). Then, the look-up table approach used to compute the CO_2 thermodynamic properties is presented in details. The numerical solvers are described from the simplest gas dynamic solver to the more complex one, AVBP. The coupling between the Navier-Stokes Characteristic Boundary Condition (NSCBC) and then tabulated EoS is then presented. Finally, an experimental test facility, available at Laboratoire des Technologies de l'Énergie (LTE) in Shawinigan is shown and will be used for comparison purpose (Appendix E).

3.1 Two-phase model - Homogeneous Equilibrium Model (HEM)

The phase transition is one of the most significant effect occurring within a two-phase ejector. Several models for two-phase flows have been developed so far in the literature. For compressible fluids, the most complete model is the seven-equation model proposed by Baer and Nunziato [12], in which the two phases are assumed in full non-equilibrium in terms of temperature, pressure and velocity. Furthermore, the six-equation model was proposed by Pelanti and Shyue [133], and Saurel *et al.* [155], which considered that the two-phases were in thermodynamic non-equilibrium. Regarding two-phase models for supersonic two-phase flows within ejectors, more simplified two-phase models are considered.

- Mixture models : the two phases are described by the mixture variables.

    1. Homogeneous Equilibrium Model (HEM) : This model assumes that the two phases always remain in mechanical and thermodynamic equilibria. It means that pressure, temperature, velocities, turbulence kinetic energy and turbulence dissipation rate are the same for both phases. The two-phase transition is considered instantaneously. No equation involves the volume or mass fraction, but they are computed by the EoS.

    2. Partial equilibrium : Two phases are in mechanical non-equilibrium or thermodynamic non-equilibrium. As an example, the HRM [23] and DEM [17] models

consider that the two phases are in mechanical equilibrium but not in thermodynamic equilibrium. The enthalpy of each phase is not equal to the saturation enthalpy. An additional equation is used to evaluate the vapor quality.

- Two-fluid models :

  1. Fully non-equilibrium model : Each phase has its own velocity and the enthalpy of each phase is not equal to its saturation value. In this case, complex physical phenomena can be modeled such as the slip between the phases, condensation and evaporation.

  2. Euler-Euler model : It considers one continuous phase and one dispersed phase. Some assumptions can be made to simplify the fully non-equilibrium model. This model is usually considered for droplets or bubbly flows. The mechanical and thermodynamic non-equilibria can be modeled. However, such approach depends on the flow topology. To use such model for two-phase CO_2 ejectors, more experimental verifications are needed.

Yazdani *et al.* [195] developed a phase change model based on the non-homogeneous mixture model used also by Li and Li [108]. An algebraic drift flux model implemented in ANSYS Fluent [8] was used. The phase change is not assumed as an instantaneous process to reach thermodynamic equilibrium, but a finite-rate phase change model is adopted to account for the non-equilibrium transition. Vaporisation and condensation rates are inherited from the dynamics of bubble growth and the kinetic theory of phase change in which there are two regimes, namely the cavitation regime and the boiling regime [195]. The Homogeneous Relaxation Model (HRM) [23, 63] was applied by Colarossi *et al.* [39], Haida *et al.* [81]. The thermodynamic non-equilibrium between the two phases is accounted through a relaxation time [156]. The Delayed Equilibrium Model (DEM) [17] was usually applied for the simulation of critical water flows through a breach in the context of a nuclear reactor. However, it has not been applied yet for two-phase CO_2 ejectors.

The most considered two-phase model for CO_2 supersonic ejector simulations is the HEM considered by Lucas *et al.* [117], Palacz *et al.* [130, 131], Smolka *et al.* [162]. The HEM is a very simplified two-phase model. Only the variables of the mixture are computed in the equations and no inter-phase source terms are involved. The main advantage of this model is the numerical robustness and the computational low cost compared to the two-fluid models. As a result, the HEM is primarily considered in this work.

The HEM is defined by a set of partial differential equations consisting of the conservations of mass (Equation (3.1)), momentum (Equation (3.2)) and total energy (Equation (3.3))

for the two-phase mixture. In one dimension, the set of equations reads :

$$\partial_t \rho + \partial_x(\rho u) = 0, \tag{3.1}$$

$$\partial_t(\rho u) + \partial_x(\rho u^2 + p) = 0, \tag{3.2}$$

$$\partial_t(\rho E) + \partial_x[(\rho E + p)u] = 0. \tag{3.3}$$

The system is written under its conservative form and the conservative variables are : ρ the density, ρu the momentum and ρE the total energy of the mixture. u and E denote the velocity of the mixture and its specific total energy, respectively, $E = e + u^2/2$, where e is the specific internal energy. A compact 1D formulation writes :

$$\partial_t U + \partial_x F(U) = 0, \tag{3.4}$$

where U is the vector form of the conservative variables and the term F represents the flux vector, expressed as :

$$U = \begin{bmatrix} \rho \\ \rho u \\ \rho E \end{bmatrix}, \quad F = \begin{bmatrix} \rho u \\ \rho u^2 + p \\ u(E + p) \end{bmatrix}. \tag{3.5}$$

This non-linear hyperbolic conservative equation system governs the dynamics of the inviscid and adiabatic compressible two-phase flow without body forces. It has formally the same structure as the single-phase Euler system. The full thermodynamic and mechanical equilibrium assumed in the HEM leads to the following constraints :

$$\begin{aligned} p_l &= p_v = p_{sat}, \\ T_l &= T_v = T_{sat}, \\ u_l &= u_v = u, \\ g_l &= g_v = g, \end{aligned} \tag{3.6}$$

where the subscripts l and v denote the liquid and the vapor phases, respectively. The term g represents the specific Gibbs free energy, $g = h - Ts$, where h is the specific enthalpy, T is the temperature and s is the specific entropy. Liquid and vapor remain always saturated, with the specific internal energy and the specific volume of the mixture being :

$$\begin{aligned} e &= x\, e_v + (1 - x)\, e_l, \\ v &= x\, v_v + (1 - x)\, v_l, \end{aligned} \tag{3.7}$$

where e_l, v_l, e_v, v_v are the quantities at saturation, $v = 1/\rho$ and x is the thermodynamic quality in the HEM frame, which is expressed as :

$$x = \frac{h - h_l}{h_v - h_l}, \tag{3.8}$$

where the specific enthalpy h is written as $h = e + pv$, and subscripts v and l relate to saturated vapor and saturated liquid, respectively.

Analysing the eigenvalues of the Jacobian of the vector F reported in Equation (3.4), one can determine the wave propagating speed of the model [47]. This speed is an intrinsic characteristic of the equation system. However, it is often estimated by the speed of sound which depends either on the mixture composition or on the degree of inter-phase equilibrium. From a thermodynamic point of view, the definition of the sound speed is :

$$c^2 = \left(\frac{\partial p}{\partial \rho}\right)_s. \tag{3.9}$$

As well known in the literature, the HEM has a discontinuous speed of sound (see Figure 3.1) at the saturation line, as explained by Flåtten and Lund [63]. The two-phase speed of sound can be computed as follows. Firstly, the primitive form of the hyperbolic system for the HEM is written as :

$$\partial_t \begin{bmatrix} \rho \\ u \\ p \end{bmatrix} + \begin{bmatrix} u & \rho & 0 \\ 0 & u & v \\ 0 & \gamma p & u \end{bmatrix} \partial_z \begin{bmatrix} \rho \\ u \\ p \end{bmatrix} = \begin{bmatrix} 0 \\ 0 \\ 0 \end{bmatrix}, \tag{3.10}$$

where the coefficient, γ, can be expressed as :

$$\gamma = \frac{1}{p\ \partial_p e}\ \left(\frac{p}{\rho} - \rho\ \partial_\rho e\right). \tag{3.11}$$

The eigenvalues of the system (3.10) are thus :

$$\lambda_1 = u - c, \qquad \lambda_2 = u, \qquad \lambda_3 = u + c. \tag{3.12}$$

The speed of sound of the HEM, c, is then defined as :

$$c \triangleq \sqrt{\frac{\gamma p}{\rho}}. \tag{3.13}$$

Substituting γ, the speed of sound reads then :

$$c^2 = \frac{\frac{p}{\rho} - \rho\left(\frac{\partial e}{\partial \rho}\right)_p}{\rho\left(\frac{\partial e}{\partial p}\right)_\rho}, \tag{3.14}$$

where :

$$\begin{aligned}\left(\frac{\partial e}{\partial \rho}\right)_p &= (e_v - e_l)\left(\frac{\partial x}{\partial \rho}\right)_p \\ &= -\frac{(e_v - e_l)}{\rho^2 (v_v - v_l)},\end{aligned} \tag{3.15}$$

and

$$\begin{aligned}\left(\frac{\partial e}{\partial p}\right)_\rho &= \left(\frac{\partial e}{\partial p}\right)_x - \left(\frac{\partial e}{\partial x}\right)_p \left(\frac{\partial \rho}{\partial p}\right)_x \left(\frac{\partial \rho}{\partial x}\right)_p^{-1} \\ &= \left(\frac{\partial e}{\partial p}\right)_x - \frac{e_v - e_l}{v_v - v_l}\left(\frac{\partial v}{\partial p}\right)_x.\end{aligned} \tag{3.16}$$

Finally, c can be determined through the following relation :

$$c^2 = \frac{p + \frac{e_v - e_l}{v_v - v_l}}{\rho^2\left[\left(\frac{\partial e}{\partial p}\right)_x - \frac{e_v - e_l}{v_v - v_l}\left(\frac{\partial v}{\partial p}\right)_x\right]}, \tag{3.17}$$

where $\left(\frac{\partial e}{\partial p}\right)_x = \left(x\frac{de_v(p)}{dp} + (1-x)\frac{de_l(p)}{dp}\right)$, and $\left(\frac{\partial v}{\partial p}\right)_x = \left(x\frac{dv_v(p)}{dp} + (1-x)\frac{dv_l(p)}{dp}\right)$.

Using the relations given above, it is obvious to calculate the speed of sound by a spline reconstruction of the saturation curve for $v_v(p), v_l(p), e_v(p), e_l(p)$. The spline coefficients can be evaluated using the original SW EoS [164]. The evaluation of the two-phase speed of sound as a function of the void fraction is shown in Figure 3.1, in which the relations of Wood [192], Nakagawa *et al.* [126], Ameur *et al.* [6] and HEM are compared. In fact, the relations of Wood [192], Nakagawa *et al.* [126] and Ameur *et al.* [6] use a mixing law by considering the saturation vapor and liquid states to model the two-phase speed of sound. Therefore, the discontinuities at the saturation line could be less important than the HEM. Figure 3.1 shows that the two-phase speed of sound of the HEM has low values for $\alpha_v = 1$ and $\alpha_v = 0$, which implies discontinuities through the saturation curve (the liquid speed of sound is about 400 $m.s^{-1}$ and the vapor speed of sound is about 200 $m.s^{-1}$). These discontinuities are model-dependent, as discussed by Flåtten and Lund [63], and Nakagawa *et al.* [126].

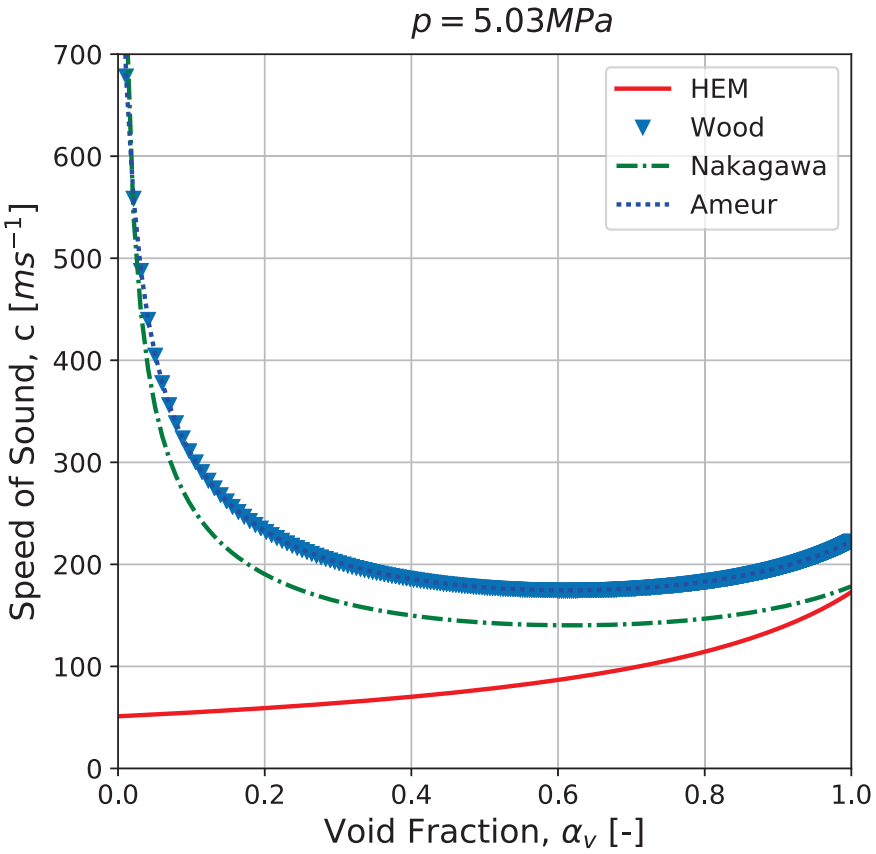

Figure 3.1 Two-phase speed of sound at $p = 5.03$ MPa computed by the HEM. Comparisons with the relations of Wood [192], Nakagawa *et al.* [126] and Ameur *et al.* [6].

In the system composed of Equations (3.1), (3.2) and (3.3), there are four unknowns (ρ, U, e, and p), but only three equations. In order to close the system, an EoS is required to compute the pressure $p(e, \rho)$ from the density and the specific internal energy.

3.2 Equation of State - Look-up table method

To solve the conservative Equations (3.1), (3.2) and (3.3), an equation of state is needed to compute the pressure and close the system. But this is not always straightforward. A function is required to compute the fluid properties in liquid, vapor, supercritical and two-phase states at a reasonable computational cost for future massive CFD simulations. Hence, an accurate and efficient approach to compute the thermodynamic fluid properties is necessary. In general, there are three types of approach to compute thermodynamic

properties : a simple equation of state, an iterative algorithm to get an accurate equation of state, and tabulated values.

3.2.1 Equation of state

In early simulations of ejectors, no specific attention was paid to the equation of state. Only the most simple EoS, perfect gas (PG) EoS was applied, specially for single-phase ejectors. Sriveerakul *et al.* [165, 166] used the perfect gas EoS to carry out a steam ejector simulation. A good agreement in terms of wall static pressure was obtained compared to their in-house experiment data, but the entrainment ratio in the off-design regime showed significant differences. The same EoS was also applied by Jeong *et al.* [93] and Ruangtrakoon *et al.* [149] in steam ejector simulations. For air ejectors [16, 36], perfect gas EoS was used and other properties remained constant. Considering two-phase states in CO_2 ejectors, the PG EoS is not adequate.

Another type of EoS is the cubic-form EoS, such as the Van der Waals EoS [183] :

$$p = \frac{rT}{v-b} - \frac{a}{v^2}, \tag{3.18}$$

where the denominator of the first term on the Right Hand Side (RHS) represents the volume occupied by the molecules themselves, and the second term on the RHS represents the attractive forces between molecules. This cubic-form EoS has a simple structure and requires a small number of coefficients, thus low computational cost is required. However, it is not accurate when the thermodynamic state is close to the saturation line. Thus, it is more suitable for gaseous states and supercritical states. Considering its generality and simplicity, it could be adequate for single-phase ejectors.

Peng-Robinson (PR) EoS [134, 135] is widely used for fluids under supercritical conditions.

$$p = \frac{\rho r T}{1-\rho b} - \frac{\rho^2 a(T)}{1+2\rho b-\rho^2 b^2}, \tag{3.19}$$

where ρ is the density, $r = R/W$ (with R the perfect-gas constant and W the molar mass). The coefficient $a(T)$ and b are defined as :

$$a(T) = 0.457236\frac{(rT_c)^2}{p_c}\left[1 + c\left(1-\sqrt{\frac{T}{T_c}}\right)\right]^2, \tag{3.20}$$

$$b = 0.077796\frac{rT_c}{p_c}, \tag{3.21}$$

where p_c and T_c are the critical pressure and critical temperature, respectively and c is defined as a function of the acentric factor ω by :

$$c = 0.37464 + 1.54226\omega - 0.26992\omega^2. \tag{3.22}$$

This EoS was used by Miller *et al.* [125] to conduct a DNS for a supercritical fluid mixing layer. The heat capacity, the compressibility and the speed of sound were computed based on Equation (3.19). The PR EoS was also used to perform an LES for supercritical-pressure round jets by Schmitt *et al.* [157] using the AVBP solver [31].

Soave-Redlich-Kwong (SRK) [135] EoS is also widely employed to provide thermodynamic properties for real gases. The difference between PR EoS and SRK EoS is the second term on the RHS of Equation (3.19), becoming $\frac{\rho^2 a(T)}{1+\rho b}$. More detailed formulations about the SRK EoS are presented in [73, 122]. Hakim *et al.* [82] carried out an LES of transcritical flames by applying the SRK EoS.

The PG EoS, SRK and the Refprop database [104] were assessed by Croquer *et al.* [43, 44] through single-phase R134a ejector simulations. The SRK and the Refprop database [104] present a significant difference in terms of density compared to the PG EoS for relevant operating conditions. The SRK provides comparable results compared to the Refprop database [104]. However, it should be noted that the cubic EoS is not suitable to describe two-phase regions and the near-saturation regions, where the square of the sound speed may become negative and non-physical values can be obtained.

In order to obtain a more accurate EoS, empirical EoS have been also developed. These EoS can involve a large number of coefficients and numerous terms, which are based on a multi-parameter fit of extensive experimental data. They are applicable in low and high ranges of temperature, pressure, density for gaseous, liquid and supercritical fluids and even in liquid-gas transition region, but more computational cost is required.

For example, Farzi and Hosseini [62] developed an empirical EoS for NH_3, Ar, C_4H_2O, CO, C_9H_2O. Duan and Zhang [50] created an EoS for H_2O and CO_2 (the presssure and the temperature are up to 10 GPa and 2573 K). For ejector-based refrigeration systems, the Refprop database [104] is widely used to compute the properties of any refrigerant. Bartosiewicz *et al.* [16] simulated R142b in an ejector by using the Refprop database [104] in ANSYS Fluent. Varga *et al.* [186] simulated R152a and R600a in ejectors using the same approach. R134a was investigated by Croquer *et al.* [43], García del Valle *et al.* [68]. The code PHOENIX with the Refprop database [104] was employed by Scott and

Aidoun [158], Scott *et al.* [159] to test R245fa and by Hakkaki-Fard *et al.* [83] to simulate R134a. IAPWS-95, published by International Association for the Properties of Water and Steam is often used for computing water properties. It is considered as the most reliable EoS for water [189]. Due to its complex and time consuming formulations, IAPWS-IF97 [188] replaces IAPWS-95 for industrial uses. Cai and He [29] investigated supersonic steam ejector in a steam turbine system by using IAPWS-IF97.

Another type of EoS is the Stiffened Gas EoS (SG EoS), as the linearization of the Mie-Gruneisen EoS [147]. It writes :

$$p = (\gamma - 1)\rho e - \gamma p_\infty, \tag{3.23}$$

where e is the specific internal energy, γ is the heat capacity ratio, γp_∞ denotes the pressure correction. Pelanti and Shyue [133] implemented the SG EoS in their six-equation two-phase model. Water cavitation tube problem, shock tube problem, high-pressure fuel injection, etc, have been tested with this EoS. However, the linearization of the SG EoS causes some errors in the non-linear regions of the thermodynamic diagram such as in the region close to the critical point. Additionally, the first-order derivatives of the thermodynamic properties can not be computed accurately due to the linearity. Besides, the choice of the reference states affects significantly its accuracy [123].

Raman and Kim [140] proved that the numerical results depend strongly on the thermodynamic properties of CO_2. Hence, the calculation of accurate thermodynamic properties of CO_2 is crucial for a reliable numerical simulation. For the simulation of two-phase transcritical CO_2 ejectors, the evaluation of the fluid properties close to the saturation line can not be avoided because the occurrence of flashing during the fluid expansion. Thus, accurate values close to the saturation line are absolutely required.

3.2.2 Span-Wagner EoS for CO_2

Span-Wagner (SW) EoS [164] is considered as the standard EoS specifically for CO_2 from the triple-point temperature to 1100 K at pressure up to 800 MPa. It is an EoS based on hundreds of parameters that are fitted by extensive experimental data in terms of pressure, heat capacity, speed of sound and other thermodynamic properties. The formulation stems from the specific Helmholtz free energy A, in dimensionless form $\phi = A/RT$, respect to the reduced temperature, $\tau = T_c/T$ and the reduced density, $\delta = \rho/\rho_c$, where ρ_c and T_c are the critical density and temperature, respectively. The formulation reads :

$$\phi(\delta,\tau) = \phi^0(\delta,\tau) + \phi^r(\delta,\tau), \tag{3.24}$$

where ϕ consists of two parts, the ideal part ϕ^0 and the residual part ϕ^r. The ideal part describes the perfect gas behavior of CO_2, while the residual part is considered as a correction part to enhance the accuracy for the specific phase states, such as in the neighbourhood of the critical point. The residual part is expressed as :

$$\begin{aligned}\phi^{\mathrm{r}} = &\sum_{i=1}^{4}\sum_{j=0}^{20} n_{i,j}\delta^i\tau^{j/4} + \sum_{i=1}^{6}\sum_{j=0}^{10} n_{i,j}\delta^i\tau^{j/2}\mathrm{e}^{-\delta} + \sum_{i=1}^{8}\sum_{j=0}^{8} n_{i,j}\delta^i\tau^j\mathrm{e}^{-\delta^2} + \sum_{i=1}^{8}\sum_{j=0}^{16} n_{i,j}\delta^i\tau^j\mathrm{e}^{-\delta^3} \\ &+ \sum_{i=1}^{10}\sum_{j=0}^{12} n_{i,j}\delta^i\tau^{2j}\mathrm{e}^{-\delta^4} + \sum_{i=1}^{10}\sum_{j=5}^{16} n_{i,j}\delta^i\tau^{2j}\mathrm{e}^{-\delta^5} + \sum_{i=8}^{15}\sum_{j=5}^{16} n_{i,j}\delta^i\tau^{2j}\mathrm{e}^{-\delta^6} \\ &+ \sum_{i=1}^{48} n_i\delta^{d_i}\tau^{t_i}\mathrm{e}^{-\alpha_i(\delta-\epsilon_i)^2-\beta_i(\tau-\gamma_i)^2} + \sum_{i=1}^{3}\sum_{j=1}^{2}\sum_{k=1}^{2}\sum_{l=1}^{3}\sum_{m=1}^{3} n_{i,j,k,l}\Delta^{b_j}\delta\mathrm{e}^{-C_l(\delta-1)^2-D_m(\tau-1)^2},\end{aligned} \tag{3.25}$$

with $\Delta = \left\{(1-\tau) + A\left[(\delta-1)^2\right]^{1/(2\beta)}\right\}^2 + B_k\left[(\delta-1)^2\right]^{a_i}$. $n_{i,j}$, d_i, α_i, t_i, ϵ_i, β_i, γ_i, b_i, C_l, D_m, A, B_k, and a_i are empirical parameters for the residual part. The required thermodynamic properties can be derived from the combination of the first and second derivatives of the Helmholtz energy respect to the reduced temperature and density. For example, the pressure and the speed of sound read :

$$p(\delta,\tau) = \rho RT(1+\delta\phi^r_\delta), \tag{3.26}$$

$$c^2(\delta,\tau) = RT\left(1 + 2\delta\phi^r_\delta + \delta^2\phi^r_{\delta\delta} - \frac{(1+\delta\phi^r_\delta - \delta\tau\phi^r_{\delta\tau})}{\tau^2(\phi^0_{\tau\tau}+\phi^r_{\tau\tau})}\right), \tag{3.27}$$

where the subscript δ and τ represent the derivatives with respect to δ and τ. Double subscripts of δ or τ represent the second derivative or the cross derivative. The isochoric heat capacity, isobaric heat capacity, specific enthalpy, specific internal energy, and specific entropy can be derived similarly as Equations (3.26) and (3.27). In this work, the SW EoS has been primarily implemented through an *in-house* FORTRAN code and prepared for the later tabulated approach. It can be noticed that the SW EoS depends basically on density and temperature. However, for a compressible solver based on the conservation

formulation, the two independent variables are the density and the specific internal energy. Hence, the tabulated approach is designed to depend on the density and the specific internal energy.

3.2.3 Look-up table method

The density ρ and the specific internal energy e can be computed directly from the conservative Equations (3.1) and (3.3). Thus, the most natural way to determine the thermodynamic properties is to use the pair of variables, (ρ, e), such as for the pressure, $p = p(\rho, e)$. The latter is called an *incomplete EoS*. On the contrary, *Complete EoS* is usually described in terms of Helmholtz free energy and the independent variables are temperature and density such as for the Span-Wagner EoS. In order to construct an *incomplete* EoS with SW EoS, it requires inversion procedures. For example, for the pressure calculation when ρ and e are initially known, the temperature should be iteratively computed by the Newton-Raphson method. Then, the pressure is computed by SW EoS through the pair of (ρ, T). Consequently, the direct use of SW EoS requires a high computational cost. Stability and robustness issues can be encountered. In a numerical simulation, the EoS is needed at each time step for each mesh point. The computational cost for the EoS can rapidly increase depending on the mesh grid and other simulation parameters. Hence, a fast EoS can significantly improve the whole efficiency of the simulation.

The look-up table method is a good candidate to achieve such a high efficiency. Inversion algorithms are used at the table construction stage in preprocessing and the properties at the grid nodes are stored in the memory. During the simulation, only finding the correct values in the table is needed at each iteration. This kind of method has been developed for the fast calculation of water-steam properties [47, 97]. It has shown not only an extreme efficiency, but also a high accuracy. It has been used in several CFD codes [142, 173] for water, but iterative algorithms were still involved depending on the construction of the EoS. The present look-up table approach is based on the work of De Lorenzo *et al.* [47]. The main difference is that De Lorenzo *et al.* [47] used a bi-cubic interpolation to compute the water properties, while the present approach uses a bilinear interpolation to compute the properties of CO_2. In the following, it has been validated that the bilinear interpolation is sufficient to achieve accurate and efficient results. It should be mentioned that for the proposed tabulated EoS, the grid is 'body-fitted' to the form of the isobaric curves and the saturation curve in the $e - v$ diagram. Another advantage of the tabulation strategy is that once the variables (ρ, e) are known, the phase location in the $e - v$ space is

determined. Therefore, the evolution of the phase state during numerical simulations can be monitored and the location of the onset of the phase change can be determined.

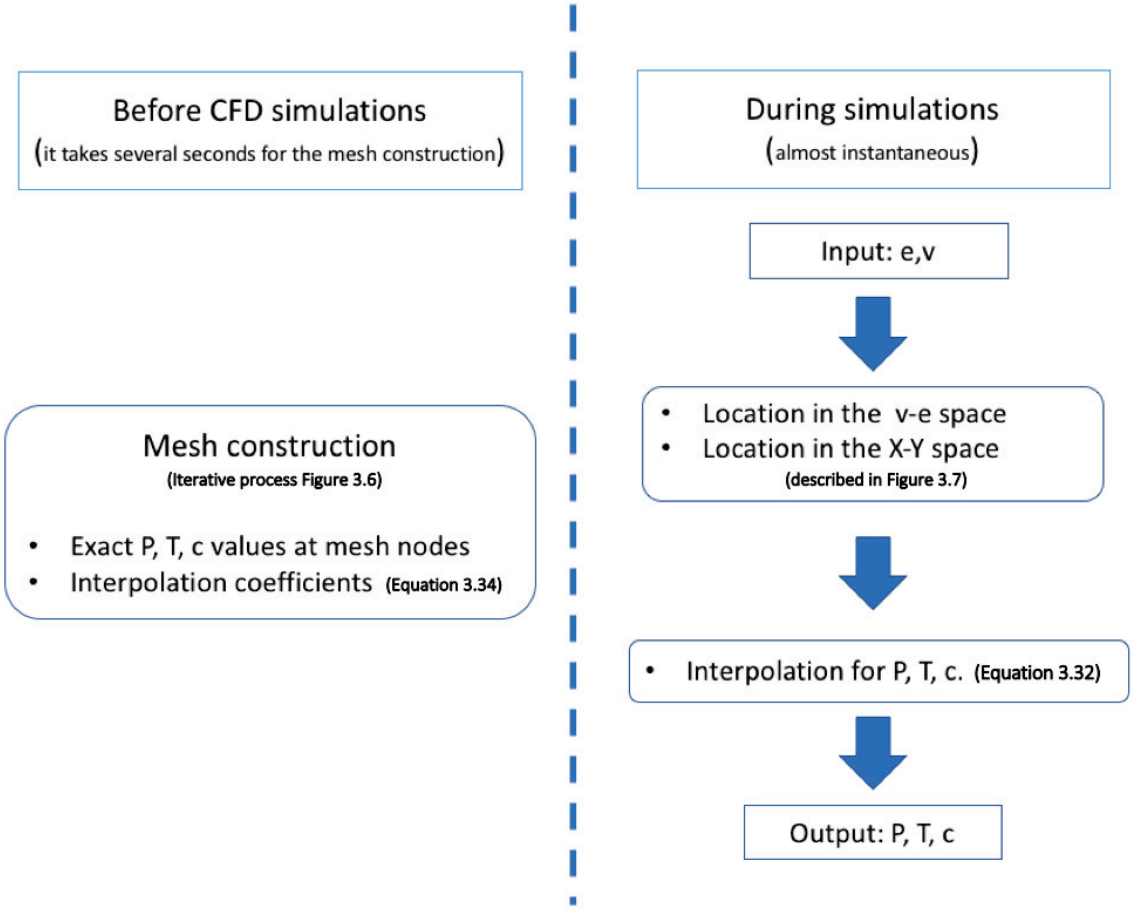

Figure 3.2 Flowchart of the look-up table method.

The procedure of the look-up table method is shown in Figure 3.2. Firstly, a grid is constructed in the $e - v$ space presented in Figure 3.3. Then, pressure, temperature and speed of sound are computed by the original SW EoS with iterative algorithms at each node with (e, v) as the input coordinates. As the interpolation is performed in the transformed space, thus the $e - v$ space is then transformed to $X - Y$ space and the interpolation coefficients are computed. Finally, pressure, temperature and sound speed can be obtained by the bilinear interpolation of the node values. As mentioned above, the tabulated method is not used in the whole domain, because the accuracy of the interpolation is not ensured for extreme deformed regions. For example at the intersection between the saturation line and the iso-internal energy boundary (in purple) in Figure 3.3, due to the high curvature of the saturation line, the errors of the bilinear interpolation is relative high. Therefore, the original SW EoS is used in tiny regions coupled to the Newton-Raphson method.

However, the tabulated values are still useful in these regions, which are considered as initial guesses to ensure the speed and the stability of the convergence. Normally, the number of iterations is less than 6. Figure 3.3 illustrates the $e - v$ diagram, called also the physical domain in the following.

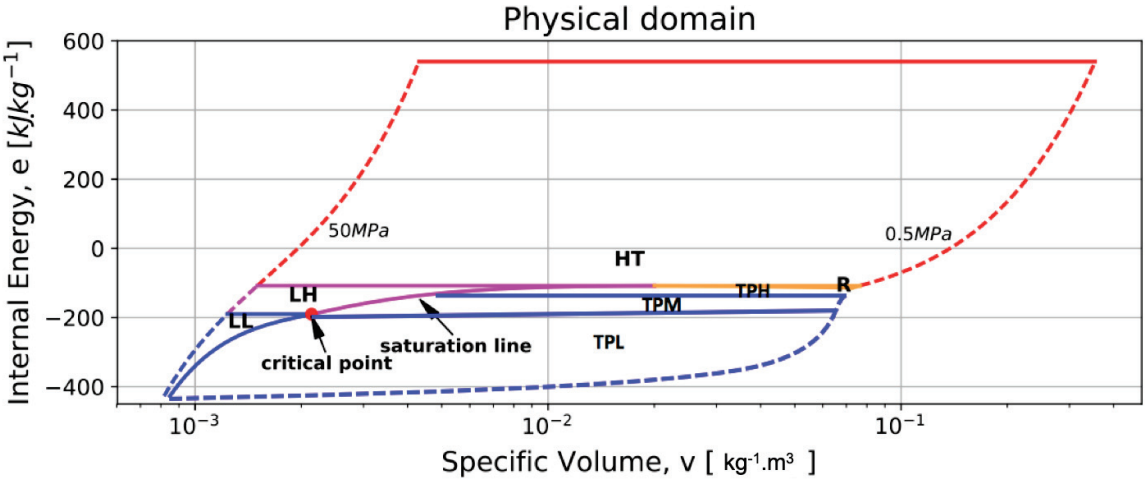

Figure 3.3 $e - v$ diagram in the physical domain with pressures from 0.5 MPa to 50 MPa and temperatures from 216.5 K to approximately 800 K.

The $e - v$ diagram is not a frequent representation of the thermodynamic properties compared to $(p - T)$ or $(T - s)$ diagrams. In $e - v$ diagram, the saturation curve is deformed. The blue curves surround the liquid region while the purple curves surround the supercritical region and the vapor region is wrapped by the red and yellow curves. The two-phase dome under the saturation line represents the two-phase region. Figures 3.4 and 3.5 show the isobaric lines and the isothermal lines provided by the tabulated values.

Considering the boundary of the table, the maximum pressure is fixed at 50 MPa as the left boundary, while the minimum pressure is fixed to the triple point pressure, $p = 0.5$ MPa as the right boundary. The maximum internal energy corresponding to approximate 800 K fixes the top boundary, while the bottom boundary is the internal energy of the triple point of liquid. It can be seen that the physical domain is large, because when a numerical simulation is performed, numerical oscillations can cause a divergence of the table. It should be noted that in the region with pressures smaller than 0.5 MPa, the PG EoS is applied. Hence, the ranges in terms of pressure and temperature are sufficiently large to cover most of industrial applications involving CO_2.

Grid construction in the $e - v$ space

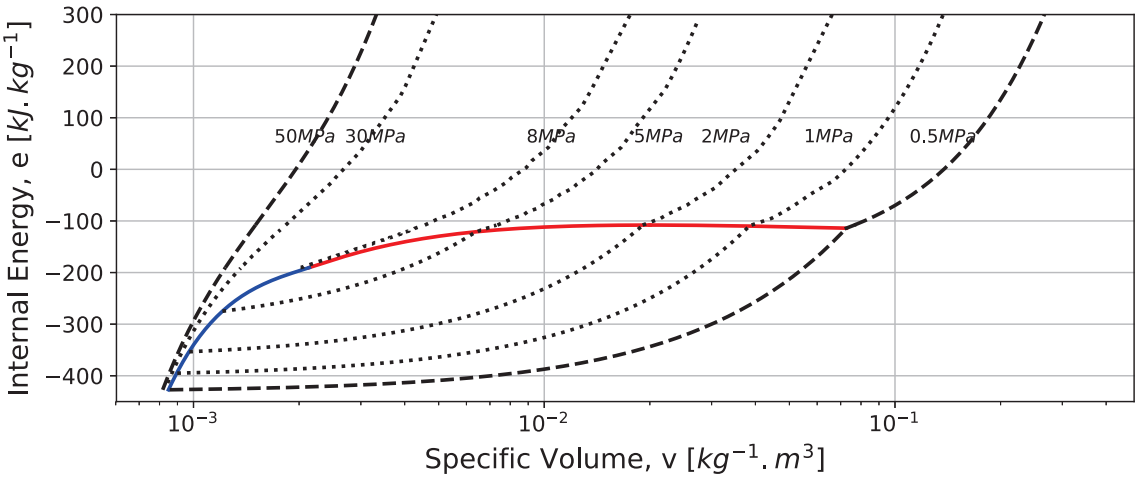

Figure 3.4 Isobaric curves in the $e - v$ diagram.

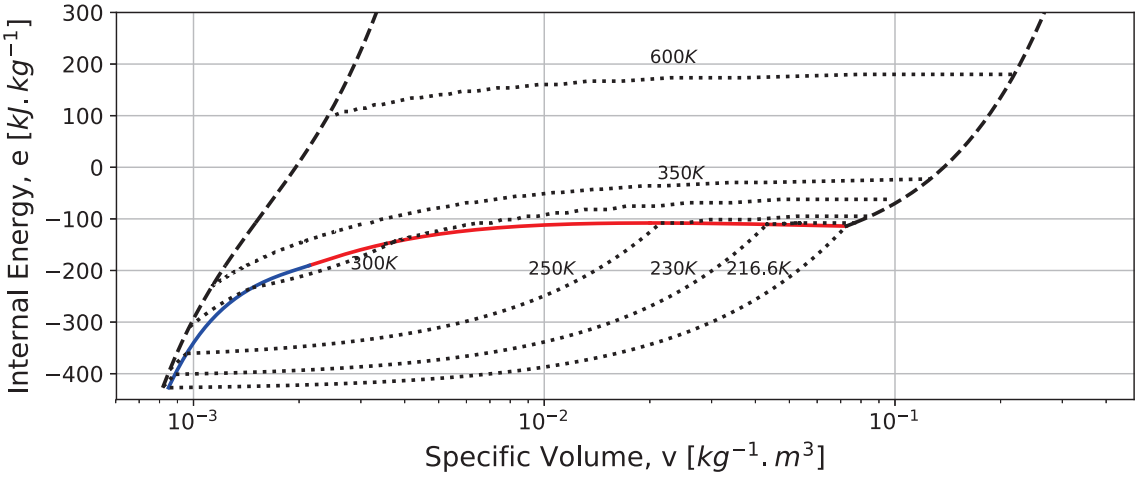

Figure 3.5 Isothermal curves in the $e - v$ diagram.

The Left-Low (LL), Left-High (LH), Right (R), and Two-phase (TP) regions are meshed with equidistant pattern of nodes for the same internal energy, whereas the High-Temperature (HT) region uses a logarithmic distribution of nodes for a given internal energy. The two-phase region is split into three subregions : Two-Phase High (TPH), Two-Phase Middle (TPM) and Two-Phase Low (TPL) subregions separated by the isoline of the critical internal energy and the triple-point internal energy of vapor (Figure 3.3). Each region is meshed with 10000 nodes. In total, 70000 nodes are used for the whole physical domain. Different meshes have been evaluated and this mesh was found to be more accurate near the critical point.

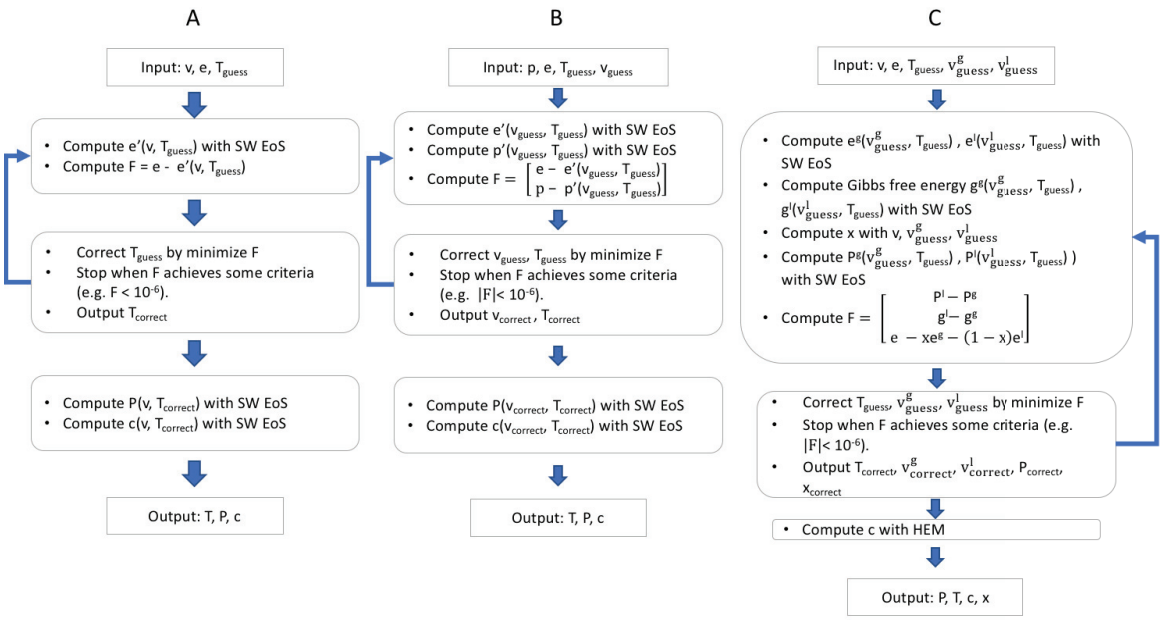

Figure 3.6 Scheme describing the iterative process to find one, two, and three roots.

At each node, values for pressure, temperature, and sound speed are computed through iterative processes which are illustrated in Figure 3.6. There are three types of iterative process, which are used for different locations in the physical domain. For example, the process A shows the iterative way to find one solution. It is used for the nodes in the middle of the domain, in which the internal energy and the density are known and only the temperature should be computed. Once the temperature and the density are available, the original SW EoS can be used to compute other properties. The process B enables to find two solutions and is used for the high pressure boundary on the left and the low pressure boundary on the right. At these two boundaries, pressure and specific internal energy are known, the two solutions are then temperature and density. The process C is used to find three solutions for the saturation line. On the saturation line, when the specific internal energy is known, the process C can compute the saturation temperature, the saturation liquid density, and the corresponding saturation vapor density.

Transformation from irregular physical space to $X - Y$ Cartesian space

To improve the accuracy of the bilinear interpolation, the irregular mesh (parallelogram) in the $e - v$ space is transformed to a $X - Y$ Cartesian space with square cells (Figure 3.7). The size of the $X - Y$ space is chosen initially, here each cell in the $X - Y$ space is fixed to unity. The numbers of cells in the $e - v$ space and in the $X - Y$ space are imposed to be equal.

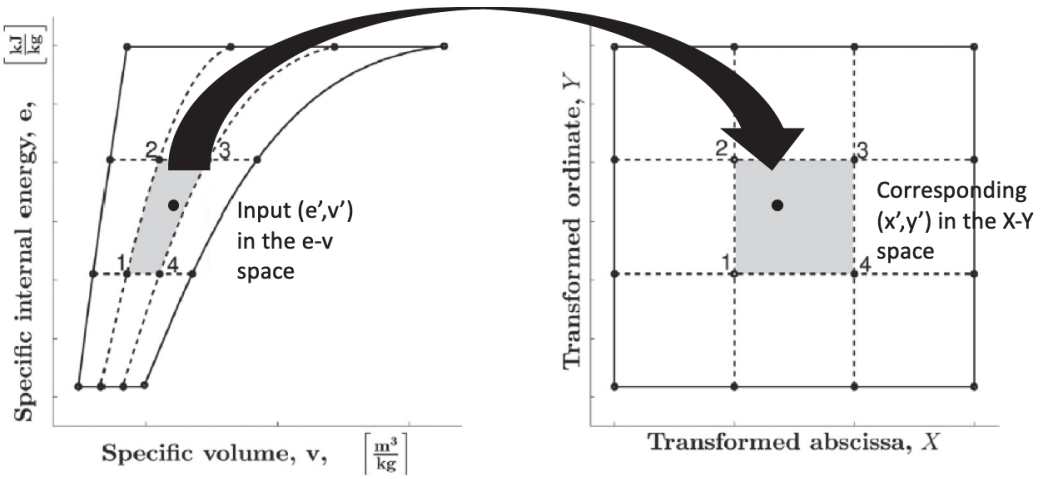

Figure 3.7 Mapped physical space and $X - Y$ space from De Lorenzo *et al.* [47]. The numbering of vertices for one cell starts from the left bottom corner and is counted in the clockwise direction.

A transformation function is defined to rescale the irregular mesh to the regular square-form mesh :

$$\Phi : \mathbb{R}^2 \to \mathbb{R}^2 \qquad \text{such that :} \quad \forall (v, e) \in \mathcal{D} \Rightarrow (X, Y) \in \mathcal{D}', \tag{3.28}$$

where $\mathcal{D}$ and $\mathcal{D}'$ denote the physical and transformed spaces, respectively. The internal energy is meshed equidistantly in both spaces, thus e is linearly scaled to Y (Equation (3.29)). On the contrary, the scaling coefficients for v are energy-dependent, because in the $e - v$ space, the boundary values for v are different and correspond to each level of the internal energy (Equation (3.30)). Therefore, the transformation function for the mesh is written as :

$$e_i = A + BY_i, \tag{3.29}$$

$$v_{i,j} = C(e_i) + D(e_i)X_{i,j}. \tag{3.30}$$

The coefficients A and B are constant values and C and D are variables depending on e, which are determined by the spline construction of the domain boundary. The subscripts i and j represent the node number in the e (Y) and v (X) directions, respectively. Then, the bilinear interpolation is performed in the $X - Y$ space. The errors from the interpolation method can be reduced by the space transformation. However, there are still errors coming

from the transformation of the irregular grid to the regular one. Hence, a very fine grid is considered to reduce these errors.

Before the bilinear interpolation, the location of the phase state in the $X-Y$ space should be determined. Similarly, a pair (e_0, v_0) is associated with its corresponding pair (X_0, Y_0) in the $X-Y$ space, by inverting Equations (3.29) and (3.30). Once (X_0, Y_0) are obtained, the coordinates (i, j) of the vertices are obtained by :

$$i = int\left(\frac{Y_0 - Y_{min}}{\Delta Y}\right), \qquad j = int\left(\frac{X_0 - X_{min}}{\Delta X}\right), \tag{3.31}$$

where (i, j) indicate the numbering of the cell, to which (X_0, Y_0) belong.

Bilinear interpolation

The interpolation coefficients are computed to determine the bilinear interpolation function in each cell (i, j) [91, 150]. For example, the function for pressure in each cell is computed as :

$$\tilde{p}_{i,j} = \gamma^1_{i,j} + \gamma^2_{i,j} X_{i,j} + \gamma^3_{i,j} Y_i + \gamma^4_{i,j} X_{i,j} Y_i, \tag{3.32}$$

where $\tilde{p}_{i,j}$ is the value from the bilinear interpolation. The coefficients $\gamma^k_{i,j}$ correspond to the k vertices in the (i, j) cell. They are obtained by solving the system constructed by the pressure at the four vertices of the cell (i, j) in the $X - Y$ space whose values in the $e - v$ space can be expressed as :

$$\begin{bmatrix} 1 & 0 & 0 & 0 \\ 1 & 0 & 1 & 0 \\ 1 & 1 & 1 & 1 \\ 1 & 1 & 0 & 0 \end{bmatrix} \begin{bmatrix} \gamma^1 \\ \gamma^2 \\ \gamma^3 \\ \gamma^4 \end{bmatrix} = \begin{bmatrix} p_1 \\ p_2 \\ p_3 \\ p_4 \end{bmatrix}. \tag{3.33}$$

The pressure at the four vertices, p_1, p_2, p_3, and p_4 correspond to the node values in the physical space, which are obtained by the original SW EoS. The explicit expressions of each coefficient read :

$$\gamma^1 = p_1, \quad \gamma^2 = -p_1 + p_4, \quad \gamma^3 = -p_1 + p_2, \quad \gamma^4 = p_1 - p_2 + p_3 - p_4. \tag{3.34}$$

Once γ_i is determined, one can directly obtain the pressure after determining the position of the couple (e_0, v_0) in the transformed space (X_0, Y_0) by :

$$p(e_0, v_0) = \tilde{p}(X_0, Y_0) = \gamma_1 + \gamma_2 X_0 + \gamma_3 Y_0 + \gamma_4 X_0 Y_0. \tag{3.35}$$

Other properties such as the speed of sound and the heat capacity, can be obtained in the same manner as described above. Considering the linear form of the bilinear interpolation, this interpolation method is extremely efficient. Only the grid construction stage costs a few seconds at the beginning of each simulation, which is negligible compared to the total time of one simulation. This method also shows a good accuracy as reported in Chapter 4.

Additionally, the transport properties, such as the dynamic viscosity and the thermal conductivity, are implemented as separated equations depending on density and temperature [87, 90, 187]. It is noted that the viscosity of the two-phase mixture is based on the mass averaged value [38] :

$$\mu_m = x\,\mu_g + (1-x)\,\mu_l, \tag{3.36}$$

where x denotes the thermodynamic quality, μ_m, μ_g and μ_l denote the mixture, vapor, and liquid dynamic viscosities. Other mixing laws to determine the two-phase viscosity can be easily evaluated, such as McAdams *et al.* [120], Beattie and Whalley [18], or Fourar and Bories [66]. The thermal conductivity of CO_2 in its different states is computed based on the experimental data of Vesovic *et al.* [187]. The same mixing law as the dynamic viscosity (Equation (3.36)) is used to determine the conductivity of the two-phase mixture. Moreover, the derivatives such as $\left(\frac{\partial p}{\partial e}\right)_v$, $\left(\frac{\partial p}{\partial \rho}\right)_e$, are not tabulated but directly evaluated through SW EoS, once the density and the temperature are determined. Contrary to the splined-based interpolation proposed by Kunick *et al.* [97] and the bicubic interpolation applied by De Lorenzo *et al.* [47] for water properties, the continuity of the derivatives of the tabulated properties through the cell boundary is not ensured. But large number of nodes are computed in each subregion to make the tabulated properties sufficiently smooth in the whole $e-v$ space. No numerical issue has been encountered caused by the discontinuity of some property in the numerical simulations hereafter. In addition, the thermodynamic consistency is naturally satisfied through the construction of pressure, entropy, internal energy by the SW EoS [170]. Validations of the look-up table approach are presented in Chapter 4. The accuracy and efficiency are evaluated between different EoS.

3.3 CLAWPACK solver

The previous tabulated EoS is firstly implemented in the open-source software CLAWPACK [107] for validation and verification purposes. Moreover this solver can also compute compressible flows in nozzles, shock tubes, etc. It can capture shocks, contact or

rarefaction waves, so it is relevant to fluid flows occurring in two-phase ejectors. It solves hyperbolic systems in 1D and 2D by using the wave propagation method [106, 107]. This method is classified as a Godunov-type finite volume scheme [74], and a HLLC-type (modified Harten, Lax and van Leer HLL solver) Riemann solver is implemented to solve the Riemann problem at each interface of the cells [177, 178]. In the subsequent sections, the main ideas of the numerical method are described in 1D and 2D, respectively.

3.3.1 One-dimensional wave-propagation method

The hyperbolic system composed of Equations (3.1), (3.2) and (3.3) can be discretized on an uniform one-dimensional grid with a constant spatial step Δx. The time-integration is achieved using the Euler explicit scheme with the time step Δt. Q_i^n denotes the approximated value of the variable U (Equation (3.4)) averaged over the i^{th} cell at time t_n (Figure 3.8).

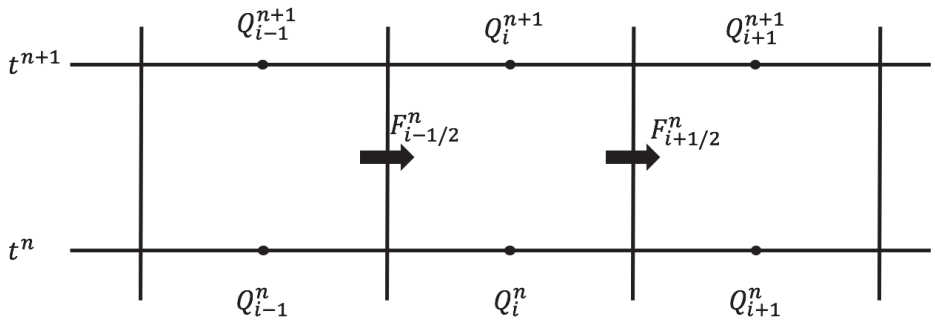

Figure 3.8 1D finite volume method for updating Q in the $(x-t)$ space.

The approximated solution Q in cell i is updated at each time step as :

$$\mathbf{Q}_i^{n+1} = \mathbf{Q}_i^n - \frac{\Delta t}{\Delta x}(\mathcal{A}^+\Delta\mathbf{Q}_{i-\frac{1}{2}} + \mathcal{A}^-\Delta\mathbf{Q}_{i+\frac{1}{2}}) + \frac{\Delta t}{\Delta x}(\tilde{\mathbf{F}}_{i-\frac{1}{2}}^{2nd} - \tilde{\mathbf{F}}_{i+\frac{1}{2}}^{2nd}). \tag{3.37}$$

In Figure 3.8, the fluxes at the interfaces of the cell i, $F_{i-\frac{1}{2}}^n$ and $F_{i+\frac{1}{2}}^n$, are decomposed into fluctuation terms and correction terms. $\mathcal{A}^{\pm}\Delta Q_{i\pm\frac{1}{2}}$ is called fluctuations at the interface $i\pm\frac{1}{2}$, where the superscripts $+$ and $-$ of $\mathcal{A}$ indicate the right-going and left-going fluctuations, respectively. $\tilde{F}_{i\pm\frac{1}{2}}^{2nd}$ represents the correction terms for the flux to achieve a second-order accuracy. The fluctuation at the interface can be obtained as [106] :

$$\mathcal{A}^+\Delta\mathbf{Q}_{i-\frac{1}{2}} = \sum_{m=1}^{M} s_{i-\frac{1}{2}}^{m+}\mathcal{W}_{i-\frac{1}{2}}^m, \qquad \mathcal{A}^-\Delta\mathbf{Q}_{i+\frac{1}{2}} = \sum_{m=1}^{M} s_{i+\frac{1}{2}}^{m-}\mathcal{W}_{i+\frac{1}{2}}^m, \tag{3.38}$$

where $s^{\pm}$ is the wave right- and left- propagating speed and $\mathcal{W}$ is the variation of the variables across the propagating waves. M is the number of waves in Equations (3.1), (3.2) and (3.3). Here, the one-dimensional Euler system is composed of three waves (Figure 3.9). The second-order accuracy is obtained by adding the correction fluxes :

$$\begin{aligned}
\tilde{\mathbf{F}}^{2nd}_{i+\frac{1}{2}} &= \frac{1}{2}\sum_{m=1}^{M} |s^m_{i+\frac{1}{2}}| \left(1 - \frac{\Delta t}{\Delta x}|s^m_{i+\frac{1}{2}}|\right) \tilde{\mathcal{W}}^{m,2nd}_{i+\frac{1}{2}}, \\
\tilde{\mathbf{F}}^{2nd}_{i-\frac{1}{2}} &= \frac{1}{2}\sum_{m=1}^{M} |s^m_{i-\frac{1}{2}}| \left(1 - \frac{\Delta t}{\Delta x}|s^m_{i-\frac{1}{2}}|\right) \tilde{\mathcal{W}}^{m,2nd}_{i-\frac{1}{2}},
\end{aligned} \tag{3.39}$$

where $\tilde{\mathcal{W}}^{m,2nd}_{i\pm\frac{1}{2}}$ denotes a modified wave strength based on a limiter function [106]. Hereafter a Riemann solver can give at each interface the wave strength $\mathcal{W}$. The associated wave propagation speed, s, is computed through the formulation of Davis [46].

3.3.2 Two-dimensional wave-propagation method

In two dimensions, the formulation is similar. The update of the numerical solution $Q_{i,j}$ from t_n to t_{n+1} is expressed as :

$$\begin{aligned}
\mathbf{Q}^{n+1}_{i,j} = \mathbf{Q}^n_{i,j} &- \frac{\Delta t}{\Delta x}(\mathcal{A}^+\Delta\mathbf{Q}_{i-\frac{1}{2},j} + \mathcal{A}^-\Delta\mathbf{Q}_{i+\frac{1}{2},j}) \\
&- \frac{\Delta t}{\Delta y}(\mathcal{B}^+\Delta\mathbf{Q}_{i,j-\frac{1}{2}} + \mathcal{B}^-\Delta\mathbf{Q}_{i,j+\frac{1}{2}}) \\
&+ \frac{\Delta t}{\Delta x}(\tilde{\mathbf{F}}^h_{i-\frac{1}{2},j} - \tilde{\mathbf{F}}^h_{i+\frac{1}{2},j}) + \frac{\Delta t}{\Delta y}(\tilde{\mathbf{G}}^h_{i,j-\frac{1}{2}} - \tilde{\mathbf{G}}^h_{i,j+\frac{1}{2}}),
\end{aligned} \tag{3.40}$$

where $\mathcal{A}^+\Delta\mathbf{Q}$ and $\mathcal{B}^+\Delta\mathbf{Q}$ are the fluctuations at the interface in the x and y directions. The correction fluxes $\tilde{\mathbf{F}}^h$ and $\tilde{\mathbf{G}}^h$ consist of second-order corrections and contributions of the transverse fluctuations [133]. Here, a dimensional splitting strategy is considered : the 1D Riemann solver is applied separately for the x and y directions at each time step [106]. This strategy may introduce a splitting error. LeVeque [106] mentioned that the splitting error is often of the same order as the errors due to the numerical method. Hence, the dimensional splitting approach could give an inexpensive way for two- or three-dimensional simulations.

Furthermore, the formulation of Equation (3.40), which relies on a Cartesian grid, is extended to quadrilateral grids (curvilinear grids) through a conformal transformation for more 2D complex computational domains [105, 106].

3.3.3 HLLC-type Riemann solver

The HLLC-type solver of Toro [178] is implemented in the CLAWPACK solver to solve the local Riemann problem at the cell interface to provide the wave strength $\mathcal{W}^m$. This type of solver has some attractive features : first, it is able to capture clean and sharp discontinuities such as shock waves and contact discontinuities. Second, it is robust and efficient for non-ideal gases compared to the exact Riemann solver.

Generally, the HLLC solver is an improvement of the HLL solver (Harten, Lax, van Leer) [86]. The contact surface is taken into account, where the temperature and the internal energy are discontinuous contrary to the pressure and the velocity. Here, in one dimension, the configuration of three waves separating four states, $\mathbf{Q}_L$, $\mathbf{Q}_L^*$, $\mathbf{Q}_R^*$, $\mathbf{Q}_R$ are assumed, as depicted in Figure 3.9.

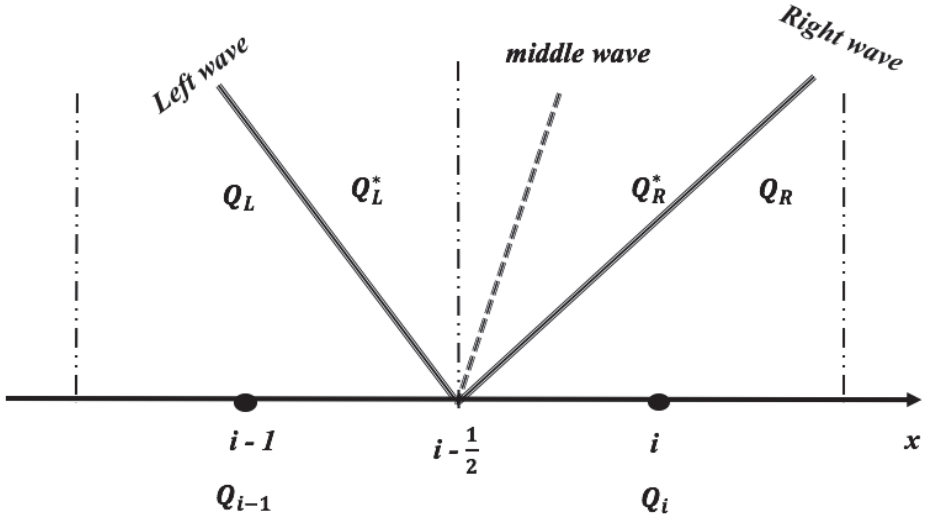

Figure 3.9 Three waves define four piecewise constant states for the Riemann problem [178].

The left and right waves are called non-linear waves and they can be either shocks or rarefactions, propagating with speed $s^1 = S_l$ and $s^3 = S_r$. The middle wave propagates at $s^2 = S_*$. Following Davis [46], the wave speeds are estimated as :

$$S_l = \min(u_l - c_l, u_r - c_r), \qquad S_r = \max(u_l + c_l, u_r + c_r). \tag{3.41}$$

To calculate S_*, Toro [177] proposed :

$$S_* = \frac{p_r - p_l + \rho_l u_l(S_l - u_l) - \rho_r u_r(S_r - u_r)}{\rho_l(S_l - u_l) - \rho_r(S_r - u_r)}. \tag{3.42}$$

The left and right-state sound speeds c_l, c_r and the pressure p_l, p_r correspond to the local thermodynamic states. They are obtained by the tabulated EoS. Furthermore, the middle states are obtained as [177] :

$$\mathbf{Q}_K^* = \rho_K \left(\frac{S_K - u_K}{S_K - S_*}\right) \begin{bmatrix} 1 \\ S_* \\ \frac{E_K}{\rho_K} + (S_* - u_K)\left[S_* + \frac{p_K}{\rho_K(S_K - u_K)}\right] \end{bmatrix}, \tag{3.43}$$

where $K = l, r$. Then the wave strengthes are computed as :

$$\mathcal{W}^1 = \mathbf{Q}_L^* - \mathbf{Q}_L, \quad \mathcal{W}^2 = \mathbf{Q}_R^* - \mathbf{Q}_L^*, \quad \mathcal{W}^3 = \mathbf{Q}_R - \mathbf{Q}_L^*, \tag{3.44}$$

where $\mathbf{Q}_L$ takes the average value of the conservative variables in cell $i-1$, $\mathbf{Q}_{i-1}$ (Figure 3.9), while $\mathbf{Q}_R$ is equal to that of cell $i-1$, $\mathbf{Q}_i$ (Figure 3.9). Finally, $\mathcal{W}$ and s are determined to compute the fluctuations at the interface through Equation (3.38). Numerical simulations are carried out for single-phase and two-phase CO_2 flows to assess the performance of the tabulated EoS in Chapter 4.

3.4 Solver for RANS simulations

3.4.1 Density-based solver

The *rhoCentralFoam* solver of the open source OpenFoam library is a density-based solver, which is originally designed for simulations of high-speed compressible flows. The original *rhoCentralFoam* solver was proposed by Greenshields *et al.* [76]. It is based on a finite volume method using semi-discrete, non-staggered central schemes for collocated variables. It is a Riemann-solver-free approach to capture discontinuities in compresssible flows, such as shock waves or contact surfaces. This solver compares fairly well to more complex

methods involving Riemann solver, characteristic decomposition or Jacobian evaluation (e.g. monotonous upstream-centered scheme for conservation laws [185], essential non-oscillatory (ENO) schemes [85] ...).

The Navier-Stokes equations are considered as the governing equations in the solver :

$$\frac{\partial \rho}{\partial t} + \nabla \cdot (\rho \mathbf{u}) = 0, \tag{3.45}$$

$$\frac{\partial (\rho \mathbf{u})}{\partial t} + \nabla \cdot (\rho \mathbf{u}\mathbf{u} + p\mathbf{I}) + \nabla \cdot \mathbf{T} = 0, \tag{3.46}$$

$$\frac{\partial (\rho E)}{\partial t} + \nabla \cdot [(\rho E + p)\mathbf{u})] + \nabla \cdot (\mathbf{T} \cdot \mathbf{u}) + \nabla \cdot \mathbf{j} = 0. \tag{3.47}$$

The conservations of mass (Equation (3.45)), momentum (Equation (3.46)) and total energy (Equation (3.47)) are expressed in their conservative formulation, in which the conservative variables are ρ, $\rho\mathbf{u}$, and ρE. u and E denote the velocity of the mixture and its specific total energy, respectively, $E = e+ \mid \mathbf{u} \mid^2 /2$, where e is the specific internal energy. $\mathbf{T}$ is the stress tensor for compressible flow using the Stoke's hypothesis, written as :

$$\mathbf{T} = -2\mu * \mathsf{dev}(\mathbf{D}), \tag{3.48}$$

where μ is the dynamic viscosity and $\mathbf{D}$ denotes the deformation gradient tensor, $\mathbf{D} = \frac{1}{2}(\nabla \mathbf{u} + \nabla \mathbf{u}^T)$. Its deviatoric component is $\mathsf{dev}(\mathbf{D}) = \mathbf{D} - \frac{1}{3}\mathrm{Tr}(\mathbf{D})\mathbf{I}$, where $\mathbf{I}$ is the unit tensor. The heat diffusion term is closed by the Fourier's Law :

$$\mathbf{j} = -k\nabla T, \tag{3.49}$$

where k is the thermal conductivity and T is temperature. In the *rhoCentralFoam* solver, the heat flux is computed based on the internal energy because of its conservative formulation. As a result, the heat flux is written as :

$$\mathbf{j} = -\frac{k}{c_v}\nabla e + \frac{k}{c_v}\left(\frac{\partial e}{\partial \rho}\right)_{T=cst} \nabla \rho, \tag{3.50}$$

where c_v denotes the isochoric heat capacity. It can be seen that a source term related to the density gradient is involved. This term is null when the perfect gas hypothesis is considered. Similar term which is related to the pressure gradient can be obtained when the

heat flux is computed based on the enthalpy. However, it was neglected in the modelling of Smolka *et al.* [162].

A first-order Euler explicit scheme is employed for the temporal discretization. The Kurganov and Tadmor (KT) or Kurganov, Noelle and Petrova (KNP) schemes [98, 99] are considered for the spatial discretization. They are both second-order semi-discrete, non-staggered schemes and the KNP is considered for the following simulations. For example, the convective terms, such as $\nabla[\mathbf{u}\rho]$, $\nabla[\mathbf{u}(\rho\mathbf{u})]$, $\nabla[\mathbf{u}(\mathbf{u}\rho E)]$, and $\nabla[\mathbf{u}(\mathbf{u}p)]$ are transformed from the volume integration to the surface integration over a control volume by using the divergence (Gauss) theorem :

$$\int_V \nabla \cdot [\mathbf{u}\boldsymbol{\Psi}] dV = \int_S [\mathbf{u}\boldsymbol{\Psi}] d\mathbf{S} \approx \sum_f \phi_f \boldsymbol{\Psi}_f, \tag{3.51}$$

where $\sum_f$ represents the summation over all surfaces of the control volume and ϕ_f is a volumetric flux at the surface defined as $\phi_f = \mathbf{S}_f \mathbf{u}_f$. $\boldsymbol{\Psi}$ denotes the convected variables, such as ρ, $\rho\mathbf{u}$, ρE, and p. The summation of all fluxes over the interface is computed by inward and outward fluxes at the interface combined with a weight factor :

$$\sum_f \phi_f \boldsymbol{\Psi}_f = \sum_f [\alpha \phi_{f+} \boldsymbol{\Psi}_{f+} + (1-\alpha)\phi_{f-} \boldsymbol{\Psi}_{f-} + \omega_f (\boldsymbol{\Psi}_{f+} - \boldsymbol{\Psi}_{f-})], \tag{3.52}$$

where the weight factor α is fixed to 0.5 for the KT scheme which is considered as a *central* scheme, while the KNP scheme is biased in the upwind direction which depends on one-sided local speed of sound. The third term on the RHS of Equation (3.52) represents a diffusion term weighted by a volumetric flux ω_f, which depends on the maximum propagation speed of the discontinuities. The detailed formulations are found in [76]. The inward and outward fluxes at the interface are determined based on the cell-centered values by interpolating methods in the OpenFOAM library, such as the upwind, Minmod [148] or van Leer [184] interpolations. The gradient terms, such as the pressure gradient, are constructed in a similar way by the weighted inward and outward fluxes. The Laplacian terms for the viscous force are split into orthogonal and non-orthogonal parts, which is suitable when using polyhedral meshes.

The equations are solved sequentially by the solver. The thermodynamic properties are computed by the previous tabulated approach. The procedure can be summarized as follows :

- Update the thermodynamic properties at the cell center.
- Construct interface fluxes by interpolating the conservative variables, $\mathbf{U}^n$, at the previous time step with limiters.
- Solve the density equation to obtain ρ^{n+1}.
- Solve the inviscid momentum equation to obtain $(\rho u)^{n+1}$.
- Solve the diffusion equation for the velocity to update u^{n+1}.
- Solve the inviscid energy equation to obtain $(\rho E)^{n+1}$.
- Solve the diffusion equation for the internal energy to update e.
- Update the conservative variables at boundaries.

3.4.2 Bulk viscosity

The bulk viscosity κ is usually set equal to zero according to the Stokes' hypothesis : $\kappa = \lambda + \frac{2}{3}\mu = 0$, with λ the second coefficient of the viscosity and μ the dynamic viscosity. This hypothesis is valid for mono-atomic gases. However, it was revealed that for some polyatomic gases, such as CO_2, the bulk viscosity may become important. The viscosity ratio κ/μ can reach indeed 10^3 at ambient temperature, which could have a significant impact on the numerical results [41, 56, 174]. Physically, the bulk viscosity is due to the relaxation of internal degrees of freedom such as vibrational and rotational degrees of freedom. It can be measured experimentally by supersonic absorption [174]. The general form of the stress tensor writes :

$$\mathbf{T} = \lambda(\nabla \cdot \mathbf{u})\mathbf{I} + \mu[\nabla\mathbf{u} + (\nabla\mathbf{u})^T]. \tag{3.53}$$

If the flow is incompressible, the first term on the RHS of Equation (3.53) is equal to zero. If the flow is compressible, the stress tensor can be rewritten as :

$$\mathbf{T} = \mu\nabla\mathbf{u} + \mu[\nabla\mathbf{u}^T - \frac{2}{3}\mathrm{Tr}(\nabla \cdot \mathbf{u})\mathbf{I}] + \kappa\,\mathrm{Tr}(\nabla \cdot \mathbf{u})\mathbf{I}, \tag{3.54}$$

where Tr represents the trace of the matrix. If the bulk viscosity is set to zero, Equation (3.54) simplifies to Equation (3.48). It can be seen that the stress tensor is separated into three parts : the orthogonal, non-orthogonal and bulk viscosity parts. It is also noticed that the bulk viscosity part has only diagonal contributions, which provides a second-order correction to the pressure prediction, arising as a consequence of both compression and

dilatation. The main difficulty remains to accurately determine the bulk viscosity. Only very limited experimental data have been reported in the literature and the results are highly dependent on the characteristic of the measurement technique [92]. In this study, a simple formulation derived by Zuckerwar and Ash [208] from Chapman and Cowling [33]'s formulation is used :

$$\kappa = \frac{2(d-3)}{d^2} p\tau, \tag{3.55}$$

where d is the number of molecular degrees of freedom ($d = 5$ for CO_2 according to [208]), p denotes the pressure and τ indicates the relaxation time. It should be mentioned that there is currently no reference to fix the relaxation time for CO_2. Its influence will be then discussed in Section 5.3.3.

3.4.3 Navier-Stokes Characteristic Boundary Condition (NSCBC)

The basic Dirichlet and Neumann type boundary conditions are available in the OpenFOAM library. However, they are not sufficient for simulations of compressible flows. For an hyperbolic system of equations, the most appropriate way to treat the inlet and outlet boundary conditions is indeed by using characteristic variables. However, imposing directly the characteristic variables at the boundary can generate non-physical spurious waves, which can affect the accuracy and the numerical stability of the simulations. Therefore, a special treatment for open boundary conditions (i.e. outlet) has been developed. This kind of issue has been extensively investigated for the high resolution of compressible flows (e.g. Large-eddy simulation (LES) and Direct numerical simulation (DNS)) [65, 137, 197]. Hence, the Navier-Stokes characteristic boundary condition (NSCBC) has been implemented for the CLAWPACK solver and the *rhoCentralFoam* solver based on the former works of Fosso *et al.* [65], Poinsot and Lele [137]. Furthermore, the NSCBC is coupled to the tabulated EoS for CO_2 compressible flow simulations.

Considering the outlet boundary condition, Navier-Stokes equations in their characteristic form following the x-direction may be written as [65] :

$$\begin{bmatrix} c^2\frac{\partial \rho}{\partial t} - \frac{\partial p}{\partial t} \\ \frac{\partial v}{\partial t} \\ \frac{\partial w}{\partial t} \\ \frac{\partial p}{\partial t} + \rho c \frac{\partial u}{\partial t} \\ \frac{\partial p}{\partial t} - \rho c \frac{\partial u}{\partial t} \end{bmatrix} + \begin{bmatrix} c^2 L_1 \\ L_2 \\ L_3 \\ \rho c L_4 \\ \rho c L_5 \end{bmatrix} + \begin{bmatrix} T_1 \\ T_2 \\ T_3 \\ T_4 \\ T_5 \end{bmatrix} + \begin{bmatrix} D_1 \\ D_2 \\ D_3 \\ D_4 \\ D_5 \end{bmatrix} = \begin{bmatrix} 0 \\ 0 \\ 0 \\ 0 \\ 0 \end{bmatrix}, \tag{3.56}$$

where T_i denotes the transverse terms, D_i represents the diffusion terms, and L_i is the vector of the characteristic wave amplitude, which writes :

$$L = \begin{bmatrix} u\left[\frac{\partial \rho}{\partial x} - \frac{1}{c^2}\frac{\partial p}{\partial x}\right] \\ u\left[\frac{\partial v}{\partial x}\right] \\ u\left[\frac{\partial w}{\partial x}\right] \\ (u+c)\left[\frac{\partial u}{\partial x} - \frac{1}{\rho c}\frac{\partial p}{\partial x}\right] \\ (u-c)\left[-\frac{\partial u}{\partial x} - \frac{1}{\rho c}\frac{\partial p}{\partial x}\right] \end{bmatrix}. \tag{3.57}$$

Depending on the sign of the propagation speed $(u, u+c, u-c)$, the characteristic waves can be defined as incoming or outgoing waves. Outgoing waves are computed using interior information with a one-sided scheme, while the incoming waves are determined by the physical information available at the boundary (i.e. the outlet pressure). At the outlet, the flow is indeed usually unidirectional. A sponge layer is often added for stabilizing the simulation. As a result, the transversal contribution has a negligible effect. Moreover, for a fully turbulent flow, viscous effects can be neglected as well. Regarding a subsonic pressure outlet boundary condition, L_5 is the only incoming wave. Hence, L_1, L_2, L_3, and L_4 are evaluated by values available inside the computational domain. Poinsot and Lele [137] proposed the following formulation to evaluate L_5 :

$$L_5 = K \times (p - p_{tar}), \tag{3.58}$$

where p is the instantaneous pressure at the boundary, while p_{tar} is the target pressure which is fixed at the boundary. K is a relaxation coefficient defined as $K = \sigma c \frac{1 - Ma_{max}^2}{l}$, where $\sigma = 0.25$. Ma_{max} denotes the maximum Mach number at the boundary and l is a characteristic length.

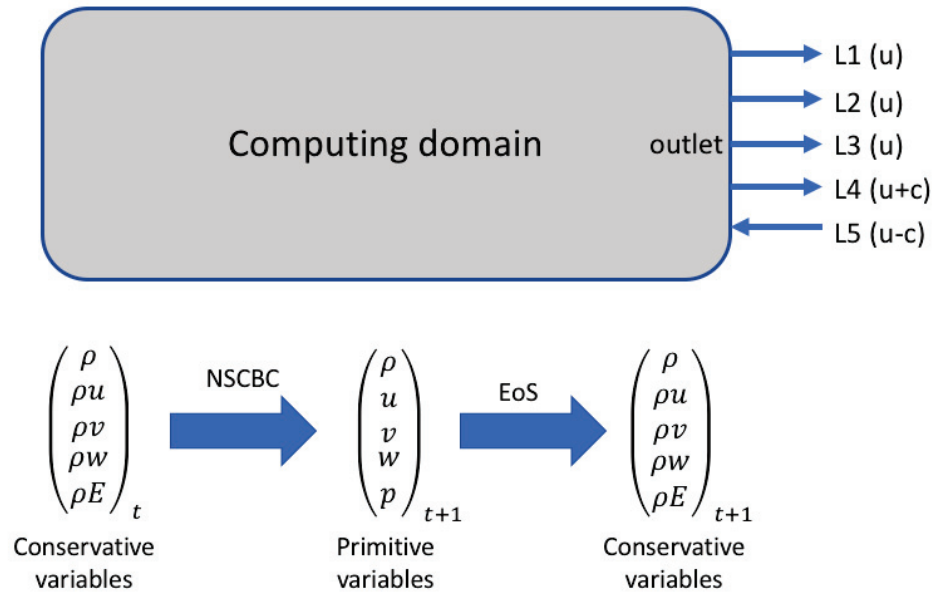

Figure 3.10 Scheme displaying the incoming and outgoing waves at the outlet boundary and the procedure to compute corrected boundary variables.

As shown in Figure 3.10, by solving Equation (3.56), one can obtain the corrected values of ρ, u, v, w, p for the next time step. However, the resolved variables at the boundary are conservative variables (ρ, ρu, ρv, ρw, ρE). Therefore, the corrected conservative variables are obtained through the updated primitive variables and the tabulated EoS. The coupling with the tabulated EoS is shown in the next section for the AVBP solver. Noting that if the Mach number is detected to be higher than one at the boundary, this subsonic pressure outlet boundary condition switches to the supersonic outlet boundary condition in which all informations come from the interior of the computational domain. As a result, the target pressure can not be maintained at the outlet boundary.

3.5 Solver for Large Eddy Simulation (LES) - AVBP

3.5.1 A brief introduction to LES for the AVBP solver

Large Eddy Simulation (LES) is recognized as an intermediate approach to the turbulence modelling between Direct Numerical Simulation (DNS) and Reynolds-averaged Navier–Stokes (RANS) closures. Due to the fast growth of the number of degrees of freedom for turbulent flows, DNS can not be adopted to simulate most of the interesting industrial applications due to its high computational cost. Contrary to DNS, RANS simulations have a reasonable computational cost to achieve relatively complex cases, but RANS simula-

tions cannot capture instantaneous fields. The LES is considered as a good compromise in terms of computational cost and accuracy. The idea of LES is the application of a scale separation operator to the original Navier-Stokes equations. This operation allows to resolve only large scales and a model is applied for the smaller scales (high wave number in the Fourier space), which reduces significantly the computational cost. Classically there are two types of scale separation operators discussed by Sagaut [151] :

- explicit filter : Filtering is represented by a convolution product in the physical space or the product of the filter spectrum and the transfer function of kernel in the Fourier space. The cut-off length δ is associated to the cut-off wave number k_c, while the cut-off time τ_c to the cut-off frequency ω_c. Explicit filtering requires a finer grid than implicit filtering, and the computational cost increases with Δx^4 [151].

- implicit filter : this level of filtering is always applied as it is actually the projection on the computational grid. This is more a truncation than a filtering process as it is impossible to recover unfiltered quantities by deconvolution.

In the AVBP solver, only the implicit filter is used. Here, rather than present the detail of LES theory, only the simplified equations implemented in the AVBP solver are shown. For LES of compressible flows, a change of variables is often used for filtered variables which are weighted by the density. It is written as :

$$\tilde{f} = \frac{\overline{\rho f}}{\overline{\rho}}. \tag{3.59}$$

This change is similar to the 'Favre averaging'. In fact, it is a filtering expression in terms of Favre variables, where $\tilde{f}$ denotes a Favre averaged quantity. As stated in [151], the motivation for using such operation is to have a similar formulation as non-filtered equations (except for the subgrid terms). The filtered governing equations of momentum, total energy and mass (species considered in the AVBP solver [31]) are presented in the following. These equations are also consistent with [151] :

$$\frac{\partial \overline{\rho}\tilde{u}_i}{\partial t} + \frac{\partial}{\partial x_j}(\overline{\rho}\tilde{u}_i\tilde{u}_j) = -\frac{\partial}{\partial x_j}[\overline{p}\delta_{ij} - \overline{\tau}_{ij} - \overline{\tau}_{ij}^{sgs}], \tag{3.60}$$

$$\frac{\overline{\rho}\tilde{E}}{\partial t} + \frac{\partial}{\partial x_j}(\overline{\rho}\tilde{E}\tilde{u}_j) = -\frac{\partial}{\partial x_j}[\overline{u_i(p\delta_{ij} - \tau_{ij})} + \overline{q}_j + \overline{q}_j^{sgs}] + \overline{\dot{\omega}_T} + \overline{Q_r}, \tag{3.61}$$

$$\frac{\partial \overline{\rho}}{\partial t} + \frac{\partial}{\partial x_j}(\overline{\rho}\tilde{u}_j) = 0, \tag{3.62}$$

The AVBP solver is mainly used for reacting flows. The chemical source terms, $\overline{\dot{\omega}_T}$, $\overline{Q_r}$, are present therefore in the total energy equation. The quantities with a superscript sgs, e.g. $\overline{\tau_{ij}}^{sgs}$, $\overline{q_j}^{sgs}$ are sub-grid scale (SGS) turbulent terms. The SGS terms are modelled through the SGS turbulence viscosity, which reads :

$$\overline{\tau_{ij}}^{sgs} = 2\overline{\rho}\nu_{sgs}(\tilde{S}_{ij} - \frac{1}{3}\delta_{ij}\tilde{S}_{ll}), \tag{3.63}$$

$$\overline{q_j}^{sgs} = -\frac{\rho\nu_{sgs}\overline{C}_p}{Pr_t}\frac{\partial\tilde{T}}{\partial x_j}, \tag{3.64}$$

with

$$\tilde{S}_{ij} = \frac{1}{2}(\frac{\partial\tilde{u}_j}{\partial x_i} + \frac{\partial\tilde{u}_i}{\partial x_j}), \tag{3.65}$$

where $\tilde{S}_{ij}$ is the filtered rate-strain tensor based on the Favre averaged quantities. The subgrid Prandtl number, Pr_t, remains constant and fixed to 0.6 by default in AVBP.

To solve the system numerically, closures need to be supplied for these SGS terms. In AVBP, six SGS models are implemented : the Smagorinsky model [161], the Wall Adapting Local Eddy model (WALE) [51], the k-equation model [198], the Filtered Smagorinsky model, the Dynamic Smagorinsky model [69] and the σ-model [176]. The most well-known SGS model is probably the Smagorinsky model [161]. The SGS-Smagorinsky viscosity writes :

$$\nu_{sgs}^{smago} = (C_S\Delta)^2\sqrt{2\tilde{S}_{ij}\tilde{S}_{ij}}, \tag{3.66}$$

where Δ denotes the filter characteristic scale, which is mesh dependent ($\Delta = \sqrt[3]{V_{cell}}$). C_S is a constant set to 0.18 and can vary from 0.1 to 0.18 depending on the flow configuration. This closure provides a satisfactory prediction of the dissipation rate of the turbulence kinetic energy in homogeneous isotropic turbulent flows. However, it is known as being too dissipative to predict turbulence intensities in high shear regions or for moderate turbulent flows. In addition, this model does not have a proper behavior near the walls.

Furthermore, a SGS model was developed for wall-bounded flow configurations, namely the Wall Adapting Local Eddy model (WALE) [51]. For this model, the SGS viscosity is

expressed as follows :

$$\nu_{sgs}^{WALE} = (C_\omega \Delta)^2 \frac{(s_{ij}^d s_{ij}^d)^{3/2}}{(\tilde{S}_{ij}\tilde{S}_{ij})^{5/2} + (s_{ij}^d s_{ij}^d)^{5/4}}, \tag{3.67}$$

with

$$s_{ij}^d = \frac{1}{2}(\tilde{g}_{ij}^2 + \tilde{g}_{ji}^2) - \frac{1}{3}\tilde{g}_{kk}^2 \delta_{ij}, \tag{3.68}$$

where constant $C_\omega = 0.424$, $\Delta = \overline{\Delta} = (\Delta_x \times \Delta_y \times \Delta_z)^{1/3}$ remains the same as the characteristic filter length, $\tilde{g}_{ij}$ denotes the resolved velocity gradient. This model is based on the gradient velocity tensor $\tilde{g}_{ij}$, which is a good candidate to represent the velocity fluctuations at the length scale $\overline{\Delta}$ [51, 82, 157]. This model has a proper asymptotic behavior near the walls, namely $\nu_{sgs} = \theta(y^{+3})$

3.5.2 AVBP

AVBP was developed originally at OUCL (Oxford University Computing Laboratory) and CERFACS in 1993. Nowadays, it is developed and supported by CERFACS and IFP (Institut Français du Pétrole). The main objective of AVBP is to solve the compressible Navier-Stokes Equations with unstructured or hybrid meshes in order to adapt to complex computational domains. The solver is developed through FORTRAN language and thanks to the MPI library, it can run in parallel on supercomputers. The speed-up obtained using AVBP on three supercomputers is shown in Figure 3.11.

The y axis represents the speed-up which is computed by $S(p) = \frac{T_p(1)}{T_p(p)}$. $T_p(1)$ and $T_p(p)$ denote the time of parallel computation with one core and with p cores, respectively. $S(p)$ is always smaller than p, which means the parallel computation can not be faster than the best sequential computation.

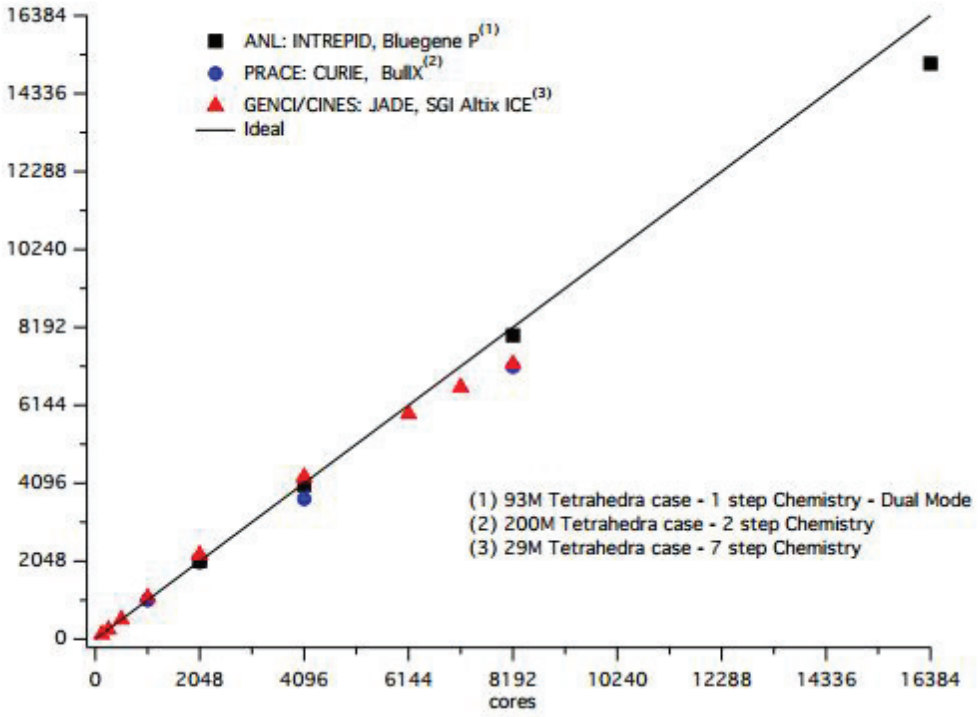

Figure 3.11 Speed-up of AVBP in ANL, PRACE and GENCI, after Riber *et al.* [143].

The AVBP solver is basically a density-based solver under the conservative formulation, in which the equations of mass, momentum, total energy are solved simultaneously in their algebraic form using the Cell-Vertex finite-volume method. The time marching uses *Runge-Kutta* multi-step method and high-order schemes for the convective terms are used, such as the Two-step Taylor-Galerkin Convective (TTGC) [40]. The finite-volume method allows to discretize the conservation laws in their integrated form :

$$\frac{\partial}{\partial t}\int_{\Omega} U dV + \oint_{\partial\Omega} \overrightarrow{F} \cdot \overrightarrow{n} dS = 0, \tag{3.69}$$

where $\mathbf{U}$ denotes the variable vector, $\overrightarrow{F}$ denotes the flux across the boundary of the control volume.

In the Cell-Vertex method, the flux is computed at the surface of the primal mesh (a) (Cell-Centered) and the solutions of the variables are saved at the nodes of the Vertex-Centered dual mesh (b), as shown in Figure 3.12.

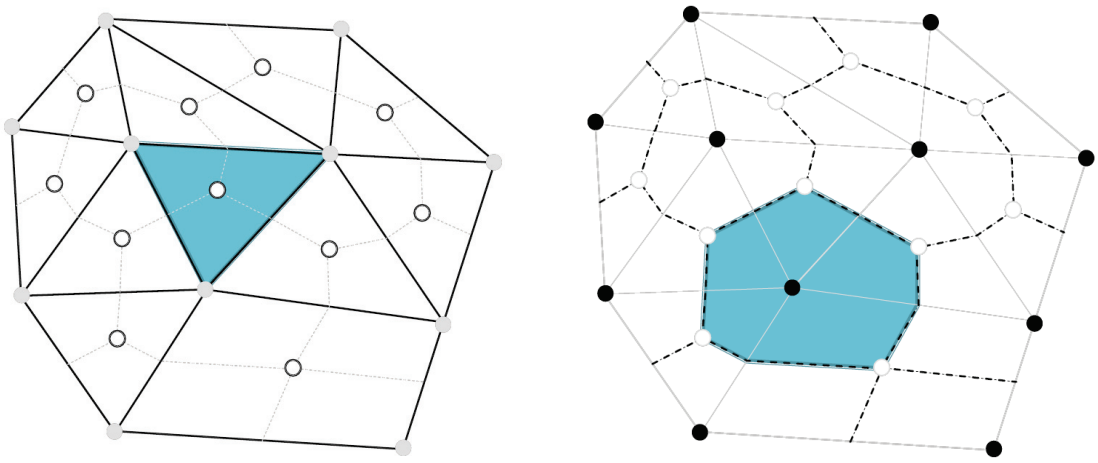

(a) (b)

Figure 3.12 (a) Primal Mesh and (b) Dual Mesh, after CERFACS [31].

The evolution of variables are computed at the primal-mesh center through the interface flux and then they are distributed to the nodes in order to update the solutions of the variables at all nodes at each time step.

Two schemes for the convective terms are available in the AVBP solver :

- Lax-Wendroff scheme (LW) : 2^{nd} order scheme in space and time, adapted to the cell-vertex approach [102]. This scheme has a good accuracy with low computational cost, but the dissipation and the dispersion are relatively high. Hence, it is adequate to use this scheme to initialize the computation.

- Two-step Taylor-Gelerkin scheme (TTG) : there are TTGC being 3^{rd} order in space [40] and TTG4A being 4^{th} order in space [49]. The high-orders in time and space ensure the low dissipation and the dispersion. Furthermore, the TTG4A scheme is more dissipative than the TTGC scheme, but more robust for hybrid meshes.

However, the centred high-order schemes have too low dissipations to properly dissipate numerical oscillations which come from the transport of the strong gradient (Gibbs phenomenon). Hence, in order to insure stability, these non-physical numerical oscillations called wiggles are dissipated by adding an artificial viscosity. A 4^{th} order artificial viscosity is applied to the whole computational domain to dissipate node-to-node oscillations [40]. The 2^{th} order artificial viscosity is applied depending on the response of a sensor which specifically detects numerical anomalies within the flow and may increase the artificial viscosity up to a limit defined by the user [40].

3.5.3 Coupling AVBP with the tabulated EoS

Characteristic wave decomposition

The method of characteristics is used to control the waves crossing the boundaries. However, the variables solved by the equation system are under their conservative formulation. Hence, transformations from the conservative variables to the characteristic variables should be considered. The idea is to build three transformation matrices which allow the passage from the conservative variables in the global basis ($\overrightarrow{i}$, $\overrightarrow{j}$, $\overrightarrow{k}$) to the primitive variables in a normal basis to the boundary ($\overrightarrow{n}$,$\overrightarrow{t1}$,$\overrightarrow{t2}$)) and then to the characteristic variables. The procedure is shown in Table 3.1.

Table 3.1 Transformation between different variables through passage matrices.

Conservative		Primitive		Primitive in a normal basis		Characteristic
∂U		∂V		∂V_n		∂W
$\begin{pmatrix} \partial(\rho) \\ \partial(\rho u) \\ \partial(\rho v) \\ \partial(\rho w) \\ \partial(\rho E) \\ \partial \rho Y_k \end{pmatrix}$	M^{-1} $\rightarrow$ $\leftarrow$ M	$\begin{pmatrix} \partial\rho \\ \partial u \\ \partial v \\ \partial w \\ \partial p \\ \partial(\rho Y_k) \end{pmatrix}$	Ω_V^{-1} $\rightarrow$ $\leftarrow$ Ω_V	$\begin{pmatrix} \partial\rho \\ \partial u_n \\ \partial u_{t1} \\ \partial u_{t2} \\ \partial p \\ \partial(\rho Y_k) \end{pmatrix}$	L $\rightarrow$ $\leftarrow$ R	$\begin{pmatrix} \partial W^1 = -\frac{1}{c^2}\partial p + \partial\rho \\ \partial W^2 = \partial u_n + \frac{\partial p}{\rho c} \\ \partial W^3 = -\partial u_n + \frac{\partial p}{\rho c} \\ \partial W^4 = \partial u_{t1} \\ \partial W^5 = \partial u_{t2} \\ \partial W^{6+k} = -\frac{Y_k}{c^2}\partial p + \partial\rho_k \end{pmatrix}$

The transformation from ∂U to ∂W can be performed as :

$$L_U = L.\Omega_V^{-1}.M^{-1}, \tag{3.70}$$

and the inverse passage matrix from ∂W to ∂U is :

$$R_U = R.\Omega_V.M. \tag{3.71}$$

The variables shown in Table 3.1 are used in the original implementation of AVBP solver which is primarily designed for multi-species. In the present model for CO_2 flows, only one specie is considered. As a result, the last variable which presents the multi-species is similar to the density. Nevertheless, this variable is not removed. It is not considered and would not affect the simulation.

Before computing the matrices M and M^{-1}, some useful differential relations are computed. In order to explicitly show the derivatives, the conservative variables are rewritten under the form : $U = (\rho, m_1, m_2, m_3, \varepsilon, \rho_1)^t$. Here, one keeps the same notations as in the AVBP manual [31], the differential of the total energy writes :

$$
\begin{aligned}
d\varepsilon &= d(\rho e_s) + d(\rho e_c) = u dm_1 + v dm_2 + w dm_3 - e_c d\rho + e_s d\rho + \rho de_s \\
&= u dm_1 + v dm_2 + w dm_3 + \left(e_s - e_c + \rho \left(\frac{\partial e_s}{\partial \rho} \right)_T - \rho \left(\frac{\partial e_s}{\partial T} \right)_\rho \left(\frac{\partial p}{\partial T} \right)_\rho^{-1} \left(\frac{\partial p}{\partial T} \right)_\rho \right) d\rho \\
&+ \rho \left(\frac{\partial e_s}{\partial T} \right)_\rho \left(\frac{\partial p}{\partial T} \right)_\rho^{-1} dp \\
&= u dm_1 + v dm_2 + w dm_3 - \left(e_c + \frac{\beta_a}{\beta} \right) d\rho + \frac{1}{\beta} dp,
\end{aligned}
\tag{3.72}
$$

where

$$
\beta = \left(\frac{\partial e_s}{\partial T} \right)_\rho^{-1} \left(\frac{\partial p}{\partial T} \right)_\rho, \tag{3.73}
$$

and

$$
\beta_a = \left(\frac{\partial p}{\partial \rho} \right)_T - \beta e_s - \beta \rho \left(\frac{\partial e_s}{\partial \rho} \right)_T. \tag{3.74}
$$

The formulations of β and β_a are compatible with the formulation in AVBP using the perfect gas EoS. e_c and e_s are the kinetic energy and internal energy. The differential of the internal energy writes :

$$
de_s(\rho, T) = \left(\frac{\partial e_s}{\partial \rho} \right)_T d\rho + \left(\frac{\partial e_s}{\partial T} \right)_\rho dT, \tag{3.75}
$$

while dT is substituted by :

$$
dp(\rho, T) = \left(\frac{\partial p}{\partial \rho} \right)_T d\rho + \left(\frac{\partial p}{\partial T} \right)_\rho dT. \tag{3.76}
$$

Similarly, the differential of pressure is written as :

$$
\begin{aligned}
dp &= \beta \left[d\varepsilon - u dm_1 - v dm_2 - w dm_3 + e_c d\rho - \left(e_s + \rho \left(\frac{\partial e_s}{\partial \rho} \right)_T \right) d\rho \right] + \left(\frac{\partial p}{\partial \rho} \right)_T d\rho \\
&= \beta (d\varepsilon - u dm_1 - v dm_2 - w dm_3) + (e_c \beta + \beta_a) d\rho.
\end{aligned}
\tag{3.77}
$$

The matrices M and M^{-1} are then computed as :

$$M = \frac{\partial U}{\partial V} = \begin{pmatrix} \frac{\partial \rho}{\partial \rho} & \frac{\partial \rho}{\partial u} & \frac{\partial \rho}{\partial v} & \frac{\partial \rho}{\partial w} & \frac{\partial \rho}{\partial p} & \frac{\partial \rho}{\partial \rho_1} \\ \frac{\partial m_1}{\partial \rho} & \frac{\partial m_1}{\partial u} & \frac{\partial m_1}{\partial v} & \frac{\partial m_1}{\partial w} & \frac{\partial m_1}{\partial p} & \frac{\partial m_1}{\partial \rho_1} \\ \frac{\partial m_2}{\partial \rho} & \frac{\partial m_2}{\partial u} & \frac{\partial m_2}{\partial v} & \frac{\partial m_2}{\partial w} & \frac{\partial m_2}{\partial p} & \frac{\partial m_2}{\partial \rho_1} \\ \frac{\partial m_3}{\partial \rho} & \frac{\partial m_3}{\partial u} & \frac{\partial m_3}{\partial v} & \frac{\partial m_3}{\partial w} & \frac{\partial m_3}{\partial p} & \frac{\partial m_3}{\partial \rho_1} \\ \frac{\partial \varepsilon}{\partial \rho} & \frac{\partial \varepsilon}{\partial u} & \frac{\partial \varepsilon}{\partial v} & \frac{\partial \varepsilon}{\partial w} & \frac{\partial \varepsilon}{\partial P} & \frac{\partial \varepsilon}{\partial \rho_1} \\ \frac{\partial \rho_1}{\partial \rho} & \frac{\partial \rho_1}{\partial u} & \frac{\partial \rho_1}{\partial v} & \frac{\partial \rho_1}{\partial w} & \frac{\partial \rho_1}{\partial P} & \frac{\partial \rho_1}{\partial \rho_1} \end{pmatrix} = \begin{pmatrix} 1 & 0 & 0 & 0 & 0 & 1 \\ u & \rho & 0 & 0 & 0 & u \\ v & 0 & \rho & 0 & 0 & v \\ w & 0 & 0 & \rho & 0 & w \\ e_c - \frac{\beta_a}{\beta} & \rho u & \rho v & \rho w & \frac{1}{\beta} & e_c - \frac{\beta_a}{\beta} \\ 1 & 0 & 0 & 0 & 0 & 1 \end{pmatrix}, \tag{3.78}$$

and

$$M^{-1} = \frac{\partial V}{\partial U} = \begin{pmatrix} \frac{\partial \rho}{\partial \rho} & \frac{\partial \rho}{\partial m_1} & \frac{\partial \rho}{\partial m_2} & \frac{\partial \rho}{\partial m_3} & \frac{\partial \rho}{\partial \varepsilon} & \frac{\partial \rho}{\partial \rho_1} \\ \frac{\partial u}{\partial \rho} & \frac{\partial u}{\partial m_1} & \frac{\partial u}{\partial m_2} & \frac{\partial u}{\partial m_3} & \frac{\partial u}{\partial \varepsilon} & \frac{\partial u}{\partial \rho_1} \\ \frac{\partial v}{\partial \rho} & \frac{\partial v}{\partial m_1} & \frac{\partial v}{\partial m_2} & \frac{\partial v}{\partial m_3} & \frac{\partial v}{\partial \varepsilon} & \frac{\partial v}{\partial \rho_1} \\ \frac{\partial w}{\partial \rho} & \frac{\partial w}{\partial m_1} & \frac{\partial w}{\partial m_2} & \frac{\partial w}{\partial m_3} & \frac{\partial w}{\partial \varepsilon} & \frac{\partial w}{\partial \rho_1} \\ \frac{\partial p}{\partial \rho} & \frac{\partial p}{\partial m_1} & \frac{\partial p}{\partial m_2} & \frac{\partial p}{\partial m_3} & \frac{\partial p}{\partial \varepsilon} & \frac{\partial p}{\partial \rho_1} \\ \frac{\partial \rho_1}{\partial \rho} & \frac{\partial \rho_1}{\partial m_1} & \frac{\partial \rho_1}{\partial m_2} & \frac{\partial \rho_1}{\partial m_3} & \frac{\partial \rho_1}{\partial \varepsilon} & \frac{\partial \rho_1}{\partial \rho_1} \end{pmatrix} = \begin{pmatrix} 1 & 0 & 0 & 0 & 0 & 1 \\ -\frac{u}{\rho} & \frac{1}{\rho} & 0 & 0 & 0 & u \\ -\frac{v}{\rho} & 0 & \rho & 0 & 0 & v \\ -\frac{w}{\rho} & 0 & 0 & \rho & 0 & w \\ \beta e_c + \beta_a & -u\beta & -v\beta & -w\beta & \beta & \beta e_c + \beta_a \\ 1 & 0 & 0 & 0 & 0 & 1 \end{pmatrix}. \tag{3.79}$$

The next step is to project the variables on the basis associated to the boundary (from (x, y, z) to $(\overrightarrow{n}, \overrightarrow{t1}, \overrightarrow{t2})$). The change of coordinates is done by using a rotation matrix. The

detailed derivations can be found in the AVBP manual [31]. Finally, the matrices Ω_V and Ω_V^{-1} read :

$$\Omega_V = \begin{pmatrix} 1 & 0 & 0 & 0 & 0 & 0 \\ 0 & n_x & t1_x & t2_x & 0 & 0 \\ 0 & n_y & t1_y & t2_y & 0 & 0 \\ 0 & n_z & t1_z & t2_z & 0 & 0 \\ 0 & 0 & 0 & 0 & 1 & 0 \\ 0 & 0 & 0 & 0 & 0 & 1 \end{pmatrix}, \tag{3.80}$$

and

$$\Omega_V^{-1} = \begin{pmatrix} 1 & 0 & 0 & 0 & 0 & 0 \\ 0 & n_x & n_y & n_z & 0 & 0 \\ 0 & t1_x & t1_y & t1_z & 0 & 0 \\ 0 & t2_x & t2_y & t2_z & 0 & 0 \\ 0 & 0 & 0 & 0 & 1 & 0 \\ 0 & 0 & 0 & 0 & 0 & 1 \end{pmatrix}. \tag{3.81}$$

The transformation matrices L and R are the matrices composed of the left and right eigenvectors of the 3D compressible Euler equations. They are written as :

$$L = \begin{pmatrix} 1 & 0 & 0 & 0 & -\frac{1}{c^2} & 0 \\ 0 & 1 & 0 & 0 & \frac{1}{\rho c} & 0 \\ 0 & -1 & 0 & 0 & \frac{1}{\rho c} & 0 \\ 0 & 0 & 1 & 0 & 0 & 0 \\ 0 & 0 & 0 & 1 & 0 & 0 \\ 0 & 0 & 0 & 0 & -\frac{1}{c^2} & 1 \end{pmatrix}, \tag{3.82}$$

and

$$R = \begin{pmatrix} 1 & \frac{\rho}{2c} & \frac{\rho}{2c} & 0 & 0 & 0 \\ 0 & \frac{1}{2} & -\frac{1}{2} & 0 & 0 & 0 \\ 0 & 0 & 0 & 1 & 0 & 0 \\ 0 & 0 & 0 & 0 & 1 & 0 \\ 0 & \frac{\rho c}{2} & \frac{\rho c}{2} & 0 & 0 & 0 \\ 0 & \frac{\rho}{2c} & \frac{\rho}{2c} & 0 & 0 & 1 \end{pmatrix}. \tag{3.83}$$

Finally, L_U and R_U can be found as :

$$L_U = \begin{pmatrix} 1 - \frac{e_c\beta+\beta_a}{c^2} & \frac{u\beta}{c^2} & \frac{v\beta}{c^2} & \frac{w\beta}{c^2} & -\frac{\beta}{c^2} & 0 \\ -\frac{\overrightarrow{u}.\overrightarrow{t1}}{\rho} & \frac{t1_x}{\rho} & \frac{t1_y}{\rho} & \frac{t1_z}{\rho} & 0 & 0 \\ -\frac{\overrightarrow{u}.\overrightarrow{t2}}{\rho} & \frac{t2_x}{\rho} & \frac{t2_y}{\rho} & \frac{t2_z}{\rho} & 0 & 0 \\ \frac{1}{\rho}\left(\frac{e_c\beta+\beta_a}{c} - \overrightarrow{u}.\overrightarrow{n}\right) & \frac{1}{\rho}\left(n_x - \frac{\beta u}{c}\right) & \frac{1}{\rho}\left(n_y - \frac{\beta v}{c}\right) & \frac{1}{\rho}\left(n_z - \frac{\beta w}{c}\right) & \frac{\beta}{\rho c} & 0 \\ \frac{1}{\rho}\left(\frac{e_c\beta+\beta_a}{c} + \overrightarrow{u}.\overrightarrow{n}\right) & -\frac{1}{\rho}\left(n_x + \frac{\beta u}{c}\right) & -\frac{1}{\rho}\left(n_y + \frac{\beta v}{c}\right) & -\frac{1}{\rho}\left(n_z + \frac{\beta w}{c}\right) & \frac{\beta}{\rho c} & 0 \\ -\frac{1}{\rho} & 0 & 0 & 0 & 0 & \frac{1}{\rho} \end{pmatrix}, \tag{3.84}$$

and

$$R_U = \begin{pmatrix} 1 & 0 & 0 & \frac{\rho}{2c} & \frac{\rho}{2c} & 0 \\ u & \rho t1_x & \rho t2_x & \frac{\rho}{2c}(u + cn_x) & \frac{\rho}{2c}(u - cn_x) & 0 \\ v & \rho t1_y & \rho t2_y & \frac{\rho}{2c}(v + cn_y) & \frac{\rho}{2c}(v - cn_y) & 0 \\ w & \rho t1_z & \rho t2_z & \frac{\rho}{2c}(w + cn_z) & \frac{\rho}{2c}(w - cn_z) & 0 \\ e_c - \frac{\beta_a}{\beta} & \rho\overrightarrow{u}.\overrightarrow{t1} & \rho\overrightarrow{u}.\overrightarrow{t1} & \frac{\rho}{2c}\left(e_c - \frac{\beta_a}{\beta} + c\overrightarrow{u}.\overrightarrow{n} + \frac{c^2}{\beta}\right) & \frac{\rho}{2c}\left(e_c - \frac{\beta_a}{\beta} - c\overrightarrow{u}.\overrightarrow{n} + \frac{c^2}{\beta}\right) & 0 \\ 1 & 0 & 0 & \frac{\rho}{2c} & \frac{\rho}{2c} & \rho \end{pmatrix}. \tag{3.85}$$

In order to compute all matrices described above, the values of β, β_a, and c can be obtained through the tabulated EoS of CO_2. As a result, one gets :

$$\begin{aligned} \partial U &= L_U \partial W, \\ \partial W &= R_U \partial U, \end{aligned} \tag{3.86}$$

which allows the passage from conservative variables in a global basis to characteristic variables at the boundary. Finally, the characteristic variables can be used to manipulate boundary conditions.

3.6 Transport tubes analysis

The transport tubes of momentum and kinetic energy were firstly introduced by Meyers and Meneveau [124] based on the concept of the mass-flux stream tube. These two transport tubes can be used as a transport visualisation tool. Lately, Lamberts *et al.* [100] extended the original formulation for compressible flows and proposed the exergy transport tube specifically for analyzing the transport phenomena within single-phase ejectors. In this thesis, the same method is used to investigate two-phase CO_2 flows within ejectors. As illustrated in Figure 3.13, a stream tube (mass) is originally constructed by choosing a closed curve C, which is nowhere tangent to the velocity, and considering the branch of all streamlines passing at the interior of this curve. As a result, a stream tube is formed by a volume Ω bounded by the tube mantle and two cross sections A_1 and A_2. In the same way, the tubes of momentum, mean-flow kinetic energy and exergy can be constructed by considering the flux of the corresponding quantities.

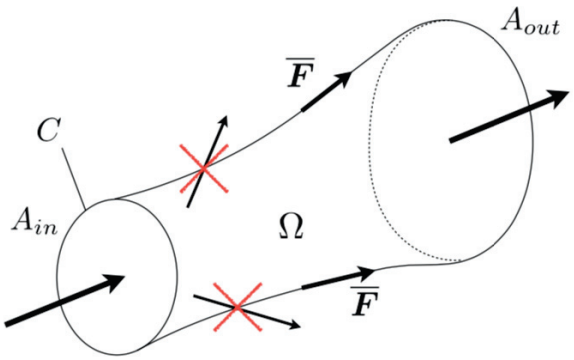

Figure 3.13 Illustration of a transport tube from Lamberts *et al.* [100].

By definition, there is on average, no flux of considered quantities through the corresponding tube's mantle. It should be noted that the flux vector and the tube geometry are related to the characterized direction. For analysing transport phenomena within ejectors, the streamwise direction x is chosen, which also makes the transport tube along the main stream. Therefore, the transport equation for the x-direction is given by :

$$\frac{\partial}{\partial x_j}\left(\overline{\rho}\widehat{u}\widehat{u}_j - \overline{\tau}_{xj} - \overline{\tau}^t_{xj}\right) = -\frac{\partial \overline{p}}{\partial x}. \tag{3.87}$$

The left-hand side of the equation represents the divergence of the total flux of the linear momentum, with its advective, molecular diffusion, and turbulent contributions. The pressure gradient is considered as a source term. Similarly, the transport tube for the mean-

kinetic energy, $K = \frac{1}{2}\overline{\rho}\widehat{u}_i\widehat{u}_i$, can be derived by projection of the momentum equation onto the mean velocity vector, which reads :

$$\frac{\partial}{\partial x_j}\left(K\widehat{u}_j - \overline{\tau}_{xj}\widehat{u} - \overline{\tau}^t_{xj}\widehat{u}\right) = -\frac{\partial\overline{p}}{\partial x_j}\widehat{u}_j - \overline{\tau}_{xj}\frac{\partial\widehat{u}}{\partial x_j} - \overline{\tau}^t_{xj}\frac{\partial\widehat{u}}{\partial x_j}. \tag{3.88}$$

The left-hand side of the equation characterizes the transport flux of the kinetic energy, including advective, molecular diffusion, and turbulent contributions. In the right-hand side, the source terms consist of the pressure gradient term, the viscous dissipation and the turbulent dissipation. The exergy is defined as the maximum theoretical work that can be extracted from a thermodynamic state not into equilibrium with a reference state. In order to consider the local acceleration and deceleration of the fluid, the total exergy is considered here as :

$$\xi_t = (h_t - h_{\text{ref}}) - T_{\text{ref}}\,(s - s_{\text{ref}})\,, \tag{3.89}$$

where the subscript "t" denotes the total or stagnation quantities. The subscript "ref" denotes the reference state. Here, the state at the secondary inlet is considered as the reference state. As a result, the exergy at the secondary inlet is zero as a reference. Finally, the transport of the total exergy was derived by Lamberts *et al.* [100] as :

$$\begin{aligned}&\frac{\partial}{\partial x_j}\left[\overline{\rho}\xi^*_t\widehat{u}_j + (\overline{q}_j + \overline{q}^t_j)\left(1 - \frac{T_{ref}}{\widehat{T}}\right) - \overline{\tau}_{xj}\widehat{u} - \overline{\tau}^t_{xj}\widehat{u}\right]\\ &= -T_{ref}\left(\frac{\Phi^*}{\widehat{T}} + \frac{\Phi^*_\Theta}{\widehat{T}^2}\right),\end{aligned} \tag{3.90}$$

where the right-hand side is the total flux of total exergy including advective, molecular plus turbulent heat transfer, and viscous diffusion plus turbulent contributions. The exergy destruction terms can be written as :

$$\Phi^* = \overline{\tau}_{xj}\frac{\partial\hat{u}_x}{\partial x_j} + \overline{\tau}^t_{xj}\frac{\partial\hat{u}_x}{\partial x_j}, \tag{3.91}$$

and

$$\Phi^*_\Theta = -\left(\overline{q}_j + \overline{q}^t_j\right)\left(\frac{\partial\hat{T}}{\partial x_j}\right), \tag{3.92}$$

They represent the entropy generation by viscous dissipation and by heat transfer, respectively. As mentioned by Lamberts *et al.* [100], the source term of the total exergy transport is negative by construction (2^{nd} principle of thermodynamics). As a result, the total exergy in its transport tube can only be destructed. However, for the momentum tube and mean-flow kinetic energy tube, the features could be different due to the pressure gradient sources, which make the analysis more complex.

3.6.1 Definitions and transfer indicators

Transfer indicators are defined in this section. First of all, as only averaged variables are involved in the analysis, the "overline" and the "hat" are omitted for all variables. Similarly for the mean-flow total exergy computed by the averaged flow quantities in Equations (3.90), (3.91), and (3.92), the superscript star is also omitted.

Considering the momentum transfer Equation (3.87), the momentum flux vector is defined as :

$$F_{m,j} = \rho u_j u_i \zeta_i - \tau_{ij}\zeta_i - \tau^t_{ij}\zeta_i, \tag{3.93}$$

where ζ_i is the direction of momentum flux which is chosen as the direction of the main flow. This momentum flux vector consists of three parts : the advective part ($\rho u_j u_i \zeta_i$), the molecular dissipation part ($\tau_{ij}\zeta_i$), and the turbulent dissipation part ($\tau^t_{ij}\zeta_i$).

The kinetic energy flux vector (LHS of Equation (3.88)) is defined as :

$$F_{K,j} = K u_j - \tau_{ij} u_i - \tau^t_{ij} u_i, \tag{3.94}$$

where $K = \frac{1}{2}\rho u u$ is the mean-flow kinetic energy. It also consists of an advective part ($K u_j$) and a viscous dissipation part ($-\tau_{ij}u_i - \tau^t_{ij}u_i$) with a molecular and a turbulent component. For the turbulent component, τ^t_{ij} is modeled through the Boussinesq assumption and according to the turbulence model.

Based on total exergy conservation Equation (3.90), the total exergy flux vector writes :

$$F_{\xi,j} = u_j(\rho\xi_t) + (q_j + q^t_j)\left(1 - \frac{T_{ref}}{T}\right) - \tau_{ij}u_i - \tau^t_{ij}u_i. \tag{3.95}$$

This flux can be separated into three parts :

1. An advective exergy flux :
$$F_{\xi,j}^{adv} = u_j(\rho\xi), \tag{3.96}$$

2. a heat flux :
$$F_{q,j} = (q_j + q_j^t)\left(1 - \frac{T_{ref}}{T}\right), \tag{3.97}$$

3. a kinetic energy flux, which is the same as $F_{K,j}$.

As a result, the total exergy flux vector can be written as : $F_{\xi,j} = F_{\xi,j}^{adv} + F_{q,j} + F_{K,j}$. The sink terms at the RHS of Equation (3.90) are defined as the total exergy destruction by the heat transfer (Equation (3.91)) and the total exergy destruction by the viscous dissipation (Equation (3.92)).

Two types of transport tubes can be analyzed : the exergy tube and the secondary stream tube. Firstly, an exergy tube is shown in Figure 3.14 for illustration purpose. It is constructed as all total exergy fluxes passing through the portion of the secondary stream at the outlet boundary (between two green points at the outlet boundary). This tube shows the path of useful exergy that the secondary stream gained through the ejector. It gives the information where this useful exergy comes from in the primary, as the primary stream is the only possible source of exergy for the secondary stream. If the tube is followed upstream to the primary inlet, it shows the exergy footprint of the exergy gain of the secondary stream. This exergy is transferred and dissipated by the different mechanisms appearing in Equation (3.89). Similarly the remaining exergy originally contained in the primary stream is either dissipated or exit the ejector without being transferred to the secondary stream.

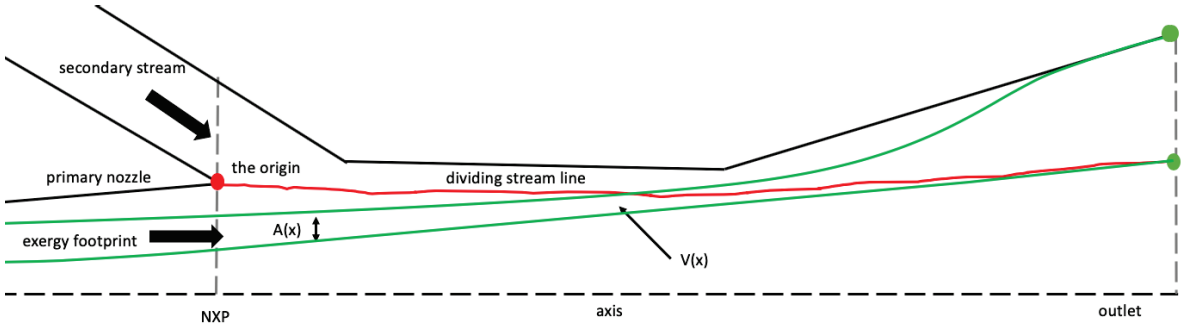

Figure 3.14 Illustration of an exergy tube.

In an exergy tube, by definition, there is, on average, no total exergy flux passing through the envelop of the tube. Hence, based on Equation (3.90), the total exergy entering into the tube can only be destructed or convected. The averaged total exergy flux in the tube is

presented as the integration of the total exergy flux vector at a cross-section $A(x)$ (Figure 3.14), which is :

$$J_\xi(x) = \frac{\iint_{A(x)} F_{\xi,j} n_j dA}{\dot{m}\xi}, \tag{3.98}$$

where $A(x)$ is the area of the exergy tube cross-section and n_j is the normal vector of the cross-section. This integrated quantity is normalized by $\dot{m}\xi$, which is the total exergy flux at the nozzle exit plan (NXP). This quantity can also be split by the integration of the advective flux ($F^{adv}_{\xi,j}$), the heat transfer flux ($F_{q,j}$), and the kinetic energy flux ($F_{K,j}$). Hence, it can be also written as $J_\xi = J^{adv}_\xi + J_q + J_K$. The averaged total exergy destruction within the tube is evaluated by integrating the destruction terms through the whole volume of the exergy tube ($V(x)$ shown in Figure 3.14). Consequently, at the outlet ($V(x) = V(x_{out})$), the total destruction can be obtained. The destruction by the viscous dissipation reads :

$$\Gamma(x) = \frac{T_{ref} \iiint_{V(x)} \Phi/T dV}{\dot{m}\xi}. \tag{3.99}$$

The integration is firstly done at the cross-section and then along the tube. As a result, this term can be presented along the x-direction. The normalization is achieved similarly as the cross-sectional total exergy flux. The destruction by the heat transfer is computed similarly as :

$$\Gamma_\Theta(x) = \frac{T_{ref} \iiint_{V(x)} \Phi_\Theta/T^2 dV}{\dot{m}\xi}. \tag{3.100}$$

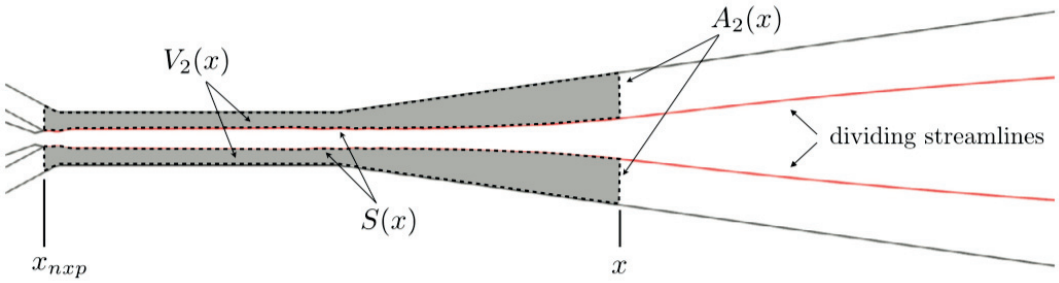

Figure 3.15 Illustration of the secondary stream proposed by Lamberts *et al.* [100].

The second type of analysis focuses on the secondary stream tube. It is defined as the region between the dividing streamline and the ejector wall, as illustrated in Figure 3.15. By construction, there is, on average, no mass flux passing through the dividing streamline. However, there is a total exergy transfer by diffusion from the primary stream to the secondary one.

Hence, two types of quantities can be computed. The first one is the local transfer. It presents the local transfer crossing the streamline, such as the local transfer of total energy, momentum, and kinetic energy. The second one is the cumulative transfer. For example, the cumulative transfer of momentum is computed by integrating the local transfer along the dividing stream line and the spanwise direction, as :

$$I_m(x) = \frac{\iint_{S(x)} F_{m,j} n_j ds}{\dot{m}_{prim} U_{prim}}, \tag{3.101}$$

where $S(x)$ is the area of the dividing surface between the NXP and a local position x, shown in Figure 3.15. A velocity is defined based on the primary inlet exergy, $U_{prim} = \sqrt{2\xi_{prim}}$ and is used to normalize the cumulative transfer of momentum.

In the same way, the local transfer of kinetic energy along the dividing streamline can be computed by :

$$I_K(x) = \frac{\iint_{S(x)} F_{K,j} n_j ds}{\dot{m}_{prim} \xi_{prim}}. \tag{3.102}$$

It is normalized by the total exergy flux at the primary inlet. As mentioned before, the mean-flow kinetic energy flux consists of an advective part (Ku_j) and a viscous part ($-\tau_{ij}u_i - \tau^t_{ij}u_i$). Since the integration is along the dividing streamline, this flux has only a viscous component, which is actually interpreted as the diffusive transfer through the shear layer.

The dimensionless cumulative transfer of total exergy by heat transfer is introduced as :

$$I_q(x) = \frac{\iint_{S(x)} F_{q,j} n_j ds}{\dot{m}_{prim} \xi_{prim}}. \tag{3.103}$$

This quantity can be positive or negative, because it depends on the local temperature gradient between the two streams and also the choice of the reference temperature for the total exergy. In this thesis, the state at the secondary inlet is always considered as the reference state. Hence, the total exergy at the secondary inlet is zero by definition.

The dimensionless cumulative transfer of the total exergy can be then defined as :

$$I_\xi(x) = \frac{\iint_{S(x)} F_{\xi,j} n_j ds}{\dot{m}_{prim} \xi_{prim}}. \tag{3.104}$$

This quantity can be also written as $I_\xi = I_q + I_K$, where there is no advective part for I_K. Indeed, the transfer of the total exergy between the primary and secondary streams are via diffusion of thermal (I_q) and mechanical (I_K) nature.

The dimensionless exergy destruction related to the viscous dissipation is defined similarly as the destruction quantity in the exergy tube (Equation (3.99)). The difference is that the integration is through the volume of the secondary stream ($V_2(x)$) instead of the volume of the exergy tube $V(x)$. It reads :

$$\Pi(x) = \frac{T_{ref} \iiint_{V_2(x)} \Phi/T dV}{\dot{m}_{prim}\xi_{prim}}. \tag{3.105}$$

Similarly, the dimensionless exergy destruction related to the heat transfer writes :

$$\Pi_\Theta(x) = \frac{T_{ref} \iiint_{V_2(x)} \Phi_\Theta/T^2 dV}{\dot{m}_{prim}\xi_{prim}}. \tag{3.106}$$

This cumulative quantity is also integrated through the entire volume of the secondary stream ($V_2(x)$). Finally, a balance between different contributions of the total exergy transfer can be obtained :

$$\Delta(x) = I_K(x) + I_q(x) - \Pi(x) - \Pi_\Theta(x). \tag{3.107}$$

This balance is the application of the exergy conservation Equation (3.90) on the secondary stream tube.

CHAPTER 4

Validations of the different approaches

In this chapter, the look-up table method, the CLAWPACK solver and the *rhoCentralFoam* solver are assessed for validations and verifications. In Section 4.1, the interpolation results are compared to the original Span-Wagner EoS in terms of pressure, temperature, and speed of sound. Moreover, the speed-up of the look-up table method for one specific simulation is evaluated through the CLAWPACK solver in Section 4.2.3. Two classical validation cases [72, 84] are performed and compared to available results in the literature in Section 4.2 and 4.3, respectively. Finally, the critical mass flow rate for the converging-diverging nozzle is verified for the CLAWPACK and the *rhoCentralFoam* solvers. It should be mentioned that other test cases have also been performed with the CLAWPACK solver, which are shown in Appendix C, such as the two-shock tube problem, the cavitation problem, and the double shock problem. Additionally, verifications of the AVBP solver have been done and shown in Appendix D.

4.1 Validation of the look-up table approach

The relative errors between the original SW EoS and the bilinear interpolation values in terms of pressure (Figure 4.1), temperature (Figure 4.2), and speed of sound (Figure 4.3) are displayed. Inside each cell, 25 test-points are calculated in the single-phase region and 250000 points in the whole two-phase region to assess the accuracy of the bilinear interpolation, which represents a total number of checkpoints equal to 2 millions.

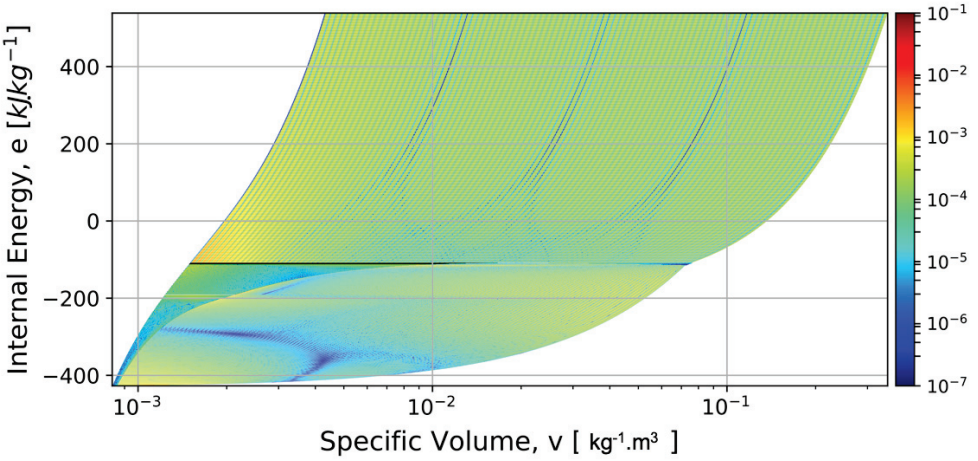

Figure 4.1 Relative errors for the pressure in the $e - v$ space.

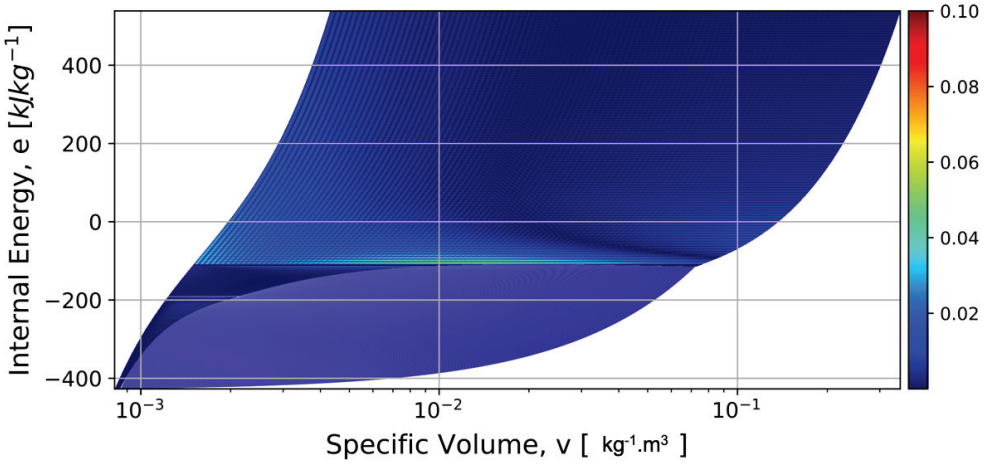

Figure 4.2 Absolute errors for the temperature in the $e - v$ space.

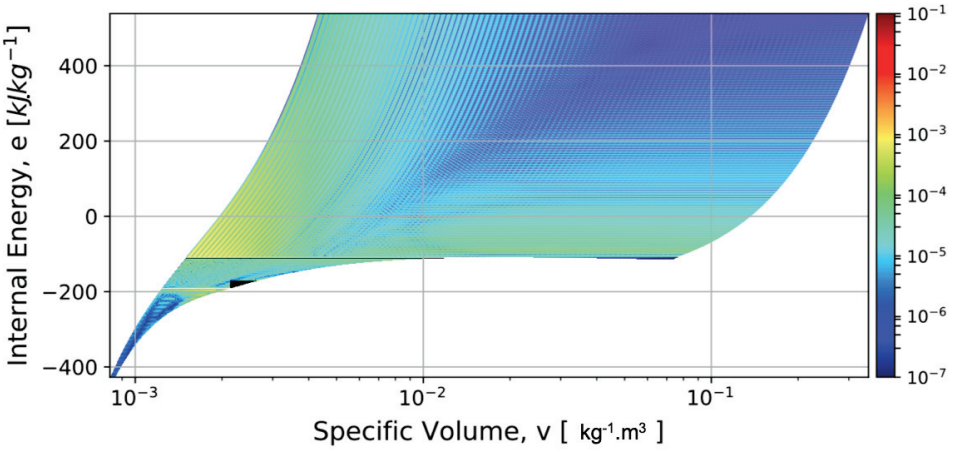

Figure 4.3 Absolute errors for the speed of sound in the $e - v$ space.

The maximum errors compared to SW EoS in each sub-region are summarized in Table 4.1. It is observed that the properties are well predicted in each sub-region. The maximum relative error for the speed of sound is around 1.2%, the maximum being located in the neighbourhood of the critical point. The region around the critical point often has an issue for evaluating the thermodynamic properties, because some properties such as the speed of sound, the heat capacity have a singularity at the critical point and exhibit a non-linear behavior. Even though the SW EoS is considered as the most accurate EoS in the critical region, it still has more than 1% uncertainty in terms of speed of sound. Moreover, it has been verified that the nearest nodes to the critical point in the LL, LH, TP subdomains have a pressure difference between 92 Pa and 1600 Pa and a temperature difference between 0.001 K and 0.09 K. These nodes define the properties in the nearest region to the critical point.

Table 4.1 Maximum relative errors for the pressure and the speed of sound ,and the maximum absolute errors for the temperature.

domain	max error for p [%]	max error for T [K]	max error for c [%]
LL	0.16	0.007	1.2
LH	0.05	0.04	0.2
HT	0.23	0.05	0.08
R	0.20	0.06	0.01
TP	0.07	0.03	-

In summary, the proposed tabulated EoS shows a good accuracy in the whole range from 0.5 MPa to 50 MPa for the pressure and from 217 K to 800 K for the temperature. It shows also the capacity to accurately and stably evaluate the properties in the critical region.

4.2 Verifications for the CLAWPACK solver

Two benchmark verifications are presented in this section to highlight the capacity of the tabulated EoS to deal with two-phase CO_2 simulations. The experimental database of the single-phase and two-phase CO_2 flows is far to be abundant in the literature. Consequently, the numerical results are utilized to validate the proposed EoS, as shown in Sections 4.2.1 and 4.2.2 for the shock tube case and the depressurization case. In Section 4.2.3, the results are compared to the Peng-Robinson, the Stiffened-Gas and the Span-Wagner EoS.

4.2.1 Shock tube

In this section, a classic shock tube problem is considered to assess the accuracy of the tabulated EoS for the CO_2 vapor. As shown in Figure 4.4, a 100-meter tube is filled with CO_2 at two different vapor states separated by a membrane at the middle of the tube. Initially, the left state is at $p_L = 3$ MPa, $T_L = 300$ K and $\rho_L = 63.376\ kg.m^{-3}$ at rest, while the right state is at $p_R = 1$ MPa, $T_R = 300$ K and $\rho_R = 18.579\ kg.m^{-3}$ at rest. The subscript 'L' and 'R' denote the left and right states, respectively.

Figure 4.4 Schematic of the shock tube problem. The left side is filled with the high pressure CO_2 while the right side is filled with the low pressure CO_2.

At $t = 0$, the membrane is removed and the high pressure CO_2 interacts with the low pressure CO_2. The left-propagating expansion waves form while a contact surface and a shock wave are generated and propagate toward the right. The 1D tube is meshed with 1000 grid points. Figure 4.5 illustrates the pressure, density, velocity and temperature distributions along the tube at $t = 0.08$ s.

The numerical results agree well with the results of Giljarhus *et al.* [72]. They performed numerical simulations by using the original SW EoS. MUSTA (MUlti-STage Approach) was used to solve the Euler system of equations [175, 179]. This approach is an alternative method to avoid using a Riemann solver. The current results show that the discontinuities are better resolved than those of Giljarhus *et al.* [72]. Except the discontinuities, for the rest part of the density in Figure 4.5, the two simulations agree well, which means that

the tabulated EoS can reach the same accuracy as the original SW EoS for the CO_2 vapor simulation.

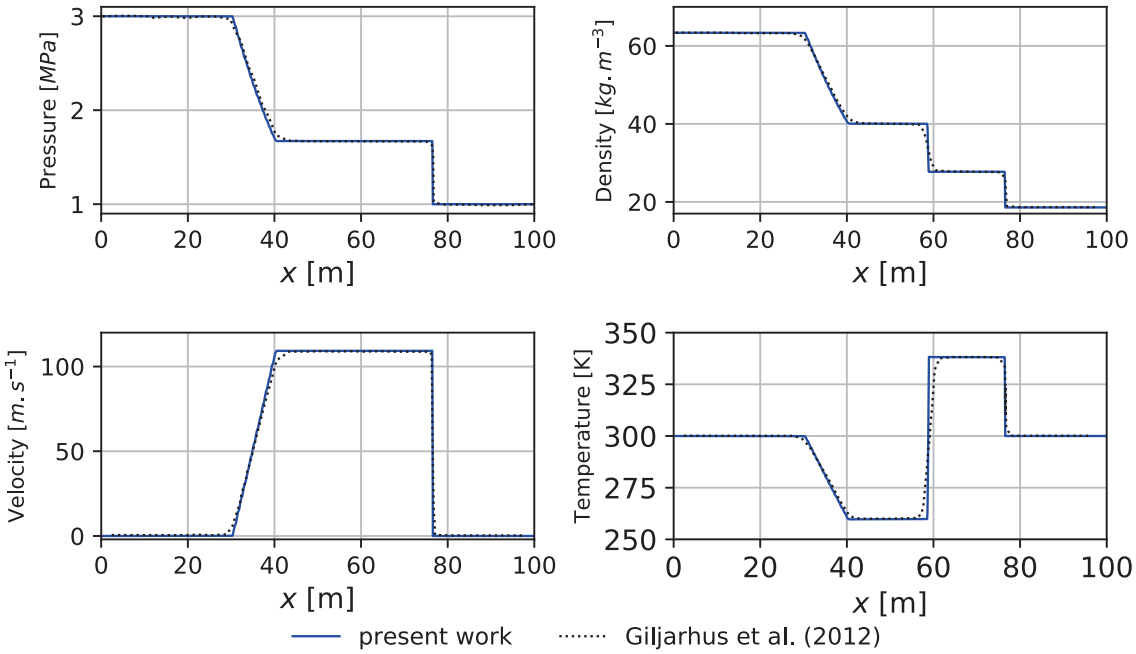

Figure 4.5 Pressure, density, velocity and temperature profiles at $t = 0.08$ s for the shock tube problem. Comparison with the numerical results of Giljarhus *et al.* [72].

4.2.2 Depressurization

The CO_2 fluid transported in a pipeline or stored in a tank remains often in the dense phase (pressure higher than the critical pressure). A damage on the container wall or the rupture of the pipeline can cause a rapid depressurization and the CO_2 fluid is subjected to a violent phase transition, namely 'flashing'. A large amount of the dense phase evaporates and the flow becomes two-phase. Similar scenario can be encountered in the CO_2 supersonic ejector. As the supercritical CO_2 expands in the motive nozzle, 'flashing' occurs near the throat and a two-phase flow further develops in the divergent.

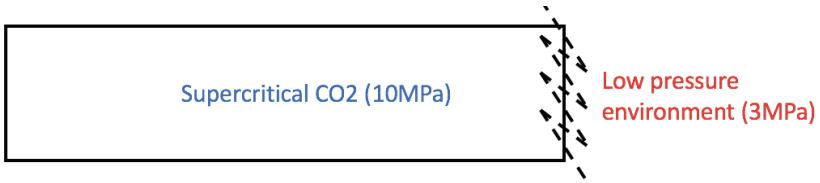

Figure 4.6 Schematic of the depressurization. The full tube is filled with supercritical CO_2 at 10 MPa and the pressure at the right boundary is fixed to 3 MPa.

In order to predict the flow behavior during the depressurization, a 100-meter tube filled with CO_2 at $p = 10$ MPa, $T = 300$ K (supercritical state) is simulated (see Figure 4.6). The pressure at the right boundary is fixed at 3 MPa. A grid composed of 1000 mesh points is used. At $t = 0$, the right side is opened and the supercritical CO_2 is exposed to the low pressure environment. Two types of expansion wave are generated and propagate to the left side. One is the expansion wave with the supercritical CO_2 and the other one is the evaporation front where the CO_2 vapor is created. The detailed discussion of these two types of expansion waves are found in [118]. Similar phenomenon has been also observed and discussed for water [52, 155]. Figure 4.7 displays the distribution of the pressure, temperature and liquid mass fraction along the tube at $t = 0.2$ s. Note that the x axis for the liquid mass fraction is presented only from 75 to 100 m.

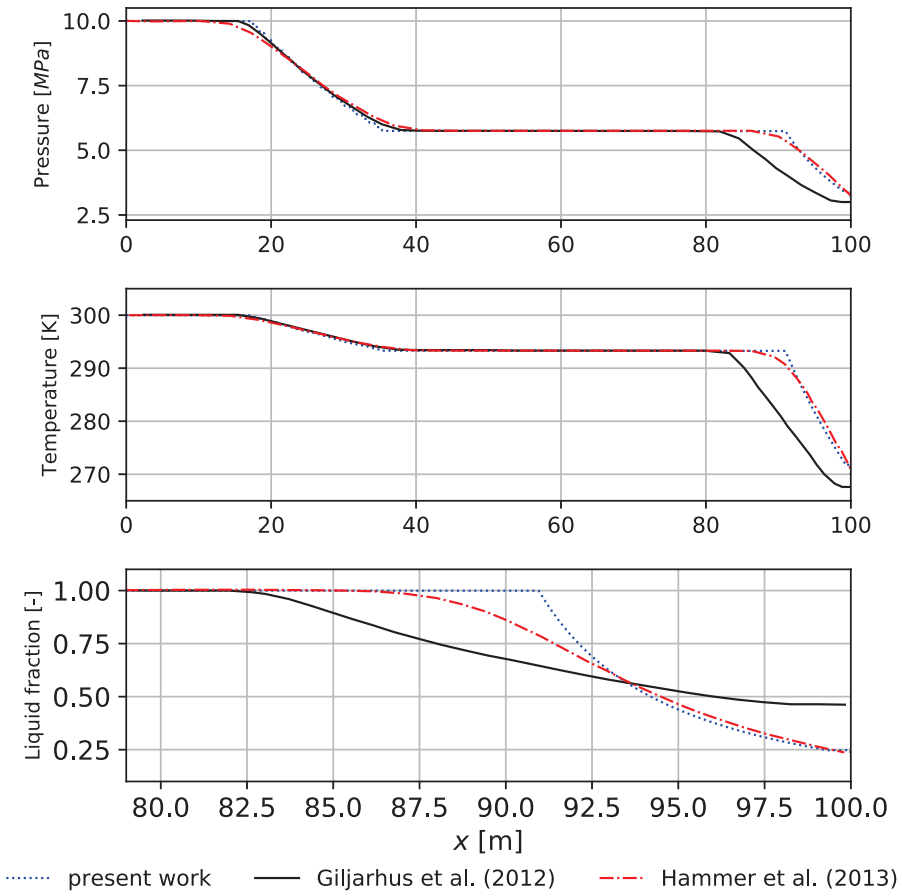

Figure 4.7 Comparisons to the numerical results of Giljarhus *et al.* [72] and Hammer *et al.* [84] in terms of pressure, temperature and liquid mass fraction distribution in the streamwise direction.

The current results are compared to those of Giljarhus *et al.* [72] and Hammer *et al.* [84]. A good agreement away from the discontinuities are observed in Figures 4.7 and 4.8. The results of Giljarhus *et al.* [72] present some discrepancies at the location of the evaporation front. As in the shock tube case, it comes from the different orders of the numerical scheme. Hammer *et al.* [84] used the MUSCL-FORCE scheme which is second-order accurate, while the MUSTA is first-order accurate in [72]. The liquid mass fraction, pressure and temperature profiles in Figure 4.7 show that the discontinuities are better captured by the CLAWPACK solver.

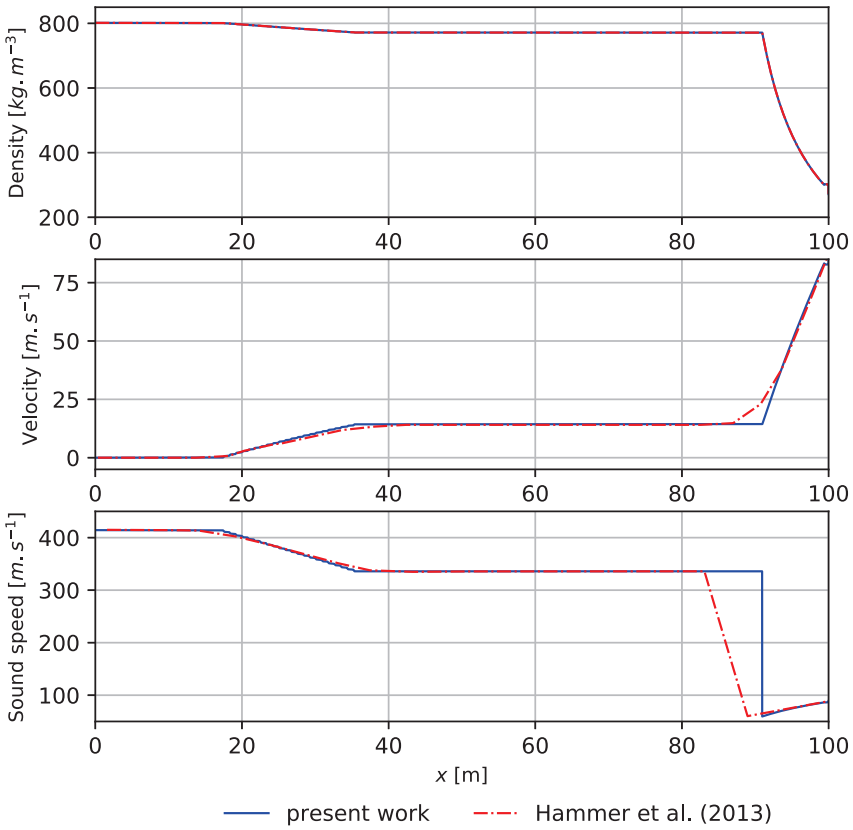

Figure 4.8 Comparisons between the present numerical results and those of Hammer *et al.* [84] in terms of pressure, temperature and liquid mass fraction for the depressurization.

Figure 4.8 shows comparisons in terms of density, velocity and speed of sound between the results of Hammer *et al.* [84] and the current results. It is observed that the proposed formulation of the two-phase speed of sound from the HEM agrees with the results of Hammer *et al.* [84] who used the formulation proposed by Flåtten and Lund [63]. Both formulations predict a discontinuity between the liquid and vapor phase (across the saturation curve), which is a feature of the HEM (see Figure 3.1).

4.2.3 Comparison between different EoS and speed-up factor

Vapor shock tube

The 1D classical shock tube problem is performed using the ClAWPACK solver, while comparing the Peng-Robinson EoS, the Stiffened Gas EoS and the original Span-Wagner EoS to the proposed tabulated EoS. The vapor phase is considered in the simulations, because the Peng-Robison EoS is not appropriate for liquid and two-phase states. The accuracy of the results and the computational time are compared between the different EoS in order to assess the performance of the tabulated EoS. A 1-meter tube is considered. The CO_2 vapor with $\rho_L = 85.31\ kg.m^{-3}$, $p_L = 5$ MPa, $T_L = 360$ K, $u_L = 0\ m.s^{-1}$ fills the left part whereas CO_2 with $\rho_R = 15.1\ kg.m^{-3}$, $p_R = 1$ MPa, $T_R = 360$ K and $u_R = 0\ m.s^{-1}$ fills the right part. The theoretical formulation and the implementation details for the Peng-Robinson EoS and the Stiffened Gas EoS [64, 123] are presented in appendix B. The numerical results are reported in Figure 4.9. It shows that the results using the original Span-Wagner EoS and those using the tabulated EoS agree well. This validates the accuracy of the tabulated EoS.

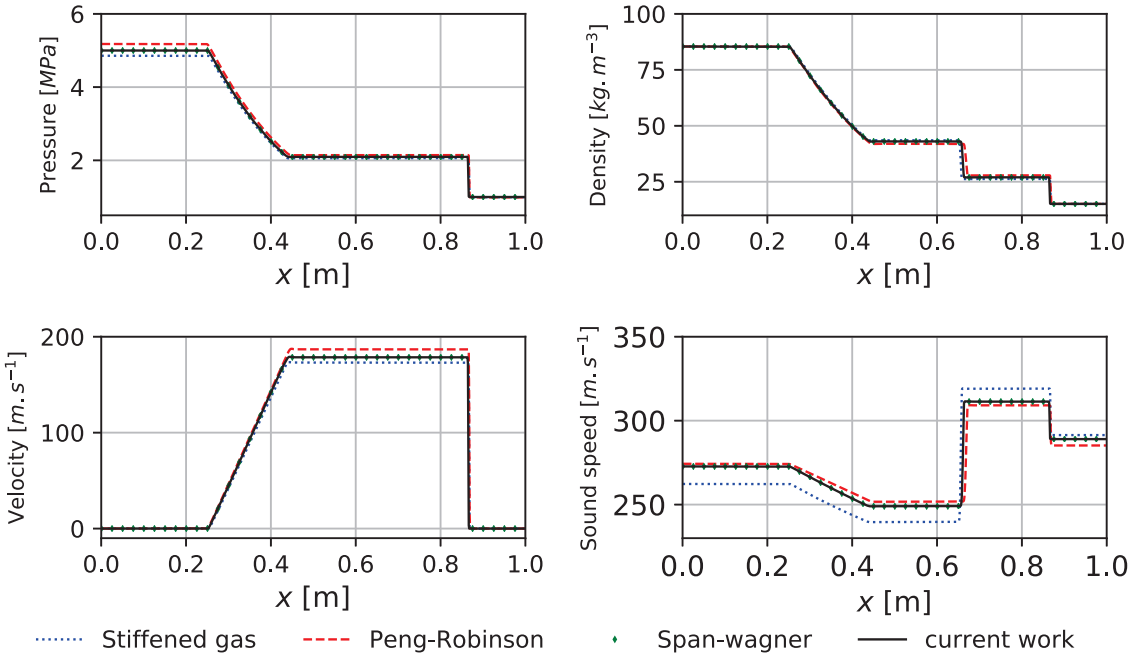

Figure 4.9 Streamwise distributions of pressure, density, velocity and speed of sound along the tube using different EoS.

The speed of sound of the SG EoS differs from that of SW EoS. This EoS depends strongly on parameters of the reference state (see Equation (8.10)). Here, a state between 5 MPa and 1 MPa is chosen as the reference state to better calibrate the density. PR EoS exhibits

also some discrepancies in terms of pressure in the high-pressure region and in terms of velocity at the contact surface.

The computational time and speed-up are summarized in Table 4.2. All computations are carried out using an Intel core i7 with 8G memory.

Table 4.2 Computational time and speed-up for different EoSs. The physical time is at 1.5 ms for the shock tube problem.

Simulation time=1.5 ms	CPU time [s]	$Ratio = t_{ref}/t$
Tabulated EoS	1.67	66.16
Peng-Robinson EoS	3.35	32.98
Stiffened gas EoS	0.85	129.9
Span-Wagner EoS	110.49	1.0

The original Span-Wagner EoS is considered as the reference, thus its CPU time is considered as the reference time t_{ref}. The speed-up is the ratio between the reference CPU time and the CPU time taken by other EoSs (t_{ref}/t). The tabulated EoS is 66 times faster than the original SW EoS and produces undistinguishable results, as shown in Figure 4.9. It is also 2 times faster than the PR EoS which is not appropriate to describe the liquid and two-phase properties as well. The SG EoS is the fastest one but it is parameter-dependant. This limits the use of SG EoS for large variation of phase states. Additionally, the SG EoS computes the properties with a linear form around the reference state. Thus, for phase states close to the critical point where large non-linear variation of the properties occurs, the choice of the reference state could be difficault. This is the case encountered for the two-phase CO_2 ejector in refrigerations, where operating conditions are near the critical point [5, 54]. Therefore, this tabulated EoS exhibits advantages in terms of high accuracy and high efficiency and it is appropriate for future massive CFD simulations.

Liquid shock tube

The same evaluation has been performed for the liquid shock tube case. Initially, the CO_2 fluid with $\rho_L = 1160\ kgm^{-3}$, $p_L = 6$ MPa, $T_L = 250$ K, $u_L = 0\ m.s^{-1}$ fills the left part, whereas the right state is $\rho_R = 1148\ kg.m^{-3}$, $p_R = 1$ MPa, $T_R = 225$ K, $u_R = 0\ m.s^{-1}$. The simulation time is 0.5 ms. The pressure and density distribution is presented in Figure 4.10 and 4.11. Small discrepancies are observed at the expansion waves. The speed of sound, Mach number, velocity, and vapor mass fraction are show in Figure 4.11.

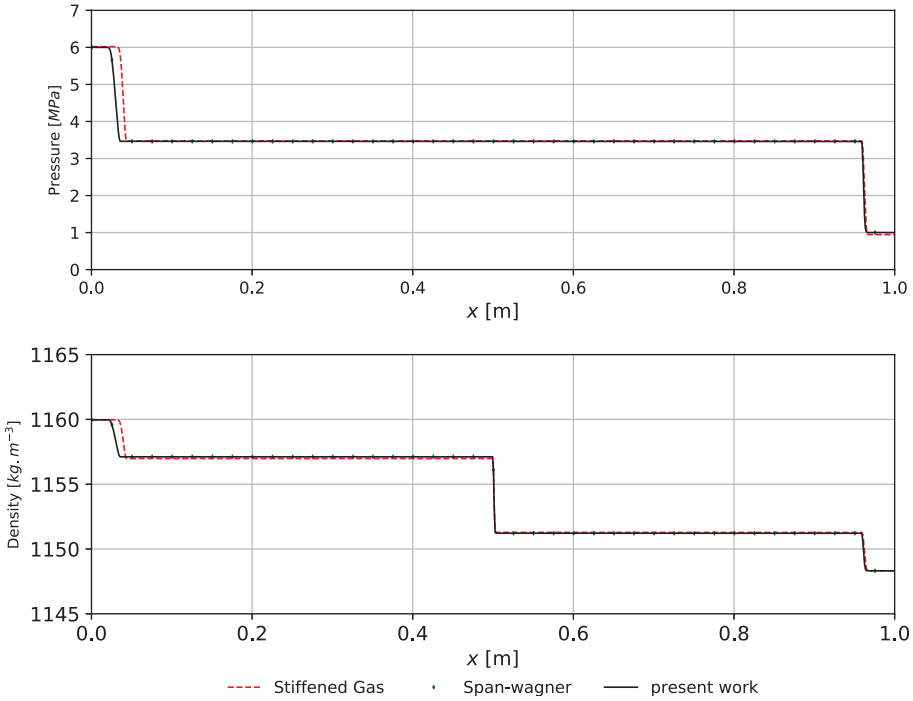

Figure 4.10 Streamwise distributions of pressure and density for different EoS.

It can be seen that a significant difference in terms of speed of sound is obtained, which is due to the differences of EoS. Finally, the speed-up factor is computed and shown in Table 4.3.

Table 4.3 Computational time and speed-up for different EoS. The physical time is at 0.5 ms for the liquid shock tube problem.

Simulation time=0.5 ms	CPU time [s]	Ratio
Span-Wagner table	0.7	90.25
Peng-Robinson EoS	-	-
Stiffened gas EoS	0.62	101.9
Span-Wagner EoS	63.18	1.0

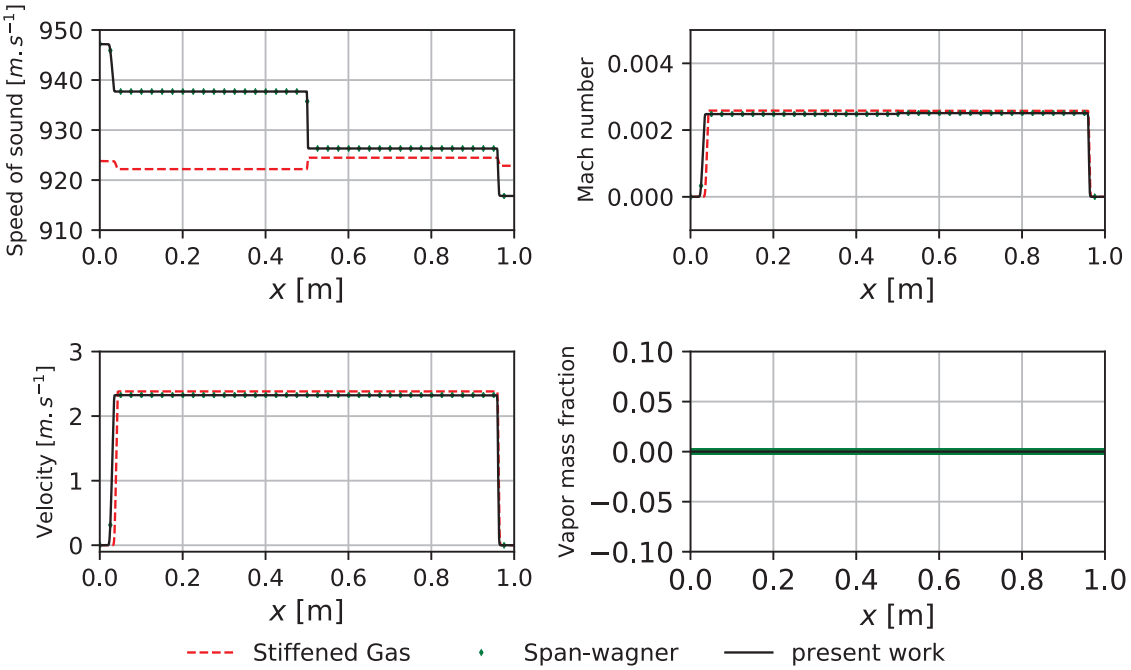

Figure 4.11 Streamwise distributions of speed of sound, Mach number, velocity, and vapor mass fraction along the tube using different EoS.

Peng-Robinson EoS is not considered, because the liquid phase is involved in the simulation. Again, a significant speed-up factor is obtained compared to the original SW EoS by achieving the same accuracy. Hence, this tabulated approach is validated and suitable for massive CFD simulations. It is noted that the speed-up is less important between the tabulated SW and the SG EoS in this case.

4.3 Verifications for the rhoCentralFoam solver

4.3.1 Configuration 1 : shock tube

The same shock tube problem as in Section 4.2.1 is simulated by applying the modified *rhoCentralFoam* solver in order to evaluate the capture of discontinuities (e.g. shock waves, expansion waves, and contact surfaces) in compressible flows.

The 1D tube is meshed with 1000 regularly spaced nodes. The time step is computed at each time step to guarantee that the Courant-Friedrich-Levy (CFL) number remains smaller than 0.2. Viscous effects are neglected, such that the code solves the Euler equations. The Van Leer interpolation is used to compute the variables at the cell-interface.

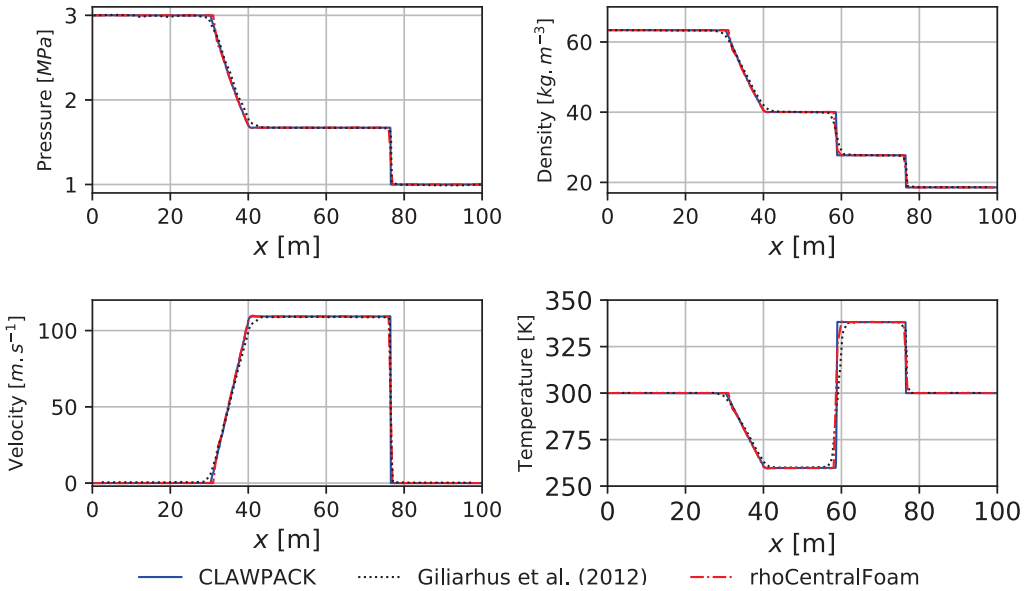

Figure 4.12 Pressure, density, velocity and temperature profiles at $t = 0.08$ s for the shock tube problem.

The present results are compared to those of the CLAWPACK solver [59] and Giljarhus *et al.* [72]. Giljarhus *et al.* [72] conducted the simulation using the MultiSTage Approach (MUSTA), which is a Riemann-solver-free approach [175]. The comparison is shown in Figure 4.12. A good agreement is obtained between these three simulations. Only some small discrepancies can be observed at the discontinuities, which come from the numerical scheme. It is noted that the *rhoCentralFoam* solver is less accurate than the CLAWPACK solver, but more accurate than the MUSTA.

This case was also simulated by the pressure-based and density-based solvers in ANSYS Fluent (Figure 4.13 and 4.14). The SIMPLEC and COUPLED schemes with PRESTO! and a second-order spatial discretization scheme for the pressure-based solver and density-based solver are compared to the *rhoCentralFoam* solver in terms of density and pressure for this vapor shock tube case. It was found that in order to capture correctly the shock waves, contact surface and expansion waves, the pressure terms must be at least discretized by a second-order accurate scheme for pressure-based solvers. Otherwise noticeable numerical oscillations appear at the locations of the contact surface and the shock waves. Moreover, in Figure 4.13, for the region away from the discontinuities, some discrepancies are observed. These are mainly due to the EoS, which means there are some differences between the tabulated EoS and the Refprop database. The tabulated EoS can reach an accuracy comparable to that of the original SW EoS. Therefore, the accuracy of the Refprop database is worth to be assessed.

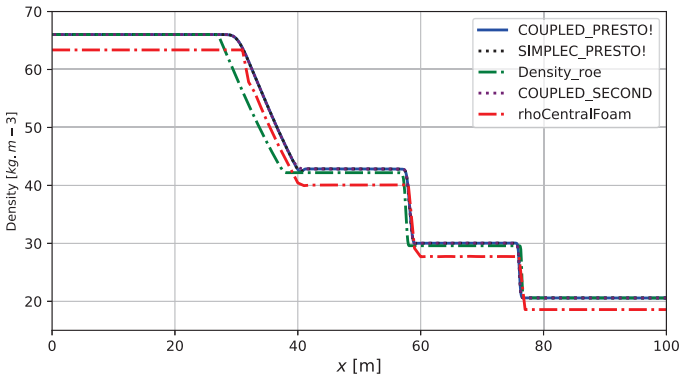

Figure 4.13 Density profiles obtained by the pressure-based and density-based solvers in ANSYS Fluent.

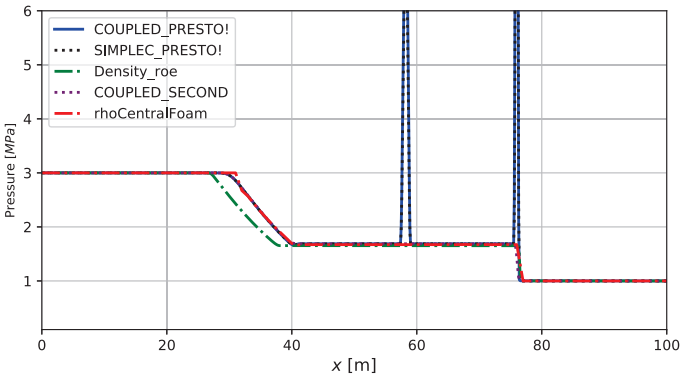

Figure 4.14 Pressure profiles obtained by the pressure-based and density-based solvers in ANSYS Fluent.

4.3.2 Configuration 2 : depressurization

The same depressurization case as in Section 4.2.2 is considered here. Hence, it was chosen to validate the HEM and meanwhile to evaluate the NSCBC for the *rhoCentralFoam* solver at the outlet boundary. A 1000-node mesh is used. The profiles of pressure, temperature and speed of sound at $t = 0.2$ s are shown in Figure 4.15. Two discontinuities can be observed for the pressure profile. The left one is the expansion wave of the supercritical CO_2, while the right one is the evaporation front where the CO_2 vapor is created. The present results are compared to those of Hammer *et al.* [84] and Fang *et al.* [59]. A second-order accurate MUSCL-FORCE scheme was used by Hammer *et al.* [84].

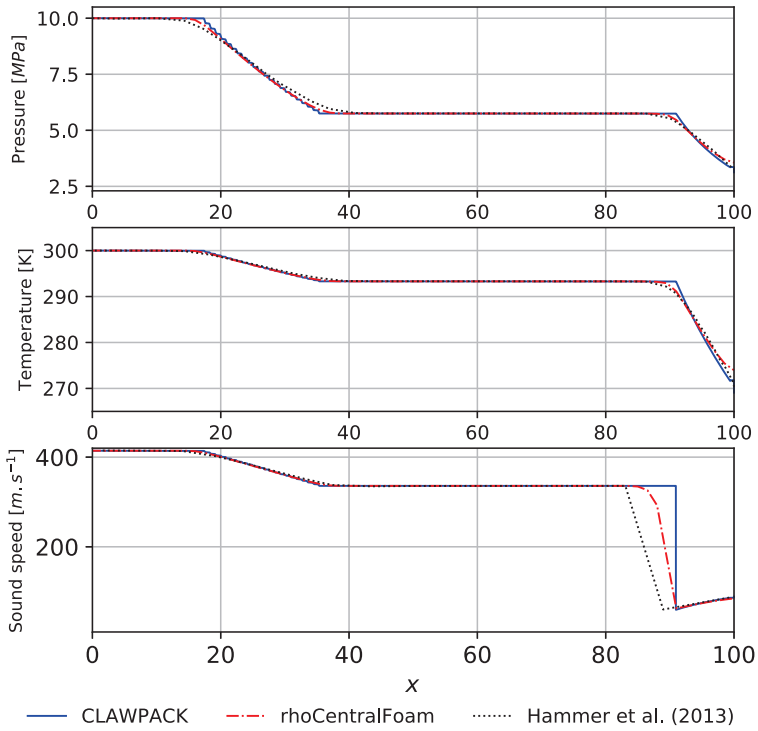

Figure 4.15 Comparisons between the present solver and the numerical results of Fang *et al.* [59] and Hammer *et al.* [84] in terms of pressure, temperature and liquid mass fraction distributions in the streamwise direction at $t = 0.2$ s.

The *rhoCentralFoam* solver provides similar results compared to the MUSCL-FORCE scheme, but being more dissipative than the CLAWPACK solver. In this simulation, the upwind interpolation instead of the Van Leer interpolation is used as the interface interpolation scheme, which is due to the instability issue. The later one is less robust for the strong discontinuities, while the upwind interpolation is more stable.

4.4 Validation in terms of the critical mass flow rate for the converging-diverging nozzle

In this section, the critical mass flow rate is computed at the nozzle throat when the nozzle is fully supersonic. The critical mass flow rate is computed through the CLAWPACK solver and the *rhoCentralFoam* solver for a converging-diverging nozzle, which can be viewed as the primary nozzle of the ejector of Smolka *et al.* [162]. Numerical results are compared

to the experimental and numerical results of [162] and to the thermodynamic models of Croquer *et al.* [45] and Taslimi Taleghani *et al.* [172].

In Smolka *et al.* [162], the whole ejector was simulated through the pressure-based solver in ANSYS Fluent. The thermodynamic properties are computed through the embedded the Refprop database. For the thermodynamic model of Croquer *et al.* [45], and Taslimi Taleghani *et al.* [172], the isentropic expansion theory is applied to compute the critical mass flow rate for the primary nozzle, but the difference between the two thermodynamic models is that the Croquer *et al.* [45] model uses Coolprop to compute all thermodynamic properties, while the Taslimi Taleghani *et al.* [172] model uses the Refprop database. Then, 2D simulations of the converging-diverging nozzle are performed through the CLAWPACK solver and the *rhoCentralFoam* solver without considering viscous and turbulent effects. It means that the Euler equation system is resolved for the flow fields. The slip-wall condition is used at the wall. A mesh with 100 elements in the streamwise direction and 20 elements in the perpendicular direction is used.

The diameters of the nozzle inlet and the nozzle throat are 6 mm and 1 mm, respectively. The lengthes of the converging and diverging parts are 9.5 mm and 3.5 mm, respectively. The results are shown in Table 4.4.

Table 4.4 Comparisons in terms of the critical mass flow rate (in $kg.s^{-1}$) between different works [45, 162, 172].

Case	p_{prim} (MPa)	T_{prim} (K)	$\dot{m}_{exp}$	$\dot{m}_{smo}$	$\dot{m}_{cro}$	$\dot{m}_{ta}$	$\dot{m}_{cla}$	$\dot{m}_{op}$
1	9.915	303.05	0.04973	0.04526	0.0574	0.05468	0.05021	0.0458
2	8.668	306.55	0.03194	0.03142	0.0368	0.0348	0.03356	0.0315
3	9.091	299.85	0.04842	0.04246	0.0529	0.0513	0.04634	0.0422
4	9.85	308.65	0.04073	0.03880	0.0477	0.04585	0.04331	0.0397
5	9.455	309.45	0.03569	0.03465	0.0421	0.03998	0.03827	0.0354
6	8.846	308.75	0.02984	0.03036	0.0352	0.03193	0.03264	0.0305
7	8.465	308.55	0.02607	0.02715	0.0321	0.02951	0.0276	0.0276

The subscript 'prim' denotes primary inlet conditions, while 'exp', 'smo', 'cro', 'ta' represent the experimental, numerical results from Smolka *et al.* [162], Croquer *et al.* [45], and Taslimi Taleghani *et al.* [172], respectively. The subscript 'cla' and 'op' denote the results computed by the CLAWPACK solver and the *rhoCentralFoam* solver. The relative errors are computed as

$$\delta = \frac{\dot{m}_{exp} - \dot{m}}{\dot{m}_{exp}} \tag{4.1}$$

The relative errors between different results are summarized in Figure 4.16.

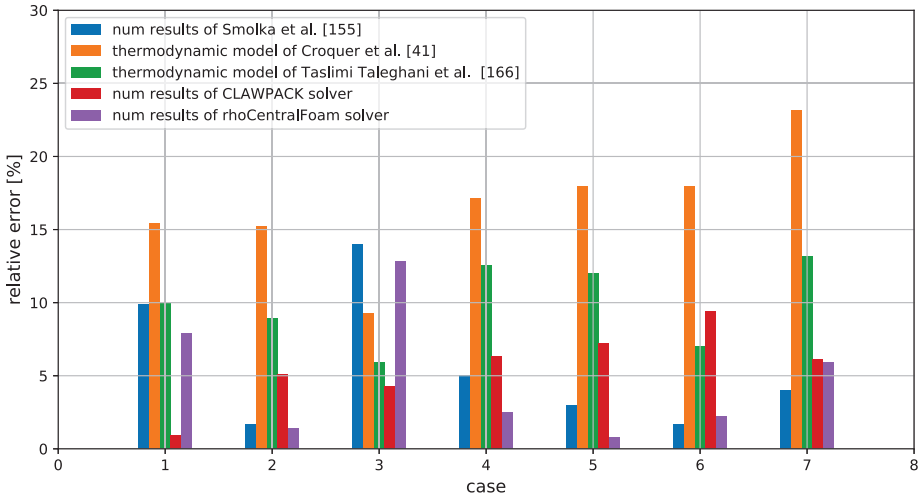

Figure 4.16 Relative errors of the critical mass flow rate (in %) between different works [45, 162, 172].

It can be observed that the CLAWPACK solver and the *rhoCentralFoam* solver can provide comparable results. The maximum error for the CLAWPACK solver is -9.4%, while that for the *rhoCentralFoam* solver is 12.8%. Moreover, as the CLAWPACK solver and the *rhoCentralFoam* solver are based on the HEM, the HEM could be suitable for CO_2 two-phase ejectors under these relevant operating conditions (pressure ranges from 8 to 10 MPa). It can be also noted that regarding the thermodynamic model of Croquer *et al.* [45], and Taslimi Taleghani *et al.* [172], different results are obtained by the same isentropic expansion theory. It means that the accuracy of these two thermodynamic models indeed depends strongly on the accuracy of the EoS (here, the Coolprop and the Refprop databases).

CHAPTER 5

CFD simulations of converging-diverging nozzles

In this chapter, two-phase CO_2 converging-diverging nozzles are investigated using the previous flow solvers coupled with the tabulated EoS and the NSCBC. Such converging-diverging nozzles can be considered as the motive nozzle in a supersonic ejector which is used as a throttling device in a refrigeration cycle. It has been proven that the flow conditions in the motive nozzle have strong effects on the efficiency of the ejector and the refrigeration cycle as well [54]. It was noted that flashing and two-phase shock waves could occur in the converging-diverging nozzle and affect significantly the flow features at the outlet of the nozzle [20]. Experimental investigations of these nozzles have been investigated by Berana *et al.* [20], Nakagawa *et al.* [126]. Their results are used to validate the present CFD results. All the results in this chapter have been already published in [60, 61]. In order to not repeatedly present the numerical set-up and clarify the different cases, a short introduction is given first.

5.1 Introduction to different cases

Several nozzles having different lengthes and diverging angles have been investigated in this chapter. All nozzles are rectangular and the general geometry is depicted in Figure 5.1.

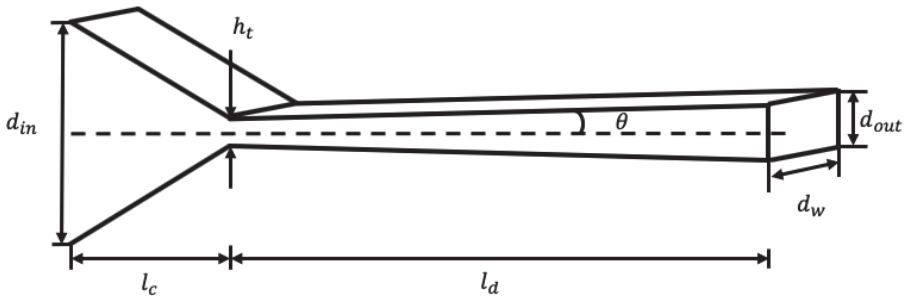

Figure 5.1 Illustration of a converging-diverging Laval nozzle.

The inlet and outlet diameters are denoted by d_{in} and d_{out}, while l_c and l_d represent the lengthes of the converging and diverging parts, respectively. The height at the throat is h_t, while d_w is the depth of the rectangular nozzle. The diverging angle is denoted by θ. The

explicit values of these parameters are summarized in Table 5.1 corresponding to three different nozzles.

Table 5.1 Geometrical parameters of the nozzles of Nakagawa *et al.* [126] and Berana *et al.* [20].

Nozzle	d_{in} [mm]	l_c [mm]	h_t [mm]	l_d [mm]	θ [^{o}]	d_{out} [mm]	d_w [mm]
Nakagawa A	10	27.35	0.24	56.15	0.302	0.84	3
Nakagawa B	10	27.35	0.24	56.15	0.612	1.44	3
Berana	10	15	0.4	8.38	0.48	0.54	1

The inlet boundary conditions are presented in a $p-h$ diagram in Figure 5.2. Three supercritical and three subcritical conditions are investigated. Red symbols in Figure 5.2 present supercritical inlet conditions, while the green ones present subcritical inlet conditions.

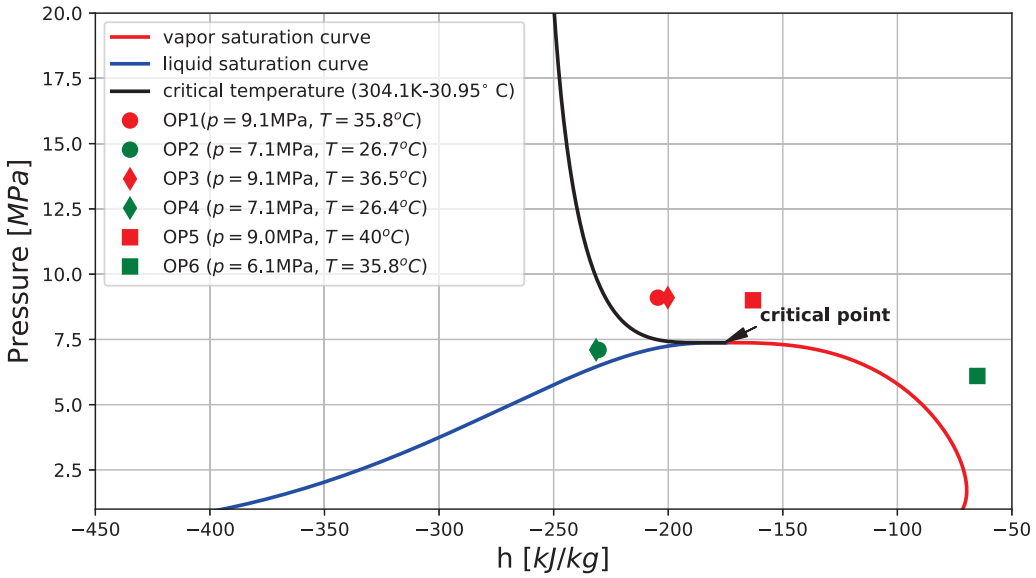

Figure 5.2 Operating conditions in the $p-h$ diagram.

For the outlet boundary condition, a low pressure is initially imposed by using the NSCBC. This pressure is lower than the critical pressure of the nozzle. As a result, the nozzle becomes finally supersonic. When the outlet boundary becomes supersonic, the NSCBC switches to the supersonic mode, in which the target pressure cannot be maintained. The details about the NSCBC are shown in Section 3.4.3. The Courant number is initially set to 0.1 and when the solution is stable, it increases up to 0.4.

The different cases are organized as follows :

- CLAWPACK solver

1. 2D inviscid simulations were performed through the CLAWPACK solver : the Nakagawa nozzle B in the supercritical condition (OP3) and the Nakagawa nozzle A in the supercritical condition (OP1).

- *rhoCentralFoam* solver

1. 2D laminar simulations for nozzles A and B in supercritical (OP1, OP3) and subcritical (OP2, OP4) conditions were performed.

2. Bulk viscosity effect was investigated for the nozzle A in the supercritical condition (OP1).

3. Effects of turbulence and near-wall modelling approaches were investigated for nozzle A in the supercritical condition (OP1) and subcritical conditions (OP2, OP6).

- Berana *et al.*'s nozzle with a shock wave was investigated by using the $k-\omega$ SST model (OP5). The shock wave was analysed and compared to experimental results of Berana *et al.* [20] and numerical results of Raman and Kim [140].

5.2 CLAWPACK solver

The nozzle B is meshed with 50000 structured elements in the whole 2D computational domain. The inlet conditions is OP3. The CO_2 flow is in supercritical state at the inlet and two-phase state at the outlet. The flow reaches the sonic condition near the throat and accelerates until $Ma = 2$ at the outlet. No shock forms in the nozzle. Experimental measurements of pressure were performed by strain gauges and the saturated pressure is also computed by the temperature along the diverging part, which are reported in the work of Nakagawa *et al.* [126]. The comparisons are shown in Figure 5.3.

Good agreements can be seen between the CLAWPACK results, experimental measurements and Isentropic Homogeneous Equilibrium (IHE) results. Moreover, regarding only on the experimental results, the direct pressure measurements away from the throat have small discrepancies to the pressure computed by the temperature. It reveals that the thermodynamic equilibrium hypothesis is less valid far from the throat than close to the throat. It is very strange, because normally the non-equilibrium effects are more important near the throat where the flashing occurs than far from the throat. Hence, more pressure measurements are needed to have an accurate pressure profile along the nozzle. Moreover, the extracting pressure from wall temperature could induce errors and it could lead a

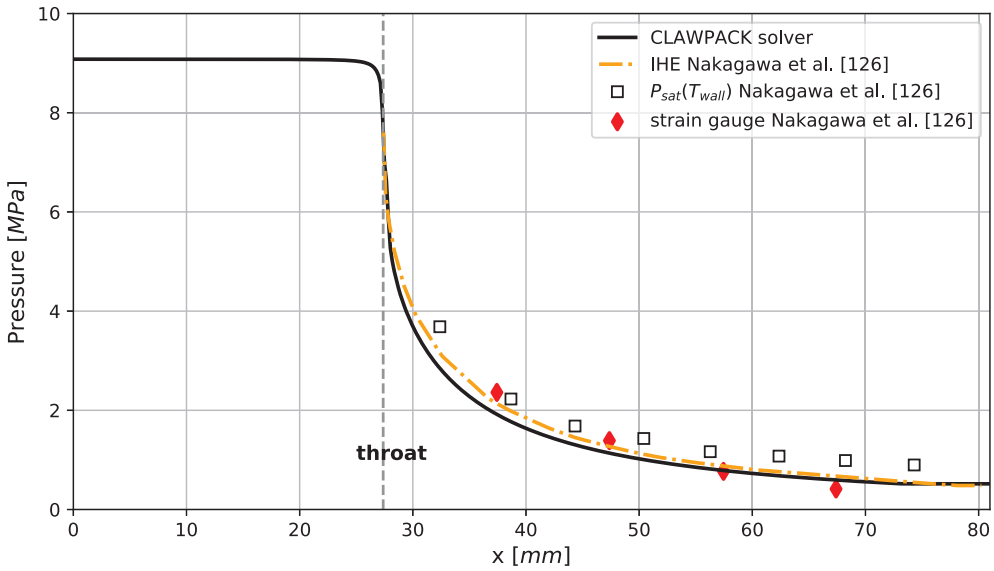

Figure 5.3 Pressure profile along the centerline of the nozzle, compared with pressure measurements and IHE results from Nakagawa *et al.* [126]. Results obtained for Nozzle B and OP3.

misinterpretation of the thermodynamic-equilibrium level. Figure 5.4 displays the Mach number and the vapor quality on the 2D map of the nozzle.

It is observed that the vapor quality changes from 0 to 0.3 at the throat, which indicates the occurrence of the flashing. Consequently, the flow is in two-phase state in the diverging part. The vapor quality continues to increase to 0.5 at the outlet of the nozzle. The Mach number map shows that the flow reaches the sonic condition at the throat and it finally attains $Ma = 2$ at the outlet. Unfortunately, the quality and the Mach are not available in the experiment.

Figure 5.5 shows the pressure profile for the nozzle A in OP1. It can be seen that the pressure shifts compared to the experimental measurements. In fact, the only difference between the nozzle A and the nozzle B is the diverging angle which is 0.306^o for the nozzle A and 0.612^o for the nozzle B. The inlet conditions are nearly the same (see OP1 and OP3 in Figure 5.2).

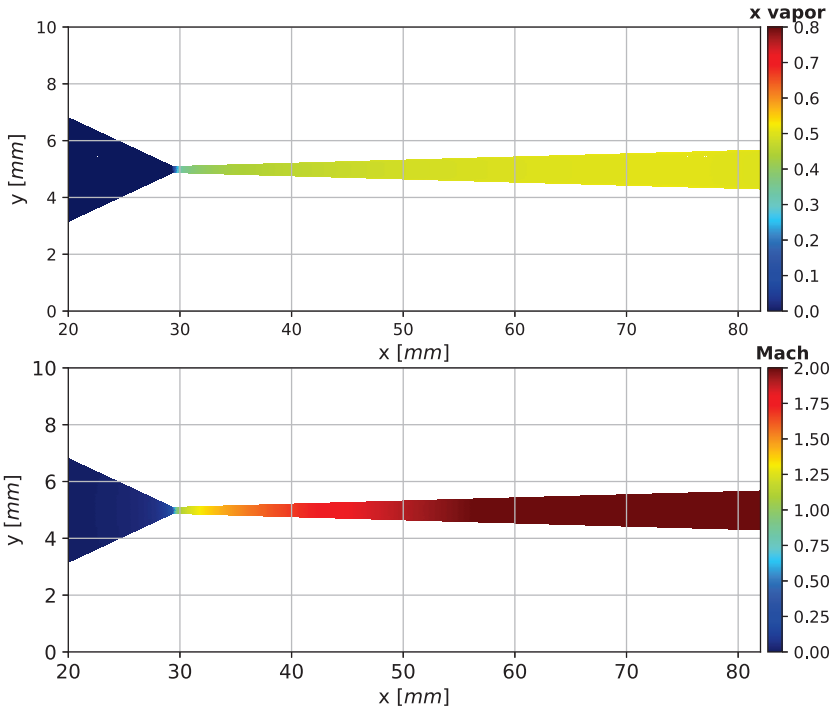

Figure 5.4 Vapor quality and Mach number map from 20 mm to 80 mm. Results obtained for Nozzle B and OP3.

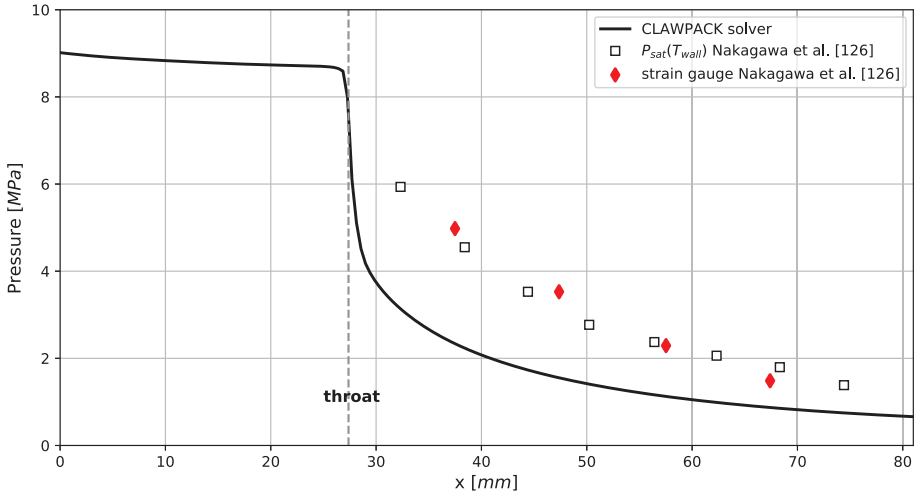

Figure 5.5 Pressure profile along the centerline of the nozzle, compared with pressure measurements by Nakagawa *et al.* [126]. Results obtained for Nozzle A and OP1.

However, the experimental results show a good agreement between the direct pressure measurement and the pressure computed by the temperature, which signifies that the hypothesis of the thermodynamic equilibrium is valid. Indeed, the computation of the pressure through the temperature is in accordance with the thermodynamic equilibrium hypothesis.

In conclusion, it is found that current numerical results have some discrepancies depending on the nozzles. For the nozzle A, we obtain some differences even compared to the pressure computed by the temperature. Hence, before focusing on the thermodynamic non-equilibrium effect, the correctly prediction of the flow field is primarily important. In the following section, a more advanced solver is used to investigate viscosity effects and turbulence model effects.

5.3 *rhoCentralFoam* solver

The *rhoCentralFoam* is a density-based solver based on the OpenFoam library. The solver has been coupled with the tabulated CO_2 table and the NSCBC (in Chapter 3, Section 3.4. A first-order Euler explicit scheme is used for the temporal discretization together with the gauss linear method to compute gradient terms at interfaces. The Gauss linear method is also applied for the divergence and Laplacian terms at interfaces. The "Gauss-Seidel" solver is enabled to solve implicitly the diffusion equation. The *rhoCentralFoam* solver is an unsteady solver. Hence, the steady state is considered to be achieved when the difference in terms of mass flow rate between the inlet and the outlet is below 0.5%.

The two-phase viscosity is computed by using the mixing law based on the vapour quality. It also compared to the mixing laws proposed by Beattie and Whalley [18], Fourar and Bories [66], McAdams *et al.* [120] and undistinguishable results are obtained. These comparisons are not shown here for sake of brevity.

The structured mesh is generated by Gmsh [70] and consists of 11514 elements. The grid convergence has been checked by considering 3 mesh grids composed of 11514, 24804, and 48032 elements, respectively. The 2D calculations are performed for the nozzle A and B on Mammoth Parallel 2b cluster at l'Université de Sherbrooke. The computational time for laminar cases is about 40 hours with 24 CPU in parallel computation, while for cases with the realizable $k-\epsilon$ model, it is about 63 hours with 40 CPU. Simulations with the $k-\omega$ SST model are extremely time-consuming because of the resolution of boundary layer, which take about 690 hours with 480 CPU.

5.3.1 Nakagawa nozzle B

The Nakagawa nozzle B which has the large diverging angle ($\theta = 0.612^o$) is investigated. 2D laminar simulations for the supercritical condition (OP3) and subcritical condition (OP4) are performed. The pressure profile for OP3 is shown in Figure 5.6 and compares to experimental measurements of Nakagawa *et al.* [126], 1D HRM results of Angielczyk *et al.* [7], CLAWPACK solver results and Yazdani *et al.* [196] results.

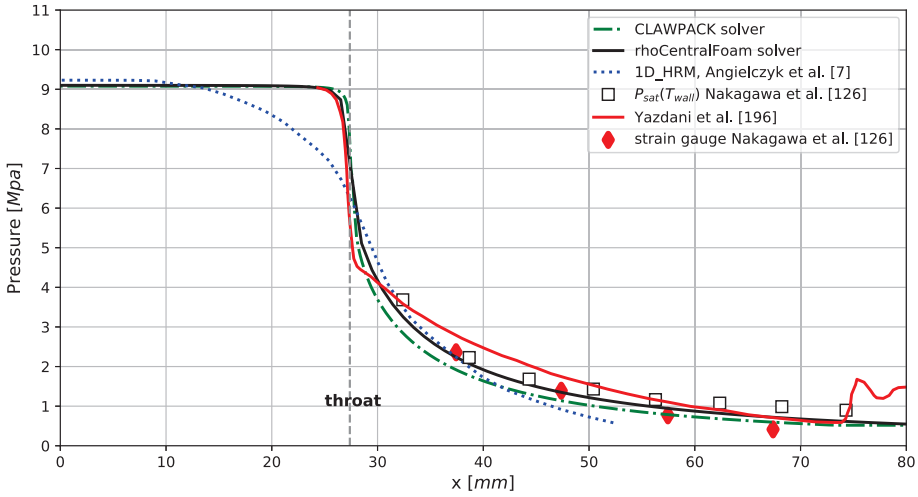

Figure 5.6 Pressure profiles for the nozzle B under supercritical operating condition (OP3). Comparisons between the experimental data of Nakagawa *et al.* [126], the 1D HRM results of Angielczyk *et al.* [7], the CLAWPACK results by [59] and the results of Yazdani *et al.* [196]. Results obtained for Nozzle B and OP3.

Angielczyk *et al.* [7] results (the blue dotted curve) stop at the middle of the diverging part because of the presence of the solid phase due to an overestimation of the expansion rate. On the contrary, the current results (the black curve) continue to the outlet and agree well with the experimental results. Furthermore, when comparing the present results to the CLAWPACK results (the green dash-dot curve), it can be seen that the present results have slightly changes toward the temperature-computed pressure. Hence, viscosity effects have a small improvement between numerical and experimental results which are both based on the thermodynamic equilibrium hypothesis.

Moreover, the results of Yazdani *et al.* [196] (red line) show some differences near the throat and some oscillations at the outlet, which may be attributed to an inappropriate outlet boundary condition. It should be mentioned that even though the pressure profiles are similar between the present results and those of Yazdani *et al.* [196], the vapor volume

fraction, the Mach number, and the streamwise velocity in the diverging part are totally different (compared to Figure 4 in Yazdani *et al.* [196] where a mixture model combining cavitation/boiling model was used). In the present simulation, the vapor starts to create at the throat and the quality has a quasi flat profile at each cross section, while in the results of Yazdani *et al.* [196], the vapor creates primarily near the wall and the vapor quality is minimum at the center of each cross section. It is besides surprising that in [196], the flow firstly becomes supersonic near the wall then at the center of the nozzle.

The subcritical condition (OP4) for the nozzle B is then investigated. The pressure profile is shown in Figure 5.7.

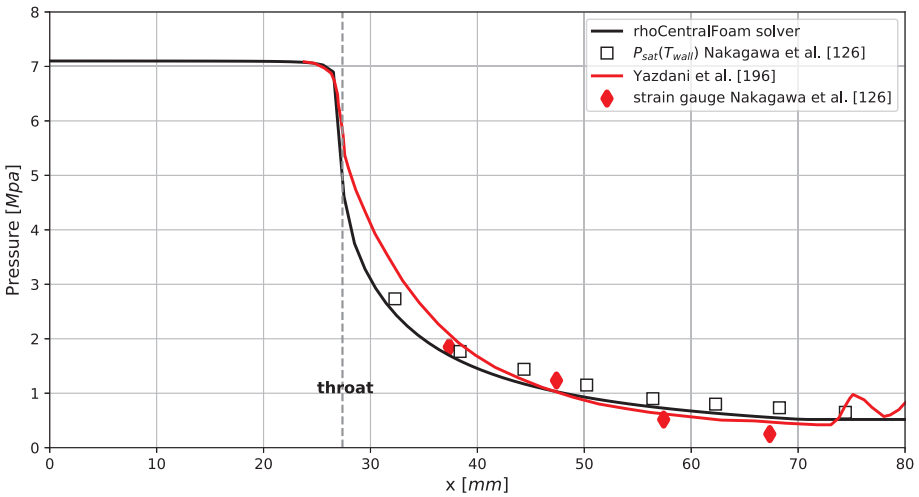

Figure 5.7 Pressure profiles for the nozzle B under the subcritical operating condition (OP4). Comparisons between the experimental data of Nakagawa *et al.* [126] and the results of Yazdani *et al.* [196]. Results obtained for Nozzle B and OP4.

Again, a good agreement is obtained for the nozzle B under the subcritical condition (OP4). It seems that the present numerical approach is appropriate for predicting two-phase CO_2 flows in a converging-diverging nozzle. Moreover, some oscillations near the outlet are still observed in the results of Yazdani *et al.* [196].

5.3.2 Nakagawa nozzle A

In order to find if viscosity effects have significant influences on nozzle, 2D laminar simulations of the nozzle A in supercritical (OP1) and subcritical (OP2) conditions are performed. In Figure 5.8(a), the *rhoCentralFoam* results (the solid black curve) are compared to the results of Angielczyk *et al.* [7] (the blue dotted curve), the CLAWPACK

results (the green dot-dashed curve), and the Nakagawa *et al.* [126] measurements for the supercritical condition (OP1). The HRM of Angielczyk *et al.* [7] predicts the flashing starting before the throat, while the HEM predicts the flashing at the throat when saturation conditions are met. Furthermore, it seems that the HRM predicts better the pressure profile near the throat than the HEM model. However, it can not ensure that the HRM is more physically appropriate, because the HRM indeed improve the results toward to the experimental results based on the thermodynamic equilibrium hypothesis. When comparing the CLAWPACK results to those of *rhoCentralFoam* results, which are both based on the thermodynamic equilibrium, significant improvements are obtained which is mainly due to viscosity effects. Nevertheless, there are still discrepancies compared to the experimental measurements (in Figure 5.8(a)). According to the direct pressure measurement and temperature-computed pressure, the thermodynamic equilibrium hypothesis is still valid.

The subcritical condition (OP2) for the nozzle A is shown in Figure 5.8(b). Similar results can be observed also in Figure 5.8(a). There are still some discrepancies compared to the experimental results. Besides, Figure 5.8(b) shows an abrupt change of the experimental pressure profile between second and third points in the diverging part. Hence, uncertainties of the experimental measurement may also have influences. Unfortunately uncertainties of experimental measurement are not reported by Nakagawa *et al.* [126].

The maximum discrepancies between the laminar cases and the experimental measurements for both cases (OP1 and OP2) are summarized in Table 5.2.

Table 5.2 Maximum discrepancies between the numerical and experimental results for four cases.

Cases	Max diff to measured pressures (%)	Max diff to saturated pressures (%)
A(OP1) supercritical	34	28
A(OP2) subcritical	31	33
B(OP3) supercritical	14	16
B(OP4) subcritical	17	11

It can be seen that for the nozzle A, under the supercritical and subcritical conditions, the discrepancies are both larger than those for the nozzle B. It seems that the discrepancies are related to the nozzle rather than operating conditions (either supercritical or subcritical conditions). Hence, effects related to fluid dynamics should be highlighted. In the following section, the investigation of the Bulk viscosity effect and the effect of turbulence models are investigated.

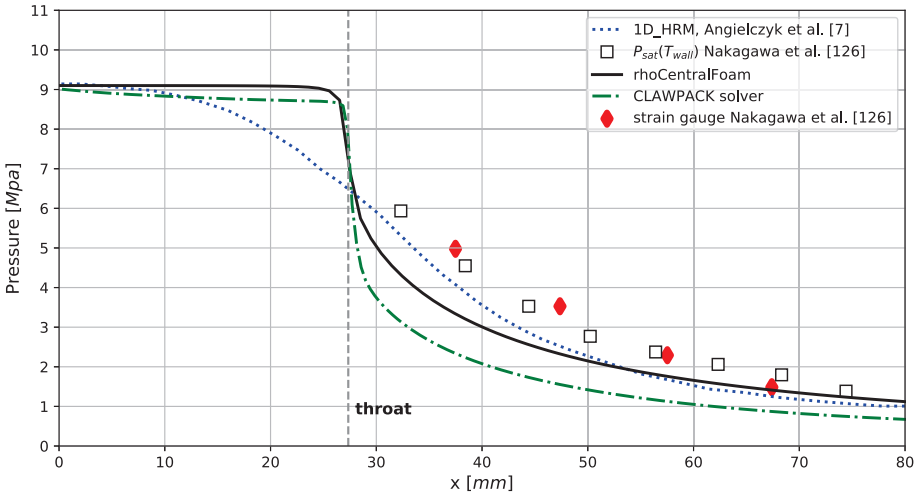

(a)

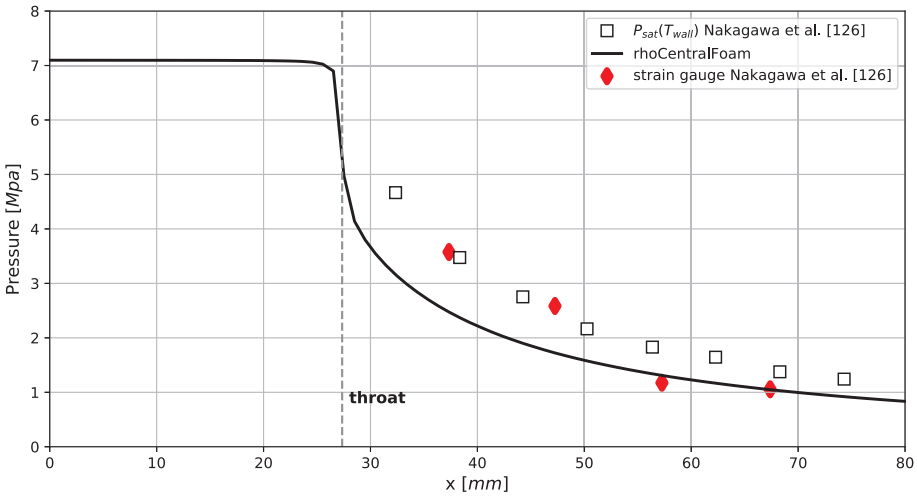

(b)

Figure 5.8 (a) Pressure profiles for the nozzle A under the supercritical operating condition (OP1). Comparisons between the experimental data of Nakagawa *et al.* [126], the 1D HRM results of Angielczyk *et al.* [7], the CLAWPACK results and the *rhoCentralFoam* results. (b) Pressure profiles for the nozzle A under the subcritical operating condition (OP2). Comparisons between the experimental data of Nakagawa *et al.* [126] and the *rhoCentralFoam* results. Results obtained for Nozzle A, OP1 and OP2.

5.3.3 Bulk viscosity effect

The bulk viscosity is usually neglected for most of the fluids. However, it may have significant influence for supersonic CO_2 flows. It has been investigated by Cramer [41], Emanuel [56], Tisza [174] and a significant impact on numerical results has been found. However, the

main problem is that there does not exist an universal law to describe the bulk viscosity. In this section, the bulk viscosity is considered in the simulation of the Nakagawa nozzle A in the supercritical condition (OP1). Two values of the relaxation time, $\tau = 10^{-5}$ and $\tau = 5 \times 10^{-6}$ have been used in a bulk viscosity model. Note that, for $\tau \geq 10^{-5}$, numerical instabilities are encountered. The implementation is shown in Chapter 3 , Section 3.4.2. Figure 5.9 displays the corresponding pressure and vapor quality profiles.

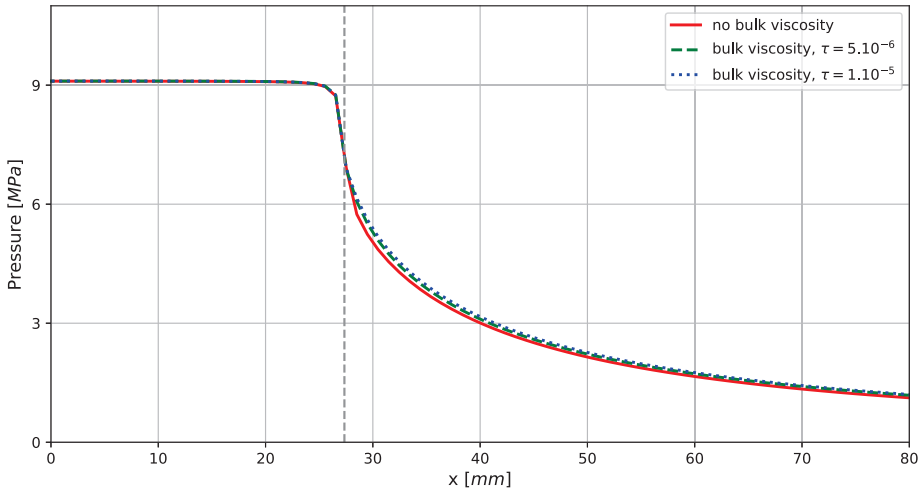

(a)

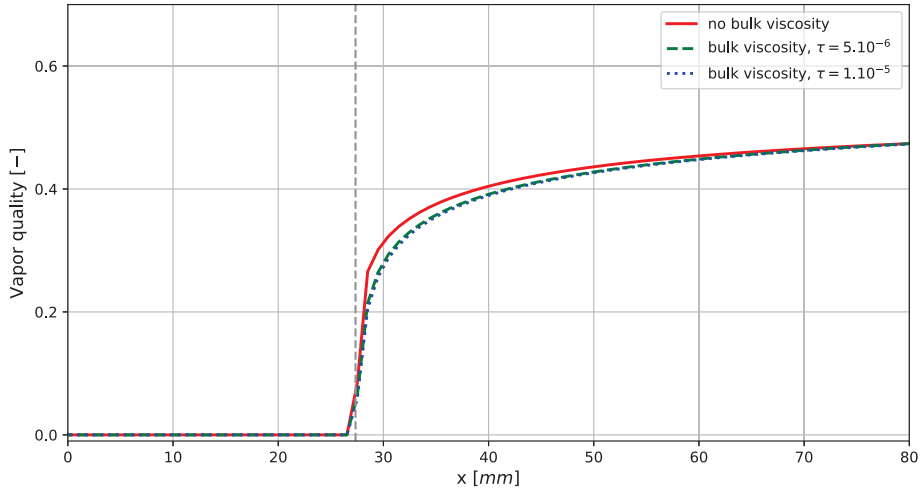

(b)

Figure 5.9 Pressure and vapor quality distributions along the streamwise direction for the nozzle A under the supercritical condition (OP1). Results obtained for Nozzle A and OP1.

A slight difference in terms of pressure and vapor quality can be observed near the throat. However, the improvement is not significant. Moreover, it is observed that the location of the flashing is not affected. In conclusion, the bulk viscosity has no noticeable effect on the flow in this condition. However, maybe if a strong compression or expansion occurs, e.g. shock waves, more significant effects could be expected.

5.3.4 Effects of turbulence and near-wall modelling

2D Reynolds-averaged Navier–Stokes (RANS) simulations have been carried out. The realizable $k-\varepsilon$ model with the standard wall function and the $k-\omega$ SST model are compared in the case of OP1. A structured mesh composed of 89072 elements is used for the realizable $k-\varepsilon$ model, which implies a maximum wall coordinate y^+ around 65. The $k-\omega$ SST model is associated with a structured mesh composed of 926054 elements to guarantee that the maximum of y^+ remains smaller than 1, in order to fully resolve the wall boundary layer.

Figure 5.10(a) displays the pressure profiles obtained by the realizable $k-\varepsilon$ and $k-\omega$ SST turbulence models (OP1). The measurements of Nakagawa *et al.* [126] are also compared. It can be seen that the $k-\omega$ SST model improves significantly the pressure profile compared to the realizable $k-\varepsilon$ model. The pressure distribution agrees particularly well with the experimental measurements after the throat, whereas the realizable $k-\varepsilon$ model predicts the similar profile as the previous laminar case, which underestimating the pressure along the diverging part (Figure 5.8(a)). To explain that, one should recall that the $k-\omega$ SST model is a two-equation eddy-viscosity model, which combines a $k-\omega$ formulation in the inner parts of the boundary layer and a standard $k-\varepsilon$ in the bulk region. Hence, there are two possible explanations for the best behavior of the $k-\omega$ SST model : (i) it is known to produce too large turbulence intensities in flow regions with strong acceleration but still less than the $k-\varepsilon$ model ; (ii) it exhibits an inherent correct asymptotic behavior near walls, without wall function. So it points out the prime importance to well resolve the boundary layer development along the walls rather than finding explanation for discrepancies into the thermodynamic model only.

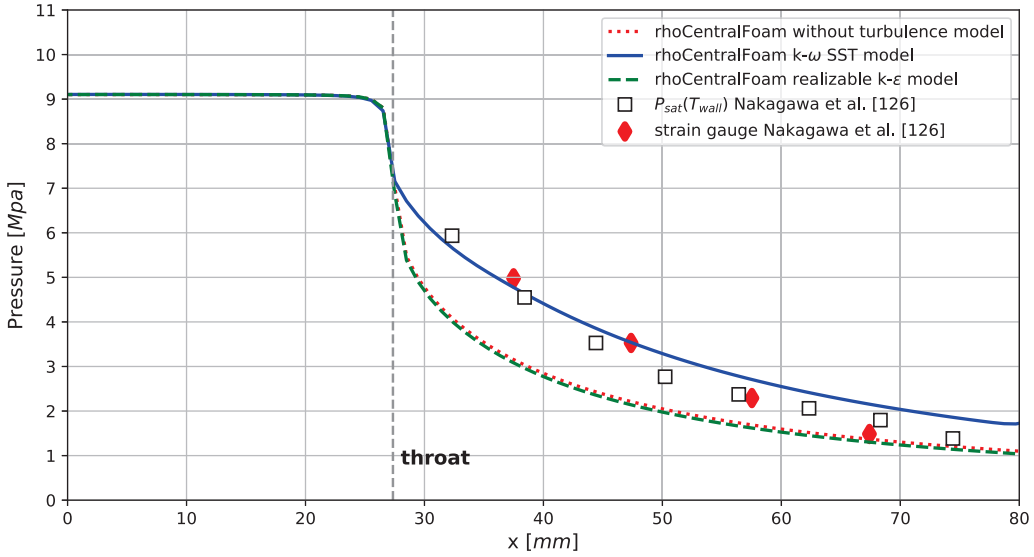

(a)

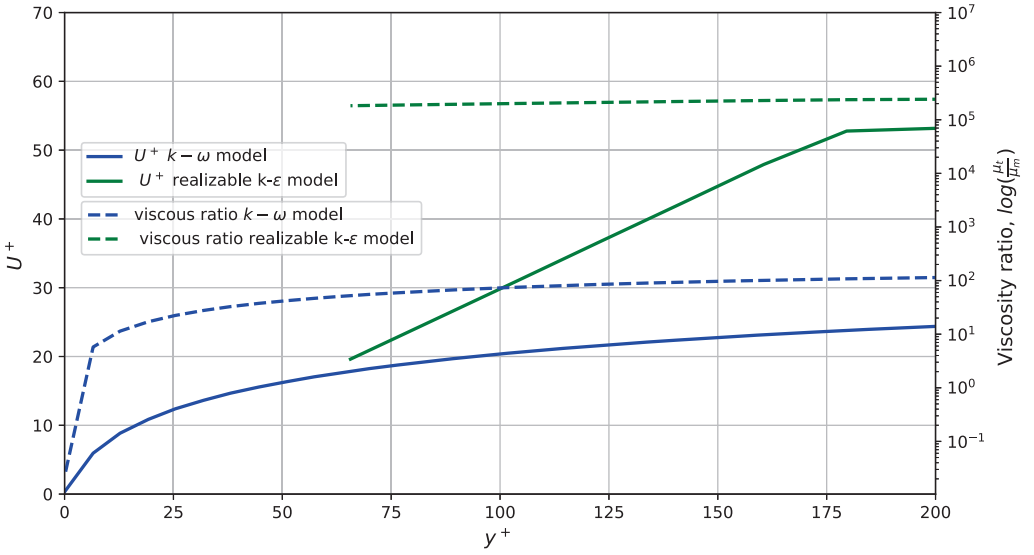

(b)

Figure 5.10 (a) Streamwise profiles of pressure obtained by the realizable $k-\varepsilon$ and $k-\omega$ SST turbulence models for the nozzle A under supercritical conditions (OP1). (b) dimensionless velocity and viscosity ratio for the realizable $k-\varepsilon$ and $k-\omega$ SST turbulence models. Results obtained for Nozzle A and OP1.

In the present case, the flow inside the nozzle is fully turbulent with the Reynolds number about 10^6 around the throat. At such a high Reynolds number, the realizable $k-\varepsilon$ model overdissipates with a viscosity ratio between turbulent viscosity and laminar viscosity, μ_t/μ_m around 10^5, whereas μ_t/μ_m for the $k-\omega$ SST closure is around 10^2 at this particular

streamwise position, $x = 28mm$ just after the throat (Figure5.10(b)). The extremely high numerical dissipation of the realizable $k-\varepsilon$ model results in a thicker boundary layer. By conservation of mass, the streamwise velocity close to the symmetry plane is then much higher than the one predicted by the $k-\omega$ SST. Thus, it explains the underprediction of the pressure by the realizable $k-\varepsilon$ previously observed. Moreover, the nozzle throat is quite narrow (total height is 0.24 mm). Hence, the boundary layer could occupy a large fraction of the duct and may give a significant effect. It can be seen in Figure 5.10(b) that the $k-\omega$ SST model predicts a thin boundary layer. It results in the different pressure distribution in Figure 5.10(a). For the simulation applying the realizable $k-\varepsilon$, the wall function is used, which cannot accurately predict the boundary layer for this case. Though using wall functions benefits a significant gain of computation time, it should be carefully assessed according to the case.

The following figures, Figures 5.11(a) and 5.11(b) show simulations with the $k-\omega$ SST model for subcritical conditions (OP2, OP6). $k-\epsilon$ cases are not performed for these conditions. Nevertheless, we can still verify if subcritical conditions give different results.

In Figure 5.11(a), the case with the $k-\omega$ SST model gives a significant improvement compared to the laminar case. In Figure 5.11(b), the present results shows a good agreement to the temperature-computed pressure. Hence, the accurate resolution of fluid dynamics is very important such as capturing the boundary layer and it seems that the HEM could be suitable for two-phase CO_2 simulation in a converging-diverging nozzle.

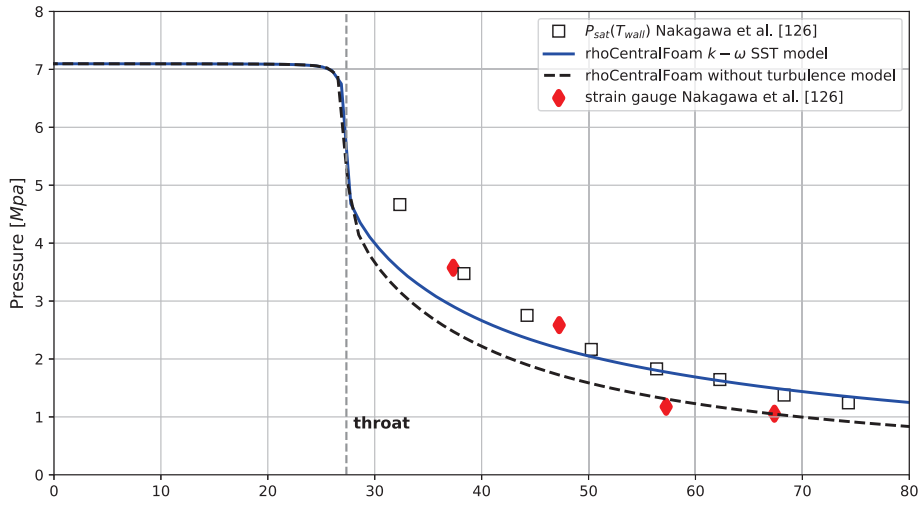

(a)

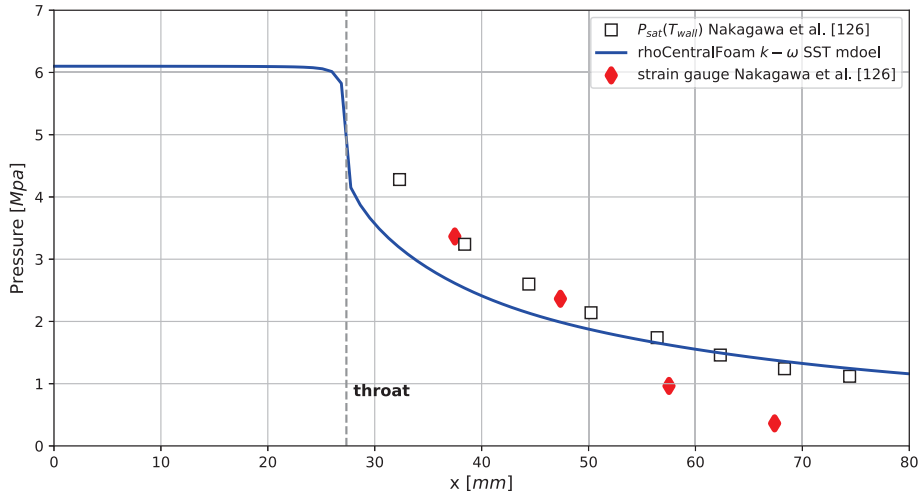

(b)

Figure 5.11 (a) Pressure profile for the nozzle A under subcritical condition (OP2) compared to the laminar case and the results of Nakagawa *et al.* [126]. (b) Pressure profile for Nozzle A under subcritical condition (OP6) compared to the results of Nakagawa *et al.* [126]. Results obtained for Nozzle A and OP2 and OP6.

5.4 Shock wave in the Berana's nozzle

A 2D RANS simulation with the $k-\omega$ SST model has been performed for the nozzle of Berana *et al.* [20] under a supercritical condition (OP5). The main difference compared to the cases of Nakagawa *et al.* [126] is that the pressure at outlet is set to higher than the critical pressure. As a result, a shock wave occurs in the converging-diverging nozzle. The strength and the location of shock waves are completely determined by flow conditions. The pressure profile along the center line of the nozzle is shown in Figure 5.12 compared to the experimental results. It should be noted that in this experiment, the pressure is computed by the wall temperature measurement instead of direct pressure measurements. As a result, the experimental results correspond to HEM assumptions.

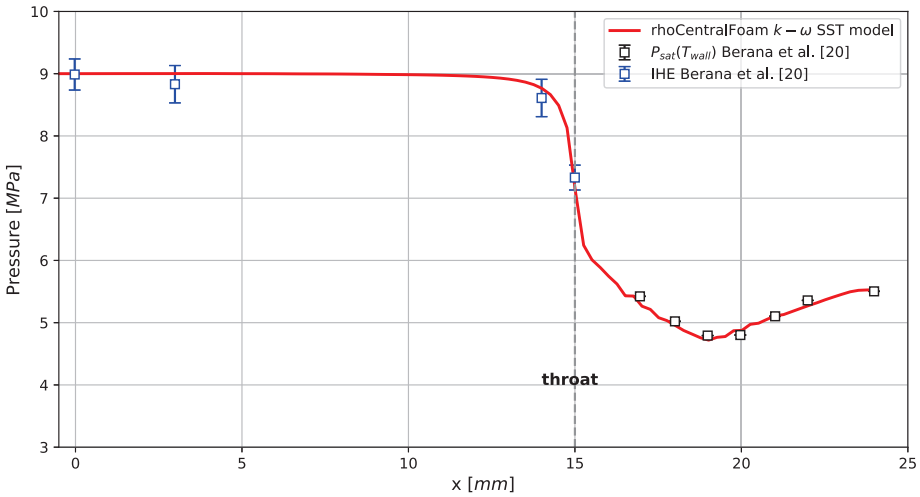

Figure 5.12 Pressure profile along the centerline of the nozzle compared to experimental results of Berana *et al.* [20]. The operating condition is $p = 9$ MPa and $T = 40^oC$ at the inlet and $p = 5.51$ MPa at the outlet (OP5). Results obtained for OP5.

The blue squares located in the converging part illustrate the isentropic calculation from Berana *et al.* [20], in which uncertainties depend on the pressure measurement at the inlet as well as the temperature measurement. As a result, the uncertainty of the pressure measurement at the inlet propagates to the throat. Conversely, black squares located in the diverging part are directly computed by the temperature measurement by assuming the saturation condition, where errors are small. A good agreement is obtained between the current numerical results and the experimental results of Berana *et al.* [20]. The shock is predicted to start around $x = 19$ mm and to finish at the outlet.

In order to clearly visualise this shock wave, the map of the density gradient in the x-direction is show in Figure 5.13. It can be seen that this shock wave in this CO_2 two-phase flow is extremely thick compared to the general normal or oblique shock in single-phase flows. As a consequence, the pressure and velocity gradients through the shock are rather small. Moreover some shock structures in the core of this thick shock is also captured, which may be due to the interaction between acoustic waves and the boundary layer.

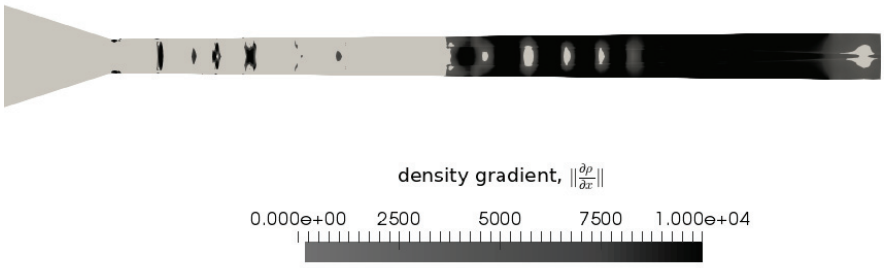

Figure 5.13 Density gradient map, $\|\frac{\partial \rho}{\partial x}\|$ zooming at the diverging part of the nozzle. Results obtained for OP5.

Figure 5.14 shows the profile of Mach number and void fraction along the nozzle. According to the void fraction, the topology of the two-phase flow after the flashing can be predicted which is probably continuous vapor phase containing liquid droplets. Through the shock, liquid (droplets) is created by the condensation. The void fraction varies from 0.88 to 0.82 across the shock wave, meanwhile the Mach number drops gradually. It can be noted that the Mach number is still higher than one in the core of the flow, which is different to a normal or oblique shock. In this case, it is often called 'condensation shock'.

The void fractions along the y-direction at the location of the throat, before the shock, and after the shock are presented in Figure 5.15. It can be seen that near the wall there is more vapor than that in the core of the flow. The condensation is also observed which corresponds to the shift from the red dashed curve to the blue dot-dashed curve.

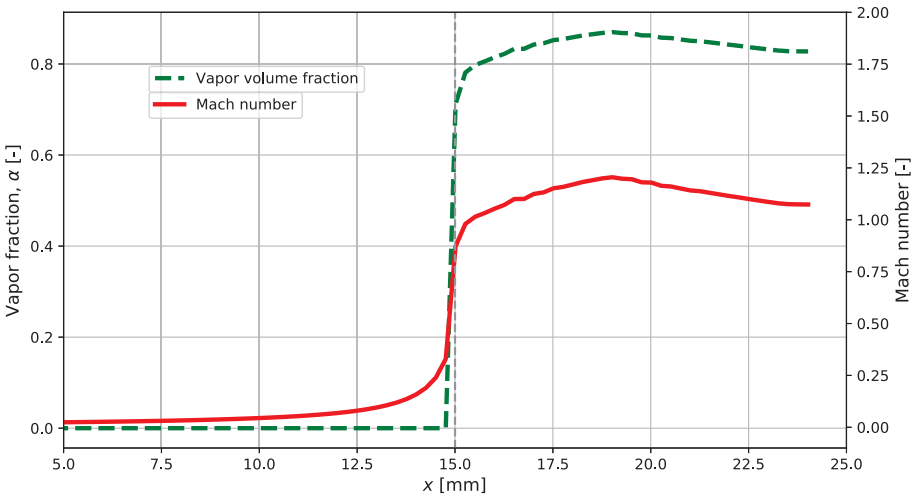

Figure 5.14 Mach number (red solid line) and void fraction (green dashed line) distributions along the nozzle of Berana *et al.* [20] for OP5.

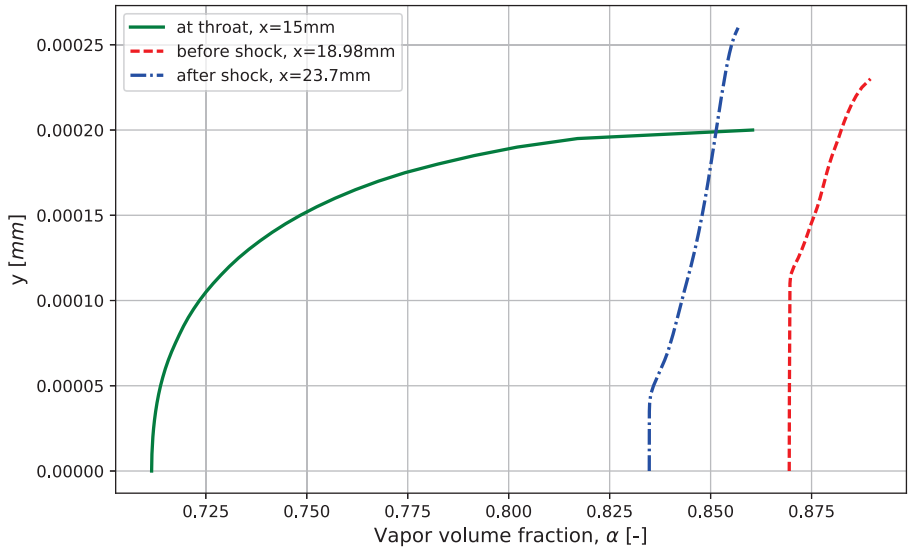

Figure 5.15 Void fraction in the y-direction at $x = 15$ mm (green solid line), 17 mm (red dashed line), and 23.7 mm (blue dot-dashed line). Results for OP5.

In the following, characteristic parameters of this thick shock wave are computed and compared to the experimental results [20]. Firstly, the shock thickness is defined as the difference between the front and back of the shock wave, which is :

$$\delta = x_2 - x_1, \tag{5.1}$$

where x_2 and x_1 are the locations after and before the shock wave, respectively. For the experimental results, the shock location is estimated depending on the pressure measurements. Secondly, the shock strength is computed as the pressure ratio through the shock, which reads :

$$\gamma = \frac{p_2}{p_1}. \tag{5.2}$$

Thirdly, the total pressure loss reads :

$$\beta = \frac{p_{02} - p_{01}}{p_{01}}, \tag{5.3}$$

where p_{02} and p_{01} denote the total pressure after and before the shock wave. Finally, the entropy change, Δs is also computed as the difference of the entropy across the shock wave. It should be noted that the mixture entropy is considered here. Hence, the vapor and liquid entropies are primarily computed, and then the mixture entropy is determined by the mixing law based on the quality (i.e. $s_m = xs_v + (1-x)s_l$). Table 5.3 summarizes the results for δ, β, γ, and Δs compared to experiments.

Table 5.3 Characteristic parameters of the shock wave.

Parameters	present simulations	experiment [20]	Relative difference [%]
δ [mm]	4.03	4.02	0.2
γ [-]	1.13	1.15	1.7
β [%]	8.5	-	-
$\Delta s[J.(kg.K)^{-1}]$	6.08	-	-

The thickness is well predicted compared to the experimental measurements with a relative difference of 0.2%. Considering the strength of the shock wave (γ), 1.7% of difference is obtained compared to the experimental measurement. The total pressure loss of 8.5% is obtained while the difference of the mixture entropy through the shock is 6.08 $[J.kg^{-1}K^{-1}]$. However, due to the experimental limitation, these two parameters cannot be compared.

Furthermore, Raman and Kim [140] have performed simulations for the same converging-diverging nozzle using the gas dynamic equations. However, the minimum back pressure ratio (the ratio between the outlet pressure and the inlet pressure) in Raman and Kim [140] work is 0.68. However, it is 0.61 for the present operating condition. Therefore, results cannot be directly compared, but regarding the linearity of results of Raman and Kim [140], the trend can be predicted. In fact, gas dynamic simulations without considering viscosity and turbulence model predict a normal shock which has at least 2 times stronger in terms of shock strength, 1.5 times higher in terms of total pressure loss, and 7 times more entropy generation.

CHAPTER 6

RANS simulations of a two-phase CO_2 ejector

A novel numerical approach has been developed combining a density-based solver, a tabulated real gas EoS, and the NSCBC boundary treatment. It has been validated and verified through different benchmark cases (Chapter 4). Furthermore, the CFD simulations have been performed through the developed numerical approach to investigate converging-diverging nozzles under supercritical and subcritical conditions (Chapter 5). In this chapter, we investigate a two-phase CO_2 ejector using the same numerical approach. The RANS simulations of the two-phase CO_2 ejector of Li *et al.* [110] have been performed to understand the complex phenomena such as shock waves, the mixing between the primary and secondary streams and the choking condition.

It can be seen in Chapter 5 that in order to resolve the boundary layers of a converging-diverging nozzle, the mesh is extremely refined near the walls. As a result, a large number of mesh elements are computed. Through OpenFoam library, we can decompose the mesh and compute these subdomains in parallel to reduce the computational time. However, the main issue remains the time step. Considering an explicit compressible solver (*rhoCentralFoam* solver), the time step relies on the CFL number, the minimum mesh size, the local velocity, and the local speed of sound. The CFL number is usually small (CFL $\sim \theta(1)$) to guarantee the stability of the numerical scheme. Therefore, the finer the mesh, the smaller the time step. Moreover, compared to the simulation of an air ejector, the density of supercritical/two-phase CO_2 is 300 to 600 times higher than air. Hence, to obtain the same y^+ with the same velocity, the mesh size is at least 10 times smaller for the two-phase CO_2 simulations. It means that the time step for two-phase CO_2 simulations is 10 times smaller than that for an air ejector simulation. The time step can easily reach 10^{-9} to 10^{-10} which makes the simulation extremely time-consuming.

The objective of this chapter is to conduct the first simulations of an entire ejector based on the developed model and extend the exergy tube and chocking analyses developed recently by Lamberts *et al.* [100, 101] for air ejectors. To this end, the realizable $k-\epsilon$ model combined with a wall function is used for all the simulations, which requires a much coarser mesh and allows a larger time step.

6.1 Geometry and numerical set-up

Two-dimensional simulations of the two-phase CO_2 flow within the ejector of Li *et al.* [110] were performed. The ejector has a rectangular cross-section which is designed for visualization purpose. The geometrical parameters are shown in Table 6.1.

Table 6.1 Geometry parameters of the ejector of Li *et al.* [110]. Dimensions are given in millimeters.

h_{in}	h_t	l_c	l_d	h_{mix}	l_{mix}	l_{diff}	h_{out}	l_{NXP}	h_{sec}	d_{prim}	d
8	0.49	17.85	11.5	2.82	38	30.5	10	8.4	8	0.78	1.78

The height is denoted by h, while the depth and the length are denoted by d and l, respectively. The primary inlet, converging part, diverging part and throat use the subscripts 'in', 'c', 'd', 't', respectively. The primary nozzle, mixing duct, diffuser, and outlet of the ejector use the subscripts 'prim', 'mix', 'diff', 'out'. The subscript 'NXP' denotes the distance between the primary nozzle exit position and the mixing duct inlet. The depth of the primary nozzle is 0.78 mm, while the depth of the rest of the ejector is 1.78 mm. Besides, the ejector depths are comparable to the ejector heights. Therefore, significant 3D effects could be expected [119]. As a result, the boundary layers along the lateral walls may have an influence and the jet expanding beyond the primary nozzle has a 3D average velocity field. However, such effects cannot be accounted for in the present 2D simulations. Nevertheless, it can be anticipated that the velocity could be overestimated, because the boundary layers along the lateral walls could decelerate the entire flow. Since the velocity is overestimated, the pressure could be underestimated. Similarly, the mass flow rate could be also overestimated, because the velocity is overestimated and the density and the cross-sectional area are constant.

The structured mesh was generated by Gmsh [70] on half of the 2D geometry. A total of 171212 elements were generated to have $y^+ \geq 60$. The CFL number is set to 0.1 to guarantee the good stability of the solver [76]. Two inlet operating conditions were considered to obtain two characteristic curves of the ejector by changing the back pressure. In Figure 6.1, the black points show the operating condition with $p = 10$ MPa, $T = 311.33$ K at the primary inlet and $p = 3.91$ MPa, $T = 295.82$ K at the secondary inlet, while the green squares present the operating condition with $p = 8$ MPa, $T = 281.84$ K at the primary inlet and $p = 3.17$ MPa, $T = 296.09$ K at the secondary inlet.

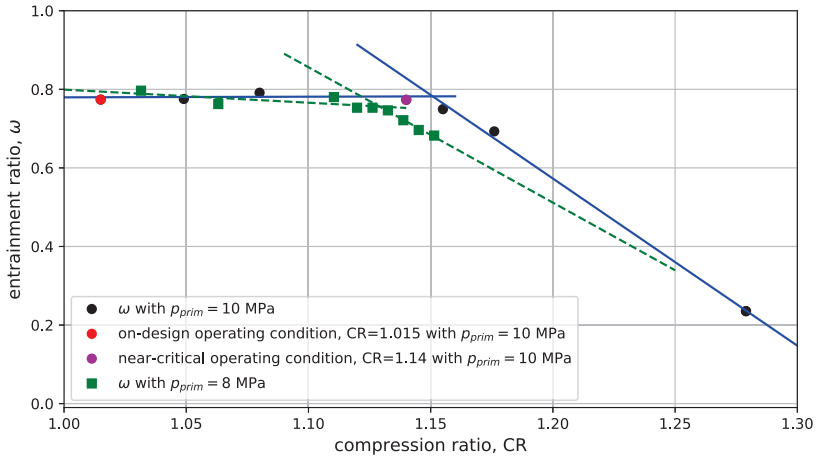

Figure 6.1 Characteristic curves of the ejector with the primary pressure $p = 10$ MPa and $p = 8$ MPa.

Linear regression was carried out to find the critical point of the characteristic curve. The intersection of the blue lines shows the critical point for the conditions with the primary pressure, $p_{prim} = 10$ MPa. Likewise, the intersection of the dashed green lines presents the critical point for the conditions with the primary pressure, $p_{prim} = 8$ MPa. The characteristic curve with $p_{prim} = 10$ MPa has a slightly wider range of the on-design regime than that with $p_{prim} = 8$ MPa. Moreover, the entrainment ratios seem to be similar for these two characteristic curves under on-design conditions.

In the following, we focus on one on-design operating condition which is shown in Figure 6.1. The primary inlet pressure is 10 MPa, the secondary inlet pressure is 3.17 MPa, and the back pressure is 3.971 MPa. The compression ratio of this on-design condition is very low ($CR = 1.015$). Compared to the experiment of Li *et al.* [110], the primary mass flow rate is predicted as 21.7 $g.s^{-1}$ considering the depth equal to 0.78 mm, which corresponds to a 0.46% discrepancy. However, the secondary mass flow rate is predicted as 19 $g.s^{-1}$ with the depth equal to 0.78 mm, which is far from the experimental value 9.98 $g.s^{-1}$. As mentioned above, this could be due to 3D effects. The structure of the flow in the experiment is strongly 3D and cannot be accounted for in this 2D simulation.

6.2 Flow fields

First, the density gradient in the x-direction is shown in Figure 6.2. The outlet of the primary nozzle and the beginning of the diffuser are highlighted in Figures 6.2(b) and (c). The black curve illustrates the sonic line.

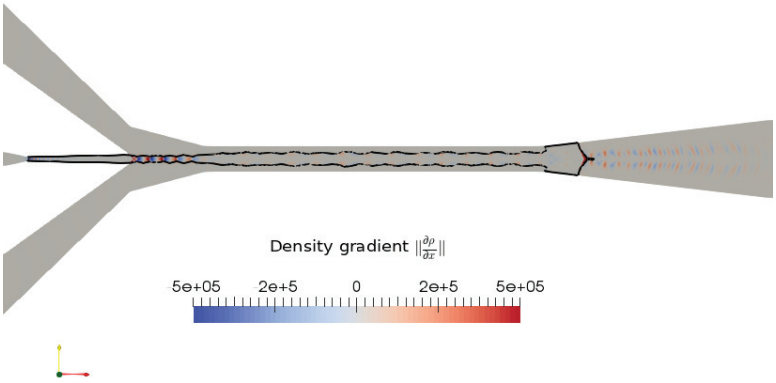

(a)

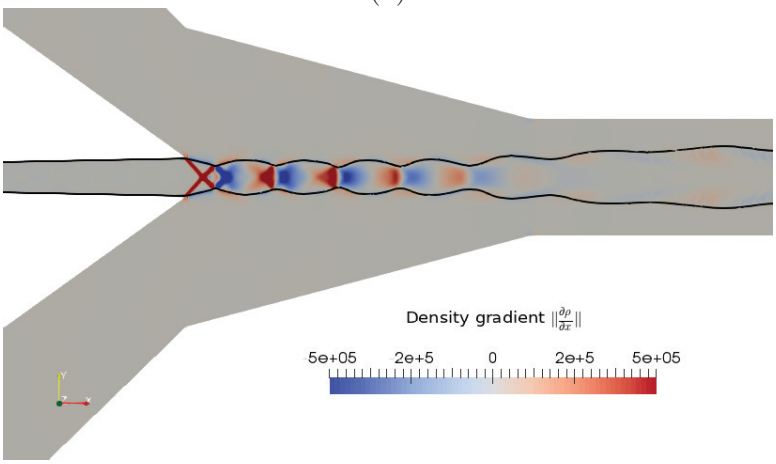

(b)

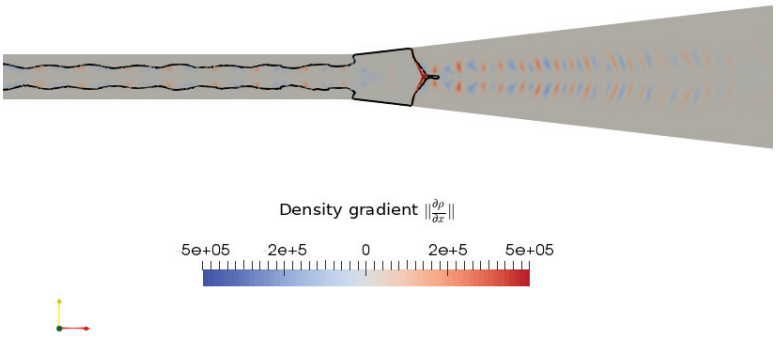

(c)

Figure 6.2 Density gradient map, $\|\frac{\partial \rho}{\partial x}\|$. The outlet of the primary nozzle and beginning of the diffuser are shown in (b) and (c). The black curve illustrates the sonic line.

A shock train is observed at the outlet of the primary nozzle, which is caused by the interaction between the primary supersonic flow and the secondary subsonic flow. The density changes alternatively across the shock waves and expansion waves. Then, the supersonic flow from the primary nozzle mixes with the subsonic flow from the secondary inlet in the mixing duct and the whole flow becomes fully supersonic at the end of the mixing duct. Thereafter, the flow decelerates and becomes subsonic across a strong oblique shock, which appears at the beginning of the diffuser. Additionally, some acoustic waves can be visible after the oblique shock.

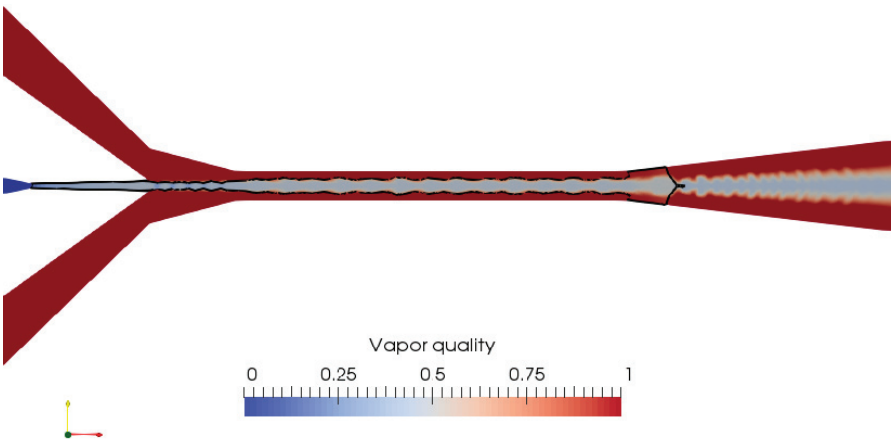

(a)

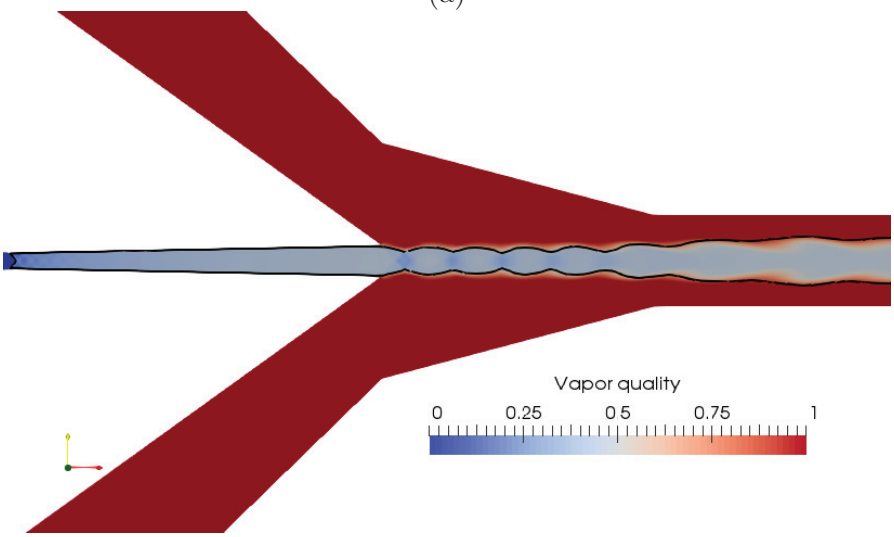

(b)

Figure 6.3 Vapor quality map. The dividing part and outlet of the primary nozzle are highlighted. The black curve illustrates the sonic line.

The vapor quality map is displayed in Figure 6.3. One observes that the flashing occurs at the primary nozzle throat. Consequently, the primary flow becomes two-phase. The vapor quality at the outlet of the primary nozzle is about 0.41. Furthermore, in Figure 6.3, the pure vapor phase remains near the wall along the ejector, while the two-phase mixture lays in the core of the ejector. Moreover, a weak condensation is observed in the shock train.

The temperature map is shown in Figure 6.4. In the primary nozzle, the temperature decreases to 263 K due to the flashing. In the mixing duct, the temperature is almost homogeneous and it decreases brutally before the oblique shock due to the local acceleration. After the oblique shock, a thermal layer arises, which corresponds to the pure vapor phase near the ejector wall. It can be observed through the iso-vapor quality line (the red line with $x = 1$) shown in Figure 6.4.

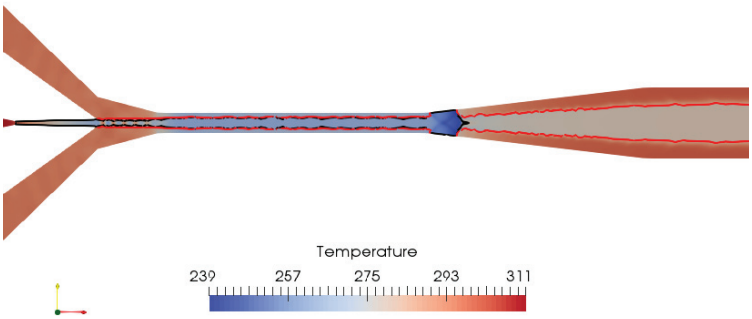

(a)

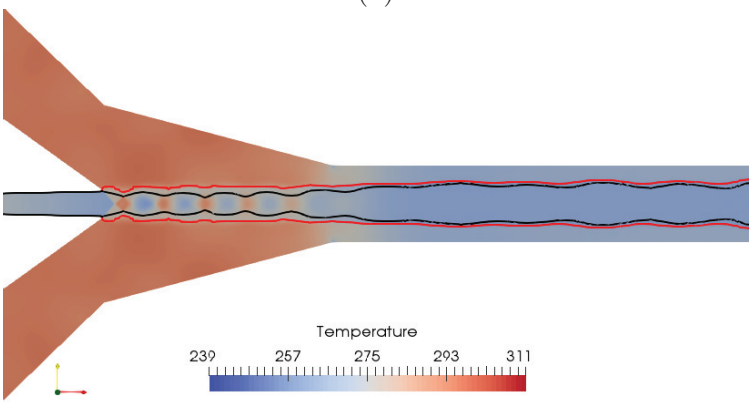

(b)

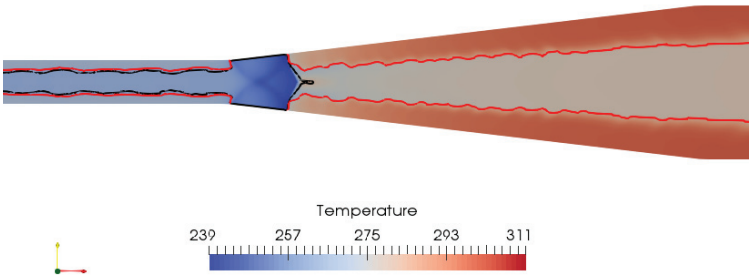

(c)

Figure 6.4 Temperature map of the ejector. The outlet of the primary nozzle and beginning of the diffuser are highlighted in (b) and (c). The black curve illustrates the sonic line and the red curve shows the iso-vapor quality line ($x = 1$).

6.3 Exergy analysis in the secondary stream tube

In this section, we applied the exergy tube analysis proposed by Lamberts *et al.* [100] for the secondary stream tube in order to understand the mixing between the primary and secondary streams. In the following, the total exergy is always considered instead of the exergy to take the local acceleration into account. In 2D, the secondary stream tube is formed by the ejector wall and the dividing streamline (Figure 3.15). The construction process of the dividing streamline is described in Section 3.6.1. By definition, on average, there is no mass flux across the dividing streamline. However, other quantities, such as the total exergy, kinetic energy, heat flux can be transferred across the dividing streamline. The total exergy transport equation is rewritten as (Equation (3.90)) :

$$\begin{aligned} &\frac{\partial}{\partial x_j}\left[\rho\xi_t u_j + (q_j + q_j^t)\left(1 - \frac{T_{ref}}{T}\right) - \tau_{ij}u_i - \tau_{ij}^t u_i\right] \\ &= -T_{ref}\left(\frac{\Phi}{T} + \frac{\Phi_\Theta}{T^2}\right), \end{aligned} \tag{6.1}$$

where the exergy destruction terms, Φ and Φ_Θ are expressed as :

$$\Phi = \tau_{ij}\frac{\partial u_i}{\partial x_j} + \tau_{ij}^t\frac{\partial u_i}{\partial x_j}, \tag{6.2}$$

$$\Phi_\Theta = -\left(q_j + q_j^t\right)\left(\frac{\partial T}{\partial x_j}\right). \tag{6.3}$$

The transfer and destruction quantities have been already defined in Section 3.6. The kinetic energy flux is defined as :

$$F_{K,j} = Ku_j - \tau_{ij}u_i - \tau_{ij}^t u_i. \tag{6.4}$$

The heat flux is defined as :

$$F_{q,j} = (q_j + q_j^t)\left(1 - \frac{T_{ref}}{T}\right). \tag{6.5}$$

The total exergy flux is defined as :

$$F_{\xi,j} = u_j(\rho\xi_t) + (q_j + q_j^t)\left(1 - \frac{T_{ref}}{T}\right) - \tau_{ij}u_i - \tau_{ij}^t u_i. \tag{6.6}$$

All variables in the above equations are averaged quantities. Considering the total exergy transport equation (Equation (6.1)) in the secondary stream tube (V_2 in Figure 3.15), the difference of the total exergy flux between the inlet and outlet of the tube is related to the destruction terms (Π and Π_θ) in the volume V_2 and the transfer terms (I_q and I_K) across the dividing streamline. If we consider that the inlet contains zero exergy as a reference, the transfer terms increase the total exergy flux in the volume, while the destruction terms decrease the total exergy flux in the volume. Hence, a balance can be defined by the transfer and destruction terms as :

$$\Delta(x) = I_K(x) + I_q(x) - \Pi(x) - \Pi_\Theta(x). \tag{6.7}$$

This balance indicates the net total exergy obtained by the secondary stream from the primary stream. Additionally, based on the total exergy transport equation, this balance should also be consistent with the cross-sectional total exergy flux. The cross-sectional total exergy flux is computed as an integration of the total exergy flux (Equation (6.6)) at each cross-section and normalized similarly as for the balance.

In the following, we compare the transfer terms, destruction terms, and balance between an on-design and a near-critical conditions, which are presented as the red and magenta points in Figure 6.1. The compression ratios are 1.015 and 1.14, respectively. First, the dividing streamlines for both conditions are shown in Figure 6.5. Some oscillations are observed at the outlet of the primary nozzle for both conditions because of the shock train. For the on-design condition, a significant change of the dividing streamline at the beginning of the diffuser is observed, which is caused by the strong oblique shock.

The local kinetic energy, heat, and exergy transfers across the dividing streamline are shown in Figures 6.6(a) and (b) for both conditions, while the local destruction terms are displayed in Figures 6.6(c) and (d) for both conditions. The local transfer terms are computed by integrating the local flux over the depth (z-direction), while the destruction terms are integrated at each cross-section. For the local total exergy flux across the dividing streamline, the first term of the local total exergy flux (Equation (6.6)) is zero, because the velocity perpendicular to the dividing streamline is zero along the dividing streamline.

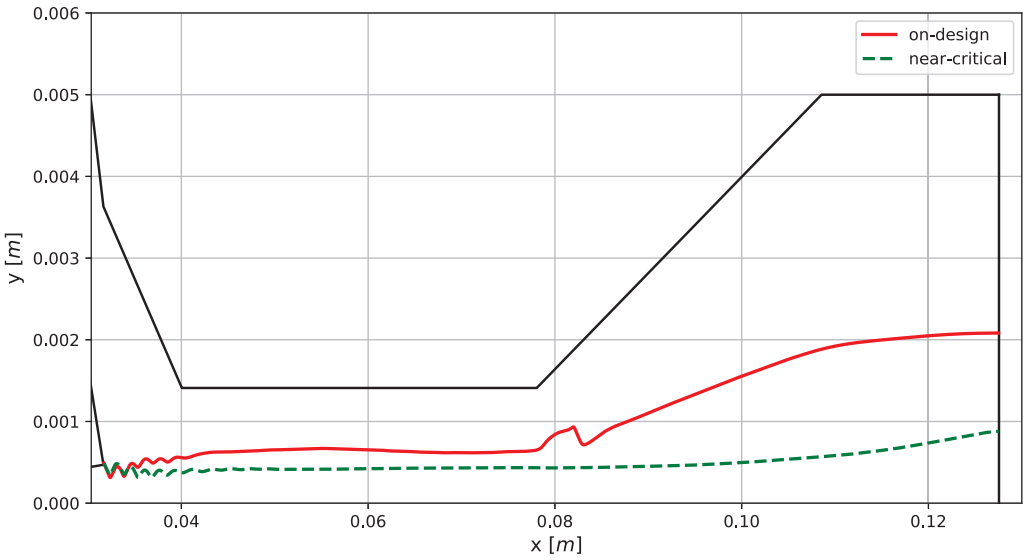

Figure 6.5 Dividing streamlines for one on-design and one near-critical conditions.

Therefore, the local total exergy flux can be divided into the heat flux and kinetic energy flux as $F_\xi = F_q + F_K$.

In Figure 6.6(a), for the on-design condition, the kinetic energy and heat transfer across the dividing streamline are very low in the mixing duct, whereas a significant heat transfer is observed near the shock in the diffuser. It can be seen that the heat transfer is negative near the shock, which means that the heat is transferred from the secondary stream to the primary stream. Moreover, we observe that the heat transfer dominates the total exergy transfer for the on-design condition. However, comparing Figures 6.6(a) and (b), for the near-critical condition, the kinetic energy transfer is more important than the heat transfer. This difference is probably due to the presence of the shock wave : a strong shock wave appears in the diffuser for the on-design condition, whereas there is no shock wave for the near-critical condition (density gradient map is not shown here). Additionally, in this two-phase CO_2 ejector, the heat transfer is comparable to the kinetic energy transfer, while in a single-phase air ejector [100], the heat transfer is much less than the kinetic energy transfer.

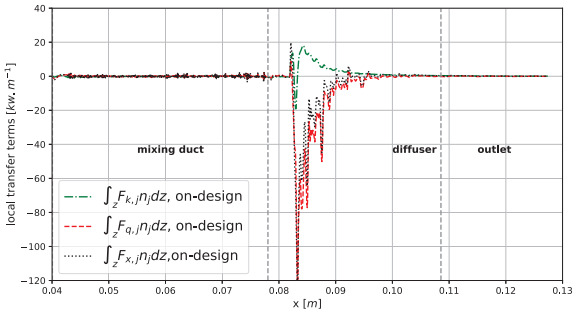

(a)

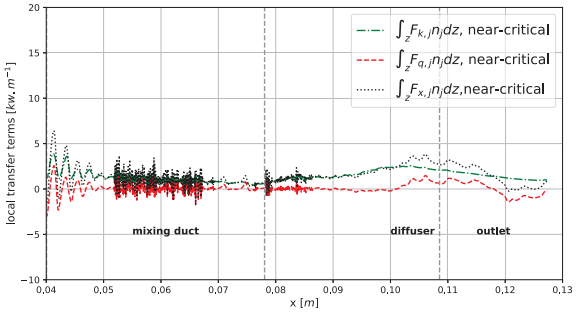

(b)

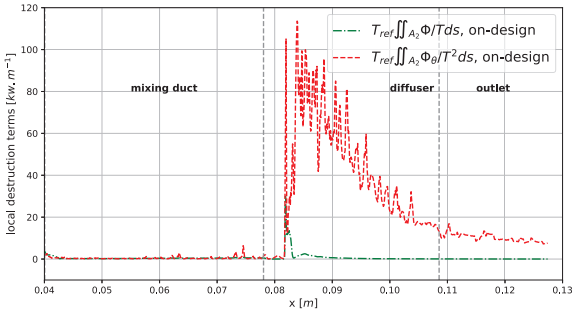

(c)

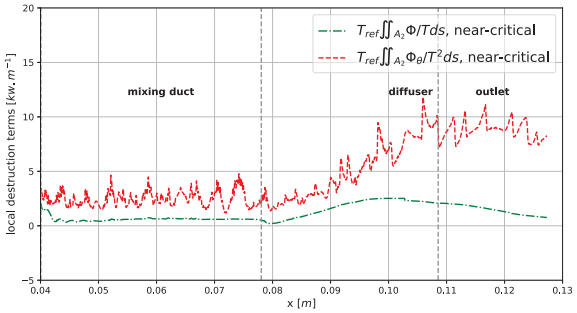

(d)

Figure 6.6 Local transfer terms for (a) on-design and (b) near-critical conditions and local destruction terms for (c) on-design and (d) near-critical conditions.

In Figures 6.6(c) and (d), the destruction term related to heat transfer is more important than that related to viscous dissipation. This observation is also different from the results of Lamberts *et al.* [100] where the destruction term related to heat transfer is negligible compared to that related to viscous dissipation. Moreover, in Figure 6.6(c), strong oscillations are observed for the destruction term related to heat transfer starting from the shock in the diffuser, which affect significantly cumulative quantities in the following.

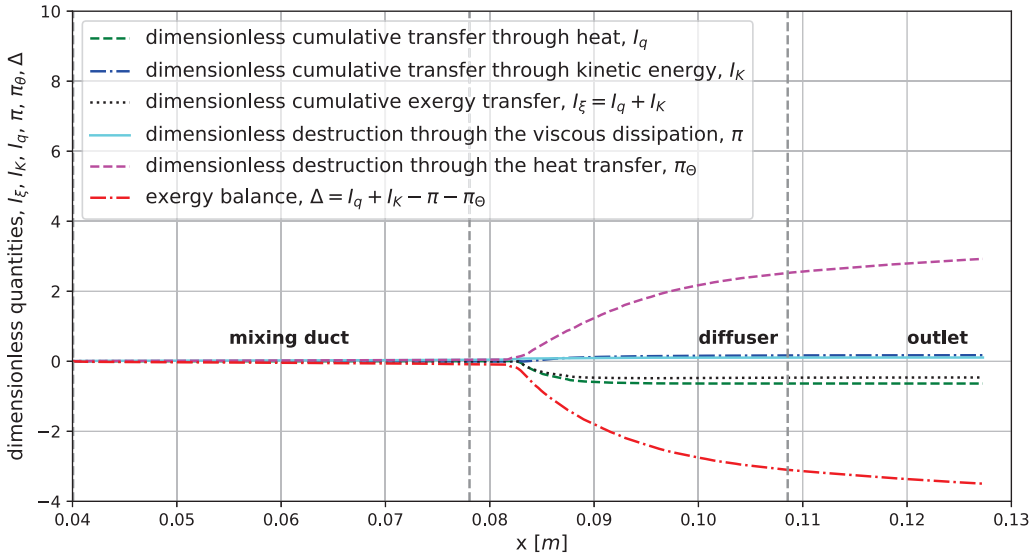

(a)

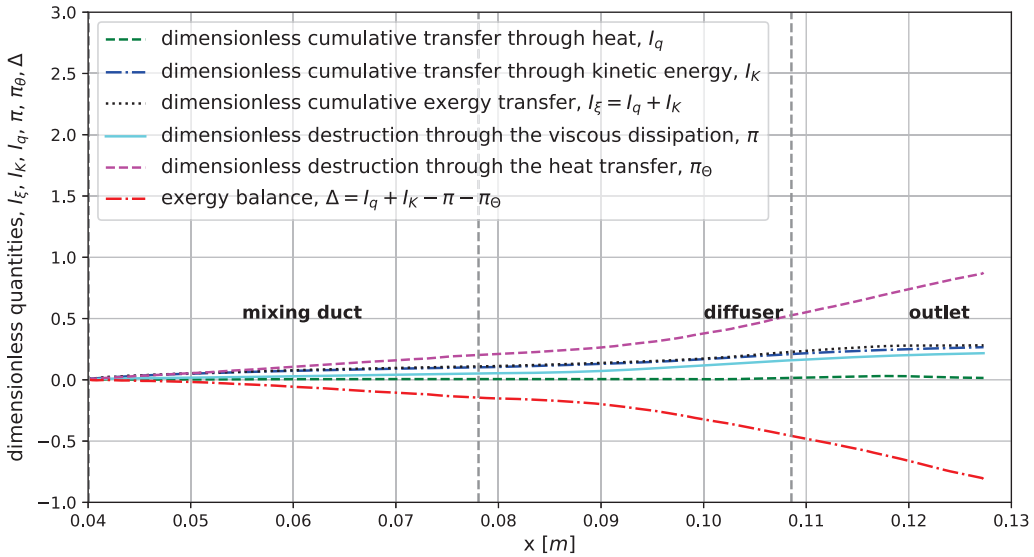

(b)

Figure 6.7 Cumulative transfer terms for (a) on-design and (b) near-critical conditions.

Subsequently, the dimensionless cumulative quantities are shown in Figure 6.7 for both conditions. The cumulative transfer terms across the dividing streamline are integrated along the dividing streamline (I_K, I_q, I_ξ), based on Equations (3.102), (3.103), and (3.104). The cumulative destruction terms are integrated over the volume of the secondary stream tube as Equation (3.105) and (3.106). The balance is computed through Equation (6.7). The total exergy flux at the primary inlet is used to normalize the cumulative quantities.

Comparing Figures 6.6(a) and (c) to Figure 6.7(a), the variations of the cumulative quantities correspond exactly to the variations of the local quantities. For example, in Figure 6.7(a), the green curve presents the dimensionless cumulative heat transfer across the dividing streamline. The decrease of this quantity between 0.08 m and 0.09 m is due to the local variation of the heat transfer term (red curve) in Figure 6.6(a) between 0.08 m and 0.09 m.

In Figure 6.7(a), the cumulative total exergy transfer is negative in the diffuser, because of a strong transfer from the secondary stream to the primary stream across the shock. Furthermore, the destruction related to heat transfer is extremely important and one finally gets a negative balance. It means the secondary stream has less total exergy than that at the tube inlet (inlet of mixing duct). For the near-critical condition in Figure 6.7(b), the cumulative kinetic energy transfer (blue curve) is more important than the cumulative heat transfer (green curve) across the dividing streamline, which matches the observation of the local transfer terms. The cumulative total exergy transfer (black curve) is positive for the near-critical condition. Nevertheless, one obtains also a negative balance due to the large destructions related to heat transfer (pink curve).

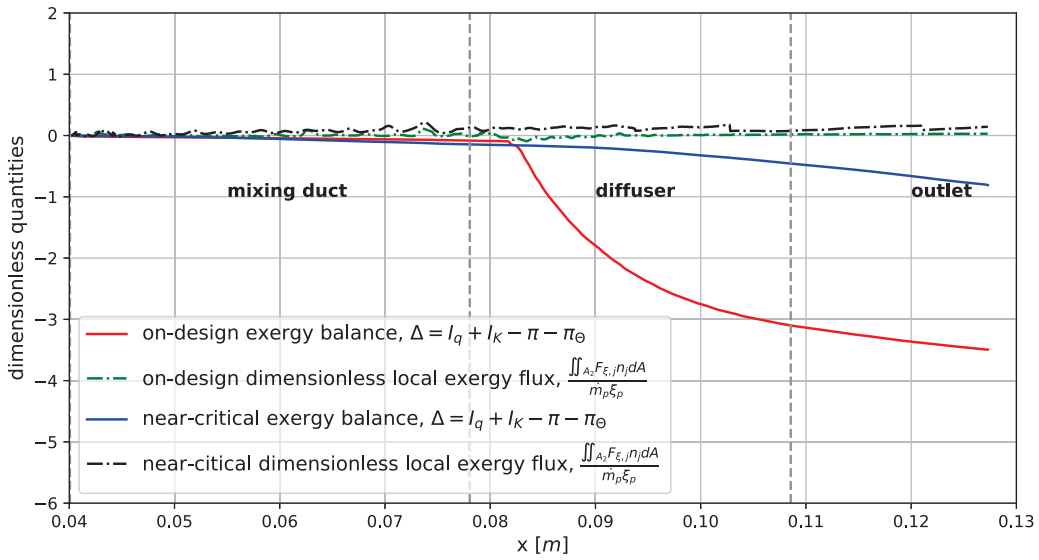

Figure 6.8 Balance and local exergy flux for the on-design and near-critical conditions.

There are two ways to determine the net total exergy obtained by the secondary stream. The first one is to compute the balance based on the transfer and destruction terms. This one is essentially achieved by reconstructing the total exergy transport equation (Equation (6.1)) term by term. The other way is to compute directly the local total exergy flux along the secondary tube. These two quantities are shown in Figure 6.8. However, one finds an inconsistency between these two quantities. In Figure 6.8, the local total exergy fluxes for both conditions are very low but positive, while the constructed balances are negative. The local total exergy flux seems more reasonable to present the net total exergy obtained by the secondary stream. This total exergy should be positive, because the secondary stream is compressed in the ejector through exergy transfer and the secondary stream is entrained by the primary stream through exergy transfer. Therefore, this negative balance may be due to numerical errors when computing transfer and destruction terms.

As a conclusion, heat effects (transfer and destruction) are important for this two-phase CO_2 ejector, compared to the single-phase ejector [100]. The two-phase change occurs in the two-phase CO_2 ejector accompanied with the heat transfer. Hence, heat effects can be as important as fluid dynamic effects in a two-phase CO_2 ejector. However, it is difficult to determine accurately how important the heat effects are, because an incoherence between the constructed balance and the local total exergy flux is obtained. It may come from numerical errors. In the following section, the possible numerical errors are discussed.

6.4 Sensibility of the tube exergy analysis

As the tube exergy analysis is a post-processing technique, it is sensitive to the calculated variables and their gradients. During the post-processing, the total exergy equation is not solved, but it is reconstructed by computing separately each term based on the calculated variables and their gradients. For example, the convective part of the total exergy flux, $\rho\xi_t u_j$ is directly computed by the quantities, ρ, ξ, and u. ξ_t is not obtained from the total exergy transport equation but is computed by the total enthalpy and entropy (Equation (3.89)). The total exergy flux (LHS of the equation) is computed by averaged quantities and gradients, while the destruction terms (RHS of the equation) are mainly computed by the square of gradients. Consequently, numerical errors affect differently the total exergy flux and the destruction terms.

In the following, one compares the simulations obtained by using the van Leer, van Albada, and upwind limiters. These limiters are used to construct the interface flux by interpolate variables from a cell center to the cell boundary (Section 3.4.1). As a result, the resolution of the gradients is strongly related to these limiters, especially near discontinuities. The van Leer limiter [184] which is recommended by Greenshields *et al.* [76] is considered as a default choice to perform all simulations. A flux limiter function $\beta(r)$ was defined based on different limiters [76]. For the van Leer limiter, $\beta(r)$ writes :

$$\beta = \frac{r + |r|}{1 + r}, \tag{6.8}$$

where r is computed by the gradient at the cell center and the gradient component normal to the interface (defined in Equation (11) in [76]). For the van Albada limiter [182], the limiter function has a similar form as the van Leer limiter :

$$\beta = \frac{r(r + 1)}{1 + r^2}. \tag{6.9}$$

These two limiters are both second-order accurate. Additionally, β for the upwind limiter is equal to 0, which means that the flux at the cell face is totally biased on the upwind flux. It is first-order accurate.

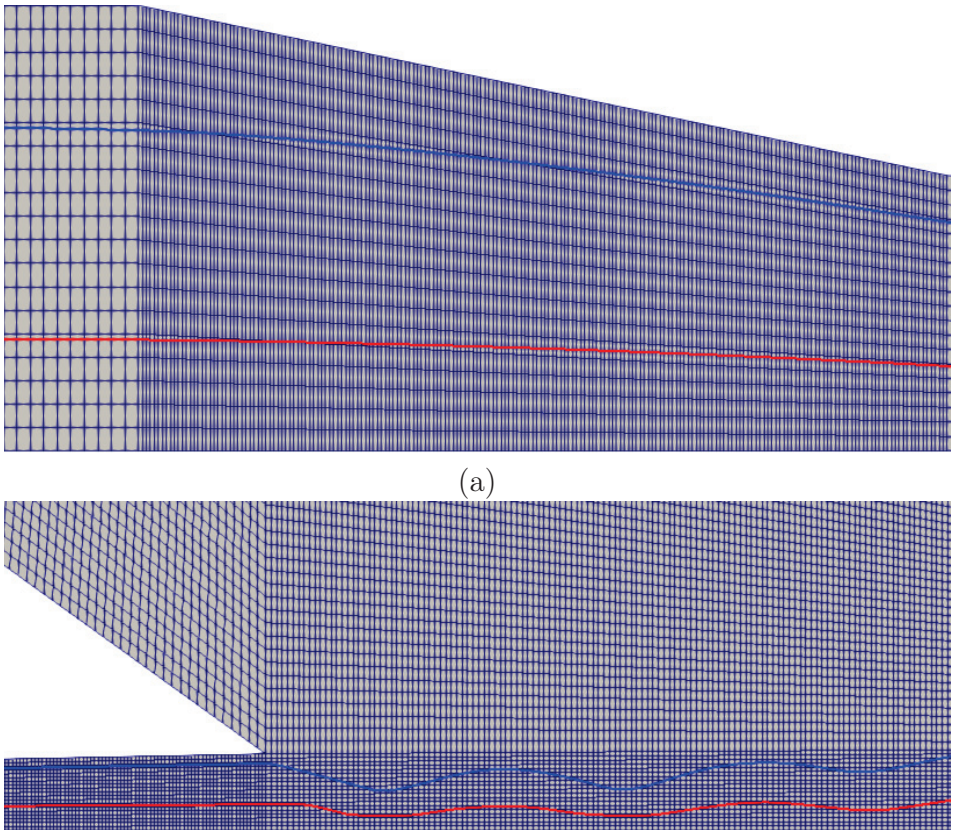

(a)

(b)

Figure 6.9 Exergy tube from the primary nozzle (a) in the converging part of the primary nozzle and (b) at the outlet of the primary nozzle with the corresponding mesh grid.

One compares the local total exergy flux and destruction terms in the exergy tubes from the primary nozzle for the on-design condition. The starting location of the exergy tube and the exergy tube at the outlet of the primary nozzle are shown in Figure 6.9. By definition, there is no exergy flux across the top and bottom boundaries. Compared to the secondary stream tube, there is no transfer contribution from the exterior of the exergy tube, therefore the balance only depends on the destruction terms. The local total exergy flux and the destruction terms are both normalized by the total exergy flux at the beginning of the exergy tube. Hence, the balance is equal to 1 at the beginning of the exergy tube and then due to the destruction terms, it decreases. According to the total exergy transport equation (Equation (6.1)), these two quantities should be equal. The local total exergy flux and constructed balance in the exergy tube are compared in Figure 6.10 between the results using the van Leer, van Albada, and upwind limiters.

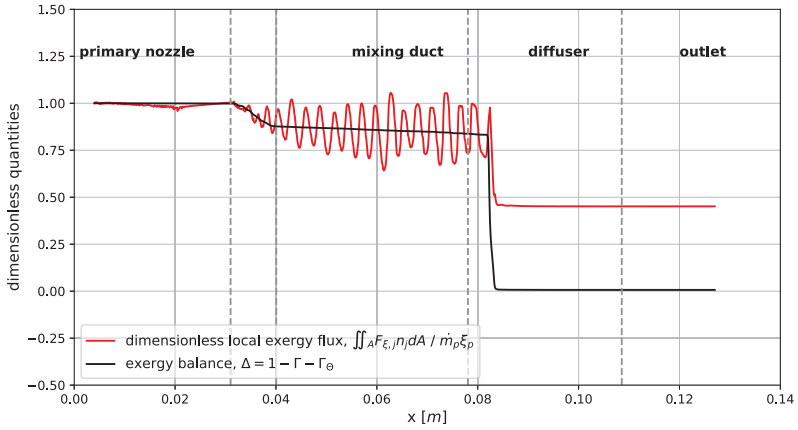

(a)

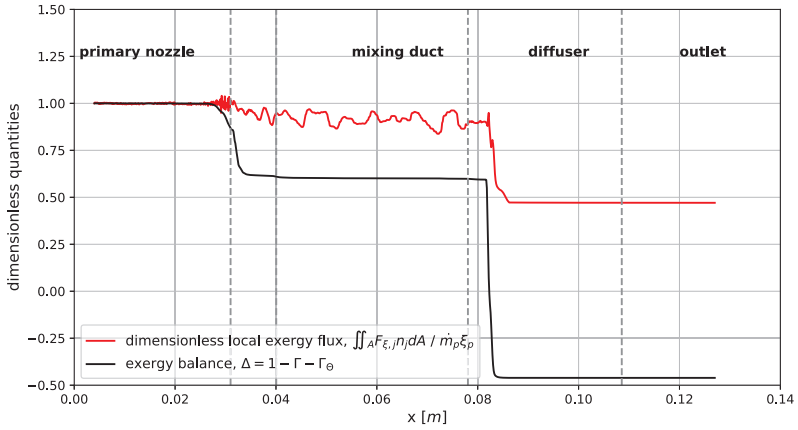

(b)

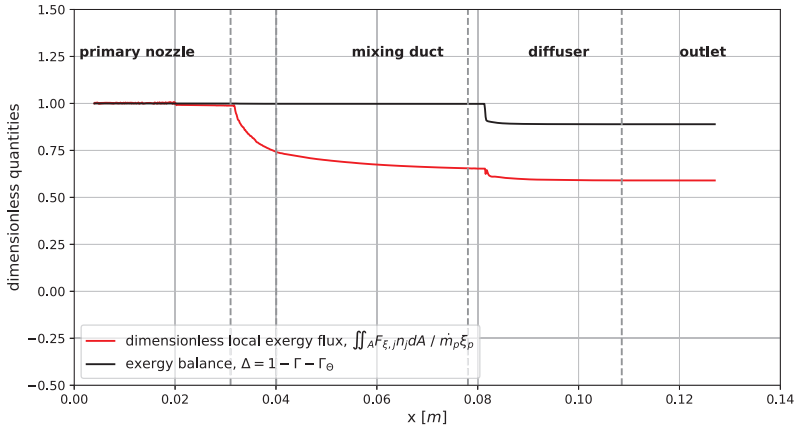

(c)

Figure 6.10 Comparison in terms of local total exergy flux and destruction terms in the exergy tube between the results obtained using the (a) van Leer, (b) van Albada and (c) upwind limiters.

In Figure 6.10(a), the balance computed by the destruction terms decreases at the outlet of the primary nozzle because of the shock train and a significant decrease is further observed near the shock in the diffuser. Although the total exergy flux has some oscillations, it agrees with the balance in the primary nozzle and in the mixing duct. A significant difference starts from the shock in the diffuser. Since the balance is a cumulative quantity, the local total exergy flux and balance are always different hereafter. It is observed that the local total exergy flux has more oscillations than the balance, because the total exergy flux is a local quantity, whereas the balance is a cumulative quantity. If we consider one local quantity in the balance, such as the local destruction terms in Figure 6.6(c) and (d), it oscillates as well.

Comparing the balances (black curves) in Figure 6.10(a) and (b), large differences appear at the locations of the shock train (between 0.3 mm and 0.4 mm) and the strong shock (approximately 0.8 mm). Considering the local total exergy fluxes in Figure 6.10(a) and (b), the results using the van Leer limiter has more oscillations than that using the van Albada limiter. Nevertheless, the local total exergy fluxes are approximately 0.9 in the mixing duct and 0.49 in the diffuser for both cases. Hence, the local total exergy fluxes agree well for both limiters.

In Figure 6.10(c), the local total exergy flux is vergy smooth. The decrease of the balance and the local total exergy flux are much smaller than those in Figure 6.10(a) and (b). Moreover, the local total exergy flux does not agree with those in Figure 6.10(a) and (b).

In conclusion, the differences between the balance and local total exergy flux are generated mainly due to the variations of destruction terms near the discontinuities (shock train and strong shock). Considering the destruction terms, they are computed by the square of gradients. Since resolution of the gradient strongly depends on the numerical scheme, the destruction terms are more sensitive to the numerical scheme than the local total exergy flux. Furthermore, the local total exergy fluxes agree well between the results using the van Leer and van Albada limiters, while they are different from the result using the upwind limiter. This may be related to the accuracy of the numerical scheme. In order to stably capture strong discontinuities, a specific numerical treatment is usually used, which brings numerical dissipation. The upwind limiter is first-order accurate, which is more dissipative than the van Leer and van Albada limiters.

In order to improve the computation of the gradients, a high order numerical scheme and a fine mesh should be used. As the total exergy equation is established manually by separately computing the different terms in the equation, the numerical errors have different

sensitivities on the local exergy flux and destruction terms. To reduce this inconsistency, it would better to solve directly an exergy transport equation by using the same numerical scheme in the solver (e.g. KNP scheme [98] in *rhoCentralFoam* solver).

The local total exergy flux and the balance for the on-design condition are also compared in the secondary stream tube in Figure 6.11. Similar conclusions can be drawn. The local total exergy fluxes are less sensitive to limiters than the balance. The inconsistency between the local total exergy flux and balance is always observed. As cumulative quantities are extremely sensitive to the resolution of gradients, when applying the exergy tube analysis, the gradients should be accurately computed.

Furthermore, other source of the numerical errors can be considered, such as the integration errors at the cross-section and the interpolation errors. The mass flow rates (MFR) in the primary and secondary tubes for the on-design condition are shown in Figure 6.12. The van Leer limiter is always used. According to the definition of the dividing streamline, the mass flow rate is conserved in the primary stream and secondary stream tubes. Hence, the oscillations of the primary and secondary mass flow rates (Figure 6.12) are mainly due to interpolation errors when performing the cross-sectional integration. Moreover, a significant decrease of the secondary mass flow rate is observed near the shock in the diffuser. This decrease may be due to the change of the dividing streamline, which can be seen in Figure 6.5. Since the integration is not strictly computed at the cross-section but at the perpendicular section, there would be some errors when the velocity in the y-direction is high. However, the integration at the perpendicular section was used in the analysis of Lamberts *et al.* [100]. They found no influence. Hence, it strongly depends on flow fields within the ejector. Moreover, when performing the integration, the points at the perpendicular section are not exactly the same as those at the mesh center, hence an interpolation technique is used. Consequently, a coarse mesh may have large interpolation errors.

Additionally, the process of constructing the exergy tube may also have an influence, because the integration limits depend on the tube boundaries. For example, if the dividing streamline is near a strong temperature gradient, a large heat transfer across the dividing streamline would be obtained and vice versa. Certainly, the tube construction depends also on the computed variables and gradients. Hence, it may be appropriate to develop an in-house tool to control the tube construction process.

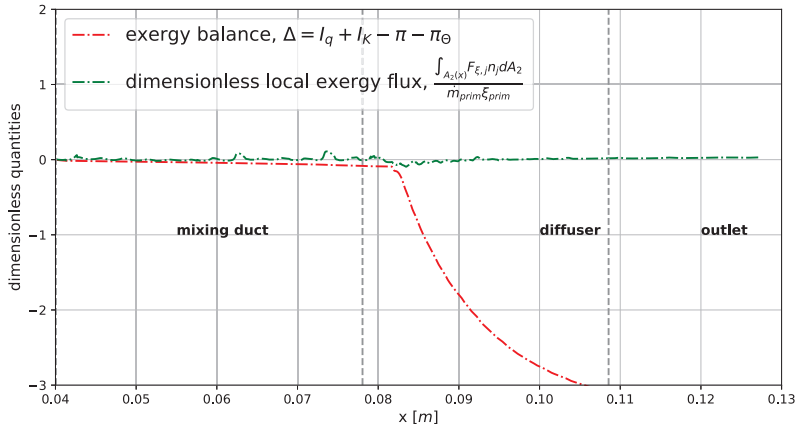

(a)

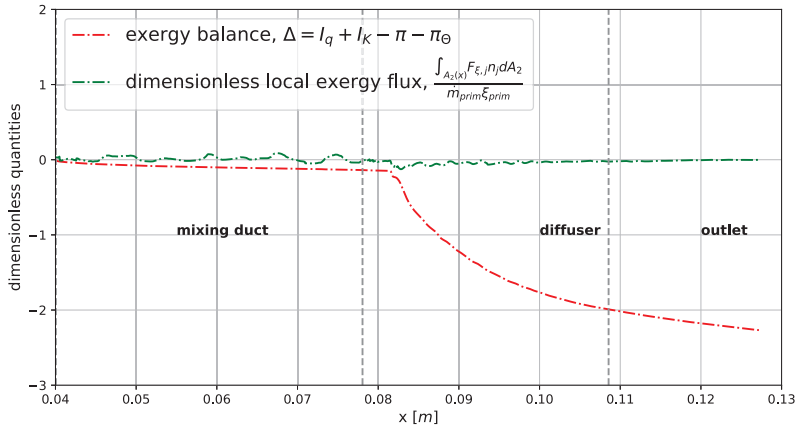

(b)

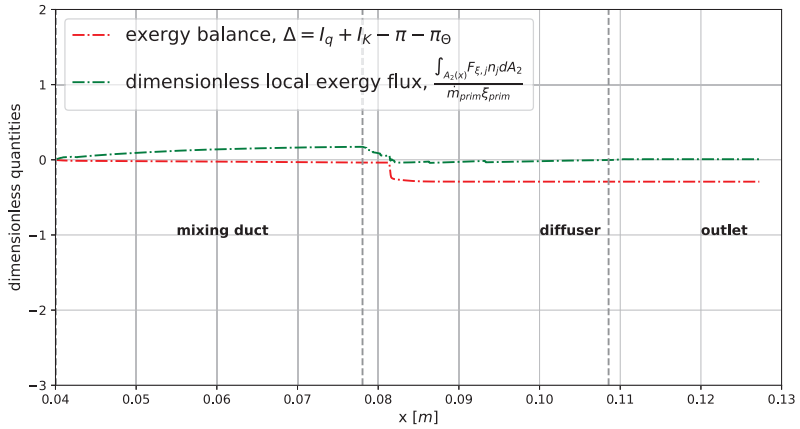

(c)

Figure 6.11 Comparison in terms of the local total exergy flux and destruction terms in the secondary stream tube between the results obtained using the (a) van Leer, (b) van Albada and (c) upwind limiters.

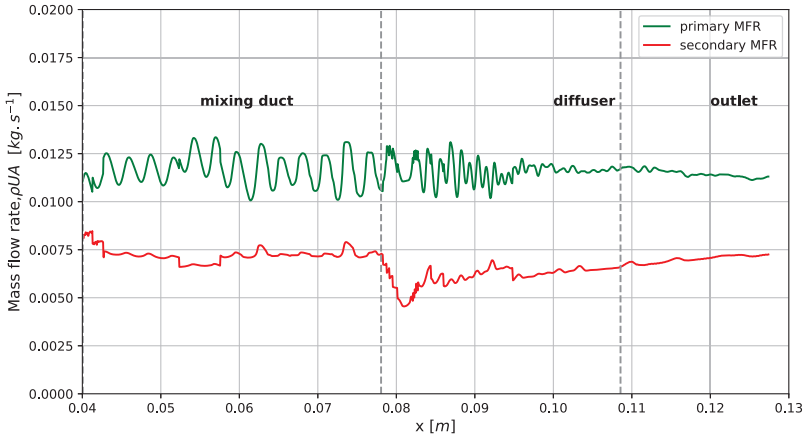

Figure 6.12 Mass flow rate in the primary and secondary streams separated by the dividing streamline.

6.5 Choking condition : the compound-choking theory

The compound-compressible flow theory was proposed by Bernstein *et al.* [21] to investigate one or more gas streams flowing through a nozzle. The schematic of the compound-compressible nozzle flow is shown in Figure 6.13. This is a one-dimensional theory that can predict flow conditions within the nozzle when the nozzle outlet condition varies. According to the compound-compressible theory, the flow is choked at the nozzle throat, though the Mach numbers of some individual streams are lower than one. It means that when chocking occurs, a compound wave cannot propagate upstream of the nozzle throat even though some of the individual streams are subsonic.

The details of the demonstration are presented in [21]. The assumptions related to the theory are :

- The flow is one-dimensional, steady, adiabatic, and isentropic.

- Each flow stream is a perfect gas with constant thermodynamic properties.

- There is no mixing between streams.

- The static pressure is constant between each stream at the nozzle cross-section, whereas it changes along the nozzle. It also means that the transverse pressure gradient caused by the streamline curvature is neglected.

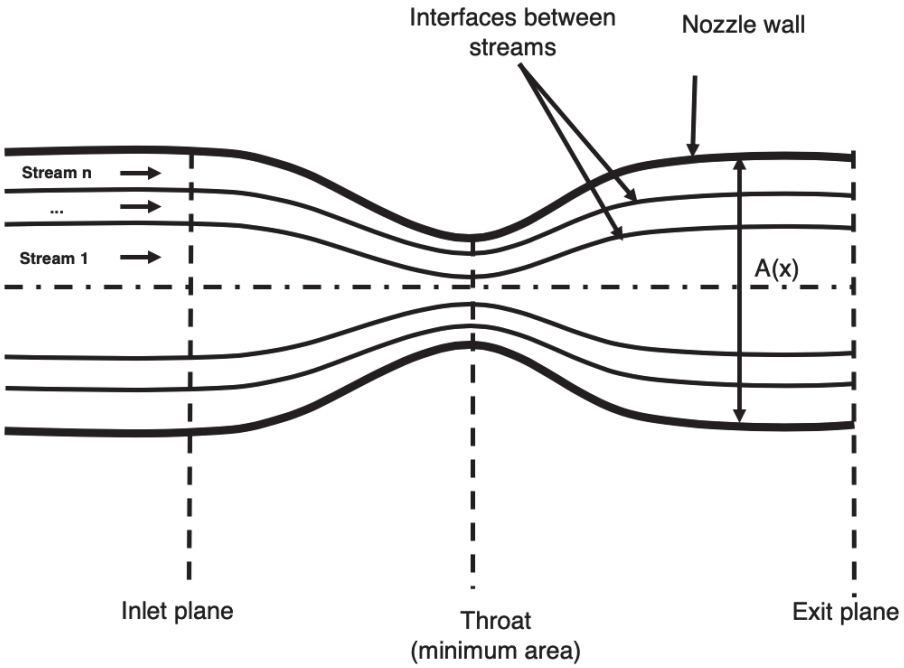

Figure 6.13 Schematic of the compound-compressible nozzle flow proposed by Bernstein *et al.* [21].

A compound-flow indicator was defined by Bernstein *et al.* [21] to determine the flow regimes :

$$\beta = \sum_{i=1}^{n} \frac{A_i}{\gamma_i} \left(\frac{1}{M_i^2} - 1 \right), \tag{6.10}$$

where A_i, γ_i, M_i denote the cross-sectional area, heat capacity ratio, and Mach number of each stream, respectively. The flow regimes are as follows :

- $\beta > 0$: the compound-subsonic flow.
- $\beta = 0$: the compound-sonic flow.
- $\beta < 0$: the compound-supersonic flow.

This theory has been applied to analyze a single-phase air ejector by Lamberts *et al.* [101]. It was found that the choking condition was different based on the compound-compressible flow theory and the classic definition, which was determined by the sonic line location along the ejector. The original formulation was developed based on the perfect gas assumption. To apply the same analysis to two-phase CO_2 ejectors, the theory was extended to the real gas. Based on the same hypothesis, the mass and momentum conservation of each stream can be written as :

$$\rho_i v_i A_i = cst \Rightarrow \frac{d\rho_i}{\rho_i} + \frac{dv_i}{v_i} + \frac{dA_i}{A_i} = 0, \tag{6.11}$$

$$\rho_i v_i A_i dv_i = -A_i dp_i, \tag{6.12}$$

where the subscript 'i' refers to each individual stream. According to Equation (6.11), one gets :

$$dv_i = -v_i(\frac{d\rho_i}{\rho_i} + \frac{dA_i}{A_i}). \tag{6.13}$$

In Equation (6.12), dv_i is substituted by using Equation (6.13). Then, $d\rho_i$ can be substituted by using $d\rho = \left(\frac{\partial \rho}{\partial p}\right)_s dp$ to introduce the speed of sound. One gets :

$$\frac{dA_i}{A_i} = \frac{dp}{\rho_i v_i^2}\left(1 - M_i^2\right), \tag{6.14}$$

As the cross-sectional pressure is constant for each stream, $dp_i = dp$. Finally, a similar formulation of β as proposed by Bernstein *et al.* [21] is obtained :

$$\beta = p \sum_i \frac{A_i}{\rho_i v_i^2}\left(1 - M_i^2\right). \tag{6.15}$$

When the perfect gas is assumed, one has $\frac{p}{\rho_i v_i^2} = \frac{r_i T_i}{v_i^2} = \frac{c_i^2}{\gamma_i v_i^2} = \frac{1}{\gamma_i M_i^2}$, which is coherent with the original formulation in [21].

After that, one verifies the relation of β in the frame of the compound wave. The evolution of one stream is illustrated in Figure 6.14. dA_i and dp_i present the variations of the cross-section and the pressure between two successive cross-sections. They are arbitrarily chosen.

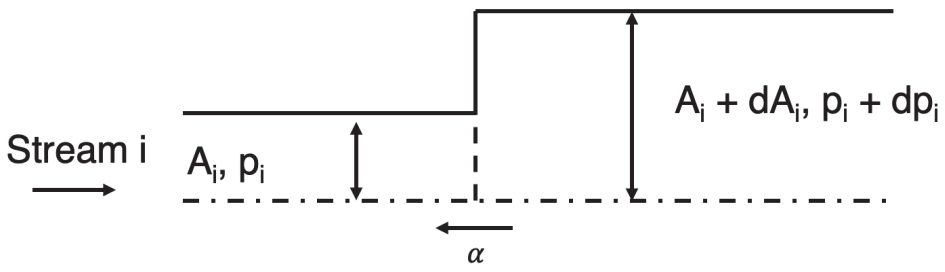

Figure 6.14 Evolution of one stream in a nozzle.

One also defines arbitrarily an upstream moving compound wave with the speed of α. If the absolute flow velocity is v_i, the flow velocity in the frame of the compound wave is :

$$v_i' = v_i + \alpha, \tag{6.16}$$

where the upstream propagating direction of the compound wave is considered directly by its sign. It follows that $\alpha > 0$ corresponds to a compound-subsonic flow ; $\alpha = 0$ corresponds to a compound-sonic flow ; $\alpha < 0$ corresponds to a compound-supersonic flow. In the frame of the compound wave, the mass and momentum conservation equations can be described as :

$$\rho_i v_i' A_i = (\rho_i + d\rho_i)(v_i' + dv_i')(A_i + dA_i) = cst, \tag{6.17}$$

$$p_i A_i - (p_i + dp_i)(A_i + dA_i) + p_i dA_i = \rho_i v_i' A_i (v_i' + dv_i' - v_i'). \tag{6.18}$$

Then, the following equations are obtained :

$$\frac{d\rho_i}{\rho_i} + \frac{dv_i}{v_i'} + \frac{dA_i}{A_i} = 0, \tag{6.19}$$

where $dv_i = dv_i'$, and

$$\frac{dp_i}{p_i} + \frac{\rho_i v_i'^2}{p_i}\frac{dv_i}{v_i'} = 0. \tag{6.20}$$

Based on the speed of sound definition, $c_i^2 = \left(\frac{\partial p_i}{\partial \rho_i}\right)_s$, one gets :

$$\frac{d\rho_i}{\rho_i} = \frac{1}{c^2}\frac{dp_i}{\rho_i}. \tag{6.21}$$

The term $\frac{d\rho_i}{\rho_i}$ in Equation (6.19) is substituted by using Equation (6.21) to obtain :

$$\frac{1}{c^2}\frac{dp_i}{\rho_i} + \frac{dv_i}{v_i'} + \frac{dA_i}{A_i} = 0 \Rightarrow \frac{dv_i}{v_i'} = -\left(\frac{dA_i}{A_i} + \frac{1}{c^2}\frac{dp_i}{\rho_i}\right). \tag{6.22}$$

Then, the term $\frac{dv_i}{v_i'}$ in Equation (6.20) is substituted by using Equation (6.22) and one gets :

$$\frac{dA_i}{A_i} = \frac{dp_i}{\rho_i}\left(\frac{1}{v_i'^2} - \frac{1}{c^2}\right). \tag{6.23}$$

v_i' is replaced by using Equation (6.16) and $p = p_i$ always holds. One gets :

$$\frac{dA_i}{A_i} = \frac{dp}{\rho_i}\left[\frac{1}{(\alpha + M_i c_i)^2} - \frac{1}{c^2}\right]. \tag{6.24}$$

The variation between two successive cross-sectional areas is assumed to be small. It reads :

$$\sum dA_i = 0 \Rightarrow \sum \frac{A_i}{\rho_i v_i^2} M_i^2 = \sum \frac{A_i}{\rho_i v_i^2} \frac{1}{\left(\frac{\alpha}{v_i} + 1\right)^2}. \tag{6.25}$$

As a result, β can be rewritten by introducing the compound-wave propagating speed :

$$\beta = p \sum_i \frac{A_i}{\rho_i v_i^2}\left[1 - \frac{1}{\left(\frac{\alpha}{v_i} + 1\right)^2}\right]. \tag{6.26}$$

This relation verifies the flow regimes corresponding to α and β, which are summarized as :

- $\alpha > 0$: compound-subsonic flow $\rightarrow \beta > 0$.
- $\alpha = 0$: compound-sonic flow $\rightarrow \beta = 0$.
- $\alpha < 0$: compound-supersonic flow $\rightarrow \beta < 0$.

Hence, to define the choking condition based on the compound-compressible flow theory, one shall find $\beta = p \sum_i \frac{A_i}{\rho_i v_i^2}(1 - M_i^2) = 0$. Additionally, in order to compare directly to the local Mach number, an equivalent Mach number can be defined as :

$$M_{eq}(x) = \left(1 - \beta \frac{\rho v^2}{pA}\right)^{\frac{1}{2}}. \tag{6.27}$$

In a two-phase CO_2 ejector, two streams are considered, which are the primary stream and the secondary stream divided by the dividing streamline. As the pressure is assumed to be uniform at each cross-section, the pressure term is not considered when computing

the equivalent Mach number. Moreover, the velocity for each stream is computed based on the mass flowrate :

$$v_i = \frac{\rho_i v_i A_i}{\rho_i A_i}, \tag{6.28}$$

where ρ_i is the averaged density of the stream i. Similarly, the stream Mach number is computed by the averaged velocity and averaged speed of sound. In the following, the equivalent Mach number is computed in the mixing duct, because one considers that the assumptions for the compound-wave theory are satisfied there.

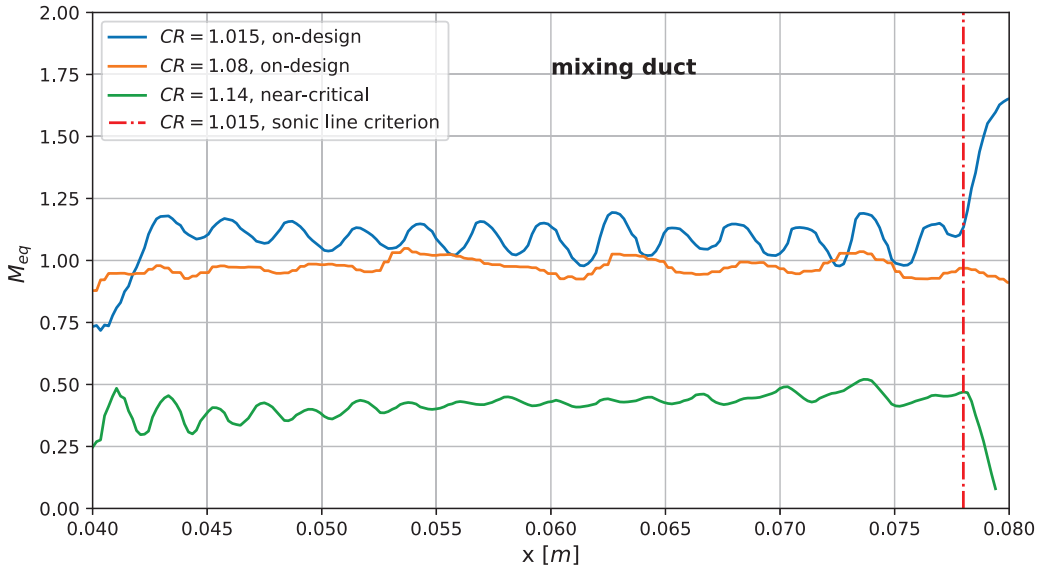

Figure 6.15 Compound-choking equivalent Mach number for different compression ratios, $CR = 1.015$, 1.08, and 1.14.

Figure 6.15 shows the equivalent Mach number for two on-design and one near-critical conditions ($CR = 1.015$, 1.08, and 1.14). According to the sonic line criterion, the secondary flow choking location is defined as where the local sonic line reaches the ejector wall. As the Mach number is always one along the sonic line, only the choking location can be indicated in Figure 6.15. The vertical red dot-dashed line shows the chocking location for the operating condition with $CR = 1.015$. For this operating condition ($CR = 1.015$), the equivalent Mach number (blue curve) reaches one at the beginning of the mixing duct, while the sonic line criterion predicts that the chocking location is at the end of the mixing duct. For the operating condition with $CR = 1.08$, the equivalent Mach number (orange curve) reaches one in the middle of the mixing duct, while the sonic line criterion predicts

a non-chocked flow. For the operating condition with $CR = 1.14$, both criteria predict a non-chocked flow.

It seems that the compound-choking theory predicts more accurate choking condition than the sonic line criterion. Similar observations have also been obtained by Lamberts *et al.* [101] in a single-phase air ejector. Hence, the compound-choking theory can be considered as a novel criterion to define the choking condition and also determine accurately the chocking location for two-phase CO_2 ejectors.

CHAPTER 7

Conclusion

The main objective of this thesis was to develop a reliable numerical tool to simulate two-phase CO_2 supersonic flows within ejectors. Therefore, most of the work was dedicated to the development of this complete and advanced numerical approach. This approach is able to predict complex phenomena in supersonic two-phase CO_2 flows, such as the shock train, flashing, phase transition ... The thesis can be mainly divided into three parts : *Development*, *Validation and Verification*, and *Analysis*.

In the *Development* part :

- A look-up table approach was developed [47, 59] first. It is based on the original Span-Wanger EoS [164] which calculates the properties of CO_2, covering from 217 K to 1000 K for the temperature and up to 50 MPa for the pressure. It includes the vapor, liquid, supercritical and two-phase states of CO_2. Hence, it is applicable to most ejector configurations used in the refrigeration industry.

  Since the variables solved by density-based solvers cannot be directly used as inputs for an EoS, an iterative process is required. However, the iterative process is very time-consuming and not robust. Therefore, to avoid the iterative process, we developed the first look-up table approach designed for density-based solvers to calculate two-phase CO_2 properties.

  Besides calculating the thermodynamic properties of CO_2 (pressure, temperature, speed of sound, and isochoric heat capacity), we implemented the formulation of Vesovic *et al.* [187] in this look-up table approach to compute the dynamic viscosity and thermal conductivity of CO_2.

- The look-up table approach was first coupled with the CLAWPACK solver for validation purpose. Then, in order to take into account more complex effects (viscosity and turbulence), we coupled this look-up table approach to the *rhoCentralFoam* solver [76, 191]. Moreover, to ensure the stability of the outlet boundary condition [137], we implemented the Navier-Stokes Characteristic Boundary Condition (NSCBC) in the CLAWPACK and *rhoCentralFoam* solvers, and also coupled it to the look-up table approach. Finally, the look-up table approach was coupled with the AVBP solver [31] for future Large-Eddy simulations (LES).

In the *Validation and Verification* part :

- The look-up table approach was validated first. The tabulated values (pressure, temperature and speed of sound) were compared to the values computed by the original Span-Wagner EoS. The maximum relative discrepancies for the pressure and for the speed of sound were 0.23%, 1.2%, respectively. The maximum absolute discrepancy for the temperature was 0.06 K. These results indicate that this look-up table approach is very accurate. Besides, the speed-up factor based on a 1D shock tube problem was from 66.6 to 90 compared to the original SW EoS. It shows that this look-up table is also highly efficient, which is suitable for future massive numerical simulations.

- Then, we verified the CLAWPACK solver coupled with the look-up table approach. The results of a shock tube and a depressurization problem agreed well with the results from the literature. After that, the same verifications were performed for the *rhoCentralFoam* solver. The CLAWPACK and *rhoCentralFoam* solvers coupled with this look-up table approach can accurately simulate two-phase CO_2 flows by capturing shock waves and relaxation waves. Additionally, we simulated the same 1D shock tube problem through the density-based and pressure-based solvers in ANSYS Fluent. It was found that density-based solvers could capture discontinuities more precisely than pressure-based solvers.

- The critical mass flow rate of a converging-diverging nozzle was computed through the CLAWPACK and *rhoCentralFoam* solvers. The results were compared to the experimental measurement of Smolka *et al.* [162], numerical results from Smolka *et al.* [162], and results from thermodynamic models [45, 172]. Good agreements were obtained between the results from the developed density-based solvers and the experimental results.

In the *Analysis* part :

- We started with investigations of converging-diverging nozzles, which are simpler cases than two-phase CO_2 ejectors. The converging-diverging nozzles of Nakagawa *et al.* [126] in supercritical and subcritical conditions were investigated through the CLAWPACK and *rhoCentralFoam* solvers. For the converging-diverging nozzles which have a relatively small diverging angle, the resolution of the boundary layers had a significant influence on the pressure profile. Hence, it is primarily important to compute accurately fluid dynamics, before investigating complex thermodynamic effects (i.e. thermodynamic non-equilibrium).

Furthermore, the HEM model which was used for the converging-diverging nozzle simulations showed a good accuracy to predict the flashing phenomenon for operating conditions with pressures from 6 MPa to 10 MPa. Hence, the HEM could be appropriate to predict the flashing for two-phase CO_2 ejector applications except for radical operating conditions (highly subcritical or subcooled conditions).

In addition, the bulk viscosity effect was evaluated through the converging-diverging simulations. Although no significant effect was observed, it should be noticed that the bulk viscosity is special for supersonic CO_2 flows compared to other fluids. The bulk viscosity effect has been proven experimentally by Tisza [174]. Therefore, it may be encountered in other supersonic CO_2 flow simulations.

Then, the converging-diverging nozzle of Berana *et al.* [20] was simulated through the *rhoCentralFoam* solver. A thick shock was predicted, which agreed well with the experimental measurements. Hence, the *rhoCentralFoam* solver coupled with the look-up table approach can accurately simulate the two-phase CO_2 flow in converging-diverging nozzles.

- Further, we focused on ejector simulations. The ejector of Li *et al.* [110] was simulated through the *rhoCentralFoam* solver. The tube exergy analysis developed by Lamberts *et al.* [100] for a single-phase perfect gas ejector was applied. However, the results were not as expected. We found that the local total exergy flux was inconsistent with the balance computed by the destruction terms, either in the exergy tube or in the secondary stream tube. Then, the simulations using van Leer, van Albada, upwind limiters were performed. By comparing these results, we found that the destruction terms were very sensitive to the gradient resolution. In reality, the total exergy transport equation is not directly solved by the solver but constructed manually by computing separately each term of the equation. Hence, numerical errors could have different influences on each term that depends on gradients or square of gradients. There are several ways to reduce these errors : (i) Compute more accurate gradients, which means that a fine mesh and a high-order numerical scheme are needed. However, it should be mindful that a fine mesh and a high-order numerical scheme could easily generate oscillations causing large gradients ; (ii) Solve directly an exergy transport equation instead of computing each term separately ; (iii) Reduce interpolation errors related to the integration computation at the tube cross-section.

Finally, we extended the compound-choking theory to investigate the choking condition within the two-phase CO_2 ejector of Li *et al.* [110]. The compound-choking theory gave a more accurate prediction of the choking condition than the sonic line criterion.

- Moreover, the simulations of the CO_2 ejector available at Laboratoire des Techonologies de l'Énergie (LTE, Shawinigan) were performed and compared to new experiments. The wall pressure profile agreed particularly well with the experiments. Besides, a recirculation zone appeared at the secondary inlet, which indicated that the ejector did not operate optimally (off-design regime). As a result, this operating condition was not appropriate for ejector-expansion cycles.

To sum up, these three solvers coupled with the look-up table approach are reliable to simulate two-phase CO_2 supersonic flows within ejectors and converging-diverging nozzles. Among the possible research paths that are worth to be further investigated, let us mention :

- The look-up table approach can be extended to the metastable phase to adapt to complex two-phase models such as the HRM. A more complex interpolation method (i.e. bi-cubic interpolation method) can be implemented to increase the interpolation accuracy. More properties can be included in the look-up table approach, such as the isobaric heat capacity, thermal conductivity, and dynamic viscosity.

- A wall-resolved 3D numerical simulation is necessary, because the boundary layers could have a significant influence on the predictions of the mass flowrate, pressure profile, and exergy analysis.

- A more sophisticated turbulence model would be necessary (i.e. LES) to assess the resolution of fluid dynamics. In this thesis, the coupling between the look-up table approach and the AVBP solver has been completed. An LES of a two-phase CO_2 ejector will be shortly performed. Further, comparisons between a wall-resolved RANS simulation and an LES simulation will be performed to determine the advantages of an LES.

- The development of an implicit solver would be useful. It was mentioned in Chapter 6 that the use of an explicit solver for supersonic two-phase CO_2 simulations was very time-consuming. The reason is that to guarantee the calculation stability, the CFL number should remain small for explicit solvers. Hence, it makes the time step extremely small. Further, comparing to air ejectors, the density in two-phase CO_2 ejectors is at least 100 times higher. If the resolution of the boundary layer is required,

the mesh size can be 10 times smaller than the mesh size in an air ejector, which means that the time step should be 10 times smaller as well. Hence, an implicit solver is necessary to reduce significantly the computational time.

- An in-depth analysis of the two-phase model would be necessary, according to different inlet conditions. Especially, the HEM would be less valid for subcooled, subcritical conditions. It is therefore envisaged to replace the HEM with a more sophisticated thermodynamic non-equilibrium model such as HRM or DEM.

Conclusion

Ce travail de thèse avait pour objectif le développement d'un outil numérique fiable destiné à la modélisation d'éjecteurs transcritiques au CO_2. Une grande partie de cette thèse a été consacrée au développement des approches numériques pour prédire des phénomènes complexes dans les écoulements supersoniques diphasiques de CO_2, par exemple les trains d'ondes de choc, le flashing, le changement de phase ... La thèse s'est principalement divisée en trois parties : *Développement*, *Validation et vérification*, et *Analyse*.

Dans la partie *Développement* :

- Une méthode tabulée a été développée pour calculer les propriétés du CO_2 [47, 59]. Elle est basée sur l'équation d'état de Span-Wagner (SW) [164], qui couvre une gamme de température allant de 217 K à 1000 K et pour des pressions allant jusqu'à 50 MPa. Cela comprend les états de vapeur, liquide, supercritique et diphasique. Par conséquent, cette méthode est applicable à la plupart des configurations d'éjecteurs rencontrés dans l'industrie de la réfrigération.

  Cette approche est conçue pour les solveurs basés sur la densité sous leur forme conservative. Il n'est, en effet, pas évident de coupler une équation d'état pour un gaz réel à un solveur basé sur la densité. Comme les variables utilisées par une équation d'état ne sont généralement pas appropriées à la formulation conservative, un processus itératif est souvent utilisé. En plus, il n'existe, pour l'heure, aucune équation d'état pour le CO_2 qui soit appropriée et compatible avec un solveur basé sur la densité (dans les logiciels commerciaux comme ANSYS notamment). C'est la raison pour laquelle nous avons tout d'abord mis au point une approche tabulée spécialement conçue pour les solveurs basés sur la densité et basée sur une formulation conservative.

  À l'exception des propriétés thermodynamiques fournies par l'équation d'état de SW (pression, température, vitesse du son, capacités calorifiques isochorique et isobarique), la viscosité dynamique et la conductivité thermique sont calculées à partir de la formulation de Vesovic *et al.* [187].

- Cette méthode tabulée a été couplée au solveur CLAWPACK [106, 107] à des fins de validation. Afin de prendre en compte des effets plus complexes (frottement visqueux, turbulence), le solveur *rhoCentralFoam* d'OpenFoam [76, 191] a également été considéré. En outre, la condition aux limites caractéristique de Navier-Stokes

(NSCBC) a été implémentée afin de traiter correctement la condition aux limites en sortie de domaine pour des écoulements compressibles [137]. La méthode a aussi été couplée au solveur AVBP [31], pour de futures simulations aux grandes échelles (LES). Ce couplage a été évalué à travers différents cas tests disponibles à l'Annexe D.

Dans la partie *Validation et Vérification* :

- Nous avons d'abord validé la méthode tabulée. Les propriétés tabulées ont été comparées à celles de l'équation d'état originelle de Span-Wagner, en termes de pression, de température et de vitesse du son. Les écarts relatifs maximaux sont de 0.23%, et 1.2% pour la pression et la vitesse du son, respectivement. L'écart absolu maximal pour la température est de 0.06 K. De plus, le facteur d'accélération basé sur un problème de tube à choc 1D est compris entre 66.6 et 90 par rapport à l'équation d'état originelle de SW.

- Nous avons vérifié le solveur CLAWPACK couplé avec la table pour le CO_2. Les résultats pour le tube à choc et la dépressurisation ont été comparés avec ceux issus de la littérature. Les mêmes vérifications ont été faites pour le solveur *rhoCentralFoam*. Les résultats ont été comparés avec ceux de CLAWPACK et de la littérature. Nous avons aussi utilisé les solveurs basés sur la densité et basés sur la pression dans ANSYS Fluent pour simuler un tube à choc.

- Le débit massique critique pour une tuyère convergente-divergente prédit par le solveur *rhoCentralFoam* a été comparé avec les résultats expérimentaux et numériques de Smolka *et al.* [162] et thermodynamiques [45, 172] issus de la littérature et à ceux du solveur CLAWPACK, démontrant un bon accord entre les approches numériques et les données expérimentales.

En conclusion de cette partie, cette méthode tabulée montre non seulement une bonne précision, mais aussi une bonne efficacité, ce qui convient aux futures simulations numériques massives. Les solveurs CLAWPACK et *rhoCentralFoam* couplés avec cette méthode tabulée sont capables de simuler les écoulements diphasiques de CO_2 avec précision, en capturant les ondes de choc et les ondes de détente. Ensuite, on a trouvé que les solveurs basés sur la densité capturent les discontinuités plus précisément que ceux basés sur la pression. Les solveurs basés sur la pression pourraient générer des oscillations à l'endroit de ces discontinuités.

Dans la partie *Analyse* :

- Les tuyères convergentes-divergentes de Nakagawa *et al.* [126] dans des conditions supercritiques et sous-critiques ont été simulées via les solveurs CLAWPACK et *rhoCentralFoam*. L'influence de la viscosité volumique a été étudiée et les résultats montrent qu'elle reste faible dans ce cas précis. Pour la tuyère convergente-divergente de Berana *et al.* [20], le solveur *rhoCentralFoam* capture un choc épais, ce qui concorde bien avec les mesures expérimentales.

- L'éjecteur de Li *et al.* [110] a été étudié pour une condition on-design. L'analyse du tube d'exergie proposée par Lamberts *et al.* [100] pour un éjecteur monophasique à air a été appliquée. La sensibilité de la méthode a été discutée. Enfin, la théorie de "compound-choking" a été étendue à l'écoulement diphasique de CO_2 pour prédire la condition de "choking". La théorie de "compound-choking" prédit que l'écoulement est choqué au début du tube de mélange, tandis que selon la ligne sonique locale, l'écoulement est choqué à la fin du tube de mélange.

- Une modélisation de l'éjecteur du LTE a aussi été effectuée. Le profil de pression correspond bien aux mesures expérimentales. Les tubes de transport de quantité du mouvement et d'énergie cinétique ont été analysés et une zone de recirculation observée à l'entrée de la chambre de mélange. L'analyse révèle que la condition de fonctionnement est largement off-design.

En conclusion, l'approche numérique basée sur le modèle HEM a montré une bonne précision pour prédire le phénomène de flashing dans des conditions de fonctionnement avec une pression de 6 MPa à 10 MPa. Par conséquent, pour les applications d'éjecteur au CO_2 diphasique (sauf pour des conditions de fonctionnement très particulières), le HEM pourrait convenir à la modélisation du flashing. Cependant, les résultats ont également montré que la résolution de la dynamique du fluide avait une influence significative sur les résultats. Par exemple, pour obtenir un profil de pression précis, la résolution de la couche limite joue un rôle important pour les tuyères divergentes-convergentes ayant un angle divergent relativement petit. Par conséquent, avant de considérer les aspects thermodynamiques (c'est-à-dire le non-équilibre thermodynamique), la dynamique du fluide doit être calculée avec précision.

Bien qu'aucun effet significatif de la viscosité volumique n'ait été observé, il convient de noter que cette viscosité était particulière pour les écoulements de CO_2 supersoniques par rapport aux autres fluides. Cet effet de viscosité volumique a été prouvé expérimentalement par Tisza [174]. Par conséquent, d'autres écoulements de CO_2 supersoniques peuvent être étudiés à l'avenir pour évaluer cet effet et obtenir des conclusions plus généralisables.

Par rapport à l'analyse des tubes d'exergie, nous avons constaté que le flux d'exergie local était incompatible avec le bilan calculé par les termes de destruction, que ce soit dans le tube d'exergie ou dans le tube d'écoulement secondaire. En comparant les résultats qui utilisent les différents limiteurs, van Leer, van Albada, et upwind, nous avons constaté que les termes de destruction étaient très sensibles à la résolution des gradients. En fait, l'équation d'exergie n'est pas résolue par le solveur mais construite manuellement en calculant séparément chaque terme de l'équation. Par conséquent, les erreurs numériques peuvent avoir des influences différentes sur les termes qui dépendent de gradients ou de carrés de gradients. Plusieurs aspects permettent de réduire ces erreurs : (i) Résolution plus précise des gradients, ce qui signifie qu'un maillage fin et des schémas numériques d'ordre élevé sont nécessaires. Cependant, il convient également de noter que la stabilité autour des discontinuités est importante, car les oscillations peuvent générer des gradients importants et sont cumulativement incluses dans les termes de destruction ; (ii) Il est plus approprié de résoudre directement l'équation d'exergie par le solveur afin de calculer de manière cohérente tous les termes ; (iii) Réduire les erreurs d'interpolation liées à l'intégration dans le tube d'exergie et à la construction du tube d'exergie.

Parmi les pistes de recherche qui mériteraient d'être approfondies pour la simulation numérique d'éjecteurs au CO_2, citons :

- La méthode tabulée pourrait être étendue à la phase métastable afin de s'adapter à des modèles diphasiques plus complexes tels que le HRM. Une méthode d'interpolation plus complexe (par exemple la méthode d'interpolation bi-cubique) pourrait être mise en oeuvre pour augmenter la précision d'interpolation et les dérivées pourraient être calculées directement dans la table. Plus de propriétés pourraient être tabulées telles que la capacité thermique isobarique, la conductivité thermique et la viscosité dynamique.

- La simulation numérique 3D avec une bonne résolution de la couche limite est nécessaire. Les couches limites aux parois pourraient avoir une influence significative sur les prédictions du débit massique, du profil de pression, et sur les analyses exergétiques.

- Un modèle de turbulence plus sophistiqué serait nécessaire (par exemple LES) pour évaluer l'influence des structures tourbillonnaires à plus petites échelles sur les mécanismes de transport et de mélange au sein de l'éjecteur. Dans cette thèse, l'adaptation du solveur AVBP pour faire une telle LES a été effectuée. Une LES d'écoulement de CO_2 transcritique débutera prochainement. Ensuite, une comparaison entre une

modélisation RANS résolue en paroi et une LES sera effectuée afin de quantifier son apport par rapport à des modèles plus simples.

- Le développement d'un solveur implicite serait utile. Au Chapitre 6, il a été mentionné que l'utilisation d'un solveur explicite pour les simulations supersoniques de CO_2 diphasique sont extrêmement coûteuses en temps de calcul. Afin d'assurer la stabilité des simulations, le nombre de CFL (et par conséquent le pas de temps) est très faible pour les solveurs explicites. De plus, par rapport aux éjecteurs à air, la densité du CO_2 est au moins 100 fois supérieure. Si la résolution de la couche limite est requise, la taille du maillage pourrait être 10 fois inférieure pour le CO_2 par rapport au cas de l'air, ce qui rend le pas de temps nécessaire 10 fois plus petit. Par conséquent, un solveur implicite est absolument nécessaire pour réduire les temps de calcul.

- Une analyse approfondie de l'influence du modèle diphasique serait nécessaire pour différentes conditions d'entrée notamment. La validité du modèle HEM est, en effet, discutable pour des conditions sous-critiques sous-refroidies. Il est donc envisagé de remplacer le modèle HEM par un modèle hors équilibre thermodynamique plus sophistiqué tel que le HRM voire le DEM.

CHAPTER 8

Appendix

Appendix A : Drop-in replacement in a R134 ejector refrigeration cycle by HFO refrigerants

Note that this work has been published in *International Journal of Refrigeration* in 2017 [58] and presented during the 26th Canadian Congress Of Applied Mechanics in Victoria [42].

Most of the refrigeration or air-conditioning systems, which include a supersonic ejector, work with HFC refrigerants, mainly R134a [67, 200] and R245fa [119, 160]. The environmental effects are the main drawbacks of these common refrigerants or any HCFCs (hydrochlorofluorocarbons) and CFCs (chlorofluocarbons). Though being stable, non-toxic and non-flammable, their high ozone depletion potential (ODP) and Global Warming Potential (GWP) demonstrate their direct impact on the environment in case of leakage or releasing to the surroundings. In 1987, during the Montreal protocol, it was decided to progressively phase out CFCs then five years later to phase out HCFCs. In 2006, the European Union initiated the F-gas regulation to completely phase out gases with fluorine starting from 2017 [129]. This may have a large impact on the commercial refrigeration, air-conditioning and heat pump sectors. It has been abrogated in 2014 [57] to lengthen the list of bans. HCFCs and CFCs will be progressively prohibited in most of the new systems by 2025 depending mainly on the system, its power and the application ... National GWP taxes in some countries like Spain will also make them less attractive.

Some alternatives have already been identified. Cabello et *al.* [28] evaluated the performance of R152a as drop-in replacement for R134a in cascade refrigeration plants. The main drawback of this fluid remains its extreme flammability. From the review of Elbel [53] on ejector refrigeration systems working with CO_2, it appears clearly that such systems require high pressure levels and exhibit relatively low efficiencies. A new class of synthetic fluids, named HydroFluoroOlefins (HFO), has been recently developed and appears very promising. Among them, R1234yf and R1234ze(E) are two good candidates for drop-in replacement of R134a in ejector refrigeration systems. These are two environmentally friendly refrigerants compared to R134a because of their zero ODP and very low GWP as shown in Table 8.1.

working fluid	*R134a*	*R1234yf*	*R1234ze(E)*
Name	1,1,1,2 tetrafluoroethane	2,3,3,3 tetrafluoroprop-1-ene	1,3,3,3 tetrafluoroprop-1-ene
Chemical formula	CF_3CFH_2	$CH_2 = CFCF_3$	$CF_3CH = CHF$
Molecular weight ($g.mol^{-1}$)	102.03	114.04	114.04
Toxicity class (Ashrae Std 34)	A (low)	A (low)	A (low)
Flammability (Ashrae Std 34)	A1 (non flammable)	A2L (low flammability)	A2L (low flammability)
GWP_{100}	1430	4	4
Ozone Depletion Potential (ODP)	0	0	0
Lifetime in the atmosphere (year)	13	0.03	0.05
Normal boiling point ($^\circ C$)	-26.1	-29.4	-18.95
Saturated vapor pressure at $20^\circ C$ (kPa)	774.3	794.3	419.2
Saturated vapor pressure at $80^\circ C$ (kPa)	2635	2519	2007
Critical temperature ($^\circ C$)	101.1	94.7	109.4
Critical pressure (MPa)	4.059	3.38	3.635
Density ($kg.m^{-3}$) at $30^\circ C$			
Liquid phase	1187	1075	1146
Vapor phase	37.54	44	30.6
Heat capacity C_p ($kJ.kg^{-1}.K^{-1}$) at $30^\circ C$			
Liquid phase	1.446	1.379	1.383
Vapor phase	1.065	1.11	0.9822
Thermal conductivity k ($W.m^{-1}.K^{-1}$) at $30^\circ C$			
Liquid phase	0.079	0.0631	0.0725
Vapor phase	0.01433	0.01143	0.014
Dynamic viscosity μ ($\mu Pa.s^{-1}$) at $30^\circ C$			
Liquid phase	185.8	152	188
Vapor phase	12.04	12.86	12.5
Latent heat of vaporization at $30^\circ C$ ($kJ.kg^{-1}$)	173.1	140.1	162.9

Table 8.1 Thermodynamic properties of R134a, R1234yf and R1234ze(E). GWP_{100} is the Global Warming Potential over a 100 year integration horizon

The performances of an ejector heat driven refrigeration cycle are investigated with an emphasis on the supersonic ejector for different operating conditions and working fluids. Three working fluids are considered : R134a, R1234yf and R1234ze(E), as well as mixtures of these fluids in different proportions. The ejector geometry depicted in Figure 8.1 corresponds to the ejector developed by Garcia del Valle et *al.* [67]. Its key dimensions are summarized in Table 8.2.

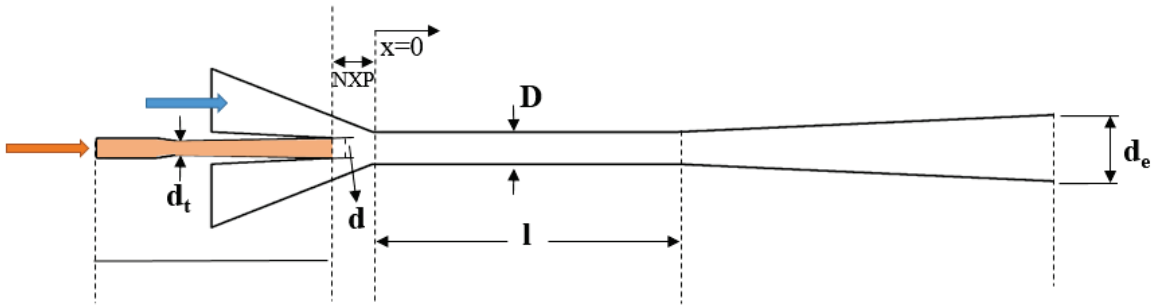

Figure 8.1 Schematic view of the ejector with relevant notations

Parameter	**Value** $[mm]$
Primary nozzle throat diameter, n_d	2.00
Primary nozzle exit diameter, d	3.00
Nozzle Exit Position, NXP	-5.38
Mixing chamber diameter, D	4.80
Mixing chamber length, l	41.39
Diffuser length, L	120.15
Diffuser exit diameter, e_d	20

Table 8.2 Main dimensions of the ejector

The experimental data of Garcia del Valle et *al.* [67] are used for the whole ejector heat driven refrigeration cycle shown in Figure 8.2 along with its pressure-enthalpy diagram. The complete process is the combination of two cycles. The inferior loop $(1-2-6-7-8)$ is similar to a standard refrigeration cycle with the compressor stage substituted by the superior loop $(1-2-3-4-5)$. This configuration is very attractive for air-conditioning applications especially, since the whole cycle is driven mostly by low grade energy (heat input to the generator) and the pump requirement represents often less than 5% of the heat input in the calculations. An overheat added to the evaporator and to the condenser ensures that the fluid inside the ejector remains in the superheated (gas) phase. A well performing supersonic ejector is the key parameter for an efficient refrigeration cycle.
Typically, two parameters are used to quantify the performance of the ejector : the entrainment ratio (ω), which relates the secondary to primary mass flows and the compression ratio (p_r), which shows the pressure increase of the secondary flow across the process. These parameters are defined as follows :

$$\omega = \frac{\dot{m}_{secondary}}{\dot{m}_{primary}} \tag{8.1}$$

$$p_r = \frac{p_{out}}{p_{secondary}} \tag{8.2}$$

where the subscripts *primary*, *secondary* and *out* refer to the conditions of streams 5, 8 and 1 on Figure 8.2 respectively. The pressure and temperature at the inlets and outlet of the ejector used in the experiments of [67] are summarized in Table 8.3. These values were obtained for R134a and include a $10K$ overheat at both inlets. In order to substitute R134a by HFO refrigerants, R1234yf and R1234ze(E), two options are considered : (i) keeping the operating conditions unchanged or (ii) maintaining the same primary inlet temperature (T_p) and adjusting the pressures along the ejector to achieve the $10K$

overheat and same pressure ratios as for pure R134a. The resulting operating conditions for the latter approach are summarized in Table 8.4. Two HFC-HFO mixtures, namely R134a-R1234yf and R134a-R1234ze(E), are investigated for mass fractions of R134a in the mixture ranging from 0% (pure HFO) to 100% (pure R134a).

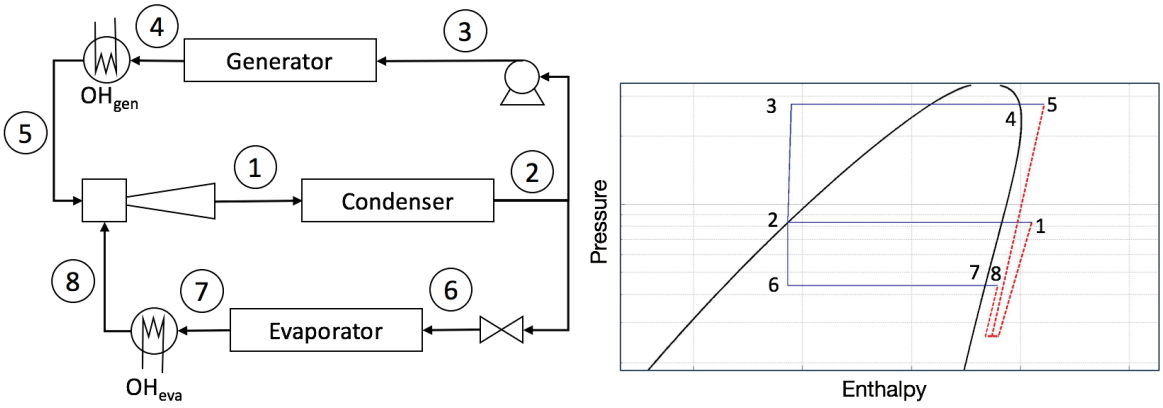

(a) (b)

Figure 8.2 Ejector heat driven refrigeration cycle : (a) Flow diagram and (b) Pressure-enthalpy diagram

Operation Point	$T_{primary}$ $[^oC]$	$T_{secondary}$ $[^oC]$	$p_{primary}$ $[kPa]$	$p_{secondary}$ $[kPa]$	p_{out} $[kPa]$	$p_{primary}/p_{out}$ $[-]$	$p_{out}/p_{secondary}$ $[-]$	$p_{primary}/p_{secondary}$ $[-]$
1	89.35	20.05	2598.0	414.6	757.2	3.43	1.83	6.27
2	94.35	20.05	2888.8	414.6	826.6	3.49	1.99	6.97
3	99.15	20.05	3188.1	414.6	897.1	3.55	2.16	7.69

Table 8.3 Operating conditions for the ejector corresponding to the experiments of Garcia del Valle et *al.* [67]

Operation Point	$T_{primary}$ $[^oC]$	**R1234yf**			**R1234ze(E)**		
		$p_{primary}[kPa]$	$p_{secondary}[kPa]$	$p_{out}[kPa]$	$p_{primary}[kPa]$	$p_{secondary}[kPa]$	$p_{out}[kPa]$
1'	89.35	2487.2	396.9	724.9	1980.5	316.1	577.2
2'	94.35	2753.9	395.3	788.0	2203.5	316.2	630.5
3'	99.15	3028.8	393.9	852.3	2432.5	316.3	684.5

Table 8.4 Operating conditions for the ejector adjusted for the HFO refrigerants R1234yf and R1234ze(E), keeping the same primary inlet temperature, pressure ratios and overheat as in the experiments of Garcia del Valle et *al.* [67]

The governing equations of continuity, momentum and energy for a steady state, compressible, 2D axisymmetric flow are solved using a finite volume approach. The advective and diffusive terms are discretized using second-order upwind and second-order central difference schemes, respectively. Gradients are evaluated using a least-square procedure. The resulting system of algebraic equations is solved using a full coupled pressure-based solver. Although density-based solvers are traditionally preferred for supersonic flows with shock-waves, pressure-based solvers have been successfully applied in supersonic ejectors [108, 195, 205] while exhibiting a better convergence compared to a density-based solver. High-order term relaxation coefficients are applied to ensure convergence smoothness. Turbulence effects are modeled using the $k-\omega$ SST model in its low-Reynolds formulation. The low-Reynolds approach implies that no wall functions are used and the flow is then resolved throughout the boundary layer up to the walls. Fluid properties for pure refrigerants and mixtures are calculated using the NIST Database [104]. The present Computational Fluid Dynamics (CFD) model is fully described in former papers [43, 44] and showed better performances in terms of entrainment ratio and shock-wave structure compared to other combinations of turbulence and thermodynamic modellings.
For all cases, a structured grid composed of 650000 elements has proven to be sufficient to get grid independent solutions, while guaranteeing a wall coordinate y^+ lower than unity as required for low-Reynolds formulation. Total pressure and temperature are imposed at the ejector inlets and static pressure is fixed at the outlet (Tables 8.3 and 8.4). The inlet velocities are assumed to be negligible and walls are considered as adiabatic with no-slip.

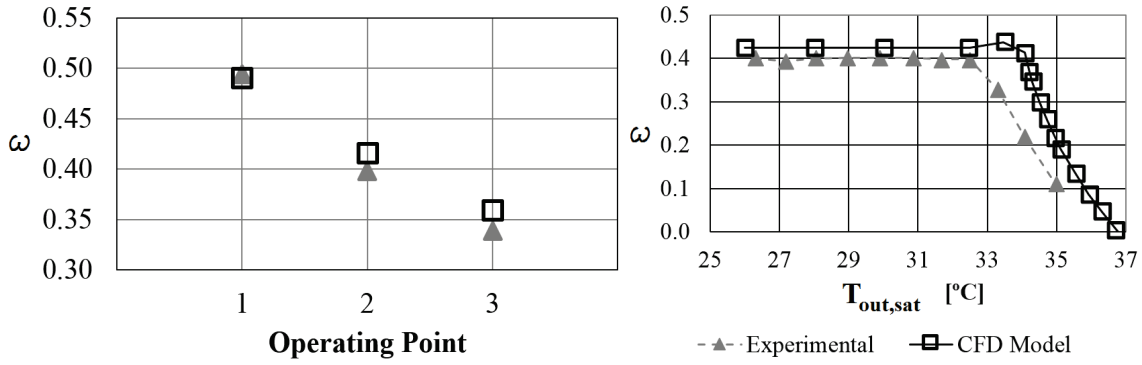

(a) (b)

Figure 8.3 Validation of the ejector CFD model versus the experimental data of Garcia del Valle et *al.* [67] : (a) Entrainment ratio for three inlet conditions ; (b) Entrainment ratio versus outlet saturation temperature for fixed inlet conditions corresponding to OP2. Results obtained for R134a

The CFD model is validated by comparing the predicted entrainment ratio to the experimental results of Garcia del Valle et *al.* [67] for pure R134a. Figure 8.3a shows the

change in entrainment ratio for varying conditions given in Table 8.3. At OP1, the deviation is within 2% of the experimental value, increasing to about 5% for OP3. Figure 8.3b compares the experimental [67] and calculated ejector operating curves for fixed inlet conditions corresponding to OP2. The difference between the predicted and experimental critical point temperature is less than 0.5%, showing that the model is thus capable of correctly estimating the entrainment ratio and the critical operating point of the ejector. Although the model validation is shown solely for R134a due to the lack of experimental data for HFOs, the similarities in properties among R134a, R1234yf and R1234ze(E) allow to assume similar deviations regarding the numerical calculations with HFOs.

Table 8.5 shows the variation in entrainment ratio when using R134a or R1234yf at fixed operating conditions (Table 8.3). For R1234ze(E), single-phase operation is maintained only at OP1, and hence is not considered in this part. For the three conditions, the change from R134a to R1234yf implies a slight decrease in terms of the entrainment ratio of 4% to 6.9%. As shown in Table 8.5, this difference is associated for the three operating conditions with both increased primary and secondary mass flows when using pure R1234yf.

	$\dot{m}_{primary}$ $[kg \cdot s^{-1}]$		$\dot{m}_{secondary}$ $[kg \cdot s^{-1}]$		ω $[-]$	
	R134a	R1234yf	R134a	R1234yf	R134a	R1234yf
OP1	0.0335	0.0357	0.0172	0.0176	0.5126	0.4919 (-4.0%)
OP2	0.0375	0.0401	0.0164	0.0167	0.4364	0.4165 (-4.6%)
OP3	0.0417	0.0450	0.0158	0.0160	0.3804	0.3543 (-6.9%)

Table 8.5 Comparison of primary and secondary mass flows and entrainment ratio for pure R134a and R1234yf at the operating conditions given in Table 8.3. The percentages indicate the deviations compared to the case with pure R134a

The effect of changing the working fluid while keeping $T_{primary}$ and the same pressure ratios (Table 8.4) is shown in Table 8.6 for the three pure refrigerants. Regarding the entrainment ratio, a slight decrease is also observed when changing from R134a to R1234yf, although the difference is weaker compared to the cases shown in Table 8.5. On the other hand, using R1234ze(E) leads to an augmentation in entrainment ratio of about 3.5% in average for the three operating conditions relative to R134a. Nonetheless, Table 8.6 shows an important decrease of the mass flow rates when R1234ze(E) is used in comparison with R134a for OP1' (Table 8.4) : 22.1% and 20.9% for the primary and secondary inlets, respectively. This tendency is alike for operating points 1', 2' and 3' of Table 8.4.

	$\dot{m}_{primary}$ $[kg \cdot s^{-1}]$			$\dot{m}_{secondary}$ $[kg \cdot s^{-1}]$			ω $[-]$		
	R134a	R1234yf	R1234ze(E)	R134a	R1234yf	R1234ze(E)	R134a	R1234yf	R1234ze(E)
OP1'	0.0335	0.0338	0.0261	0.0172	0.0170	0.0136	0.5126	0.5044 (-1.6%)	0.5201 (+3.1%)
OP2'	0.0375	0.0376	0.0292	0.0164	0.0162	0.0130	0.4364	0.4297 (-1.5%)	0.4442 (+3.4%)
OP3'	0.0417	0.0417	0.0323	0.0158	0.0157	0.0126	0.3804	0.3752 (-1.4%)	0.3907 (+4.1%)

Table 8.6 Comparison of primary and secondary mass flows and entrainment ratio for R134a, R1234yf and R1234ze(E) at the operating conditions of Table 8.4. The percentages indicate the deviations compared to the case with pure R134a

The numerical results for the HFO-R134a mixtures are discussed in the following. In Figure 8.4a, the entrainment ratio is presented as a function of the mass fraction of R134a in both HFO-R134a mixtures. For a mixture with 20% of R134a, the R1234yf mixture provides a higher entrainment ratio than the R1234ze(E) mixture at OP1. With an increasing percentage of R134a in both mixtures, the entrainment ratio increases in both cases. When the proportion of R134a reaches 60%, the two mixtures have the same entrainment ratio which means that, from the 60% R134a fraction onwards, the properties of the HFC dominate the mixture. Moreover, increasing the R134a in the mixture can improve the entrainment ratio for R1234ze(E) from 0.45 to 0.5 and for R1234yf from 0.48 to 0.5. The differences being not quite large, in terms of entrainment ratio, the R1234yf appears as a better potential substitute of R134a in future refrigeration systems than R1234ze(E). Note that for pure R1234ze(E) at OP1, the fluid is a mixture of liquid and gas phases, and so it has not been simulated here.

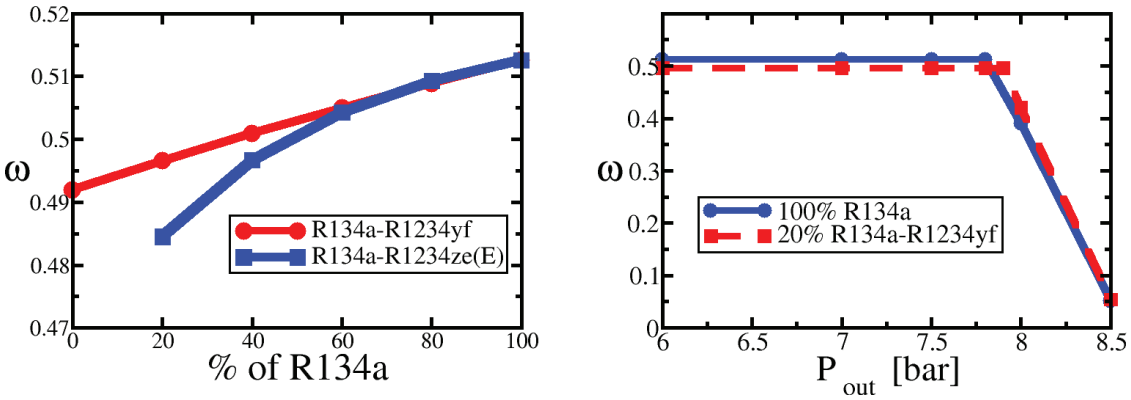

(a) (b)

Figure 8.4 (a) Variation in ejector entrainment ratio with the percentage of R134a for mixtures of R134a-R1234yf and R134a-R1234ze(E) at OP1; (b) Variation of entrainment ratio versus outlet pressure for OP1 between R134a and mixture R134a-R1234yf. Results obtained at the Operating Conditions 1 of Table 8.3

Figure 8.4b compares the entrainment ratio ω as a function of the outlet pressure for pure R134a and a mixture composed of 20% R134a - 80% R1234yf. The R134a provides a slightly higher entrainment ratio (+4.0%) at on-design conditions compared to the R1234yf-R134a mixture. However, the critical outlet pressure is slightly higher for the R134a-R1234yf mixture ($p_{out,c} = 7.9$ bars, +1.3% compared to the case with pure R134a) expanding the range of on-design conditions. The limit critical outlet pressure remains the same ($p_{out,lc} = 8.55$ bars) for both fluids.

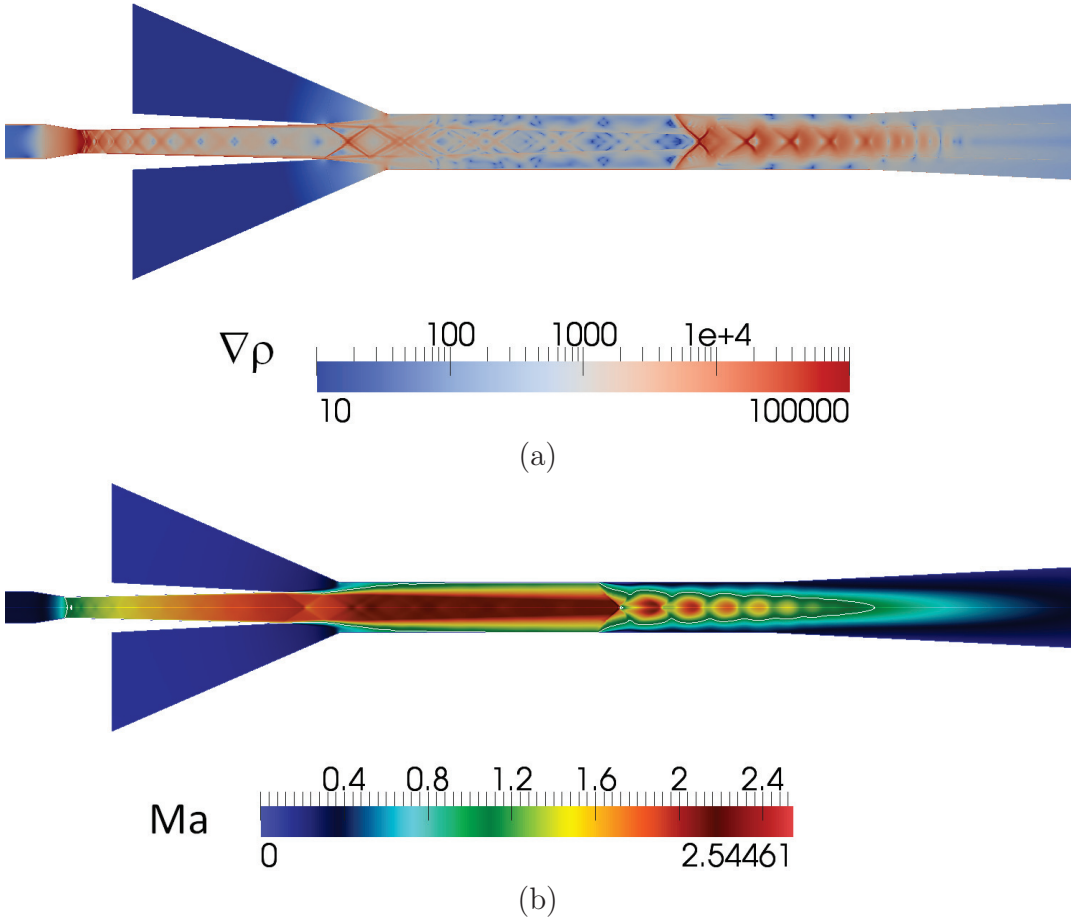

Figure 8.5 Iso-contours along the ejector of the (a) density gradient $\nabla\rho$ and (b) Mach number Ma for 40% of R134a in a R134a-R1234ze(E) mixture. Results obtained at the Operating Conditions 1 of Table 8.3

Figures 8.5a and b show iso-contours of the density gradient and Mach number along the ejector for 40% of R134a in a R134a-R1234ze(E) mixture at OP1. The iso-contours of the density gradient enable to visualize more easily the intensity and the structure of the shock train as well as relaxation waves, which appear in the divergent part of the primary nozzle. A train of oblique relaxation waves appears at the throat of the primary nozzle and gets progressively weaker when moving to the outlet. A second train of oblique relaxation

waves appear also at the outlet section of the primary nozzle. Reflexions with the wall of the constant section area may be also observed. From the contours of the density gradient, the train of oblique shock-waves is also clearly visible in the latter half of the constant section together with Mach disks. Figure 8.5b presents the Mach number distribution for the same case and highlights in particular the sonic line (white line) for which $Ma = 1$. It confirms two results formerly published in the literature : for the primary fluid, the sonic condition is obtained just after the throat as already observed by Garcia del Valle et *al.* [68] and the mixing between the primary and secondary fluids is mainly due to the shear stress between the two flows as demonstrated by Croquer et *al.* [44]. Note that similar behaviors have been obtained for the other mixtures. Changing the percentage of R134a in the mixture just shifts the shock train at other locations within the constant section area.

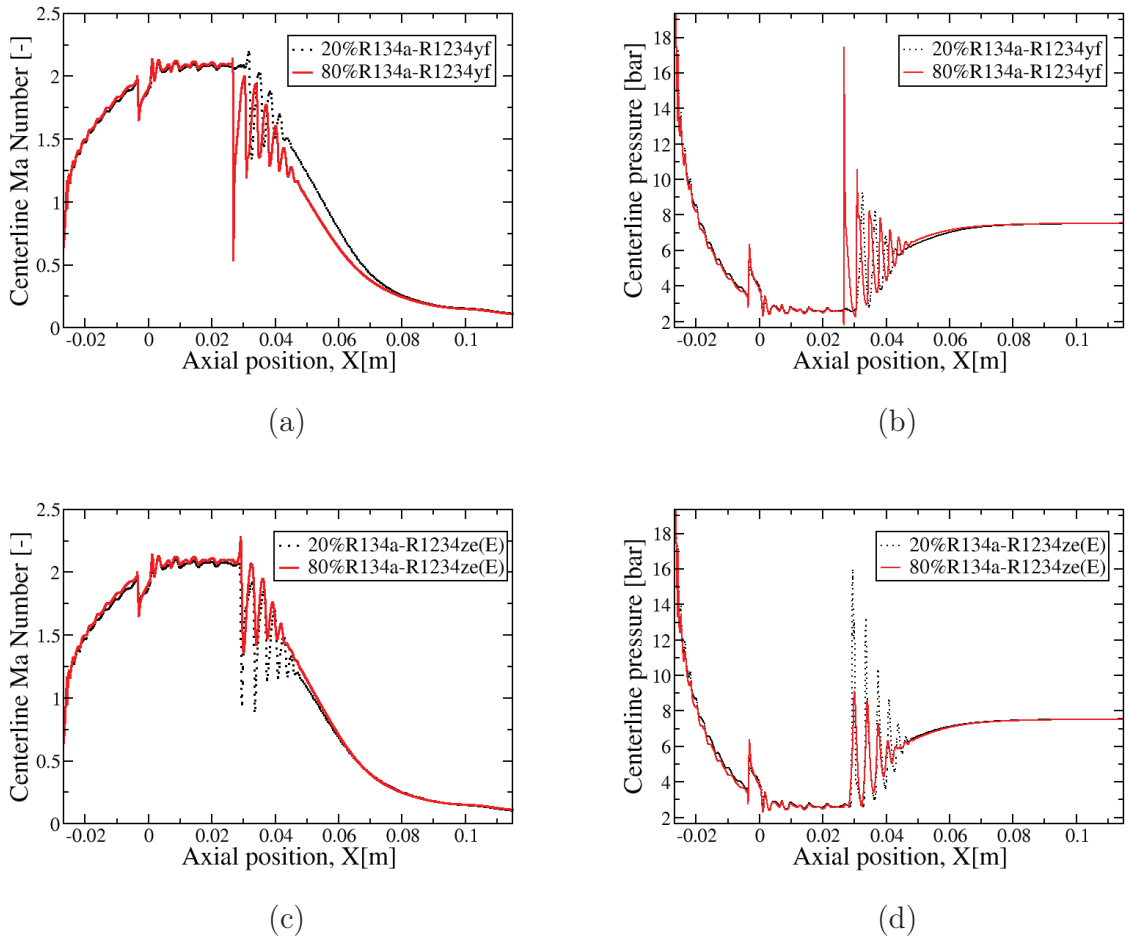

Figure 8.6 Distributions along the ejector centerline of the (a,c) Mach number Ma and (b,d) static pressure p for mixtures of R134a with (a,b) either 20% or 80% of R1234yf then (c,d) either 20% or 80% of R1234ze(E). Results obtained at the Operating Conditions 1 of Table 8.3

In order to analyze more precisely the pressure and Mach number changes, distributions of these quantities along the ejector center-line for the R134a-R1234yf and R134a-R1234ze(E) mixtures are shown in Figure 8.6. The three fluids having similar properties, there are no large differences by varying the proportion of R134a between 20% and 80%, except in the shock-train region. It is observed that in the latter half of the constant section (from 0.02 to 0.05 m), where the shocks develop, the mixture with more R1234yf provides lower pressure. For example, at the first pressure jump, the difference is around 7.10^6 Pa. The intensity of the first pressure jump does not vary monotonously with the proportion of HFO (not shown here) but the intensity of the shock train remains always weaker for R1234ze(E). Concerning the position of the shock-train, identified by the first pressure drop, it starts

earlier when using R1234yf rather than R1234ze(E) for the same proportion of R134a. By increasing the percentage of R134a, the shock-train appears earlier in the constant section area for R1234yf but it does not change its position for R1234ze(E).

One major drawback of R1234ze(E) lies in the higher friction losses obtained compared to R134a [95]. High friction losses (up to 2.5 times compared to R1234ze(E)) are the main reason for which R1234ze(Z) is not considered so far for refrigeration or heating applications [95]. In 1D thermodynamic models, these friction losses are taken into account either by introducing efficiency coefficients [204] or friction coefficients [181]. To compare the three present refrigerants, let us consider the friction coefficients introduced by Untea et *al.* [181] to reduce the streamwise velocity because of gas friction. They defined the three following coefficients :

$$\Phi_1 = \frac{v_1}{\sqrt{2(h_0 - h_1)}} \tag{8.3}$$

$$\Phi_2 = \frac{v_2(1+\omega)}{v_1} \tag{8.4}$$

$$\Phi_3 = \sqrt{\frac{h_{3s} - h_2}{h_3 - h_2}} \tag{8.5}$$

where the indexes 0 and 1 denote quantities evaluated at the inlet and outlet of the primary nozzle respectively, 2 at the outlet of the constant section area and 3 at the outlet of the diffuser. v represents the magnitude of the velocity vector, ω the entrainment ratio and h the static enthalpy. Note that h_{3s} is the enthalpy at the outlet of the diffuser for an isentropic transformation.

	OP1		OP2		OP3		Untea et *al.* [181]	
	R134a	R1234yf	R134a	R1234yf	R134a	R1234yf	R134a	Range
Φ_1	1.000	1.000	1.000	1.000	1.000	1.000	0.95	0.92-0.96
Φ_2	0.712	0.717	0.629	0.653	0.609	0.611	0.975	-
Φ_3	0.839	0.825	0.847	0.822	0.854	0.852	0.9	0.88-0.92

	OP1'			OP2'			OP3'		
	R134a	R1234yf	R1234ze(E)	R134a	R1234yf	R1234ze(E)	R134a	R1234yf	R1234ze(E)
Φ_1	1.000	1.000	1.000	1.000	1.000	1.000	1.000	1.000	1.000
Φ_2	0.675	0.727	0.636	0.625	0.676	0.634	0.601	0.586	0.614
Φ_3	0.822	0.847	0.877	0.841	0.995	0.849	0.871	0.836	0.87

Table 8.7 Friction losses in the three characteristic sections for the three pure refrigerants

The results obtained for the three friction coefficients for the six operating conditions, namely OP1 to 3 and OP1' to 3', are summarized in Table 8.7 and compared to the values used by Untea et *al.* [181]. The friction losses are almost negligible in the primary nozzle such that $\Phi_1 \simeq 1$. This result is not surprising as by construction, Φ_1 reflects the

conservation of energy for an adiabatic system. In the same way, the friction losses in the diffuser are also quite weak as Φ_3 varies between 0.839 for R134a, 0.825 for R1234yf at OP1 to 0.854 for R134a, 0.852 for R1234yf at OP3. The global values used by these authors for sections 1 (primary nozzle) and 3 (diffuser) appear to be relatively reliable for the present configuration. On the contrary, the predicted friction coefficient for section 2 (mixing chamber) is much lower than the one proposed by [181] : 0.609 for R134a and 0.611 for R1234yf at OP3, far from $\Phi_2 = 0.975$. The friction losses are much higher in the mixing area than in the two other sections and the recommended value seems to be inappropriate. It can be also noticed that similar values of Φ_1, Φ_2 and Φ_3 are obtained for R134a and R1234yf whatever the operating conditions (OP1 to 3). Between R1234yf and R1234ze(E) at OP1'-3', it is observed that R1234ze(E) provides always slightly higher Φ_3 than R1234yf, which means that in section 3 (diffuser), R1234ze(E) has less friction losses than R1234yf. Globally, both HFOs induce very similar friction losses. The present conclusions may be fully explained by the slight differences in terms of dynamic viscosity between the three refrigerants (Table 8.1).

Appendix B : Theoretical formulations of EoS and their implementations in CLAWPACK

The Peng-Robinson EoS is a classical cubic form EoS, which can provide relatively reasonable results in the high-pressure and vapor regions for most fluids. However, it is also well known that in the two-phase region, the speed of sound could become negative and generate unphysical wave propagation. Therefore, the Peng-Robinson EoS is only used here for the simulations of CO_2 vapor. The general Peng-Robinson EoS reads [139] :

$$p = \frac{RT}{v-b} - \frac{a}{v(v+b)+b(v-b)} \tag{8.6}$$

where $b = 0.77796\frac{RT_c}{\rho_c}$ represents the covolume. The second term takes into account the attractive forces between molecules, with $a = 0.45724\frac{R^2T_c^2}{\rho_c}$. We note that the formulation of the Peng-Robinson EoS is based on variables ρ and T, therefore an iterative process is needed to compute the corresponding (ρ, T) for given (ρ, e), as :

$$F(\rho, T) = e - e(\rho, T) \tag{8.7}$$

Once the variables are transformed from (ρ, e) to (ρ, T), the pressure can be computed by Equation (8.6) and the speed of sound is expressed as follows :

$$c^2 = -v^2 \frac{c_p}{c_v} \left(\frac{\partial p}{\partial v}\right)_T \tag{8.8}$$

with

$$\left(\frac{\partial p}{\partial v}\right)_T = \frac{-RT}{(v-b)^2} + \frac{2a(v+b)}{(v(v+b)+b(v-b))^2} \tag{8.9}$$

where c_p and c_v are the isobaric heat capacity and the volumetric heat capacity, respectively. The formulations of the heat capacities refer to Equations (10) to (18) in the paper of Pratt [139].

The Stiffened-Gas EoS is the linearization of the Mie-Grüneisen EoS, which is widely applied for steam-water simulations. It is also used here to assess the proposed tabulated EoS in terms of accuracy and computational time in Section 4.2.3. The formulation of the Stiffened-Gas reads :

$$p = (\gamma - 1)(e - q)\rho - \gamma P_\infty \tag{8.10}$$

where γ, q and P_∞ are parameters chosen by the user. Hence, the accuracy of the EoS depends greatly on these parameters. Furthermore, the linear form of the EoS does not

ensure the accuracy in the non-linear region, such as in the neighborhood of the critical point. The errors are shown also in terms of the first-order derivatives of the thermodynamic properties, as seen for the speed of sound (Figure 4.9). We note that ρ and e are the variables of Equation (8.10), thus no iterative process is required to transform the variables. The computations then are extremely fast. The speed of sound can be computed as follows [64] :

$$c^2 = \gamma \frac{p + P_\infty}{\rho} \tag{8.11}$$

Appendix C : CLAWPACK 1D cases

1D numerical tests are performed through the CLAWPACK solver for the shock tube, cavitation and double shock problems. The vapor, liquid, and two-phase conditions are evaluated through these problems. These kinds of numerical simulations are generally used to assess a new solver, two-phase models, or equation of states for various fluids. However, the numerical or experimental works on CO_2 are limited in the literature. The existing works for the shock tube and depressurization problems have been presented in Chapter 4. The cavitation and double shock problems of CO_2 are simulated and presented here.

Two-phase shock tube

The single phase shock tube problem has been already validated. Here, a two-phase shock tube problem is presented, where the left side is filled with the liquid CO_2 and the right side is filled with the vapor CO_2. No initial velocity is imposed for both side flows. The shock and the expansion waves are generated by the differences of pressure and density. The left-side state is $p = 6.7$ MPa, $T = 245.7$ K, and $\rho = 679.2\ kg.m^{-3}$, whereas the right-side state is $p = 1.99$ MPa, $T = 220.7$ K, and $\rho = 52\ kg.m^{-3}$. Figure 8.7 shows that the pressure, density, velocity profiles are similar compared to the single phase shock tube. However, considering the vapor mass fraction profile, a two-phase region can be observed in the middle of the tube. It is also observed that the phase transition across the shock is faster than that across expansion waves.

Cavitation (double rarefraction)

The cavitation problem is often used to assess the prediction of expansion waves. Initially, the tube is filled with one homogeneous fluid and then starting from the middle of the tube, the flow moves to the opposite direction (Figure 8.8). As a result, the expansion waves are created and propagate to each side and cavitation is generated in the middle of the tube. In this section, the cavitation is simulated for the pure vapour phase and pure liquid phase. Finally, the vaporisation is obtained due to cavitation.

Vapor

CO_2 vapor is initially filled in the tube with $p = 1$ MPa, $T = 300$ K, $\rho = 18.579\ kg.m^{-3}$. The velocity is set to 20 $m.s^{-1}$ for the opposite direction. The results are presented at $t = 1.44$ ms. The profiles of pressure, density, velocity, and vapor mass fraction are shown in Figure 8.9. It can be seen that the expansion waves are well captured by the solver,

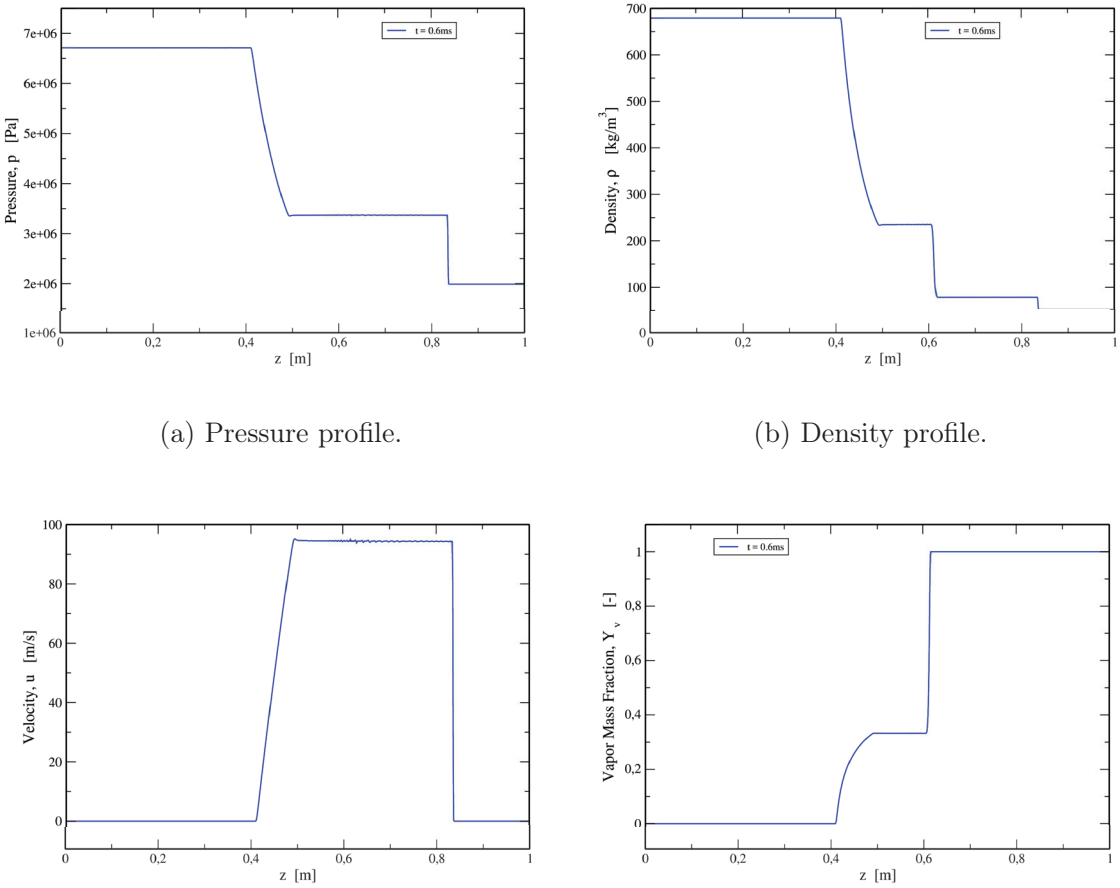

(a) Pressure profile.

(b) Density profile.

(c) Velocity profile.

(d) Vapor mass fraction profile.

Figure 8.7 Liquid-vapor shock tube.

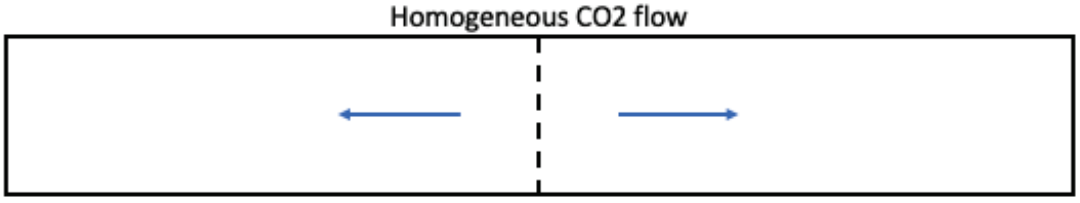

Figure 8.8 Cavitation problem.

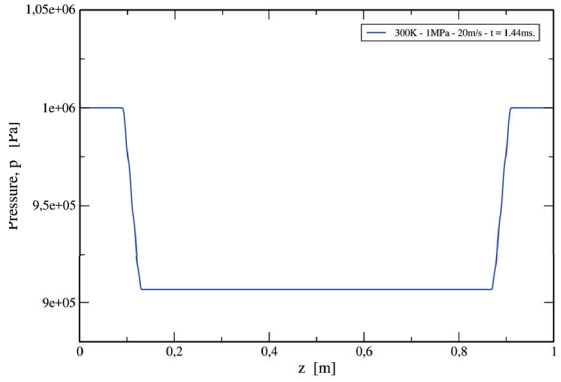

(a) Pressure profile.

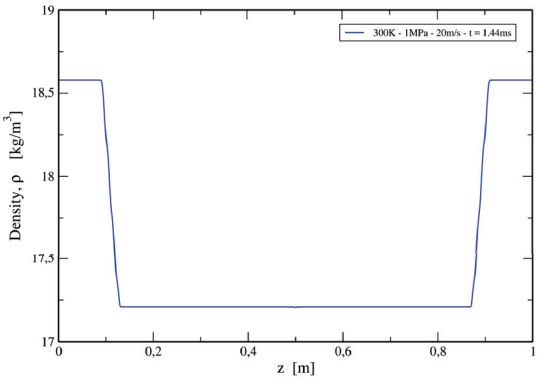

(b) Density profile.

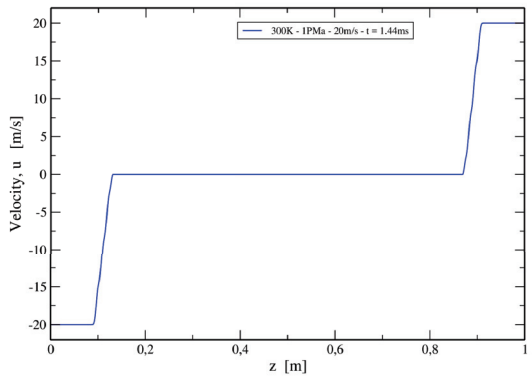

(c) Velocity profile.

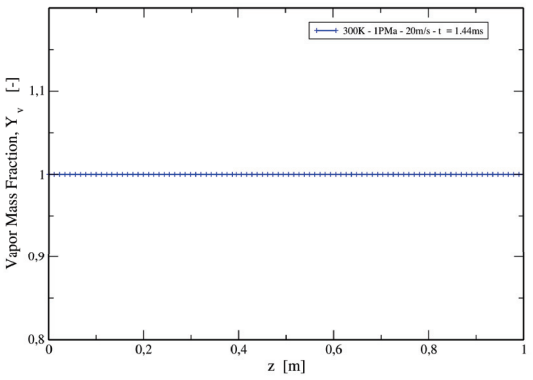

(d) Vapor mass fraction profile.

Figure 8.9 Vapor cavitation.

through they are very steep. The velocity is relatively high compared to the liquid case.

Liquid

In the liquid case, the tube is full of liquid with $p = 6$ MPa, $T = 250$ K, and $\rho = 1062.59$ $kg.m^{-3}$. The velocity is fixed to 0.2 $m.s^{-1}$. The simulation time is 0.6 ms in order to show the expansion waves clearly. The profiles of pressure, density, velocity, and vapor mass fraction are shown in Figure 8.10. It is noted that the simulation time for the liquid case is

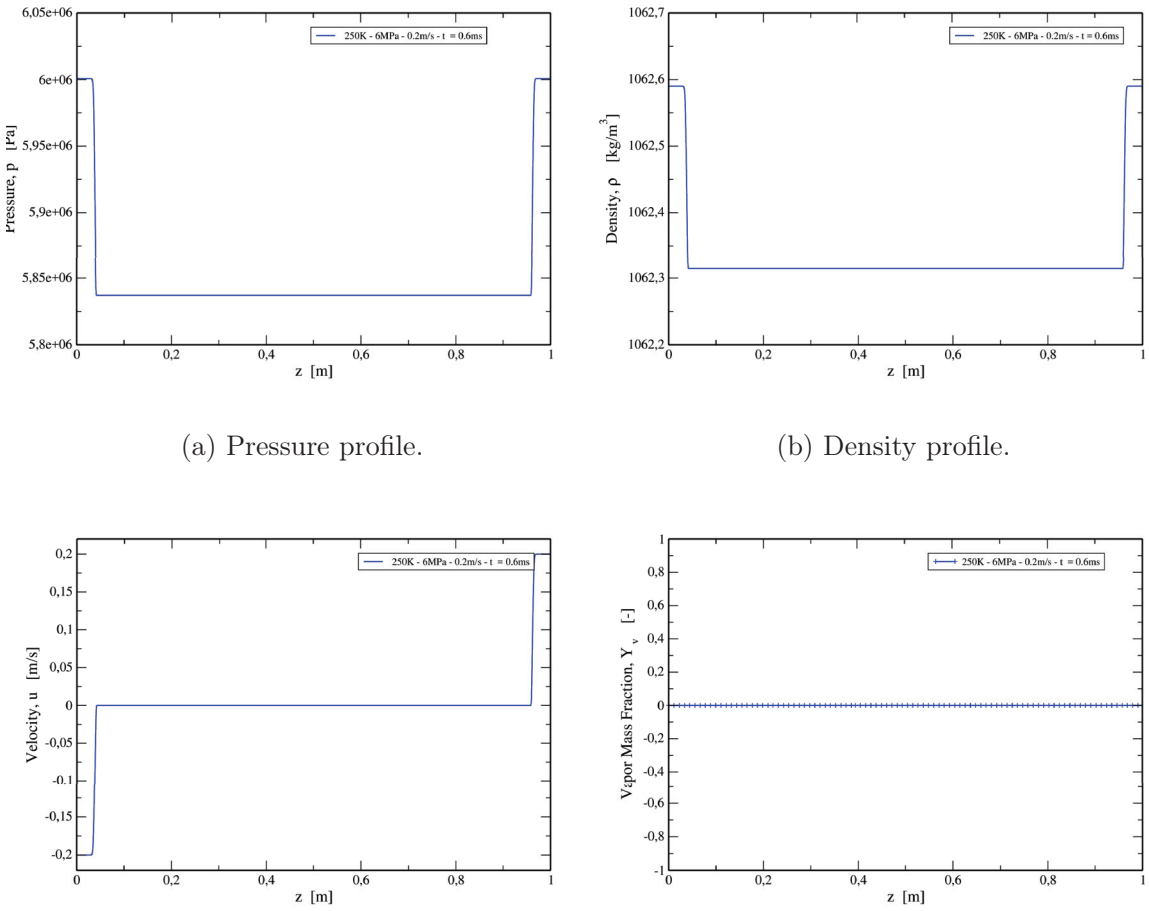

(a) Pressure profile.

(b) Density profile.

(c) Velocity profile.

(d) Vapor mass fraction profile.

Figure 8.10 Liquid cavitation.

shorter than the vapor case, just because the acoustic waves propagate faster in the liquid than in the vapor phase. For $u = 0.2$ $m.s^{-1}$, no vaporisation is observed.

Evaporation

In order to observe evaporation in the cavitation problem, the velocity is increased up to 8 $m.s^{-1}$. The initial state is $p = 8$ MPa, $T = 250$ K, and $\rho = 1069.7$ $kg.m^{-3}$. It is observed

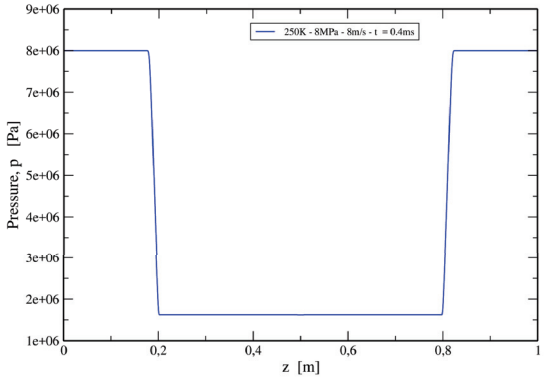

(a) Pressure profile.

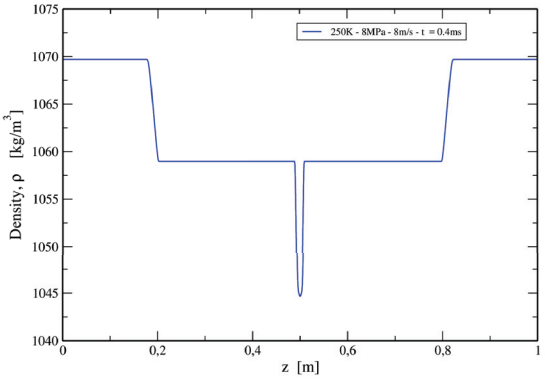

(b) Density profile.

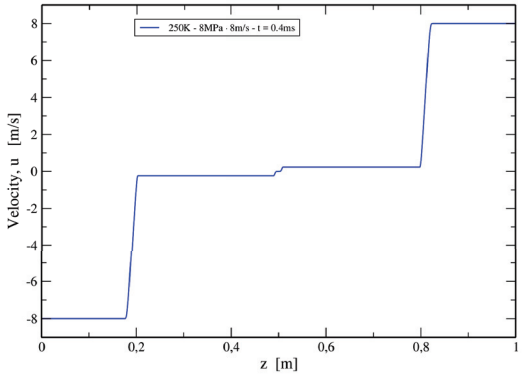

(c) Velocity profile.

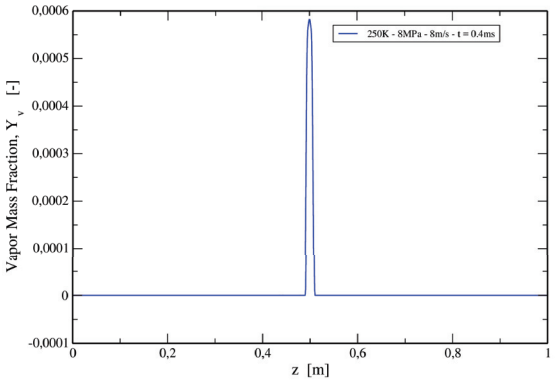

(d) Vapor mass fraction profile.

Figure 8.11 Cavitation problem with evaporation.

in Figure 8.11 that a small portion of the CO_2 vapor is created in the middle of the tube. This results in a significant decrease of the density.

Double shock

The double shock problem is similar to the shock tube problem. The difference is that as initial state, the fluids at the two sides of the tube have an initial counter-current velocity. As a result, one shock is created due to the counter-current velocity, the other shock is created due to the difference of initial states (density and pressure). The double shock problem is illustrated in Figure 8.12. In the following, the double shock is created

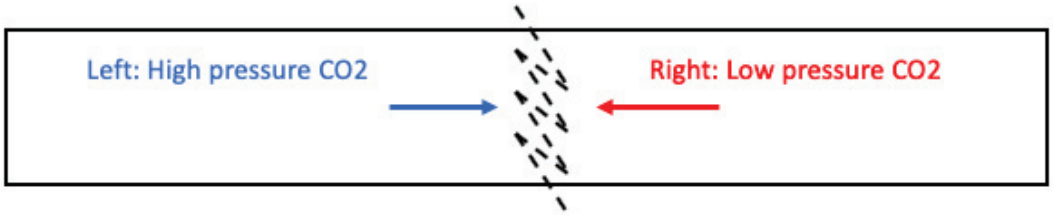

Figure 8.12 Double shock problem.

in vapor, liquid, and two-phase states.

Vapor

Considering only the pure vapor phase for the double shock problem, the left-side state is $p = 6$ MPa, $T = 400$ K, $\rho = 89.16\ kg.m^{-3}$, and $u = 200\ m.s^{-1}$, whereas the right-side state is $p = 4$ MPa, $T = 305$ K, $\rho = 88.54\ kg.m^{-3}$, and $u = -100\ m.s^{-1}$. The profiles of pressure, density, velocity, and vapor mass fraction are shown in Figure 8.13.

Two shocks are observed, one propagating to the left side while the other one propagates to the right side. Moreover, the intensity of the two shocks are quite comparable.

Liquid

The velocity ratio is the same as for the vapor case. The left-side state is $p = 4$ MPa, $T = 225$ K, $\rho = 1155.43\ kg.m^{-3}$, and $u = 2\ m.s^{-1}$, whereas the right-side state is $p = 1$ MPa, $T = 225$ K, $\rho = 1148.32\ kg.m^{-3}$, and $u = -1\ m.s^{-1}$.

Figure 8.14 shows that the left shock exhibits a lower intensity than the right one.

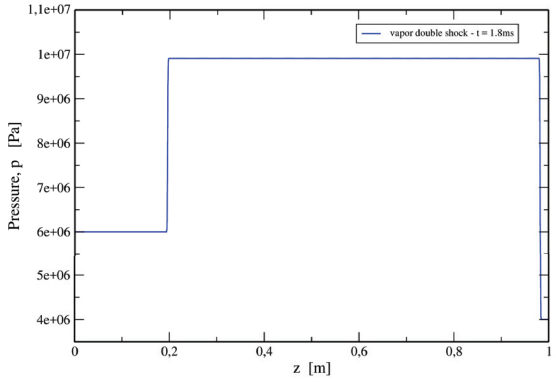

(a) Pressure profile.

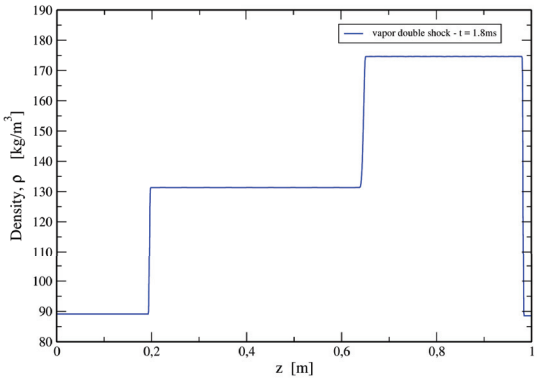

(b) Density profile.

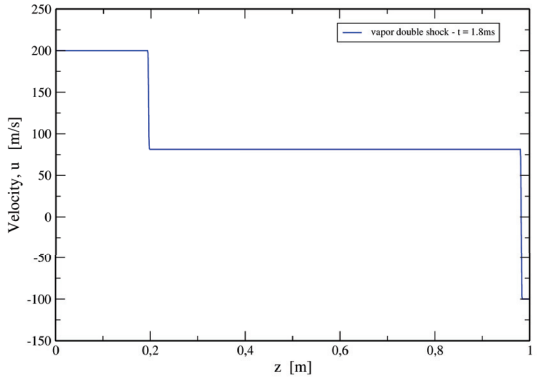

(c) Velocity profile.

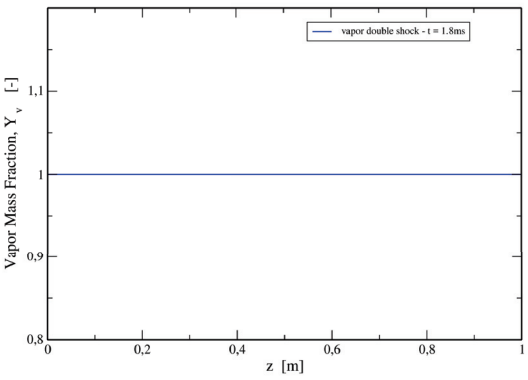

(d) Vapor mass fraction profile.

Figure 8.13 Vapor double shock problem.

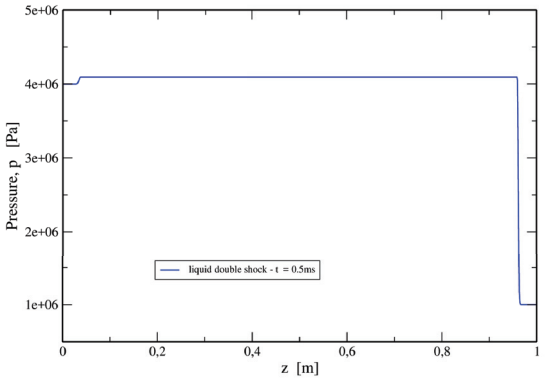

(a) Pressure profile.

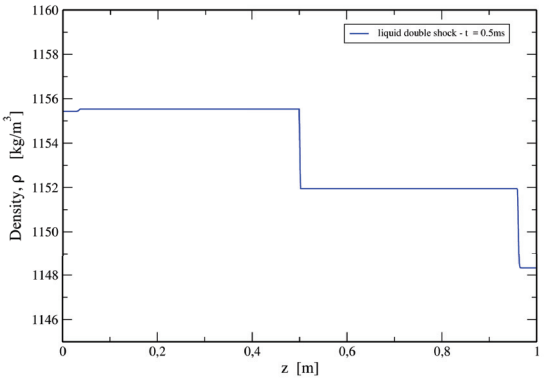

(b) Density profile.

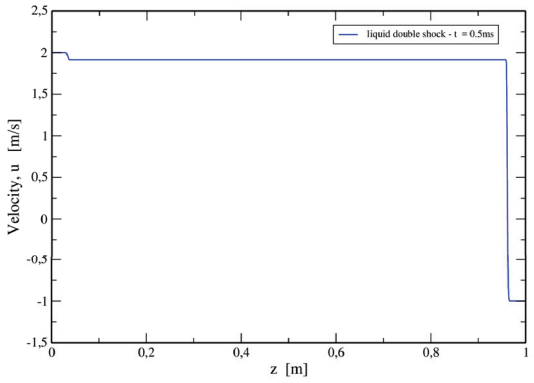

(c) Velocity profile.

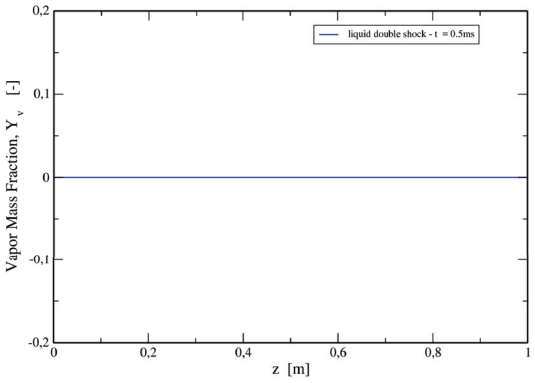

(d) Vapor mass fraction profile.

Figure 8.14 Liquid double shock.

Appendix D : Verification cases for the AVBP solver

Three verification cases are shown here, namely a shock tube problem (Figure 8.15), a cavitation problem (Figure 8.16), and a depressurizaion problem (Figure 8.17). For the shock tube problem, it can be seen that there are small oscillations at the contact surface in terms of density and temperature. However, good agreements are obtained compared to the CLAWPACK solver in terms of pressure and velocity.

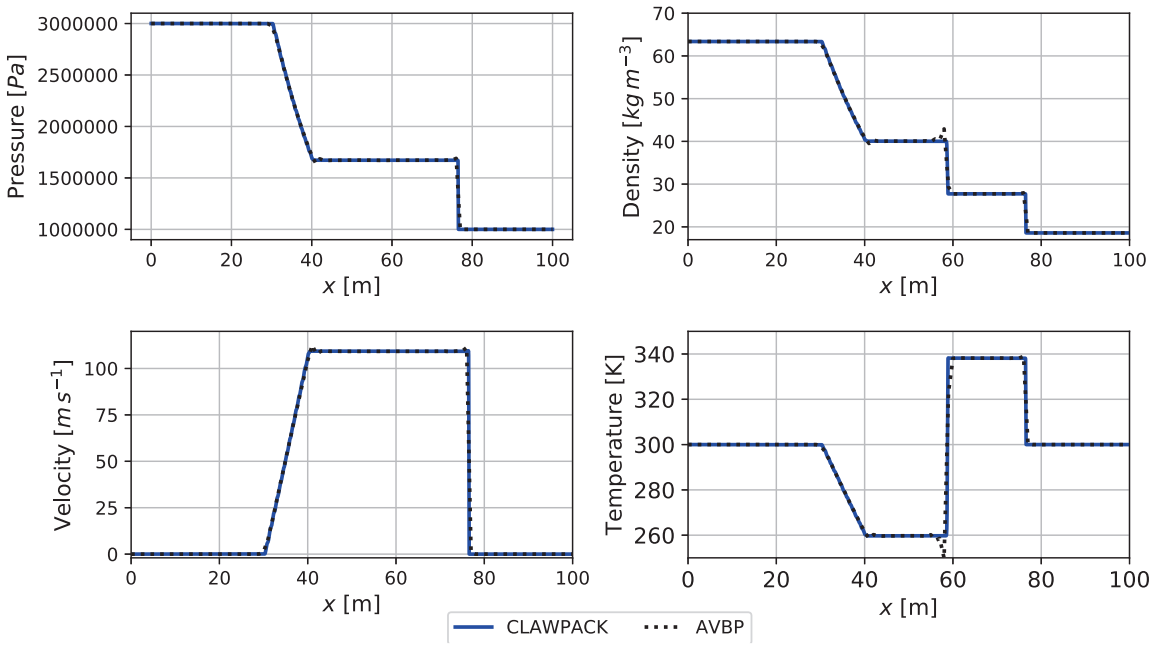

Figure 8.15 Comparison between the AVBP and CLAWPACK solvers for the shock tube problem.

For the cavitation problem, large diffusions are observed at discontinuities. Indeed, in the AVBP solver, in order to capture the discontinuities, an artificial viscosity is applied. When the discontinuities are too steep, the artificial viscosity causes a large diffusion in order to avoid numerical instabilities.

For the depressurization problem, good agreements with the CLAWPACK solver are obtained for all variables.

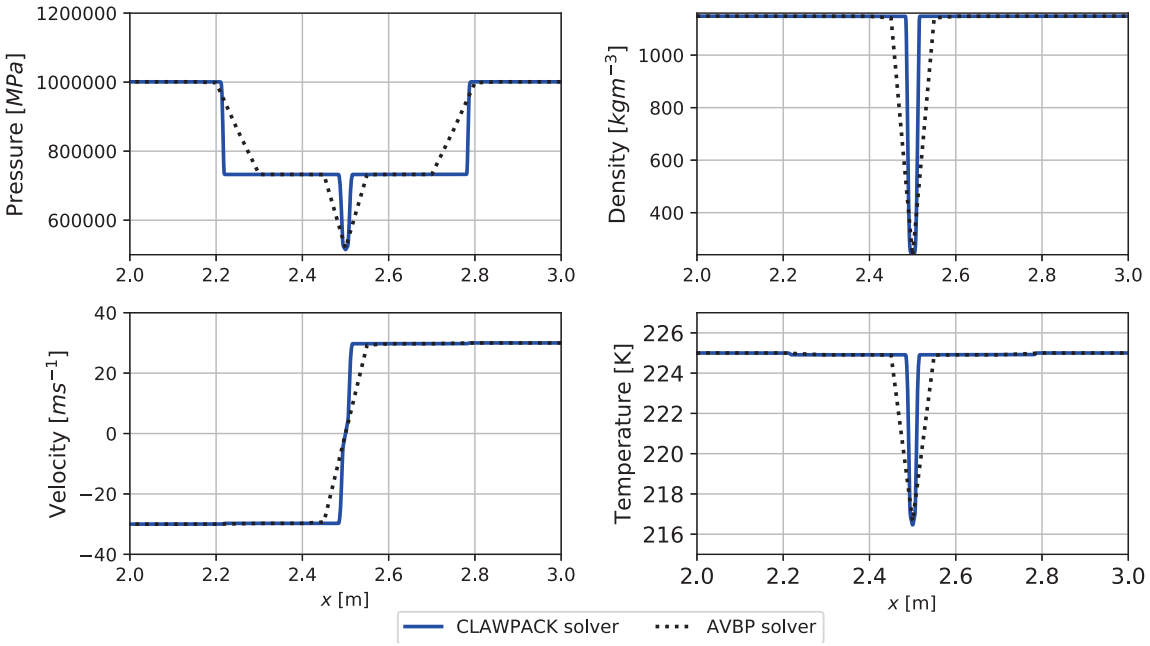

Figure 8.16 Comparison between the AVBP and CLAWPACK solvers for the cavitation problem.

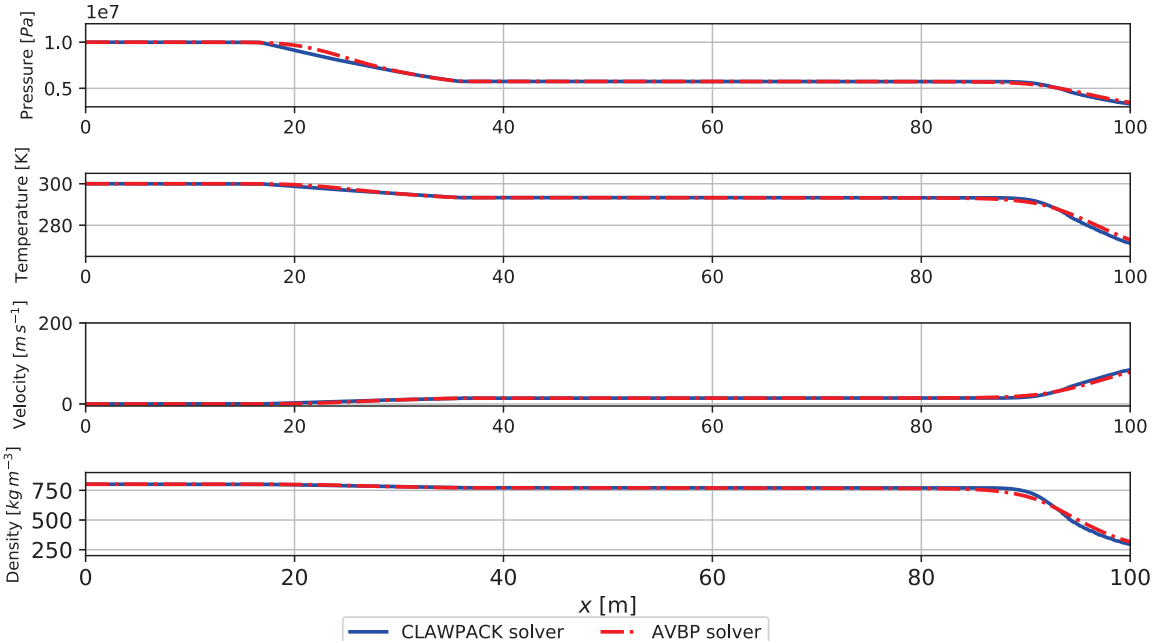

Figure 8.17 Comparison between the AVBP and CLAWPACK solvers for the depressurization problem.

Appendix E : Ejector of LTE

Experimental test facility

Experimental tests have been carried out at Laboraoire des Technologies de l'Énergie (LTE) in Shawinigan (Canada). The cycle consisting in a condenser, an evaporator, an ejector and a generator has been produced by OBRIST Engineering. The whole system is depicted in Figure 8.18.

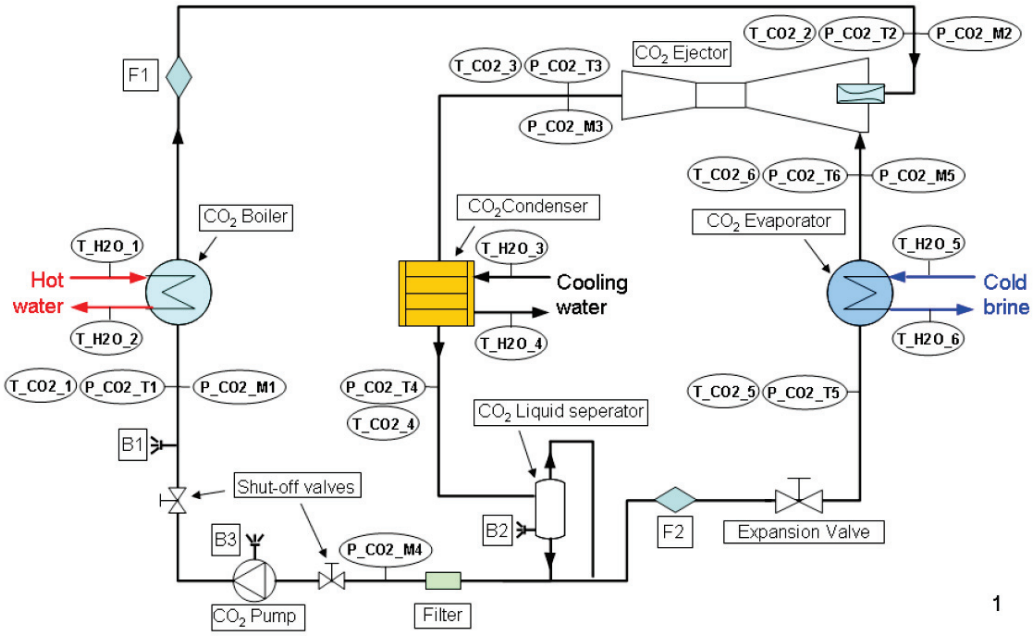

Figure 8.18 Standard ejector refrigeration system at LTE.

The temperature and the pressure of CO_2 can be registered at the inlet and outlet of the boiler, evaporator, condenser and ejector. The mass flow rates at the primary, secondary and outlet of the ejector are measured by mass flow meters. The full characteristics for each component are shown in Figure 8.19 together with their uncertainties.

The unit PSIG for the pressure means *pounds per square inch gauge*. For the primary and secondary inlets and the outlet of the ejector, 0, 1500, 2000 PSIG (relative to atmosphere) correspond to 1 bar, 104 bars and 137 bars, respectively.

Parameters	Symbol	Range	Accuracy
Hot water temperature (heat exchanger inlet)	T_H_2O_1	30-60°C	±0.5 °C
Hot water temperature(heat exchanger outlet)	T_H_2O_2	25-55°C	±0.5 °C
Boiler inlet temperature, CO_2	T_CO_2_1	10-30°C	±2.2 or 1.1 °C
Boiler outlet temperature, CO_2	T_CO_2_2	20-40°C	±2.2 or 1.1 °C
Condenser inlet temperature, CO_2	T_CO_2_3	20-40°C	±2.2 or 1.1 °C
Condenser outlet temperature, CO_2	T_CO_2_4	10-30°C	±2.2 or 1.1 °C
Evaporator inlet temperature, CO_2	T_CO_2_5	-10-10°C	±2.2 or 1.1 °C
Evaporator outlet temperature, CO_2	T_CO_2_6	-5-15°C	±2.2 or 1.1 °C
Condenser inlet temperature, cooling water	T_H_2O_3	5-20°C	±2.2 or 1.1 °C
Condenser outlet temperature, cooling water	T_H_2O_4	5-30°C	±2.2 or 1.1 °C
evaporator inlet temperature, glycol	T_H_2O_5	-5-30°C	±2.2 or 1.1 °C
evaporator outlet temperature, glycol	T_H_2O_6	-10-10°C	±2.2 or 1.1 °C
Ejector inlet pressure, high pressure,CO_2	P_CO_2_2	0-2000 PSIG	0.25% full scale
Ejector outlet pressure,CO_2	P_CO_2_3	0-1500 PSIG	0.25% full scale
Condenser outlet pressure,CO_2	P_CO_2_4	0-1500 PSIG	0.25% full scale
Evaporator outlet pressure ,CO_2	P_CO_2_5	0-1000 PSIG	0.25% full scale
Boiler mass flow ,CO_2	F1	0-20 kg/min	0.15~ 0.5 %
Evaporator mass flow, CO_2	F2	0-20 kg/min	0.15~ 0.5 %
Pump power, CO_2		2.64 kW	
Boiler electric power		48 kW	

Figure 8.19 Main characteristics of the ejector-based refrigeration system at LTE.

The geometry of the ejector is depicted in Figure 8.21. The measurements of the pressures at the inlets and the outlet can be realized by two pressure probes in the ejector or by manometers apart of the ejector (denoted by P-CO2-M2 and P-CO2-M3 in Figure 8.18). The wall pressure is measured by five sensors along the wall (Figure 8.21(b)). Moreover, the temperature is measured at the inner wall of the mixing duct and diffuser by Ni-CrNi thermocouples (Figures 8.18 P-CO2-2 and P-CO2-3).

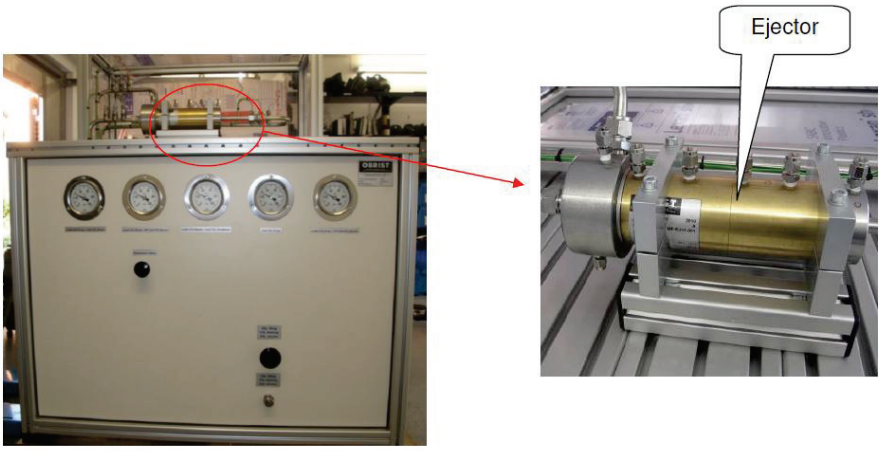

Figure 8.20 CO_2 ejector installation at LTE.

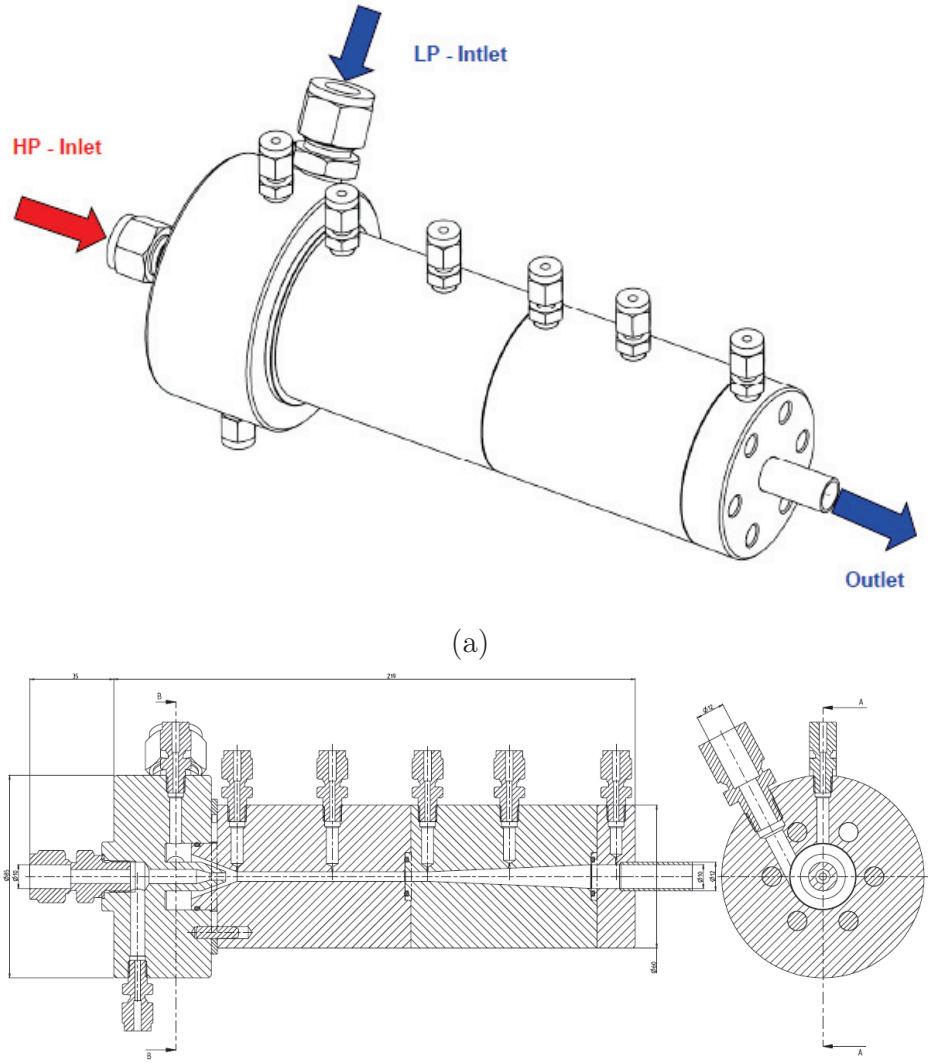

(a)

(b)

Figure 8.21 Schematic views of the CO_2 ejector at LTE.

It can be seen that this system is not arranged as an ejector-expansion cycle because it was designed to test only the ejector for multiple conditions. However, during the experimental campaign, it has been observed that the current design did not allow to provide ejector operation relevant to real conditions, e.g. as an expansion device in a transcritical cycle. Furthermore, it was not possible to cover a full characteristic curve, from on-design to off-design conditions. Indeed, all possible measurements were in the off-design regime and mostly as supercritical states at the vapor side at the primary inlet rather that at the liquid side. However, those results still provide data to be used for partial validation of the model.

Geometry and numerical set-up

The ejector of LTE has been designed and fabricated by the OBRIST ENGINEERING GmbH. It is implemented in a R744 (CO_2) ejector test rig which is modified and optimised at Laboratoire des Technologies de l'Énergie (LTE, Hydro-Québec, Shawinigan). The ejector is cylindrical and the details of the geometry are shown in Figure 8.22.

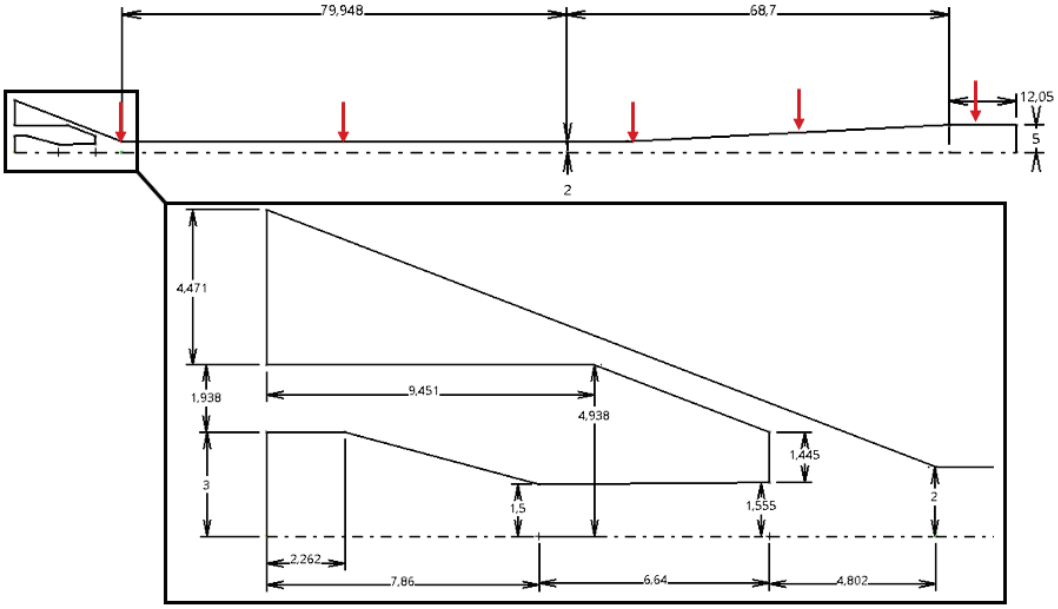

Figure 8.22 Geometry of the two-phase CO_2 ejector at LTE. All dimensions are in millimeters. The dash-dotted line is the symmetry axis.

Table 8.8 summarized the key geometrical parameters of this ejector.

Table 8.8 Geometrical parameters of the ejector (dimensions in millimeters).

r_{in}	r_t	r_{prim}	l_c	l_d	r_{mix}	l_{mix}	l_{diff}	r_{out}
3	1.5	1.55	5.598	6.64	4	80	69.2	5

The radii of the primary inlet, throat, and outlet are denoted by r_{in}, r_t, r_{prim}, while r_{mix} and r_{out} denote the radius of the mixing duct, and the diffuser outlet. It should be noted that the diameter of the primary throat is 3 mm. It is a very large throat compared to other CO_2 ejectors found in the literature [81, 110, 162]. The lengthes of the primary converging part, the primary diverging part, the mixing duct and the diffuser are denoted by l_c, l_d, l_{mix}, and l_{diff}, respectively. Four pressure probes along the ejector wall are used to measure the static pressure. In the simulation, the origin is fixed at the center of the primary inlet. Then, the probe locations are at 19.32 mm, 59.302 mm, 99.302 mm, 133.65 mm, and 178.45 mm, respectively, which correspond to the beginning of the mixing duct,

the middle of the mixing duct, the beginning of the diffuser, the middle of the diffuser, and at the outlet. The probes are also depicted in Figure 8.22 by red arrows.

A semi-cylindrical ejector is meshed with 278640 elements. The structured mesh is generated via Gmsh [70] with y^+ around 85. The realizable $k-\epsilon$ turbulence model is combined with a standard wall function. The Courant number is set to 0.1 at the beginning of the simulation and then increases to 0.4. In accordance with the experimental operating conditions, the static pressure and temperature are imposed at 7.59 MPa and 311.88 K for the primary inlet. It corresponds to a supercritical condition with the density equal to 665 $kg.m^{-3}$, whereas the dynamic viscosity is 5.16 10^{-5} $Pa.s$. At the secondary inlet, the static pressure and temperature are 4.7 MPa and 284.42 K, respectively. It corresponds to a saturated vapor phase with the density equal to 92 $kg.m^{-3}$. At the outlet, the static pressure is imposed at 5.6 MPa. It can be noted that the compression ratio is not very high (= 1.19). Regarding other experiments of two-phase CO_2 ejectors [79, 110, 162, 206], the compression ratio for CO_2 ejectors is indeed relative low compared to ejectors working with other refrigerants. The turbulence intensity at the inlet is 5%, while the turbulence dissipation ϵ is computed based on a specific mixing length l defined as $l = 0.07d_h$ (d_h the hydraulic diameter of the corresponding inlet [8]).

Numerical results

At the first place, the pressure distribution along the centerline of the ejector is compared to the experimental measurements in Figure 8.23. The position of the experimental measurements and the relative errors are also presented.

It can be observed that a shock wave appears at the outlet of the primary nozzle, which causes an abrupt increase of pressure (see Figure 8.23). After that the flow becomes totally subsonic along the mixing duct and diffuser. The relatively large discrepancies are obtained in terms of pressure in the mixing duct, which are 11.7% and 12.3%. It may be due to the turbulence model. One recalls that the realizable $k-\epsilon$ model is here combined with a wall function, which greatly affects the prediction of the boundary layer flow. Similar effects have been already observed for converging-diverging nozzles (Chapter 5). Moreover, in this special case, the results are also sensitive to the inlet and outlet conditions, because this operating condition is extremely off-design.

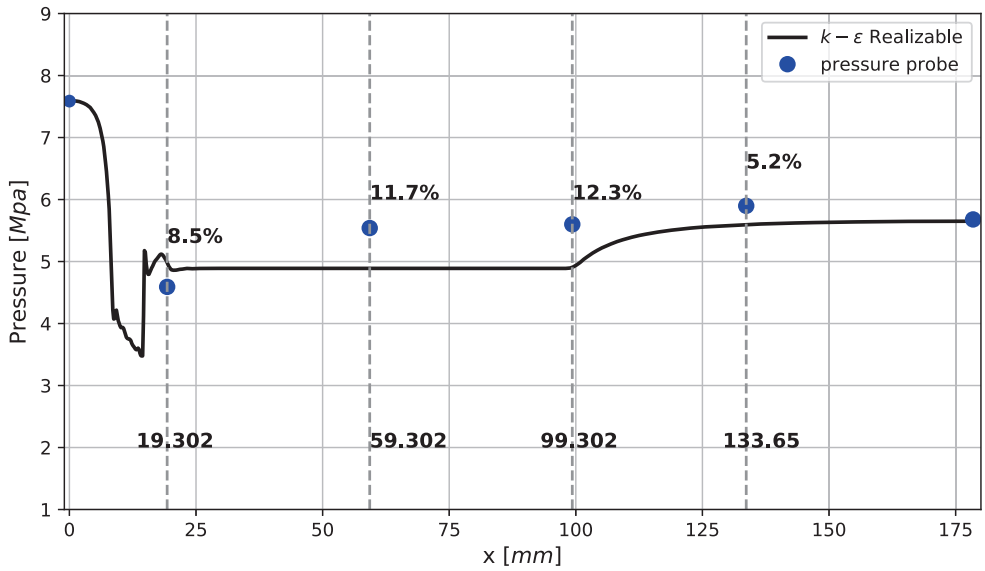

Figure 8.23 Pressure distribution along the centreline of the LTE's ejector. Blue points represent the experimental pressure measurements.

The density gradient map is shown in Figure 8.24. A strong expansion is observed at the throat of the primary nozzle. Then, at the outlet of the primary nozzle, a quasi-normal shock is predicted, which causes an abrupt pressure increase. Moreover, some acoustic waves are captured through this compressible solver as well as their reflections at the wall of the primary nozzle, which are in accordance with the wiggles in the pressure distribution (Figure 8.23). After that, no significant gradient is obtained in the rest of the ejector.

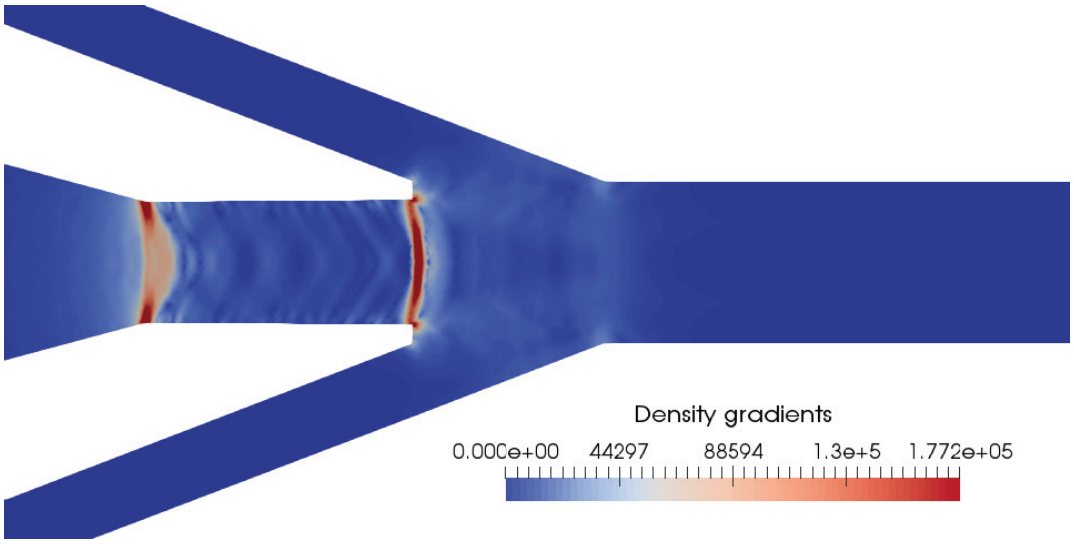

Figure 8.24 Map of the density gradient for the LTE's ejector.

The vapor mass fraction is displayed in Figure 8.25. It can be observed that the flow in the supercritical state at the primary inlet becomes primarily vapor before the nozzle throat. Then, the flow becomes two-phase at the throat due to the expansion. Actually, the initial supercritical state is located at the vapor saturation side (at the right side of the critical point in the $p-h$ diagram). As the expansion is quasi-isentropic, before dropping into the two-phase dome, the phase state crosses the super-heated vapor region and the vapor saturation line. That makes the flow becomes vapor then two-phase. This operating condition is not appropriate for the real application of the EERC. In an EERC, passing through the gas cooler, the CO_2 flow loses energy to produce heating effect. As a result, the CO_2 flow has a low enthalpy with a high pressure. It means that the phase state is probably at the liquid saturation side (the left side of the critical point in the $p-h$ diagram). Hence, when the expansion occurs, the phase state crosses the pressed-liquid region and the liquid saturation line. It means here one does not have a flashing ejector but more a wet vapor ejector.

Moreover, due to the large diameter of the throat, a more powerful compressor is required to have the initial supercritical state at the liquid saturation side. Otherwise the diameter of the throat should be decreased. Hence, appropriate operating conditions are investigated for the ejector of Li *et al.* [110] in the next section. However, this case can still be analyzed to understand flow features in an off-design condition.

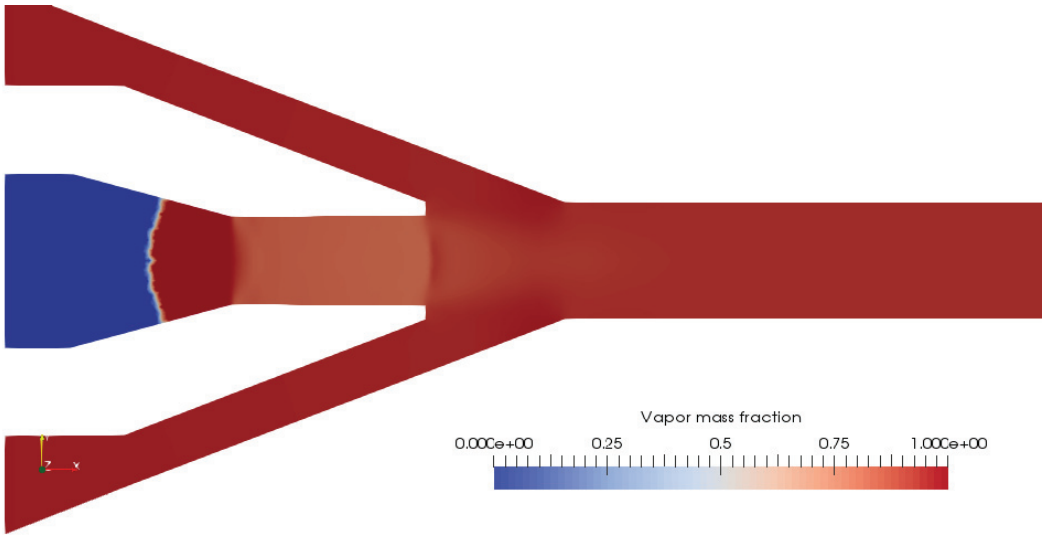

Figure 8.25 Vapor mass fraction for the LTE's ejector.

In order to visualize the transport of mass, momentum, and kinetic energy, the corresponding transport tubes are illustrated in red, green, and blue, respectively at the top half of the ejector in Figure 8.26 (definitions of transport tubes are presented in Section 3.6.1). In a 2D plane, the transport tubes are presented by transport lines instead of surfaces in 3D. For building the transport lines, the corresponding vector fields are first computed in each cell of the computational domain. Then, the transport line is build up with an integrator using a 4^{th}-order Runge-Kutta method in Paraview. The origins of the transport lines are taken from the tip between the upper wall of the primary nozzle and the bottom wall of the secondary nozzle at the NXP. The location of this origin is shown in Figure 3.14.

For example, the mass transport line (in red) is the classical streamline, also called the dividing streamline in the following. By construction, there is no average mass flux passing through the dividing streamline. Hence, the part below the dividing streamline contains the mass flow of the primary stream, whereas the part above contains the mass flow of the secondary stream. This is an average point of view. In reality, there is a transfer of mass across a shear layer. Moreover, it should be noted that there are transfers of momentum and kinetic energy through this dividing streamline but only by diffusion, which causes the change of the dividing streamline. It is also important to note that the dividing streamline never touches the wall, because the mass in the secondary stream is always conserved and it cannot vanish. Similar for the momentum (in green) and the kinetic energy (in blue) transport lines, one can visualise how they are transported from the primary stream to the secondary stream.

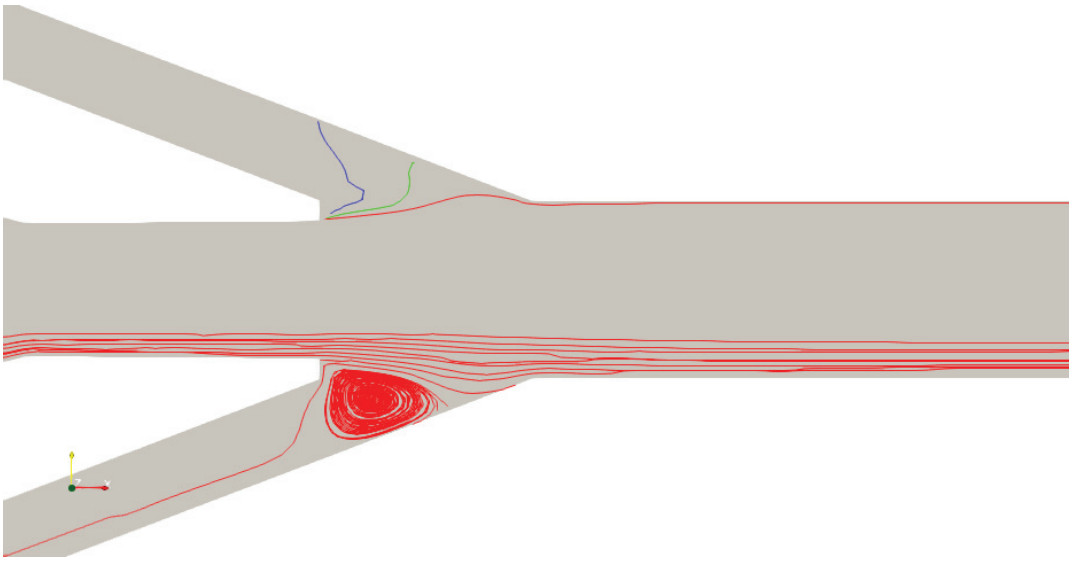

Figure 8.26 Dividing streamline (—), momentum transport line (—), and kinetic energy transport line (—) are illustrated at the top half. At the bottom half, the stream lines at the entrance of mixing duct are presented.

It can be seen that the dividing stream line directs toward the wall of the ejector. This is mainly due to the transfer of momentum and kinetic energy, which cause the increase of the velocity and phase change. The dividing stream line nearly touches the ejector wall at the beginning of the mixing duct, which indicates that all the secondary mass flow is limited in this tiny zone. Then, the dividing stream line is parallel to the ejector wall in the mixing duct and diffuser, which means transfers is nearly finished before the mixing duct.

Regarding the momentum, its transport line touches the wall before the mixing duct. It means that at this point, all momentum originated from the secondary stream are removed by the viscous dissipation or the pressure gradient (Equation (3.87)). Consequently, all the momentum in the secondary stream after this point comes from the primary stream.

A similar trend for the kinetic energy transport line is observed in Figure 8.26. All the mean-flow kinetic energy originated from the secondary stream vanishes at the point where the transport line touches the wall. This is due to the dissipation and the work done by pressure (Equation (3.88)). After this point, only the kinetic energy from the primary stream remains in the ejector.

The streamlines are shown in the bottom half of Figure 8.26. A very important recirculation zone appears between the NXP and the mixing duct. This recirculation zone may induce a significant mixing and dissipation between the primary and the secondary stream.

However, this recirculation zone locates at the exit of the secondary nozzle, which clogs the secondary stream. As a result, only a small amount of the secondary flow is entrained into the ejector. Furthermore, due to this recirculation zone, the transport of momentum and kinetic energy is almost finished before the mixing duct, which makes the ejector not efficient. This kind of recirculation zone was also observed by Lamberts *et al.* [100] in a supersonic air ejector. They found that as the back pressure increases, a recirculation zone moves upstream from the diffuser to the mixing duct. When the operating condition was off-design, the recirculation zone was located at the head of the mixing duct. Compared to the present case, the present recirculation zone is located even more upstream. Hence, the operating condition should be extremely off-design.

In conclusion, the operating condition in this case is not appropriate to EERC applications, which is mainly due to the design of the ejector. Secondly, by analyzing the numerical results, one found that this operating condition was extremely off-design, which means the ejector did not work properly.

LIST OF REFERENCES

[1] Ahammed, M. E., Bhattacharyya, S. and Ramgopal, M. (2014). Thermodynamic design and simulation of a CO_2 based transcritical vapour compression refrigeration system with an ejector. *International Journal of Refrigeration*, volume 45, p. 177–188.

[2] Aidoun, Z., Ameur, K., Falsafioon, M. and Badache, M. (2019). Current advances in ejector modeling, experimentation and applications for refrigeration and heat pumps. Part 1 : Single-phase ejectors. *Inventions*, volume 4(15), pp. 1–73.

[3] Aidoun, Z., Ameur, K., Falsafioon, M. and Badache, M. (2019). Current advances in ejector modeling, experimentation and applications for refrigeration and heat pumps. Part 2 : Two-phase ejectors. *Inventions*, volume 4(16), pp. 1–54.

[4] Alimohammadi, S., Persoons, T., Murray, D. B., Tehrani, M. S., Farhanieh, B. and Koehler, J. (2014). A validated numerical-experimental design methodology for a movable supersonic ejector compressor for waste-heat recovery. *Journal of Thermal Science and Engineering Applications*, volume 6, pp. 2–9.

[5] Ameli, A., Afzalifar, A. and Turunen-Saaresti, T. (2017). Non-equilibrium condensation of supercritical carbon dioxide in a converging-diverging nozzle. In *International Seminar on Non-Ideal Compressible-Fluid Dynamics for Propulsion & Power at Varenna, Italy*. pp. 12–25.

[6] Ameur, K., Aidoun, Z. and Ouzzane, M. (2016). Modeling and numerical approach for the design and operation of two-phase ejectors. *Applied Thermal Engineering*, volume 109, pp. 809–818.

[7] Angielczyk, W., Bartosiewicz, Y., Butrymowicz, D. and Seynhaeve, J. M. (2010). 1D modeling of supersonic carbon dioxide two-phase flow through ejector motive nozzle. In 13^{th} *International Refrigeration and Air Conditioning Conference at West Lafayette, USA*. pp. 1–8.

[8] ANSYS (2010). *Fluent User's Gide* (Technical report). ANSYS.Inc.

[9] ANSYS Academic Research (2015). ANSYS CFX, release 17.0, ANSYS.Inc.

[10] Asproulias, I., Revell, A. J. and Craft, T. J. (2011). An investigation into solver strategies for the modelling of compressible turbulent flow. In *Proceedings of 28th International Symposium on Shock Waves, Manchester, England*.

[11] Aungier, R. H. (1995). A fast, accurate real gas equation of state for fluid dynamic analysis applications. *Journal of Fluids Engineering*, volume 117, pp. 277–281.

[12] Baer, M. R. and Nunziato, J. W. (1986). A two-phase mixture theory for the deflagration-to-detonation transition (ddt) in reactive granular materials. *International Journal of Multiphase Flow*, volume 12, pp. 861–889.

[13] Bai, T., Yan, G. and Yu, J. (2015). Thermodynamic analyses on an ejector enhanced CO_2 transcritical heat pump cycle with vapor-injection. *International Journal of Refrigeration*, volume 58, p. 22–34.

[14] Banasiak, K. and Hafner, A. (2011). 1D computational model of a two-phase R744 ejector for expansion work recovery. *International Journal of Thermal Sciences*, volume 50, pp. 2235–2247.

[15] Banasiak, K. and Hafner, A. (2013). A CFD-based investigation of the energy performance of two-phase R744 ejectors to recover the expansion work in refrigeration systems : An irreversibility analysis. *International Journal of Refrigeration*, volume 40, pp. 328–337.

[16] Bartosiewicz, Y., Aidoun, Z., Desevaux, P. and Mercadier, Y. (2005). Numerical and experimental investigations on supersonic ejectors. *International Journal of Heat and Fluid Flow*, volume 26, pp. 56–70.

[17] Bartosiewicz, Y. and Seynhaeve, J. M. (2013). Delayed equilibrium model (DEM) of flashing flows relevant to LOCA. *Multiphase Science and Technology*, volume 25, pp. 117–131.

[18] Beattie, D. R. H. and Whalley, P. B. (1982). Simple two-phase frictional pressure drop calculation method. *International Journal of Multiphase Flow*, volume 8, pp. 83–87.

[19] Bell, I. H., Wronski, J., Quoilin, S. and Lemort, V. (2014). Pure and pseudo-pure fluid thermophysical property evaluation and the open-source thermophysical property library coolprop. *Industrial & Engineering Chemistry Research*, volume 53, number 6, pp. 2498–2508.

[20] Berana, M. S., Nakagawa, M. and Harada, A. (2010). Shock waves in supersonic two-phase flow of CO_2 converging-diverging nozzles. *HVAC&R Research*, volume 15, pp. 1080–1098.

[21] Bernstein, A., Heiser, W. H. and Hevenor, C. (1967). Compound-compressible nozzle flow. *Journal of Applied Mechanics*, volume 34, pp. 548–554.

[22] Besagni, G., Mereu, R. and Inzoli, F. (2015). CFD study of ejector flow behavior in a blast furnace gas galvanizing plant. *Journal of Thermal Science*, volume 24, pp. 58–66.

[23] Bilicki, Z. and Kestin, J. (1990). Physical aspects of the relaxation model in two-phase flow. *Proceedings of the Royal Society London A*, volume 428, pp. 379–397.

[24] Body, J., Palacz, M., Haida, M., Smolka, J., Nowak, A. J., Banasiak, K. and Hafner, A. (2017). Full- scale multi-ejector module for a carbon dioxide supermarket refrigeration system : numerical study of performance evaluation. *Energy Conversion and Management*, volume 138, pp. 312–326.

[25] Body, J., Smolka, J., Palacz, M., Haida, M., Banasiak, K., Nowak, A. J. and Hafner, A. (2016). Performance of fixed geometry ejectors with a swirl motion installed in a

multi-ejector module of a CO_2 refrigeration system. *Energy*, volume 117, pp. 620–631.

[26] Boger, M. (2013). *Numerical Modeling of Compressible Two-Phase Flows with a Pressure-Based Method*. Ph.D. thesis, Institute of Aerodynamics and Gas Dynamics University of Stuttgart, Stuttgart, Germany.

[27] Boston, J. and Mathias, P. (1980). Phase equilibria in a third-generation process simulator. In *Proceedings of the 2nd International Conference on Phase Equilibria and Fluid Properties in the Chemical Process Industries at Berlin (West), Gemany.* pp. 823–848.

[28] Cabello, R., Sanchez, D., Lopis, R., Catalan, J., Nebot-Andres, L. and Torrella, E. (2017). Energy evaluation of R152a as drop in replacement for R134a in cascade refrigeration plants. *Applied Thermal Engineering*, volume 110, pp. 972–984.

[29] Cai, L. and He, M. (2013). A numerical study on the supersonic steam ejector use in steam turbine system. *Mathematical Problems in Engineering*, volume 2013, pp. 1–10.

[30] Cen, J., Liu, P. and Jiang, F. (2012). A novel transcritical CO_2 refrigeration cycle with two ejectors. *International Journal of Refrigeration*, volume 35, pp. 2233–2239.

[31] CERFACS (2016). AVBP handbook.

[32] Chaiwongsa, P. and Wongwises, S. (2007). Effect of throat diameters of the ejector on the performance of the refrigeration cycle using a two-phase ejector as an expansion device. *International Journal of Refrigeration*, volume 30, pp. 601–608.

[33] Chapman, S. and Cowling, T. G. (1970). *The Mathematical Theory of Uniform Gases*. Cambridge University Press, Cambridge, U.K.

[34] Chen, F., Liu, C. F. and Yang, J. Y. (1994). Supersonic flow in the second-throat ejector-diffuser system. *Journal of Spacecraft Rocket*, volume 31, pp. 123–129.

[35] Chen, X. J., Omer, S., Worall, M. and Riffat, S. (2012). Recent developments in ejector refrigeration technologies. *Renewable & Sustainable Energy Reviews*, volume 19, pp. 629–651.

[36] Chong, D. T., Hu, M., Chen, W., Wang, J., Liu, J. and Yan, J. (2014). Experimental and numerical analysis of supersonic air ejector. *Applied Energy*, volume 130, pp. 679–684.

[37] Chunnanond, K. and Aphornratana, S. (2004). Ejectors : applications in refrigeration technology. *Renewable & Sustainable Energy Reviews*, volume 8, pp. 129–155.

[38] Cicchitti, A., Lombaradi, C., Silversti, M., Soldaini, G. and Zavattarlli, R. (1960). Two-phase cooling experiments pressure drop heat transfer burnout measurements. *Energia Nucleare*, volume 7, pp. 407–425.

[39] Colarossi, M., Trask, N., Schmidt, D. and Bergander, M. (2012). Multidimensional modelling of condension two-phase ejector flow. *International Journal of Refrigeration*, volume 35, pp. 290–299.

[40] Colin, O. and Rudgyard, M. (2000). Development of high-order Taylor–Galerkin schemes for LES. *Journal of Computational Physics*, volume 162, pp. 338–371.

[41] Cramer, M. S. (2012). Numerical estimates for the bulk viscosity of ideal gases. *Physics of Fluids*, volume 24, p. 066102.

[42] Croquer, S., Fang, Y., Poncet, S., Aidoun, Z. and Bartosiewicz, Y. (2017). Turbulence modeling of single-phase ejector working with HFO refrigerants. In *26th Canadian Congress Of Applied Mechanics at Victoria, Canada*.

[43] Croquer, S., Poncet, S. and Aidoun, Z. (2015). Turbulence modelling of a single-phase R134a supersonic ejector. Part 1 : Numerical benchmark. *International Journal of Refrigeration*, volume 61, pp. 140–152.

[44] Croquer, S., Poncet, S. and Aidoun, Z. (2015). Turbulence modelling of a single-phase R134a supersonic ejector. Part 2 : Local flow structure and exergy analysis. *International Journal of Refrigeration*, volume 61, pp. 153–165.

[45] Croquer, S., Poncet, S. and Aidoun, Z. (2017). Thermodynamic modelling of supersonic gas ejector with droplets. *Entropy*, volume 19(579), pp. 1–21.

[46] Davis, S. F. (1988). Simplified second-order Godunov-type methods. *SIAM Journal on Scientific and Statistical Computing*, volume 9, pp. 445–473.

[47] De Lorenzo, M., Lafon, P., Di Matteo, M., Pelanti, M., Seynhaeve, J. M. and Bartosiewicz, Y. (2017). Homogeneous two-phase flow models and accurate steam-water table look-up method for fast transient simulations. *International Journal of Multiphase Flow*, volume 95, pp. 199–219.

[48] Deng, J. Q., Jiang, P. X., Lu, T. and Lu, W. (2007). Particular characteristics of transcritical CO_2 refrigeration cycle with an ejector. *Applied Thermal Engineering*, volume 27, pp. 381–388.

[49] Donea, J. and Huerta, A. (2003). Finite element methods for flow problems. *Wiley*, volume 107, pp. 108–109.

[50] Duan, Z. and Zhang, Z. (2006). Equation of state of the H_2O, CO_2, and H_2O – CO_2 systems up to 10 GPa and 2573.15 K : Molecular dynamics simulations with potential surface. *Geochimica & Cosmochimica Acta*, volume 70, pp. 2311–2324.

[51] Ducros, F., Nicoud, F. and Poinsot, T. (1999). Wall-adapting local eddy-viscosity models for simulations in conplex geometries. In *6th ICFD at Tohoku University, Japan*. pp. 293–299.

[52] Dumbser, M., Iben, U. and Munz, C. D. (2013). Efficient implementation of high order unstructured WENO schemes for cavitating flows. *Computers & Fluids*, volume 86, pp. 141–168.

[53] Elbel, S. (2011). Historical and present developments of ejector refrigeration systems with emphasis on transcritical carbon dioxide air-conditioning applications. *International Journal Refrigeration*, volume 34, pp. 1545–1561.

[54] Elbel, S. and Hrnjak, P. (2008). Experimental validation of a prototype ejector designed to reduce throttling losses encountered in transcritical R744 system operation. *International Journal of Refrigeration*, volume 31, pp. 411–422.

[55] Elbel, S. and Lawrence, N. (2015). Review of recent developments in advanced ejector technology. *International Journal of Refrigeration*, volume 62, pp. 1–18.

[56] Emanuel, G. (1992). Effect of bulk viscosity on a hypersonic boundary layer. *Physics of Fluids*, volume 4, number 491.

[57] European Parliament and the Council (2014). Regulation (EU) No 517/2014 of the European Parliament and the Council of 16 April 2014 on fluorinated greenhouse gases and repealing Regulation (EC) No 842/2006. *Official Journal of the European Union*, volume 150, pp. 195–230.

[58] Fang, Y., Croquer, S., Poncet, S., Aidoun, Z. and Bartosiewicz, Y. (2017). Drop-in replacement in a R134 ejector refrigeration cycle by HFO refrigerants. *International Journal of Refrigeration*, volume 77, pp. 87–98.

[59] Fang, Y., De Lorenzo, M., Lafon, P., Poncet, S. and Bartosiewicz, Y. (2018). An accurate and efficient look-up table equation of state for two-phase compressible flow simulations of carbon dioxide. *Industrial & Engineering Chemistry Research*, volume 57, p. 7676–7691.

[60] Fang, Y., Poncet, S., Bartosiewicz, Y. and Nesreddine, H. (2019). Shock analysis for two-phase CO_2 flows in a converging-diverging nozzle. In *10th International Conference on Multiphase Flow at Rio de Janeiro, Brazil*.

[61] Fang, Y., Poncet, S., Nesreddine, H. and Bartosiewicz, Y. (2019). An open-source density-based solver for two-phase CO_2 compressible flows : verification and validation. *International Journal of Refrigeration*, volume 106, pp. 526–538.

[62] Farzi, N. and Hosseini, P. (2015). A new equation of state for gaseous, liquid, and supercritical fluids. *Fluid Phase Equilibria*, volume 409, pp. 59–71.

[63] Flåtten, T. and Lund, H. (2012). Relaxation two-phase flow models and the subcharacteristic conditions. *Mathematical Models and Methods in Applied Sciences*, volume 21, pp. 2374–2407.

[64] Flåtten, T., Morin, A. and Munkejord, S. T. (2011). On solutions to equilibrium problems for systems of stiffened gases. *SIAM Journal on Applied Mathematics*, volume 71, pp. 41–67.

[65] Fosso, A. P., Deniau, H., Lamarque, N. and Poinsot, T. (2012). Comparison of outflow boundary conditions for subsonic aeroacoustic simulations. *International Journal for Numerical Methods in Fluids*, volume 68, pp. 1207–1233.

[66] Fourar, M. and Bories, S. (1995). Experimental study of air-water two-phase flow through a fracture (narrow channel). *International Journal of Multiphase Flow*, volume 4, pp. 621–637.

[67] García del Valle, J. V., Jabardo, J. M. S., Ruiz, F. C. and Alonso, J. F. S. J. (2014). An experimental investigation of a R-134a ejector refrigeration system. *International Journal of Refrigeration*, volume 46, pp. 105–113.

[68] García del Valle, J. V., Sierra-Pallares, J., Carrascal, P. G. and Ruiz, F. C. (2015). An experimental and computational study of the flow pattern in a refrigerant ejector : Validation of turbulence models and real-gas effects. *Applied Thermal Engineering*, volume 89, pp. 795–811.

[69] Germano, M., Piomelli, U., Moin, P. and Cabot, W. H. (1991). A dynamic subgrid-scale eddy viscosity model. *Physics of Fluids A : Fluid Dynamics*, volume 3, pp. 1760–1765.

[70] Geuzaine, C. and Remacle, J. F. (2009). Gmsh : a three-dimensional finite element mesh generator with built-in pre- and post-processing facilities. *International Journal for Numerical Methods in Engineering*, volume 79, pp. 1309–1331.

[71] Giacomelli, F., Mazzelli, F. and Milazzo, A. (2018). A novel CFD approach for the computation of R744 flashing nozzles in compressible and metastable conditions. *Energy*, volume 162, pp. 1092–1105.

[72] Giljarhus, K. E. T., Munkejord, S. T. and Skaugen, G. (2012). Solution of the Span-Wagner equation of state using a density-energy state function for fluid-dynamic simulation of carbon dioxide. *Industrial & Engineering Chemistry Research*, volume 51, pp. 1006–1014.

[73] Giovangigli, V. and Matuszewskib, L. (2011). Supercritical fluid thermodynamics from equations of state. *Physica D*, volume 241, pp. 649–670.

[74] Godunov, S. K. (1959). A difference method for numerical calculation of discontinuous solutions of the equations of hydrodynamics. *Matematicheskii Sbornik*, volume 47, pp. 271–306.

[75] Grazzini, G., Milazzo, A. and Mazzelli, F. (2018). *Ejectors for Efficient Refrigeration*. Springer International Publishing.

[76] Greenshields, C. J., Weller, H. G., Gasparini, L. and Reese, J. M. (2010). Implementation of semi-discrete, non-staggered central schemes in a colocated, polyhedral, finite volume framework, for high-speed viscous flows. *International Journal for Numerical Methods in Fluids*, volume 63, pp. 1–21.

[77] Guelfi, A., Bestion, D., Boucker, M., an P. Fillion, P. B., Grandotto, M., Hérard, J.-M., Hervieu, E. and Péturaud, P. (2007). Neptune : a new software platform for advanced nuclear thermal hydraulics. *Nuclear Science and Engineering*, volume 156, pp. 281–324.

[78] Hafner, A., Forsterling, S. and Banasiak, K. (2014). Multi-ejector concept for R744 supermarket refrigeration. *International Journal of Refrigeration*, volume 43, pp. 1–13.

[79] Haida, M., Banasiak, K., Smolka, J., Hafner, A. and Eikevik, T. M. (2016). Experimental analysis of the R744 vapour compression rack equipped with the multi-ejector expansion work recovery module. *International Journal of Refrigeration*, volume 64, pp. 93–107.

[80] Haida, M., Smolka, J., Hafner, A., Mastrowski, M., Palacz, M., Madsen, K. B., Nowak, A. J. and Banasiak, K. (2018). Numerical investigation of heat transfer in a CO_2 two-phase ejector. *Energy*, volume 163, pp. 682–698.

[81] Haida, M., Smolka, J., Hafner, A., Palacz, M., Banasiak, K. and Nowak, A. J. (2018). Modified homogeneous relaxation model for the R744 trans-critical flow in a two-phase ejector. *International Journal of Refrigeration*, volume 85, pp. 314–333.

[82] Hakim, L., Ruiz, A., Schmitt, T., Boileau, M., Staffelbach, G., Ducruix, S., Cuenot, B. and Candel, S. (2014). Large eddy simulations of multiple transcritical coaxial flames submitted to a high-frequency transverse acoustic modulation. *Proceedings of the Combustion Institute*, volume 35, number 2, pp. 1461–1468.

[83] Hakkaki-Fard, A., Poirier, M., Aidoun, Z., Ouzzane, M. and Giguère, D. (2015). An experimental study of ejectors supported by CFD. In *Proceedings of the 24th IIR International Congress of Refrigeration at Yokohama, Japan*.

[84] Hammer, M., Ervik, A. and Munkejord, S. T. (2013). Method using a density-energy state function with a reference equation of state for fluid-dynamic of vapor-liquid-solid carbon dioxide. *Industrial & Engineering Chemistry Research*, volume 52, pp. 9965–9978.

[85] Harten, A., Engquist, B., Osher, S. and Chakravarthy, S. R. (1987). Uniformly high order accuracy essentially non-oscillatory schemes III. *Journal of Computational Physics*, volume 71, pp. 231–303.

[86] Harten, A., Lax, P. D. and Leer, B. V. (1983). On upstream differencing and Godunov-type schemes for hyperbolic conservation laws. *SIAM Review*, volume 25, pp. 35–61.

[87] Harvey, A. H. (2016). *Thermophysical properties of carbon dioxide and CO_2-rich mixtures* (Technical report). Applied Chemicals and Materials Division National Institute of Standards and Technology.

[88] Hemidi, A., Henry, F., Leclaire, S., Seynhaeve, J. M. and Bartosiewicz, Y. (2009). CFD analysis of a supersonic air ejector. Part I : Experimental validation of single-phase and two-phase operation. *Applied Thermal Engineering*, volume 29, pp. 1523–1531.

[89] Hemidi, A., Henry, F., Leclaire, S., Seynhaeve, J. M. and Bartosiewicz, Y. (2009). CFD analysis of a supersonic air ejector. Part II : Relation between global operation and local flow features. *Applied Thermal Engineering*, volume 29, pp. 2990–2998.

[90] Huber, M. L., Sykioti, E. A., Assael, M. J. and Perkins, R. A. (2016). Reference correlation of the thermal conductivity of carbon dioxide from the triple point to 1100 K and up to 200 MPa. *Journal of Physical and Chemical Reference Data*, volume 45, p. 013102.

[91] Hughes, T. J. R. (2000). *The finite element method :linear static and dynamic finite element analysis*. Dover Publications.

[92] Jaeger, F., Matar, O. K. and Müller, E. A. (2018). Bulk viscosity of molecular fluids. *Journal of Chemical Physics*, volume 148, p. 174504.

[93] Jeong, H., Utomo, T., Ji, M., Lee, Y., Lee, G. and Hanshik, C. (2009). CFD analysis of flow phenomena inside thermo vapor compressor influenced by operating conditions and converging duct angles. *Journal of Thermal Science*, volume 23, pp. 2366–2375.

[94] Kim, M. H., Pettersen, J. and Bullard, C. W. (2004). Fundamental process and system design issues in CO_2 vapor compression systems. *Progress in Energy and Combustion Science*, volume 30, pp. 119–174.

[95] Kondou, C., Mishima, F., Liu, J. and Koyama, S. (2014). Condensation and evaporation of R134a, R1234ze(E) and R1234ze(Z) flow in horizontal microfin tubes at higher temperature. In *International Refrigeration and Air Conditioning Conference at Purdue, USA*. pp. 1–10.

[96] Kornhauser, A. A. (1990). The use of an ejector as a refrigerant expander. In *Proceedings of 1990 USNC/IIR-Purdue Refrigeration conference at Purdue, USA*.

[97] Kunick, M., Kretzschmar, H. J. and Gampe, U. (2008). Fast calculation of thermodynamic properties of water and steam in process modelling using spline interpolation. In *International Conference on the Properties of Water and Steam at Berlin, Gemany*.

[98] Kurganov, A., Noelle, S. and Petrova, G. (2001). Semi-discrete central-upwind schemes for hyperbolic conservation laws and Hamilton-Jacobi equations. *SIAM Journal on Scientific Computing*, volume 23, pp. 707–740.

[99] Kurganov, A. and Tadmor, E. (2001). New high-resolution central schemes for nonlinear conservation laws and convection-diffusion equations. *Journal of Computational Physics*, volume 160, pp. 241–282.

[100] Lamberts, O., Chatelain, P. and Bartosiewicz, Y. (2017). New methods for analyzing transport phenomena in supersonic ejectors. *International Journal of Heat and Fluid Flow*, volume 64, pp. 23–40.

[101] Lamberts, O., Chatelain, P., Bourgeois, N. and Bartosiewicz, Y. (2018). The compound-choking theory as an explanation of the entrainment limitation in supersonic ejectors. *Energy*, volume 158, pp. 524–536.

[102] Lax, P. and Wendroff, B. (1960). System of conservation laws. *Communications on Pure and Applied Mathematics*, volume 13, pp. 217–237.

[103] Lee, J. S. and Kim, M. S. (2011). Experimental study on the improvement of CO_2 air conditioning system performance using an ejector. *International Journal of Refrigeration*, volume 34, pp. 1614–1625.

[104] Lemmon, E., Huber, M. and McLinden, M. (2010). NIST Standard Reference Database 23 : Reference Fluid Thermodynamic and Transport Properties. In *REFPROP, Version 9.0*, National Institute of Standards and Technology ; Standard Reference Data Program at Gaithersburg, USA.

[105] LeVeque, R. J. (1997). Wave propagation algorithms for multi-dimensional hyperbolic systems. *Journal of Computational Physics*, volume 131, pp. 327–353.

[106] LeVeque, R. J. (2002). *Finite Volume Methods for Hyperbolic Problems*. Cambridge University Press, Cambridge, UK.

[107] LeVeque, R. J. and Berger, M. J. (2017). Clawpack software, version 4.3, http ://www.clawpack.org.

[108] Li, C. and Li, Y. Z. (2010). Investigation of entrainment behavior and characteristics of gas–liquid ejectors based on CFD simulation. *Chemical Engineering Science*, volume 66, pp. 405–416.

[109] Li, D. Q. and Groll, E. A. (2004). Transcritical CO_2 refrigeration cycle with ejector-expansion device. *International Journal of Refrigeration*, volume 28, pp. 766–773.

[110] Li, Y. F., Deng, J. Q., Ma, L. and Zhang, Y. Z. (2018). Visualization of two-phase flow in primary nozzle of a transcritical CO_2 ejector. *Energy Conversion and Management*, volume 171, pp. 729–741.

[111] Liu, F., Groll, E. and Li, D. (2012). Modeling study of an ejector expansion residential CO_2 air conditioning system. *Energy and Buildings*, volume 53, number 53, pp. 127–136.

[112] Liu, F., Groll, E. A. and Li, D. (2012). Investigation of performance of variable geometry ejectors for CO_2 refrigeration cycles. *Energy*, volume 45, number 1, pp. 829–839.

[113] Liu, F., Groll, E. A. and Ren, J. X. (2016). Comprehensive experimental performance analyses of an ejector expansion transcritical CO_2 system. *Applied Thermal Enginerring*, volume 98, pp. 1061–1069.

[114] Liu, J. P., Chen, J. P. and Chen, Z. J. (2002). Thermodynamic analysis on transcritical R744 vapor compression/ejector hybrid refrigeration cycle. In *Proceedings*

of 5th IIR-Gustav Lorentzen Conference on Natural Working Fluids at Guangzhou, China.

[115] Lorentzen, G. (1980). Throttling loss as an internal hemorrhage of refrigeration system. *Chodnictwo*, volume 25, pp. 22–26.

[116] Lucas, C. and Koehler, J. (2013). Experimental investigation of the COP improvement of a refrigeration cycle by use of an ejector. *International Journal of Refrigeration*, volume 6, pp. 1595–1603.

[117] Lucas, C., Rusche, H., Schroeder, A. and Koehler, J. (2014). Numerical investigation of a two-phase CO_2 ejector. *International Journal of Refrigeration*, volume 43, pp. 154–166.

[118] Lund, H., Flåtten, T. and Munkejord, S. T. (2011). Depressurization of carbon dioxide in pipelines - models and methods. *Energy Procedia*, volume 4, pp. 2984–2991.

[119] Mazzelli, F., Little, A. B., Garimella, S. and Bartosiewicz, Y. (2015). Computational and experimental analysis of supersonic air ejector : Turbulence modelling and assessment of 3D effects. *International Journal of Heat and Fluid Flow*, volume 56, pp. 305–316.

[120] McAdams, W. H., Woods, W. K. and Heroman, L. C. (1942). Vaporization inside horizontal tubes II-benzene-oil mixture. *Transactions of ASME*, volume 64, pp. 193–200.

[121] Menegay, P. (1997). *A computational model for two-phase ejector flow.* Ph.D. thesis, Virginia Polytechnic Institute, Blacksburg, USA.

[122] Meng, H. and Yang, V. (2003). A unified treatment of general fluid thermodynamics and its application to a preconditioning scheme. *Journal of Computational Physics*, volume 189, p. 277–304.

[123] Métayer, O. L., Massoni, J. and Saurel, R. (2004). Elaboration equation of state of a liquid and its vapor for two-phase flow models. *International Journal of Thermal Sciences*, volume 43, pp. 265–276.

[124] Meyers, J. and Meneveau, C. (2012). Flow visualisation using momentum and energy transport tubes and applications to turbulent flow in wind farms. *Journal of Fluid Mechanics*, volume 64, pp. 335–358.

[125] Miller, S., Harstad, K. G. and Bellan, J. (2001). Direct numerical simulations of supercritical fluid mixing layers applied to heptane-nitrogen. *Journal of Fluid Mechanics*, volume 436, pp. 1–39.

[126] Nakagawa, M., Berana, M. S. and Kishine, A. (2009). Supersonic two-phase flow of CO_2 through converging-diverging nozzles for the ejector refrigeration cycles. *International Journal of Refrigeration*, volume 32, pp. 1195–1202.

[127] Nakagawa, M., Marasigan, A. R. and Matsukawa, T. (2010). Inhomogeneous compressible numerical analysis with phase change of the mixing phenomena in two-phase ejector using CO_2. In *Proceedings of 7th International Conference on Multiphase Flow at Tampa, USA*.

[128] Nakagawa, M., Marasigan, A. R., Matsukawa, T. and Kurashina, A. (2011). A experimental investigation on the effect of mixing length on the performance of two-phase ejector for CO_2 refrigeration cycle with and without heat exchanger. *International Journal of Refrigeration*, volume 34, number 7, pp. 1604–1613.

[129] National Archives (2006). Regulation (EC) No 842/2006 of the European Parliament and the Council of 17 May 2006 on certain fluorinated greenhouse gases.

[130] Palacz, M., Haida, M., Smolka, J., Nowak, A. J., Banasiak, K. and Hafner, A. (2016). HEM and HRM accuracy comparison for the simulation of CO_2 expansion in two-phase ejectors for supermarket refrigeration systems. *Applied Thermal Engineering*, volume 115, pp. 160–169.

[131] Palacz, M., Smolka, J., Fic, A., Bulinski, Z., Nowak, A. J., Banasiak, K. and Hafner, A. (2015). Application range of the HEM approach for CO_2 expansion inside two-phase ejectors for supermarket refrigeration systems. *International Journal of Refrigeration*, volume 59, pp. 251–258.

[132] Park, S. and Rhee, S. H. (2015). Comparative study of incompressible and isothermal compressible flow solvers for cavitating flow dynamics. *Journal of Mechanical Science and Technology*, volume 29(8), pp. 3287–3296.

[133] Pelanti, M. and Shyue, K. M. (2014). A mixture-energy-consistent six-equation two-phase numerical model for fluids with interfaces, cavitation and evaporation waves. *Journal of Computational Physics*, volume 259, pp. 331–357.

[134] Peng, D. Y. and Robinson, D. B. (1976). A new two-constant equation of state. *Industrial & Engineering Chemistry Fundamentals*, volume 15, number 1, pp. 59–64.

[135] Perrot, P. (1998). *A to Z Thermodynamic*. Oxford University Press.

[136] Plöcker, U., Knap, H. and Prausnitz, J. (1978). Calculation of high-pressure vapour-liquid equilibria from a corresponding-states correlation with emphasis on asymmetric mixtures. *Industrial & Engineering Chemistry Process Design and Development*, volume 17, number 3, pp. 324–332.

[137] Poinsot, T. and Lele, S. K. (1992). Boundary condition for direct simulations of compressible viscous flows. *Journal of Computational Physics*, volume 101, pp. 104–129.

[138] Pope, S. B. (2012). *Turbulent Flows*. Cambridge University Press.

[139] Pratt, R. M. (2001). Thermodynamic properties involving derivatives using the Peng-Robinson equation of state. *Chemical Engineering Education*, volume 35, pp. 112–115.

[140] Raman, S. K. and Kim, H. D. (2018). Solutions of supercritical CO_2 flow through a converging-diverging nozzle with real gas effects. *International Journal of Heat and Mass Transfer*, volume 116, pp. 127–135.

[141] Reddick, J. C. (2012). *Conception, construction et analyse d'un système de réfrigération à éjecteur*. Master's thesis, Université de Sherbrooke, Canada.

[142] RELAP5/MOD3.3 (2001). Code manuel, Idaho falls, USA.

[143] Riber, E., Vermorel, O., Gicquel, L. Y. M., Staffelbach, G., Duchaine, F., Dauptain, A. and Poinsot, T. (2013). Large eddy simulation of two-phase flow combustion. In *Proceedings of MUSAF II Colloquium at Toulouse, France*.

[144] Riffat, S. B., Gan, G. and Smith, S. (1996). Computational fluid dynamics applied to ejector heat pumps. *Applied Thermal Engineering*, volume 16, pp. 291–297.

[145] Riffat, S. B., Jiang, L. and Gan, G. (2005). Recent development in ejector technology-a review. *International Journal of Ambient Energy*, volume 26, number 1, pp. 13–26.

[146] Riffat, S. B. and Omer, S. A. (2001). CFD modelling and experimental investigation of an ejector refrigeration system using methanol as the working fluid. *International Journal of Energy Research*, volume 25, pp. 115–128.

[147] Robert, J. K. and Miller, A. R. (1954). *Heat and thermodynamic*. Interscience Publishers.

[148] Roe, P. L. (1986). Characteristic-based schemes for the Euler equations. *Annual Review of Fluid Mechanics*, volume 18, pp. 337–365.

[149] Ruangtrakoon, N., Thongtip, T., Aphornratana, S. and Sriveerakul, T. (2012). CFD simulation on the effect of primary nozzle geometries for a steam ejector in refrigeration cycle. *International Journal of Thermal Sciences*, volume 32, pp. 1203–1211.

[150] Ruas, V. (2016). *Numerical methods for partial differential equations : An introduction*. Wiley, New-York.

[151] Sagaut, P. (2009). *Large eddy simulation for compressible flows*. Springer Science.

[152] Samaké, O. (2016). *Analyse thermo-économique d'un système de dessalement par thermocompression de vapeur et conception de l'éjecteur*. Ph.D. thesis, Université de Sherbrooke, Sherbrooke, Canada.

[153] Sarevski, M. N. and Sarevski, V. N. (2014). Preliminary study of a novel R718 refrigeration cycle with single stage centrifugal compressor and two-phase ejector. *International Journal of Refrigeration*, volume 40, pp. 435–449.

[154] Sarkar, J. (2012). Ejector enhanced vapor compression refrigeration and heat pump systems—a review. *Renewable and Sustainable Energy Reviews*, volume 16, pp. 6647–6659.

[155] Saurel, R., Petitpas, E. and Berry, R. A. (2009). Simple and efficient relaxation methods for interfaces separating compressible fluids, cavitating flows and shocks in multiphase mixture. *Journal of Computational Physics*, volume 228, pp. 1678–1772.

[156] Schmidt, D. P., Gopalakrishnan, S. and Jasak, H. (2016). Multi-dimensional simulation of thermal non-equilibrium channel flow. *International Journal of Multiphase Flow*, volume 36, pp. 284–292.

[157] Schmitt, T., Selle, L., Ruiz, A. and Cuenot, B. (2010). Large-eddy simulation of supercritical-pressure round jets. *AIAA Journal*, volume 48, number 9, pp. 2133–2144.

[158] Scott, D. and Aidoun, Z. (2011). *CFD analysis of an ejector for cooling applications* (Technical Report 347). Resources Natural Canada, Varennes, Canada.

[159] Scott, D., Aidoun, Z., Bellache, O. and Ouzzane, M. (2008). CFD simulations of a supersonic ejector for use in refrigeration applications. In *International Refrigeration and Air Conditioning Conference at Purdue, USA*. pp. 1717–1723.

[160] Shestopalov, K. O., Huang, B. J., Petrenko, V. O. and Volovyk, O. S. (2015). Investigation of an experimental ejector refrigeration machine operating with refrigerant R245fa at design and off-design working conditions. part 2. theoretical and experimental results. *International Journal of Refrigeration*, volume 55, pp. 212–223.

[161] Smagorinsky, J. (1963). General circulation experiments with the primitive equations. *Monthly Weather Review*, volume 91, number 3, pp. 150–182.

[162] Smolka, J., Bulinski, Z., Fic, A., Nowak, A. and Banasiak, K. (2013). A computational model of transcrritical R744 ejector based on a homogeneous real fluid approach. *Applied Mathematic Model*, volume 37, pp. 1208–1224.

[163] Sobieski, W. (2003). Performance of an air-air ejector : an attempt at numerical modelling. *Task quarterly 7*, volume 3, pp. 449–457.

[164] Span, R. and Wagner, W. (1994). A new equation of state for carbon dioxide covering the fluid region from the triple-point temperature to 1100 K at pressures up to 800 MPa. *Journal of Physical and Chemical Reference Data*, volume 25, number 6, pp. 1509–1596.

[165] Sriveerakul, T., Aphornratana, S. and Chunnanond, K. (2007). Performance prediction of steam ejector using computational fluid dynamics : Part 1. Validation of the CFD results. *International Journal of Thermal Sciences*, volume 46, pp. 812–822.

[166] Sriveerakul, T., Aphornratana, S. and Chunnanond, K. (2007). Performance prediction of steam ejector using computational fluid dynamics : Part 2. Flow structure of a steam ejector influenced by operating pressures and geometries. *International Journal of Thermal Sciences*, volume 46, pp. 823–833.

[167] Starling, K. E. and Han, M. S. (1972). Thermo data refined for LPG. *Part 14 : Mixtures, Hydrocarbon Process*, volume 51, number 5, pp. 129–132.

[168] Sumeru, K., Nasution, H. and Ani, F. (2012). A review on two-phase ejector as an expansion device in vapor compression refrigeration cycle. *Renewable and Sustainable Energy Reviews*, volume 16, pp. 4927–4937.

[169] Sun, D. W. (1997). Solar powered combined ejector-vapour compression cycle for air conditioning and refrigeration. *Energy Conversion and Management*, volume 38, pp. 479–491.

[170] Swesty, F. D. (1996). Thermodynamically consistent interpolation for equation of state tables. *Journal of Computational Physics*, volume 127, pp. 118–127.

[171] Taslimi Taleghani, S., Sorin, M. and Poncet, S. (2018). Energy and exergy efficiencies of different configurations of the ejector-based CO_2 refrigeration systems. *International Journal of Energy Production and Management*, volume 87, pp. 22–33.

[172] Taslimi Taleghani, S., Sorin, M. and Poncet, S. (2018). Modeling of two-phase transcritical CO_2 ejectors for on-design and off-design conditions. *International Journal of Refrigeration*, volume 87, pp. 91–105.

[173] Tiselj, I., Horvat, A. and Gale, J. (2008). Numerical scheme of the WAHA code. *Multiphase Science Technology*, volume 20, pp. 323–354.

[174] Tisza, L. (1941). Supersonic absorption and Stokes' viscosity relation. *Physical Review*, volume 61, pp. 531–536.

[175] Titarev, V. A. and Toro, E. F. (2005). Musta schemes for multi-dimensional hyperbolic systems : analysis and improvements. *International Journal of Numerical Methods in Fluids*, volume 49, pp. 117–147.

[176] Toda, H. B., Cabrit, O., Balarac, G., Bosek, S., Lee, J., Choi, H. and Nicoud, F. (2010). Subgrid-scale model based on singular values for LES in complex geometries. In *Proceedings of the Summer Program 2010 at Center for Turbulence Research, Stanford, USA*. pp. 293–299.

[177] Toro, E. F. (1997). *Riemann solvers and numerical methods for fluids dynamics*. Springer-Verlag, Berlin.

[178] Toro, E. F., Spruce, M. and Speares, W. (1994). Restoration of the contact surface in the HLL Riemann solver. *Shock Waves*, volume 4, pp. 25–34.

[179] Toro, E. F. and Titarev, V. A. (2006). MUSTA fluxes for systems of conservation laws. *Journal of Computational Physics*, volume 216, pp. 403–429.

[180] Toyota (2007). *Toyota hybrid system* (Technical report). University of Toyota.

[181] Untea, G. A., Dobrovicescu, A., Grosu, L. and Mladin, E. C. (2013). Energy and exergy analysis of an ejector refrigeration system. *UPB Scientific Bulletin, Series D Mechanical Engineering*, volume 75, pp. 111–126.

[182] van Albada, G. D., van Leer, B. and Roberts Jr., W. W. (1982). A comparative study of computational methods in cosmic gas dynamics. *Astronomy & Astrophysics*, volume 108(1), pp. 76–84.

[183] Van Der Waals, J. D. (1910). The equation of state for gases and liquids. *Nobel Lectures Physics*, volume 4, pp. 254–265.

[184] van Leer, B. (1974). Towards the ultimate conservative difference scheme, II : monotonicity and conservation combined in a second-order scheme. *Journal of Computational Physics*, volume 14, number 4, pp. 361–370.

[185] van Leer, B. (1979). Towards the ultimate conservative difference scheme, V : a second-order sequel to Godunov's method. *Journal of Computational Physics*, volume 54, pp. 101–136.

[186] Varga, S., Pedro, M. S. L. and Oliveira, A. C. (2012). CFD study of a variable area ratio ejector using R600a and R152a refrigerants. *International Journal of Refrigeration*, volume 36, pp. 157–165.

[187] Vesovic, V., Wakeham, W. A., Olchowy, G. A., Sengers, J. V., Watson, J. T. R. and Millat, J. (1989). The transport properties of carbon dioxide. *Journal of Physical and Chemical Reference Data*, volume 19, pp. 763–808.

[188] Wagner, W., Cooper, J., Dittmann, A., Kijima, J., Kretzschmar, H., Kruse, A., Mares, R., Oguchi, K., Sato, H., Stocker, I., Sifner, O., Takaishi, Y., Tanishita, I., Trubenbach, J. and Willkommen, T. (2000). The IAPWS industrial formulation 1997 for the thermodynamic properties of water and steam. *ASME Journal of Engineering Gas Turbine and Power*, volume 122, pp. 150–182.

[189] Wagner, W. and PruB, A. (2002). The IAPWS formulation 1995 for the thermodynamic properties of ordinary water substance for general and scientific use. *Journal of Physical and Chemical Reference Data*, volume 31, number 2, pp. 387–535.

[190] Wang, J. J. and Chen, F. (1996). On the start condition of a second-throat ejector-diffuser. *Aeronautical Journal*, volume 10, pp. 321–326.

[191] Weller, H. G., Tabor, G., Jasak, H. and Fureby, C. (1998). A tensorial approach to computational continuum mechanics using object-oriented techniques. *Computers In Physics*, volume 12, pp. 620–631.

[192] Wood, A. A. (1964). *A textbook of sound*. G. Bell and Sons, London.

[193] Xu, X. X., Chen, G. M., Tang, L. M. and Zhu, Z. J. (2012). Experimental investigation on performance of transcritical CO_2 heat pump system with ejector under optimum high-side pressure. *Energy*, volume 44, pp. 870–877.

[194] Yari, M. and Sirousazar, M. (2008). Cycle improvement to ejector–expansion transcritical CO_2 two-stage refrigeration cycle. *International Journal Energy Research*, volume 32, pp. 677–687.

[195] Yazdani, M., Abbas, A. and Radcliff, T. (2012). Numerical modelling of two-phase supersonic ejectors for work-recovery applications. *International Journal of Heat and Mass Transfer*, volume 55, pp. 5744–5753.

[196] Yazdani, M., Alahyari, A. and Radcliff, T. D. (2014). Numerical modelling and validation of supersonic two-phase flow of CO_2 in converging-diverging nozzles. *Journal of Fluids Engineering*, volume 136, number 1, pp. 014503–1–014503–6.

[197] Yoo, C. S. and Im, H. G. (2007). Characteristic boundary conditions for simulations of compressible reacting flows with multidimensional, viscous and reaction effects. *Combustion Theory and Modelling*, volume 11, pp. 259–286.

[198] Yoshizawa, A. and Horiuti, K. (1985). A statistically-derived subgrid-scale kinetic energy model for the large-eddy simulation of turbulent flows. *Journal of the Physical Society of Japan*, volume 54, pp. 2834–2839.

[199] Yu, J. and Du, Z. (2010). Theoretical study of a transcritical ejector refrigeration cycle with refrigerant R143a. *Renewable Energy*, volume 35, pp. 2034–2039.

[200] Zegenhagen, T. and Ziegler, F. (2015). Experimental investigation of the characteristics of a jet-ejector and a jet-ejector cooling system operating with R134a as a refrigerant. *International Journal of Refrigeration*, volume 56, pp. 173–185.

[201] Zhang, Z. and Tian, L. (2014). Effect of suction nozzle pressure drop on the performance of an ejector-expansion transcritical CO_2 refrigeration cycle. *Entropy*, volume 16, pp. 4309–4321.

[202] Zheng, B. and Wang, Y. W. (2010). A combined power and ejector refrigeration cycle for low temperature heat sources. *Solar Energy*, volume 84, pp. 784–791.

[203] Zhu, Y. and Jiang, P. (2012). Hybrid vapor compression regfrigeration system with an integrated ejector cooling cycle. *International Journal of Refrigeration*, volume 35, pp. 68–78.

[204] Zhu, Y. and Jiang, P. (2013). Experimental and numerical investigation of the effect of shock wave characteristics on the ejector performance. *International Journal of Refrigeration*, volume 40, pp. 31–42.

[205] Zhu, Y. H. and Jiang, P. X. (2014). Experimental and analytical studies on the shock wave length in convergent and convergent-divergent nozzle ejectors. *Energy Conversion and Management*, volume 88, pp. 907–914.

[206] Zhu, Y. H., Li, C. H., Zhang, F. Z. and Jiang, P. X. (2017). Comprehensive experimental study on a transcriticcal CO_2 ejector-expansion refrigeration system. *Energy Conversion and Management*, volume 151, pp. 98–106.

[207] Zhu, Y. H., Wang, Z. C., Yang, Y. P. and Jiang, P. X. (2017). Flow visualization of supersonic two-phase transcritical flow of CO_2 in an ejector of a refrigeration system. *International Journal of Refrigeration*, volume 74, pp. 352–359.

[208] Zuckerwar, A. J. and Ash, R. L. (2006). Variational approach to the volume viscosity of fluids. *Physics of Fluids*, volume 8, p. 047101.